



THÈSE

Présentée à L'Université de Lille

Laboratoire de PhysicoChimie des Processus de Combustion et de l'Atmosphère

En vue de l'obtention du grade de Docteur de l'Université de Lille

École Doctorale des Sciences de la Matière, du Rayonnement et de l'Environnement

Understanding of atmospheric and indoor air chemistry through HO_x radical measurements

Compréhension de la chimie de l'atmosphère et de l'air intérieur grâce aux mesures des radicaux HO_x

Présentée Par

Nesrine SHAMAS

Thèse soutenue le 23 Novembre 2023

Rapporteur	Abdelwahid MELLOUKI	Professeur, Université Mohammed VI Polytechnic, Ben Guerir (Maroc)
Rapporteur	Dwayne HEARD	Professeur, Université de Leeds
Examineur	Sébastien DUSANTER	Maître de conférences, IMT Lille Nord Europe
Président de jury	Véronique DAËLE	Directrice de recherche, ICARE, CNRS Orléans
Directrice de thèse	Coralie SCHOEMAECCKER	Directrice de recherche, Université de Lille - PC2A
Co-directrice de thèse	Christa FITTSCHEN	Directrice de recherche, Université de Lille - PC2A



Acknowledgements

First and foremost, I would like to express my deepest appreciation to my supervisor Coralie Schoemaeker. Your exceptional academic expertise, guidance, advice and encouragement throughout the duration of this project have been invaluable. I cannot envision a better PhD supervisor. I would like also to thank my co-supervisor Christa Fittschen for her support and suggestions. Your insights have greatly enriched the quality of my work. Many thanks to Laure Pillier for your kindness and for sacrificing your time when we needed it. It was greatly appreciated.

My sincere thanks to my PhD thesis committee members for evaluating this work. Thank you Dwayne Heard and Abdelwahid Mellouki for your time and effort reading my manuscript for providing valuable feedback. Thanks to the examiner Sébastien Dusanter and president of the jury Veronique Daële for your remarks and suggestions during these three years.

Many thanks to the director of the PC2A laboratory, Benjamin Hanoune for his time and effort devoted to our research. Also, I would like also to thank all the technical and administrative staff of the laboratory who indirectly contributed to this project.

Among the most memorable highlights of my PhD journey was the opportunity to participate in two field campaigns, in the Rambouillet forest and in Jülich. This enriching experience would not have been possible without the dedication and support of Sebastien Batut and Amaury Lahccen. I am deeply grateful for the knowledge, connections and friendships that were forged during that period.

A special appreciation goes to my great friends in the lab for your help, kindness and the nice moments that we shared. Thanks to Sabah, Nour, Maria, Thi, Kanika, Mohamed G., Cuihong, Mohamed A., Mona and Tirthankar. I want to thank also Rima, Mikel, Mohamad T., Nour and Ghoufrane for all the laughs and great memories we had together.

On personal level, I would like to express my deepest gratitude to my wonderful family whose belief in my abilities and support me. To my role models, mom and dad, BIG thank you from the bottom of my heart for everything! To my great brothers, Hussien, Mohamad, Hasan and beloved Abbas and to my sister's amazing family, Layal, Ali and Mart, thanks a lot for your never-ending love and care.

Lastly, I would like to dedicate this PhD thesis to the reason of my success, happiness and hard work, to my dear sister, Mirna.

Abstract

HO_x ($\text{OH}+\text{HO}_2$) and RO_2 radicals are involved in oxidation processes in the gas phase, generating secondary products impacting the air quality and human health. Understanding these oxidation processes through the quantification of these radicals is still challenging because of their low concentrations ($< \text{ppt}$) and high reactivity. There are only a few instruments worldwide allowing to perform such measurements, among them, the UL (University of Lille)-FAGE (Fluorescence Assay by Gas Expansion) instrument. It is based on LIF (Laser Induced Fluorescence) detection of OH at low pressure. It allows the direct measurement of OH and indirect measurement of HO_2 after chemical conversion to OH through the addition of low NO concentrations at the entrance of the FAGE cell. During this thesis, the instrument has been improved for the quantification of RO_2 radicals. Two complementary measurements allow to access to RO_2 concentration, either by using the HO_2 cell and injecting high NO concentration at the entrance of the FAGE cell or by adding a RO_x -conversion reactor on top of a FAGE cell. This technique is based on a two-step chemical conversion of RO_2 radicals into HO_2 in the conversion reactor coupled to a FAGE cell and its subsequent detection in the FAGE cell after conversion in OH. We can also measure another useful parameter using a FAGE cell coupled to a photolysis reactor: the OH reactivity (sum of OH losses).

The UL-FAGE instrument has been improved and used during this work for laboratory measurements (reactivity configuration) to study the oxidation mechanisms of reactions important for indoor and outdoor chemistry involving HO_x radicals. During summer 2022, the UL-FAGE participated in an RO_2 intercomparison campaign which took place at the SAPHIR chamber (Jülich, Germany). Nine groups using different instruments participated in this campaign. The performance of the UL-FAGE instrument for the OH, HO_2 and RO_2 measurement under a wide range of atmospherically relevant chemical conditions (e.g. water vapor, nitrogen oxide, various organic compound, day and night chemistry) has been investigated during this campaign. Finally, the UL-FAGE in both quantification and reactivity configuration was deployed to a field campaign (ACROSS) in the Rambouillet forest. The reactivity was measured at two different heights (at the ground and above the canopy) whereas the radical concentrations were measured only at the ground.

Keywords: Atmospheric chemistry, HO_x and RO_2 radicals, FAGE instrument, field campaigns, simulation chamber, kinetic studies

Table of Contents

Abstract	5
Table of Contents	7
List of Figures	12
List of Tables.....	18
General Introduction	20
Chapter 1: Tropospheric Radical Chemistry	24
1.1. General context	24
1.1.1. Tropospheric Chemical Composition	24
1.1.2. Chemistry of the main oxidants in the troposphere	24
1.1.2.1. OH chemistry.....	25
1.1.2.2. O ₃ chemistry	29
1.1.2.3. NO ₃ chemistry	31
1.1.3. Indoor Chemistry	31
1.1.3.1. Sources and types of organosiloxanes	32
1.1.3.2. Chemistry of siloxanes	33
1.2. Measurement of HO _x and RO _x radicals in the atmosphere.....	36
1.2.1. Quantification of OH radicals in the atmosphere.....	37
1.2.1.1. The FAGE technique	37
1.2.1.2. The DOAS technique.....	38
1.2.1.3. The CIMS technique.....	39
1.2.2. Detection of tropospheric HO ₂ and RO ₂	39
1.2.2.1. The FAGE technique	40
1.2.2.2. The PERCA technique.....	40
1.2.2.3. The PeRCIMS technique	41
1.2.3. Field measurements of HO _x and RO _x radicals in the troposphere and modeling	42

1.2.4.	Interferences on HO _x measurements.....	43
1.2.4.1.	Interferences on OH measurements using FAGE technique	43
1.2.4.2.	Interferences on HO ₂ measurements using FAGE technique.....	45
1.2.5.	Principle of the OH reactivity	46
1.2.5.1.	Measurement techniques of tropospheric OH reactivity	46
1.2.5.2.	Field measurements of OH reactivity in the troposphere and modeling	48
1.3.	Conclusion.....	51
2.	Chapter 2: Experimental Set-up	53
2.1.	The UL-FAGE Technique.....	53
2.1.1.	Measurement Configuration used during Atmospheric Measurements.....	54
2.1.1.1.	ACROSS campaign	54
2.1.1.2.	RO ₂ intercomparison campaign : SAPHIR chamber	55
2.1.2.	Measurement Configuration used during Laboratory Studies	55
2.1.2.1.	Influence of humidity on radical + radical reaction	55
2.1.2.2.	Chemistry of Siloxanes.....	56
2.2.	Description of the FAGE cells used in the different configurations	56
2.3.	The Excitation Laser	59
2.4.	The Reference Cell.....	62
2.5.	Description of the UL-FAGE in the Quantification Mode.....	63
2.5.1.	FAGE instrument for HO _x quantification	63
2.5.2.	RO _x -FAGE instrument for RO ₂ quantification	64
2.5.2.1.	Conversion principle.....	65
2.5.2.2.	Experimental Setup.....	67
2.5.3.	Calibration of the FAGE instrument.....	68
2.5.3.1.	Calibration cell setup	69
2.5.3.2.	Determination of calibration parameters	70
2.5.3.3.	Calibration uncertainties	74

2.5.3.4.	Radical losses in the calibration cell.....	75
2.5.4.	H ₂ O dependence of the FAGE instrument sensitivity	78
2.5.5.	O ₃ interferences.....	78
2.6.	Description of the UL-FAGE technique for OH reactivity and kinetic studies .	79
2.6.1.	The photolysis cell and photolysis laser	80
2.6.2.	The Gas Flow	81
2.6.3.	Validation of the reactivity setup	83
2.7.	Improvements and validation of the different instruments	84
2.7.1.	Validation of the Sirah CREDO dye laser	84
2.7.2.	Optimization of the UL-RO _x -FAGE setup: (for RO ₂ measurement).....	86
2.7.2.1.	Reaction time and Pressure dependence.....	86
2.7.2.2.	NO dependence.....	89
2.7.2.3.	CO dependence	90
2.8.	Conclusion.....	91
3.	Chapter 3: Kinetic Studies in Laboratory	93
3.1.	The dependence of humidity on the HO ₂ yield in the RO ₂ + OH reaction	93
3.1.1.	Introduction.....	94
3.1.2.	Experimental description	97
3.1.3.	Method	99
3.1.3.1.	Extract of the HO ₂ profiles for the reference reaction CO+OH	100
3.1.3.2.	Determination of the experimental conditions for C ₂ H ₅ O ₂ + OH reaction study	106
3.1.4.	Experimental results and discussion	110
3.1.5.	Conclusion and Perspective of the work on RO ₂ + OH.....	113
3.2.	Chemistry of Siloxanes	114
3.2.1.	Preliminary tests on Siloxanes	114
3.2.2.	Conclusion and Perspective of the work on siloxane reactivity	117

4.	Chapter 4: SAPHIR Intercomparison Campaign.....	119
4.1.	State of the art of intercomparison measurements for radicals	119
4.1.1.	OH intercomparison measurements	119
4.1.2.	HO ₂ and RO ₂ intercomparison measurements	121
4.2.	The atmosphere simulation chamber SAPHIR	122
4.2.1.	Description of the SAPHIR chamber.....	122
4.2.2.	Measurement Protocol at the SAPHIR chamber.....	123
4.2.3.	Instruments coupled to the SAPHIR chamber	124
4.2.3.1.	FAGE instruments for HO _x radical measurements	125
4.2.3.2.	FAGE instruments for RO _x radical measurements.....	127
4.3.	Experiments performed at the SAPHIR chamber	128
4.3.1.	Simple chemistry: CO and CH ₄ oxidation by OH	130
4.3.1.1.	CO and CH ₄ oxidation by OH experiment done on August 8.....	131
4.3.1.2.	CO and CH ₄ oxidation by OH experiment done on August 20.....	134
4.3.2.	Night-time chemistry	137
4.3.2.1.	Trans-2-hexene ozonolysis done on August 19.....	138
4.3.2.2.	β-pinene NO ₃ oxidation experiment done on August 22.....	141
4.3.3.	BVOCs oxidation by OH.....	144
4.3.3.1.	Experimental conditions	144
4.3.3.2.	Experimental results	144
4.3.3.3.	Comparison between Lille and Jülich measurements.....	146
4.3.4.	Anthropogenic chemistry	147
4.3.4.1.	Experimental conditions	147
4.3.4.2.	Experimental results	147
4.3.4.3.	Comparison between Lille and Jülich measurements.....	149
4.3.5.	Ambient chemistry	149
4.3.5.1.	Experimental Conditions	150

4.3.5.2.	Experimental results	150
4.3.5.3.	Comparison between Lille and Jülich measurements.....	152
4.3.6.	Summary of the intercomparison results of all experiments.....	153
4.3.7.	Calibration source exchange	157
4.4.	Conclusion.....	162
5.	Chapter 5: ACROSS Field Campaign	165
5.1.	Introduction	165
5.2.	Site description	167
5.3.	Deployment of radical measurements in the ACROSS field campaign.....	168
5.3.1.	Experimental details.....	168
5.3.2.	Complementary measurements	171
5.4.	Results and discussion.....	172
5.4.1.	OH reactivity	172
5.4.1.1.	OH reactivity measured and meteorological parameters.....	173
5.4.1.2.	OH reactivity calculation	179
5.4.1.3.	Measured and calculated OH reactivity below and above the canopy .	183
5.4.1.4.	Contribution of VOCs to calculated OH reactivity at two heights.....	186
5.4.2.	Radical Quantification	188
5.4.2.1.	OH quantification	189
5.4.2.2.	HO ₂ quantification	191
5.4.2.3.	RO _x quantification	193
5.5.	Conclusion.....	195
	General conclusion and perspectives	197
	Bibliography	200
	Annex	223
	Résumé.....	240

List of Figures

Figure 1: Scheme representing the oxidation processes in the troposphere.....	26
Figure 2: Reaction scheme of the isoprene oxidation (Stavrakou et al., 2010).....	29
Figure 3: Ozonolysis of alkenes reaction	30
Figure 4: Simplified scheme of the reaction of NO ₃ with isoprene producing HO _x and peroxy radicals during nighttime (Geyer et al., 2003)	31
Figure 5: HO ₂ /OH measured (during the TRAMP campaign) and modeled as function of NO concentration (Chen et al., 2010)	43
Figure 6: Schematic representation of the CRM concept	48
Figure 7: Classification of different types of environments depending on the VOCs reactivities and NO _x concentration (Rohrer et al., 2014).....	49
Figure 8: Measurement configuration used during ACROSS campaign.....	54
Figure 9: Measurement configuration used during the RO ₂ intercomparison campaign...	55
Figure 10: Measurement configuration used during the study of humidity effect on RO ₂ + OH reaction	55
Figure 11: Measurement configuration used during the siloxanes kinetic studies.....	56
Figure 12: Representative schemes of the multi-pass cell	57
Figure 13: Schematic representation of a CPM (Perkin Elmer) connected to a negative and positive switch.....	58
Figure 14: Diagram to illustrate the detection of the OH fluorescence controlled by the gate timing of the CPM detector and the photon counting card (Amedro, 2012)	59
Figure 15: Excitation spectrum of OH at the spectral range 307 - 308 nm.....	60
Figure 16: Diagram of the Sirah dye laser pumped by Spectra Physics high speed Vanadate laser	61
Figure 17: The reference cell used to select and stabilize the OH excitation laser wavelength	62
Figure 18: Typical reference cell signal for FAGE measurement sequence.....	63
Figure 19: Scheme of the UL-FAGE instrument for OH and HO ₂ radical quantification (CPM: Channel Photon Multiplier).....	63
Figure 20: Scheme of the UL-FAGE instrument for OH, HO ₂ and RO ₂ measurement	65
Figure 21: General scheme of the radical chemistry in the RO _x conversion tube.....	66
Figure 22: Alternating measurement in different modes (HO _x and RO _x mode).....	67
Figure 23: FAGE calibration cell	69

Figure 24: Evolution of the UL-FAGE sensitivity as function of H ₂ O. Bottom: HO ₂ cell and Top: OH cell.....	76
Figure 25: Signal-noise/P as a function of the [OH] generate in the calibration cell.....	77
Figure 26: Schematic diagram of the UL-FAGE for the OH reactivity setup	79
Figure 27: OH decays obtained in the absence (blue) and presence of reactive species (pink)	80
Figure 28: Optical setup used for the photolysis laser beam alignment.....	81
Figure 29: Diagram of the gas flow distribution in the photolysis cell.....	82
Figure 30: CEM system (Bronkhorst, 2015).....	83
Figure 31: Determination of the rate constant of CO + OH reaction.....	84
Figure 32: Variation of the laser power at the YAG laser ($\lambda = 532$ nm, upper graph) and exit of the dye ($\lambda = 308$ nm, lower graph) and ($C = 31.8$ A)	84
Figure 33: OH fluorescence signals measured using the two different excitation dye lasers (old and new).....	86
Figure 34: Experimental measurements of the sensitivity of HO ₂ and CH ₃ O ₂ radicals as function of the reaction time (symbols). Model simulations of the concentration of the HO ₂ and CH ₃ O ₂ radicals (solid and dashed lines) (Fuchs et al., 2008).....	88
Figure 35: Experimental measurements of the sensitivity of HO ₂ and CH ₃ O ₂ radicals as function of the NO mixing ratio (symbols). Model simulations of the concentration of the HO ₂ and CH ₃ O ₂ radicals (solid and dashed lines) (Fuchs et al., 2008).....	89
Figure 36: Experimental measurements of the RO _x yield as function of the NO with CO flow = 20 sccm, constant ($[CO] = 6.2 \times 10^{12}$ molecule cm ⁻³).....	90
Figure 37: Experimental measurements of the HO ₂ yield as function of the CO flow using a mercury lamp to generate OH and HO ₂	91
Figure 38: Scheme of the experimental setup occupying two photolysis lasers.....	98
Figure 39: Left graph: The OH concentration time profile obtained during step 1: OH not reacting profile, step 2: OH not reacting + bkg and background profile. Right graph: background profile with a y-axis scale: 0.3 – 0.7	101
Figure 40: The OH concentration time profile obtained from CO + OH reaction during step 3: OH reacting and step 4: HO ₂ formed + OH reacting + bkg and fit for OH reacting decay. Right graph: zoom with x-axis scale: 0– 0.2.....	101
Figure 41: The HO ₂ formed concentration time profile obtained from CO + OH reaction	102
Figure 42: The OH concentration time profile obtained CO+OH reaction during step 3: OH	

reacting showing ΔOH	102
Figure 43 : HO_2 formed/ ΔOH time profile obtained from $\text{CO}+\text{OH}$ reaction	103
Figure 44: $\Delta(\text{HO}_2 \text{ formed}/\Delta\text{OH})$ obtained at different RH (%) for two days measurement	103
Figure 45: ΔHO_2 formed/ ΔOH obtained at different NO level injected into the FAGE cell	104
Figure 46: The grey symbols show the background/ $\Delta\text{OH}_{\text{initial}}$ measured and the orange symbol correspond to model calculations	105
Figure 47: $\Delta\text{HO}_2/\Delta\text{OH}$ obtained at different RH (%) for two days measurement and $\Delta\text{HO}_2/\Delta\text{OH}$ obtained from the model	106
Figure 48: - left graph: the blue symbols show the ΔHO_2 formed/ ΔOH measured profile before correction and the orange symbol correspond to the model calculations and right graph: the blue symbols show ΔHO_2 formed/ ΔOH measured profile after correction by a factor of 3 and the orange symbol correspond to the model calculations.....	106
Figure 49: ΔHO_2 formed/ ΔOH for the reaction $\text{C}_2\text{H}_5\text{O}_2 + \text{OH}$ obtained under all experimental conditions given in Table 16	110
Figure 50: OH reacting/ ΔOH (left) and ΔHO_2 formed/ ΔOH (right) profiles for all experimental conditions given in Table 16 (except for the profiles in the absence of C_2H_6). The blue symbols show the measured profile, and the orange symbols correspond to model calculations using rate constants such as given in Table 15	113
Figure 51: Pseudo first order rate constant as a function of [L2] for 3 different measurements	115
Figure 52 : The potential energy surface of $\text{L}_2 + \text{OH}$ reaction. Numbers (in kcal/mol) are the 0-K energies relative to reactants.	116
Figure 53 : Rate coefficient of L_2+OH reaction as function of temperature (K) determined experimentally (at 298 K at university of Lille) and theoretically (at university of Melbourne) and compared to the literature (Bernard et al. 2018).....	116
Figure 54: Photos of the SAPHIR chamber in 2 measurement mode	123
Figure 55 : Scheme of the three UL-FAGE cells (OH, HO_2 and RO_2 cells) used for the measurement of OH, HO_2 , HO_2^* and RO_2 radicals during the intercomparison campaign at the SAPHIR chamber	125
Figure 56 : Measurement cycle between HO_2 and HO_2^* in the HO_2 FAGE cell and between HO_2^* and RO_2 radicals in the RO_x FAGE cell	128
Figure 57: Measurement profiles for August 8 experiment, From bottom to top:	132

Figure 58: Scatter plot between Lille and Jülich OH, HO ₂ , HO ₂ [*] and RO ₂ measurements for August 8 experiment	134
Figure 59: Measurement profiles for August 20 experiment, caption: same as Figure 57	136
Figure 60: Scatter plot between Lille and Jülich OH, HO ₂ , HO ₂ [*] and RO ₂ measurements for August 20 experiment	137
Figure 61: Measurement profiles for August 19 experiment, caption: same as Figure 57	139
Figure 62: Scatter plot between Lille and Jülich OH, HO ₂ , HO ₂ [*] and RO ₂ measurements for August 19 experiment	140
Figure 63: Measurement profiles for August 22 experiment, caption: same as Figure 57	142
Figure 64: Scatter plot between Lille and Jülich OH, HO ₂ , HO ₂ [*] and RO ₂ measurements for August 22 experiment	143
Figure 65: Measurement profiles for August 9 experiment, caption: same as Figure 57	145
Figure 66: Scatter plot between Lille and Jülich OH, HO ₂ , HO ₂ [*] and RO ₂ measurements for August 9 experiment	146
Figure 67: Measurement profiles for August 12 experiment, caption: same as Figure 57	148
Figure 68 : Scatter plot between Lille and Jülich OH, HO ₂ , HO ₂ [*] and RO ₂ measurements for August 12 experiment.....	149
Figure 69: Measurement profiles for August 23 experiment, caption: same as Figure 57	151
Figure 70: Ratio between measured radical concentration depending on the NO concentration during experiment done on August 23	152
Figure 71: Scatter plot between Lille and Jülich OH, HO ₂ , HO ₂ [*] and RO ₂ measurements for August 23 experiment	152
Figure 72: Scatter plots for Lille and Jülich OH, HO ₂ , HO ₂ [*] and RO ₂ measurements for the experiments that were not discussed in this chapter.....	157
Figure 73: Calibration source exchange. Form bottom to top:	160
Figure 74: Calibration source exchange. Form bottom to top:	162
Figure 75: Map of the ACROSS measurement locations in the Paris region. (C. Cantrell, 2020).....	167
Figure 76: Schematic diagram of the configuration of observation platforms relative to the	

urban and rural emission areas to be studies during the comprehensive summertime ACROSS project.....	168
Figure 77: The four FAGE cells used during the ACROSS campaign measurements	169
Figure 78: UL-FAGE sampling line for OH reactivity measurement.....	170
Figure 79: OH reactivity results from published measurements conducted worldwide at forested environments. (Zannoni et al., 2016)	173
Figure 80: (A) Measured OH reactivity by UL-FAGE below and above the canopy and global radiation, (B) Temperature and friction velocity, red dashes indicate the temperature thresholds to distinguish between warm and cool days and nights. Yellow stripes indicate daytime and grey stripes indicate nighttime. Cn and Cd stand for cooler nights and says, respectively. Wn and Wd stand for warm nights and warm days, respectively.....	175
Figure 81: Averaged OH reactivity (s^{-1}) measured below (left figure) and above (right figure) the canopy as function of temperature (K).....	176
Figure 82: June 23 – 24, (A) wind speed and wind direction data collected at 40 m height, (B) OH reactivity measured below and above the canopy	176
Figure 83: July 17 to 20, (A) wind speed and wind direction data collected at 40 m height, (B) OH reactivity measured below and above the canopy	177
Figure 84: OH reactivity measured above and below canopy (upper graph) and sum of monoterpenes and isoprene mixing ratios (L1: LISA-PTR-MS and L2: IMT- PTR-MS) (lower graph)	178
Figure 85: The sum of monoterpenes measured with the IMT-PTR-MS and ICARE-GC above the canopy and with the LISA-PTR-MS and EPOC-PTR-MS below the canopy.....	180
Figure 86: upper graph shows the X_i and lower graph shows the $k_{weighted}$ determined from the speciated monoterpenes measured by the IMT-GC	181
Figure 87: The isoprene measured with the IMT-PTR-MS and ICARE-GC above the canopy and with the LISA-PTR-MS and EPOC-PTR-MS below the canopy	182
Figure 88 : Scatter plot between the LISA-PTR-MS and LISA-GC-FID isoprene mixing ratio.....	182
Figure 89: (A) Variability of measured and calculated OH reactivity (B) the difference between measured and calculated OH reactivity (missing OH reactivity) and (C) percentage of the missing OH reactivity at both heights	185
Figure 90: The components of calculated OH reactivity inside and above the canopy during the campaign period (from July 10 to July 23) from bottom to top: day and nighttime, only daytime and only nighttime.....	187

Figure 91: The components of calculated OH reactivity inside and above the canopy during the LANDEX campaign	188
Figure 92: Time series of the OH concentration (upper graph) measured below the canopy by the UL-FAGE and LPC2E-CIMS and time series of the O ₃ and HONO concentration and the temperature evolution (lower graph) during the ACROSS campaign.....	190
Figure 93: OH concentration as function of temperature (measured at 5 m).....	191
Figure 94 : Scatter plot between UL-FAGE and LPC2E-CIMS OH measurements during the ACROSS campaign	191
Figure 95: Time series of the HO ₂ and HO ₂ [*] concentration measured below the canopy by the UL-FAGE and the temperature evolution	192
Figure 96: Time series of the HO ₂ [*] concentration measured below the canopy in the HO ₂ FAGE cell and RO _x FAGE cell (in the HO _x mode)	192
Figure 97: Time series of the RO _x concentration measured below the canopy by the UL-FAGE and LPC2E-CIMS and above canopy by the IMT-PERCA and the temperature evolution	194
Figure 98: RO _x concentration measured by the UL-FAGE and IMT-PERCA during the β-pinene oxidation experiment at the SAPIR chamber (August 16)	194

List of Tables

Table 1 : Rate constants of some selected VOCs with OH, NO ₃ , and O ₃ and their lifetimes during the daytime and nighttime (Warneke et al., 2004).....	25
Table 2 : Physiochemical properties of different LVMS and cVMS (Kim et al., 2018) ...	33
Table 3: Hydroxyl radical reaction constant values of different VMS in the literature and in this work (at 25 °C).....	34
Table 4: The different FAGE cells used for different measurements and the CPM used on each cell.....	59
Table 5: Sensitivities measured for OH and HO ₂ * radicals in the UL _x -FAGE instrument	71
Table 6: Gas flows in the calibration cell, RO _x conversion tube and FAGE cell at each step.....	72
Table 7: Sensitivities measured for different radicals in the RO _x -FAGE instrument (HO _x and RO _x mode)	74
Table 8: Uncertainty on the parameters used to determine the UL-FAGE sensitivity (Amedro, 2012).....	75
Table 9: [OH] and [HO ₂] measured at high H ₂ O concentration ([H ₂ O] = 0.4 %) using the sensitivity determined at low H ₂ O concentration ([H ₂ O] = 0.06 %), the radical concentration generated in the calibrator and the ratio	77
Table 10: Power stability at the exit of the dye and YAG laser (old and new laser)	85
Table 11 : Experimental conditions of the Julich RO _x -FAGE (Hendrik Fuchs et al., 2008), Indiana RO _x -FAGE (Lahib, 2019), Leeds-RO _x -FAGE (Worksh et al., 2016) instrument and the UL-RO _x -FAGE instrument (this work).....	87
Table 12: Experimental measurements of the HO ₂ signal at different conversion tube pressure.....	88
Table 13: Four different steps required to determine the HO ₂ formed concentration time profile	100
Table 14 : Model used for CO + OH reaction, all rate constants have been taken from the preferred IUPAC evaluations	104
Table 15: Model used for C ₂ H ₅ O ₂ + OH reaction, all rate constants have been taken from the preferred IUPAC evaluations	107
Table 16: Experimental conditions for all experiments, measured and calculated values	109
Table 17: Different groups involved in the RO _x intercomparison campaign and different instruments used.....	124

Table 18 : Characteristics and performance of the UL-FAGE and FZJ-FAGE instruments during the intercomparison campaign	126
Table 19 : Experimental conditions of the Jülich RO _x -FAGE (H. Fuchs et al., 2008) and UL-RO _x -FAGE instrument (this work).....	127
Table 20: List of the different experiments performed during the intercomparison campaign	129
Table 21: Summary of the comparison between the measurements done by the Lille and Jülich instruments with the slopes of the scatter plots for each OH, HO ₂ , HO ₂ * and RO ₂ measurement.....	154
Table 22: Lille OH concentration measured and Jülich calculated for the calibration source exchange.....	158
Table 23: Lille HO ₂ concentration measured and Jülich calculated for the calibration source exchange.....	158
Table 24: Lille RO ₂ concentration measured and Jülich calculated for the calibration source exchange.....	159
Table 25: Jülich OH concentration measured and Lille calculated for the calibration source exchange.....	160
Table 26: Jülich HO ₂ concentration measured and calculated for the calibration source exchange.....	161
Table 27: Jülich RO ₂ concentration measured and Lille calculated for the calibration source exchange.....	161
Table 28: The three techniques intercompared for the radical quantification during the ACROSS campaign.....	169
Table 29: Performance of the UL-FAGE instrument measuring OH reactivity during the ACROSS campaign.....	171
Table 30: List of the instruments measuring VOCs and sampling location; list of species measured available in Table 32	172
Table 31 : Rate constant of the reaction of OH with monoterpenes (R. Atkinson, 2006)	180
Table 32 : Measured species used for calculating OH reactivity below and above the canopy	183

General Introduction

The atmosphere composition is changing and evolving over time. This is mainly due to the variation of chemical compounds emission: natural emissions related to biogenic processes (Atkinson & Arey, 2003) and anthropogenic emissions which are linked mainly to transport, residential, agricultural and industrial activities (Atkinson, 2000; Wang et al., 2013). Both types of emission are responsible of the presence of a large quantity of organic pollutants such as volatile organic compounds (VOCs) into the atmosphere with an estimated total emission of VOCs of 1300 Tg.year⁻¹ (Galbally & Goldstein, 2007). In the troposphere, which is the atmospheric layer closest to the Earth's surface and where most of the chemical transformations take place (Atkinson, 2000), VOCs will react in the gas phase with oxidants such as hydroxyl (OH), nitrate (NO₃) and ozone (O₃) (Heard & Pilling, 2003). The OH radical is the dominant oxidant during the day and plays a major role in the tropospheric chemistry due to its high reactivity with VOCs (Matsumi et al., 2002; Montzka et al., 2011). The tropospheric chemical transformations of VOCs involves generally a reaction cycle initiated by reaction with OH radicals (Cantrell, 1984), leading to the production of hydroperoxy (HO₂) and peroxy (RO₂) radicals. These radicals then can react with other radicals or with nitrogen monoxide (NO) and thereby regenerate OH. The branching between the different paths depends on the type of environment constrained by the relative levels of VOCs (and then RO₂) and NO: high VOCs and low NO levels in remote, biogenic environments such as pristine forests to have mainly radicals reaction, or higher NO level in urban environment, involving the major loss of RO₂ through the reaction with NO. This fast cycling of radicals controls the oxidizing capacity of the atmosphere and the formation of ozone (Tyndall et al., 2001) and secondary organic aerosols (Bonn et al., 2007). This chemistry has then an impact on the earth's climate, and the air quality. Thus, it is essential to identify the sources, sinks and the lifetime of these radicals to evaluate and predict their impacts on the environment and human health. It can be performed through complementary approaches: in the laboratory with the determination of kinetic parameters relevant for HO_x chemistry and during field measurements campaigns in various environments.

Chemical processes involving HO_x radicals may also occur indoors. Indeed, the VOCs concentration level are often higher in indoor environments compared to outdoors. Indoor materials, furniture, direct human emissions or human indoor activities are known to contribute to VOCs in indoor environments and can be oxidized by oxidants present indoors such as HO_x, NO₃, O₃ (Carslaw, 2007; Won et al., 2019). As people spend as much as 90% of their time in indoor environments (Pekey & Arslanbaş, 2008), the VOC fate triggers an interest to evaluate

their impacts on human health and air quality. However, the indoor chemistry has received far less attention than has the outdoor atmospheric chemistry. Therefore, it is essential to fill the knowledge gaps in the indoor chemistry through a methodology close to the one developed for understanding the atmospheric chemistry such as through coupling of laboratory kinetic measurements, chamber and real building measurements with comparison between measured and modelled concentration profiles of interesting species.

The aim of the current research project is divided into 3 main parts related to 3 scientific questions:

1. What is the influence of humidity on the HO₂ yield in the reaction RO₂ + OH?

This question is linked to the radical reactions taking place in low NO environment and for which kinetic data are sparse. Based on an experimental approach using Laser Induced Fluorescence Assay by Gas Expansion (LIF-FAGE) technique in its reactivity configuration at the university of Lille in the PC2A laboratory, we measured the HO₂ yield of the RO₂+OH reaction at different humidity levels. The RO₂ investigated during this study is C₂H₅O₂.

2. What is the role of VMS (volatile methyl siloxanes) oxidation in indoor environments?

This question will be analyzed through kinetic studies in laboratory, in particular on the reactions between VMS and OH radicals using the same technique as mentioned above. A theoretical approach was done at the university of Melbourne.

3. How to better understand HO_x (OH / HO₂) and RO_x chemistry in the atmosphere?

The measurement of RO₂ with the UL-FAGE was developed and an intercomparison campaign was performed at SAPHIR chamber (summer 2022).

The UL-FAGE instrument was deployed in a field campaign dedicated to the understanding of oxidation processes in a forest influenced by oceanic or urban plumes depending on the meteorological conditions (ACROSS campaign, summer 2022).

This manuscript consists of five chapters and is organized as following:

Chapter 1 provides a bibliographic context about the atmospheric chemistry of the troposphere involving HO_x and RO_x radicals and the potential role of indoor chemistry. Furthermore, experimental techniques available for the characterization of these key radicals as well as the potential interferences on the technique used during this work are discussed.

Chapter 2 describes in detail the experimental setup used in this thesis: the FAGE instrument in the quantification mode measuring OH, HO₂ and RO₂ radicals and in the OH reactivity mode measuring OH lifetime and kinetic parameters. It also includes the optimization of the new RO_x-LIF setup.

Chapter 3 concerns the laboratory kinetic studies using the FAGE instrument in its reactivity mode including two different topics: studying the influence of humidity on the HO₂ yield on the C₂H₅O₂ + OH reaction (article form) and studying the chemistry of siloxanes.

Chapter 4 reports an RO₂ intercomparison exercise that was conducted at the SAPHIR chamber (Forschungszentrum, Jülich) where different techniques from different laboratories were involved. This chapter describes the conditions tested and the comparison between the RO₂ measurements done by the newly developed RO_x-LIF setup at the University of Lille (UL, PC2A laboratory) for RO₂ measurement with the RO_x-LIF instrument from Forschungszentrum Jülich (FZJ).

Chapter 5 presents the results of the deployment of the UL-FAGE during the ACROSS campaign that was conducted in summer 2022 at the Rambouillet forest in Paris, where the HO_x concentrations and OH reactivity was measured. This campaign involved different groups at different sites to study the impact of anthropogenic pollution on BVOC oxidation chemistry. This chapter presents the OH reactivity measured by the UL-FAGE at two different levels (below and above the canopy) and the HO_x and RO_x radical measurements done by UL-FAGE below the canopy.

Chapter 1: Tropospheric Radical Chemistry

This chapter highlights the complexity of the atmosphere and the importance to study the tropospheric chemistry. It provides a description of the chemistry of HO_x (OH and HO₂) and RO_x (HO₂ and RO₂) radicals in the atmosphere and indoors. Due to the high reactivity and the subsequent low concentration of these radicals, different experimental techniques, specifically designed for measuring these radicals in the atmosphere and for carrying kinetic studies have been developed and are also described.

1.1. General context

1.1.1. Tropospheric Chemical Composition

The troposphere corresponds to the lowest layer of the atmosphere extending from the earth's surface to the tropopause (the region separating the troposphere from the stratosphere) at 10 to 18 km, with the altitude of the tropopause depending on the latitude and season. In the troposphere the temperature generally decreases with altitude (Showman & Dowling, 2014), ranging from around 289 K at the ground level to 210–215 K at the tropopause (Atkinson, 2000). This layer can be divided into two parts: the planetary boundary layer (PBL) and the free troposphere (FT). The PBL is the air layer in immediate contact with the Earth's surface and is highly influenced by the diurnal heat, moisture, and earth surface.

The troposphere is well mixed and composed of 78 % nitrogen (N₂), 21 % oxygen (O₂), 1% argon (Ar), and 0.042 % carbon dioxide (CO₂), a varying amount of water vapor ranging from less than 1 % to 4 % depending on the altitude and temperature, and minute amounts of a number of trace gases (Atkinson, 2000). Trace gases are low in concentration (around 1 ppm) but play a key role in determining the air quality (Atkinson, 2000). They are emitted into the atmosphere through natural or anthropogenic processes. The fate of the emitted trace gases depends on different processes such as wet and dry depositions, transport or chemical transformation. For example, the chemical oxidation can alter the lifetime of long-lived greenhouse gases (i.e. methane), and also enhance the formation of secondary organic aerosols (SOA) and other toxic products. Thus, an accurate exploration of the oxidative species such as the hydroxyl radical (OH) and several minor oxidants such as nitrate radical (NO₃) and ozone (O₃) (Monks, 2005) and their reactions in the atmosphere is critical to develop the modelling of the atmospheric chemistry and to better estimate the evolution of the atmospheric oxidizing capacity.

1.1.2. Chemistry of the main oxidants in the troposphere

The rate constants of some selected anthropogenic and biogenic VOCs with the different

oxidants and their associated lifetime are reported in Table 1. Oxidation reactions initiated by OH are considered the most important during daytime with most of the VOCs due to its high reactivity (rate constant ranging from 10^{-13} to 10^{-10} $\text{cm}^3 \text{ molecule}^{-1} \text{ s}^{-1}$). However, O_3 is also an important oxidant during daytime for unsaturated VOCs with a rate constant several orders of magnitude lower than for OH, but with a larger concentration ($[\text{O}_3] = 1.75 \times 10^{12}$ molecule cm^{-3} and $[\text{OH}] = 2 \times 10^6$ molecule cm^{-3}) which can balance its lower reactivity. NO_3 oxidation is not important during the day due to its rapid photolysis in sunlight and its reaction with NO. However, it arises in dark conditions leading to a significant impact of this strong oxidant on the VOC oxidation rates at night, considering the OH concentration around zero and high NO_3 concentration ($[\text{NO}_3] = 2.5 \times 10^8$ molecule cm^{-3}).

Table 1 : Rate constants of some selected VOCs with OH, NO_3 , and O_3 and their lifetimes during the daytime and nighttime (Warneke et al., 2004)

Compound ^a	k_{OH} ($\times 10^{-12}$ $\text{cm}^{-3} \text{ s}^{-1}$)	k_{NO_3} ($\times 10^{-12}$ $\text{cm}^{-3} \text{ s}^{-1}$)	k_{O_3} ($\times 10^{-18}$ $\text{cm}^{-3} \text{ s}^{-1}$)	τ Day, ^b hours	τ Night, ^c hours
Isoprene	101	0.68	12.8	1.2	1.4
Methacrolein	33	0.0033	1.14	4	100
Methyl vinyl ketone	19	<0.0006	4.56	6	34
α -pinene	53.7	6.2	87	1.1	0.2
β -pinene	78.9	2.5	15	1.5	0.4
124-trimethylbenzene	32.5	0.0018	0.0013	3	12
Benzene	1.23	<0.00006	0.00007	110	>18300
Methanol	0.93	<0.00024	-	150	>4600
Acetone	0.22	<0.00003	-	630	>37000
Ethene	8.52	0.00021	1.59	14	55
Propene	26.3	0.009	10.1	4	16
Acetaldehyde	15.8	0.0027	<0.006	9	400

^aRate constants are taken from Atkinson [1994], Atkinson et al. [1984], R. Atkinson et al. (Summary of evaluated kinetic and photochemical data for atmospheric chemistry, IUPAC Subcommittee for Gas Kinetic Data Evaluation for Atmospheric Chemistry, Web version, November 2003, available at <http://www.iupac-kinetic.ch.cam.ac.uk/>), and DeMore et al. [1997].

^b $[\text{OH}] = 2 \times 10^6 \text{ cm}^{-3}$; $[\text{NO}_3] = 0$; $[\text{O}_3] = 1.75 \times 10^{12} \text{ cm}^{-3}$ (70 ppbv).

^c $[\text{OH}] = 0$; $[\text{NO}_3] = 2.5 \times 10^8 \text{ cm}^{-3}$ (10 pptv); $[\text{O}_3] = 1.75 \times 10^{12} \text{ cm}^{-3}$ (70 ppbv).

1.1.2.1. OH chemistry

The hydroxyl (OH) radical is classified as one of the most important oxidants in the troposphere. It acts as a detergent for the troposphere due to its high reactivity during the day. This reactive species initiates the oxidation reactions of compounds emitted in the troposphere, in particular VOCs, and leads to the formation of hydroperoxy (HO_2) and peroxy (RO_2) radical. HO_2 and RO_2 radicals are intermediate short-lived species that play significant roles in the tropospheric chemistry (Liu & Zhang, 2014; Monks, 2005). The short atmospheric lifetimes for OH (~ 1 s), HO_2 and RO_2 (~ 100 s) (Atkinson, 2000) and consequently their low concentrations: $[\text{OH}] = 10^5$ - 10^7 molecule cm^{-3} (Tanner & Eisele, 1995), $[\text{HO}_2] = 10^7$ - 10^8 molecule cm^{-3} and $[\text{RO}_2] = 10^8$ - 10^9 molecule.cm^{-3} (Hornbrook et al., 2011), provide a serious challenge for accurate detection and understanding of their role in the atmosphere.

Figure 1 shows a simplified scheme of the radical oxidation reactions involving the

interconversion of NO_x and several key radical species such as HO₂, RO₂ and RO. This fast-radical reactivity cycle controls many aspects of atmospheric chemistry such as the removal of primary contaminants (VOCs), the formation of tropospheric ozone and secondary pollutants (sulfuric and nitric acids, peroxyacetyl nitrates (PAN), particles, SOA, etc...) and influence global warming.

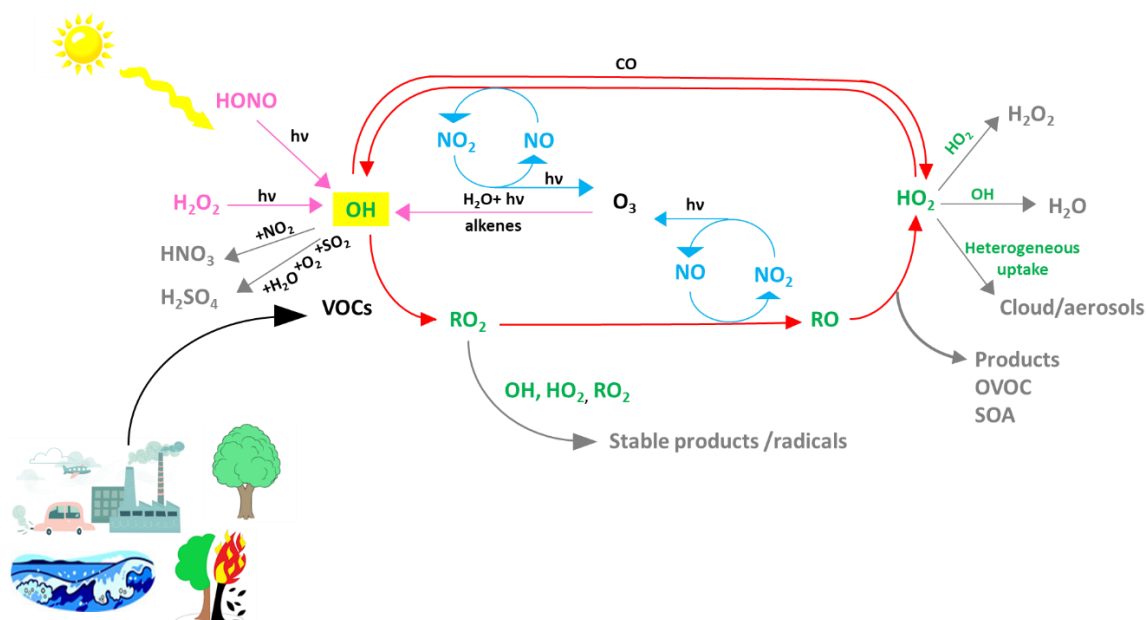
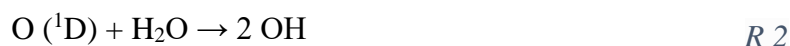
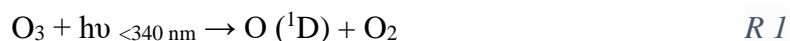


Figure 1: Scheme representing the oxidation processes in the troposphere

The tropospheric chemistry involving OH, HO₂ and RO₂ radicals has been widely described in the literature, in particular in several review articles (Jenkin et al., 2019; Orlando & Tyndall, 2012; Heard & Pilling, 2003; Stone et al., 2012) and is summarized here.

During daytime, the major source of OH radicals is through the ozone photolysis at wavelengths lower than 340 nm to form an excited oxygen atom O (¹D) which then reacts with water vapor (H₂O) to generate OH radicals (Atkinson & Arey, 2003).



However, only a small fraction of electronically excited O (¹D) reacts with water, most of them are quenched by collision with other molecules (N₂ and O₂) to produce ground state O(³P), which further react with O₂ to recycle O₃.



The photolysis of other species such as nitrous acid (HONO) and hydrogen peroxide

(H₂O₂) are other sources of OH radicals. The HONO photolysis at short wavelength ($\lambda < 400$ nm) is considered a dominant source of OH radicals in the early morning, before O₃ photolysis becomes important ($\lambda < 310$ nm) (Atkinson & Arey, 2003).



Then, OH radicals can be consumed through various reaction pathways including its reactions with carbon monoxide (CO) to form HO₂ radicals and with hydrocarbons (RH, R: alkyl radical) to form RO₂ radicals.



Indeed, the atmospheric cycling of HO_x (OH and HO₂) and RO_x radicals depends on the termination and propagation pathways, involving radical - NO_x reactions, in polluted areas close to human activities and radical recombination reactions in clean areas such as forested environments and the marine boundary layer.

In polluted environments, characterized by elevated NO_x levels, additional to the reaction of OH with VOCs, an important sink of OH radicals come from its reaction with the inorganic species such as NO₂ leading to the production of nitric acid (HNO₃) (R 11), which will mainly be lost via wet deposition. The importance of this reaction mainly depends on the VOC level in the atmosphere.



RO₂ radicals from the reaction of OH with VOCs (R10) react predominantly with NO forming NO₂ and alkoxy radical (RO). NO₂ is then photolyzed to form O₃ and RO will react with O₂ to form R'CHO (R' is the radical R with one H less) and HO₂, which in turn reacts with NO to regenerate OH radical.



The reaction of RO₂ radicals with NO can also act as an important terminating channel

through the formation of alkyl nitrates (RONO₂), thus reducing the O₃ production. This reaction can be considered negligible for short chain organic radicals (C < 4), but becomes increasingly important with increasing chain length of R (Orlando & Tyndall, 2012).



The association reaction between RO and NO is not important under atmospheric conditions but can be important in laboratory experiments, especially when high NO concentration is needed to quantify peroxy radicals as described in Chapter 2.



In remote environments, characterized by low NO_x level, OH and HO₂ radicals can be consumed and produced through reactions of HO₂ and OH with O₃. The rate constant for OH + O₃ reaction ($7.3 \times 10^{-14} \text{ cm}^3 \text{ molecule}^{-1} \text{ s}^{-1}$ (Atkinson et al., 2004)) is approximately 37 times faster than HO₂ + O₃ reaction ($2.0 \times 10^{-15} \text{ cm}^3 \text{ molecule}^{-1} \text{ s}^{-1}$ (Atkinson et al., 2004)) which will favor partitioning towards HO₂.



In addition, HO_x and RO_x radicals can significantly react through cross- and self-reactions. It can also undergo other phenomena such as isomerization, photolysis or heterogeneous reactions. The loss of HO_x and RO_x radicals can be terminated by radical recombination reactions forming peroxide species such as H₂O₂, ROOR and ROOH.



Interestingly, *R 24* has been neglected until recently when the rate constant and product yields of this reaction have been measured experimentally for short alkyl (C1-C4) (Bossolasco, et al., 2014; Faragó et al., 2015; Fittschen, 2019; Yan et al., 2016). It has been shown that the chemistry involving this type of reactions is extremely fast and complex and can be of importance in remote areas such as marine boundary layer. More details about this chemistry will be discussed in Chapter 3.

Oxidation pathways of larger organic peroxy radicals, and in particular biogenic ones such as isoprene have been the subject of a strong interest in the literature. As shown in Figure 2, in isoprene-rich environments, the isomerization and decomposition of isoprene-based

peroxy radicals can produce HO₂ and OH radicals. For instance, the 1,6-H-shift isomerization of the Z-δ-hydroxyperoxy radicals produced from OH addition to the 1 and 4 carbons of isoprene can lead, upon reaction with O₂, to the formation of HO₂ and hydroperoxyl aldehydes (HPALD) (Peeters et al., 2009; Peeters & Müller, 2010).

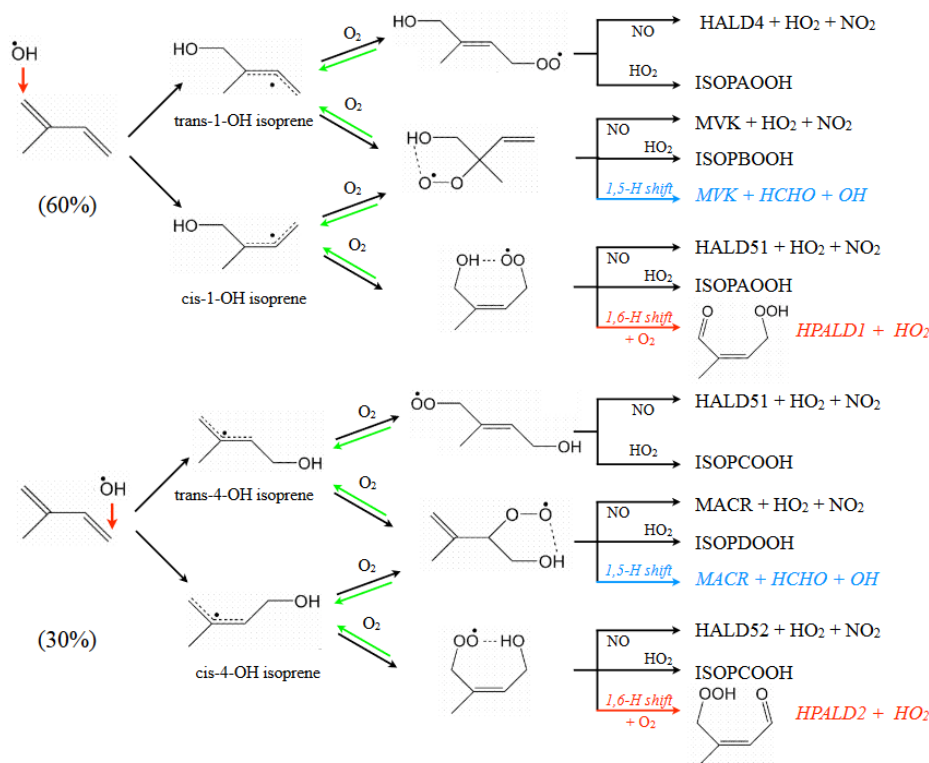


Figure 2: Reaction scheme of the isoprene oxidation (Stavrakou et al., 2010)

The heterogeneous uptake of the HO₂ radicals into the clouds (Hermann et al., 2015) or aerosols (solids or droplets) has been suggested to be a significant sink of HO₂ radicals, thereby influencing the atmospheric oxidation capacity. Numerous investigations have focused on determining the HO₂ uptake coefficient for different types of aerosols (Li et al., 2019; Whalley et al., 2015; Song et al., 2020) revealing significant variability in uptake coefficients depending on aerosol composition. These studies diagnosed that the impact of the HO₂ uptake on the calculated HO_x concentration is about 10 to 40 %. In clouds, where reaction times extend to minutes or longer, gas-phase OH can constitute between 10 to 30% of the OH source in the liquid phase, varying with environmental conditions (Mauldin et al., 1997; Ervens et al., 2003).

1.1.2.2. O₃ chemistry

The ozonolysis of alkenes has received particular attention because of their major role in the tropospheric chemistry (Johnson & Marston, 2008; Ariya et al., 2000; Avzianova & Ariya, 2002; Koch et al., 2000). These reactions lead to the formation of numerous oxidized products

which can form atmospheric particles that have an important effect on the climate and the chemistry of the atmosphere (Koch et al., 2000). Moreover, this reaction is an important source of tropospheric HO_x and RO₂ radicals (Geyer et al., 2003; Kroll et al., 2002). The initial step of these reactions (Figure 3) is the addition of the O₃ molecule to the double bond of the alkene forming a primary ozonide which decomposes in a carbonyl compound and a carbonyl oxide biradical called Criegee intermediate (Zeng & Wilson, 2020; Ariya et al., 2000; Atkinson, 1997; Grosjean & Grosjean, 1997, 1998; Kroll et al., 2002). For symmetrical alkenes, one carbonyl and one biradical is produced from this reaction ; while for non-symmetrical alkenes (such as trans-2-hexene), this may be an oversimplification because the product yields are different depending on the nature and the number of the alkyl substituents (Grosjean & Grosjean, 1997, 1998). The excited Criegee intermediate may either be stabilized collisionally or undergo other complex reaction sequences including unimolecular (leading to OH formation) or bimolecular reactions. Stabilized Criegee radicals can react further with atmospheric species (H₂O, CO, NO, SO₂ and NO₂) leading to the formation of aldehydes (major product), ketones and organic acids or may isomerize to other more stable configuration (Khan et al., 2018; Chhantyal-Pun et al., 2012; Niki et al., 1983). The decomposition of the isomerized Criegee intermediate leads to the formation of two HO_x radicals or non-radical products. Excited Criegee intermediates can form stable products such as alkanes, CO, CO₂ and H₂O. Further reactions can lead to the formation of radicals (HO_x and RO₂).

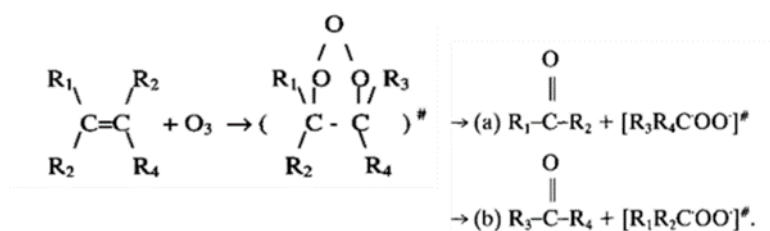


Figure 3: Ozonolysis of alkenes reaction

At night, the major daytime source of HO_x and RO_x radicals, ozone photolysis, disappears. However, significant concentrations of these radicals were measured in different sites of the troposphere during nighttime (Hu and Stedman, 1995; Kanaya et al., 1999; Mihelcic et al., 1993; Tanner and Eisele, 1995; Stone et al., 2014; Vrekoussis et al., 2004; Wang et al., 2020) . Two important species appear to act as key initiators of the nighttime HO_x cycle by their reaction with VOCs: (1) ozone (O₃) which remains in significant concentrations at night if not removed by dry deposition or titrated by reaction with NO and (2) the nitrate radical (NO₃) which is solely produced from the slow reaction of NO₂ with O₃ (Bey et al., 2001; Geyer et al., 2003).

1.1.2.3. NO_3 chemistry

The reaction of NO_3 with VOCs is initiated by the addition of NO_3 to the double bond forming a radical intermediate which rapidly reacts with O_2 forming a nitratealkyl-peroxy radical (Figure 4). The formed peroxy radical can undergo several reactions producing either stable products or nitratealkoxy radicals. The latter undergoes three depletion mechanisms, the reaction with O_2 , thermal decay and isomerization (Geyer et al., 2003; Moo et al., 2024; Wennberg et al., 2018; Perring et al. 2009).

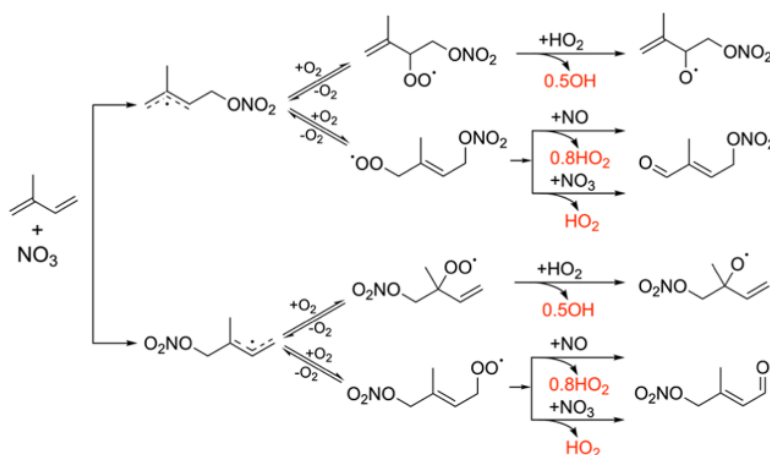


Figure 4: Simplified scheme of the reaction of NO_3 with isoprene producing HO_x and peroxy radicals during nighttime (Moo et al., 2024)

Oxidation processes involving HO_x radicals take place outdoors but also indoors. The following section is dedicated to the understanding of the indoor HO_x chemistry and in particular the reaction of OH with siloxanes.

1.1.3. Indoor Chemistry

Indoor air is subject to numerous sources of pollution. Number of pollutants such as ozone (O_3), nitrogen oxides (NO_x) and particulate matter (PM) can be transported from outdoors to indoors. However, there are also direct indoor pollutants such as PM, NO_x and VOCs emitted particularly from human activities such as cooking, heating, cleaning, smoking and use of personal care products (Carslaw et al., 2017; Weschler & Carslaw, 2018). As we spend more than 90% of our time in indoor environments (Pieri et al., 2013), the indoor air quality is a very important factor impacting our health.

Indoor activities can lead to a pollutant concentration level significantly higher indoors than outdoors and provide the basis for reactive chemistry involving oxidants (such as OH) that lead to the formation of secondary pollutants similarly to what is observed outdoors. However, there are important differences between both environments such as higher surface-to-volume ratios indoors, the different spectral distribution of sunlight due to the presence of windows or indoor artificial lights and the confined conditions (Abbatt & Wang, 2020; Alvarez et al., 2013;

[Blocquet et al., 2018](#); [Verrielle et al., 2016](#)).

Most of the indoor air research studies have indicated that the reactions of O₃ with alkenes and monoterpenes appear to be a potentially important source of OH radicals which is considered as a main indoor oxidant. For many years, and in absence of any measurements, models predicted that the indoor OH concentration is around 10⁵ molecule cm⁻³ (0.01 ppt) , comparable to the OH concentration observed during the nighttime outdoor OH concentration or during daytime in winter ([Carslaw, 2007](#); [Sarwar et al., 2002](#)). However, direct indoor OH measurements have demonstrated the presence of much higher indoor OH concentrations. Their formation is possibly dependent on the presence of high HONO concentration close to the sunlit windows ([Alvarez et al., 2013](#)) or appears during cleaning activities ([Carslaw et al., 2017](#)). Once OH is generated it can react with any other organic species present indoors ([Abbatt & Wang, 2020](#)).

A family of species important to study in term of reactivity with OH is the organosiloxanes because over the last three decades organosiloxanes such as cyclic and linear siloxanes have been commonly used in many consumer products such as cosmetics, health-care products, medical and pharmaceutical preparations, electronics and furniture ([Horii & Kannan, 2008](#)) and they can react with OH and generate secondary species such as formaldehyde ([Alton & Browne, 2020](#)).

1.1.3.1. Sources and types of organosiloxanes

Applications of organosiloxanes stem from their distinct physicochemical properties such as high hydrophobicity, low surface tension, high volatility, and high thermal stability ([Wang et al., 2001](#)) and a high degree of compatibility with many formulation ingredients. Siloxanes form a large group of chemicals with molecular weights ranging from a few hundreds to several hundred thousand. Siloxanes consist of silicone atoms linked via oxygen atoms [Si–O] with organic side chain attached to each silicone atom (–[R₂Si–O]–), R substituent usually representing the groups such as: methyl, ethyl, propyl, phenyl, fluoroalkyl, aminoalkyl, hydroxy, mercapto, hydrogen, vinyl ([Mojsiewicz-Pienkowska et al., 2016](#)). The most significant siloxane building block is the dimethyl-siloxane group (–Si(CH₃)₂ O–) due to its unique physico-chemical properties, based on the large size (10 atoms per unit) and only a moderate ability to accept hydrogen bonds. Siloxanes have no known natural source and are considered as anthropogenic compounds ([Bernard et al., 2018](#)). Depending on the structure, siloxanes can be classified into two groups: linear and cyclic compounds. Methyl siloxanes with small and medium molecular weights are volatile under normal conditions, thus they are called volatile methyl siloxanes (VMS).

Every year, about two million tons of linear and cyclic volatile methyl siloxanes (“L”VMS and “c”VMS, respectively) are produced globally for many usages (Alton & Browne, 2020). These high production volumes coupled to the prevalence of VMS in consumer products have led to an increased worldwide awareness and interest, in recent years, in the environmental behavior and fate of these compounds. VMS are readily emitted into the environment during the process of their production, transportation and usage. VMS have been found in both indoor and outdoor atmospheres at different locations, although the VMS concentrations in the outdoor atmosphere are usually much lower than those in the indoor environment (Fu et al., 2020). Both, linear and cyclic VMSs, can be easily released into the atmosphere, because of their high vapor pressure and low water solubility and thus an extremely high water/air partition coefficients (K_{AW}) (Table 2). In addition, these compounds are easily evaporated into the atmosphere from water and moist soil after waste disposal and wastewater treatment.

Table 2 : Physicochemical properties of different LVMS and cVMS (Kim et al., 2018)

Chemical Name	L2	L3	L4	L5	D3	D4	D5	D6
Molecular Mass (g/mol)	162.8	236.53	310.69	384.84	222.46	296.62	370.77	444.93
Vapor Pressure (Pa at 25 °C)	5500	535	58.1	6	671	140	33.2	6
Water solubility (mg/L)	0.93	0.0345	0.00674	7.04E-05	1.56	0.056	0.017	0.0053
Log K_{AW} (at 25 °C)	2.49	3.06	3.45	3.95	0.41	2.74	3.16	3.01

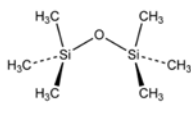
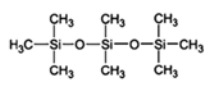
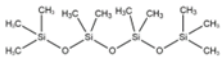
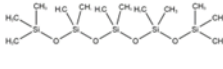
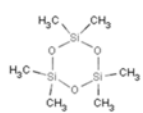
1.1.3.2. Chemistry of siloxanes

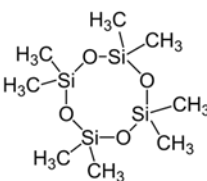
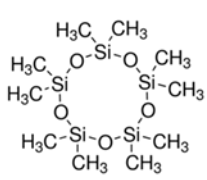
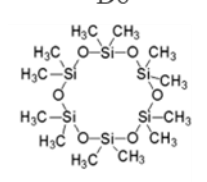
The gas-phase chemistry plays a major role in the environmental processing of the VMS compounds. The predominant gas-phase removal process of VMS compounds is thought to be via hydroxyl radicals. The VMS atmospheric lifetimes are expected to be in the range of several days to few weeks (Bernard et al., 2018). Knowledge of the rate coefficients of the OH radical reactions with VMS and the resulting products is of great importance for the evaluation of the VMS atmospheric lifetimes and to better understand the environmental risks of these compounds in indoor environments or in the atmosphere.

Table 3 represents a summary of various experimental studies that have been performed on measuring the rate constant for the hydroxyl radical gas-phase reaction with different VMS compounds (linear and cyclic VMS) using different experimental techniques. The results show that the cyclic molecules (D3, D4, D5 and D6) are less reactive than the linear molecules (L2, L3, L4 and L5) with equivalent number of methyl ($-CH_3$) groups, while the reactivity of both the linear and cyclic molecules increase with the increase of the number of $-CH_3$ groups.

Table 3: Hydroxyl radical reaction constant values of different VMS in the literature and in this work (at 25 °C)

L2: hexamethyldisiloxane, L3: octamethyltrisiloxane, L4: decamethyltetrasiloxane
 L5: dodecamethylpentasiloxane, D3: hexamethylcyclotrisiloxane, D4: octamethylcyclotetrasiloxane,
 D5: decamethylcyclopentasiloxane, D6: Dodecamethylcyclohexasiloxane

Compound	k_{OH} (10^{-12} cm ³ molecule ⁻¹ s ⁻¹)		Source
	Mean	Uncertainty	
Linear VMS	1.20	0.09	(Alton & Browne, 2020)
L2	1.1	0.10	(Alton & Browne, 2020)
	1.58	0.16	(Kim & Xu, 2017)
	1.38	0.36	(Roger Atkinson, 1991)
	1.32	0.36	(Markgraf & Wells, 1997)
	1.28	0.08	(Bernard et al., 2018)
L3	1.70	0.10	(Alton & Browne, 2020)
	1.53	0.04	(Alton & Browne, 2020)
	1.70	0.2	(Alton & Browne, 2020)
	2.15	0.15	(Kim & Xu, 2017)
	1.83	0.09	(Markgraf & Wells, 1997)
	1.72	0.10	(Bernard et al., 2018)
L4	2.50	0.20	(Alton & Browne, 2020)
	1.90	0.10	(Alton & Browne, 2020)
	2.50	0.50	(Alton & Browne, 2020)
	3.37	0.40	(Kim & Xu, 2017)
	2.66	0.13	(Markgraf & Wells, 1997)
L5	3.40	0.70	(Alton & Browne, 2020)
	2.80	0.20	(Alton & Browne, 2020)
	3.40	0.60	(Alton & Browne, 2020)
	4.03	1.14	(Kim & Xu, 2017)
Cyclic VMS	0.9	0.10	(Alton & Browne, 2020)
D3	0.67	0.02	(Alton & Browne, 2020)
	0.91	0.23	(Kim & Xu, 2017)
	0.52	0.17	(Roger Atkinson, 1991)
	1.84	1.76 - 1.93	(Xiao et al., 2015)
	0.82	0.05	(Bernard et al., 2018)

<p style="text-align: center;">D4</p> 	1.30	0.20	(Alton & Browne, 2020)
	1.10	0.10	(Alton & Browne, 2020)
	1.28	0.10	(Alton & Browne, 2020)
	0.95	0.18	(Kim & Xu, 2017)
	1.01	0.32	(Roger Atkinson, 1991)
	1.90	1.7 – 2.2	(Safron et al., 2015)
	2.34	1.93 – 2.85	(Xiao et al., 2015)
	1.12	0.10	(Bernard et al., 2018)
<p style="text-align: center;">D5</p> 	2.2	0.20	(Alton & Browne, 2020)
	1.8	0.20	(Alton & Browne, 2020)
	2.1	0.20	(Alton & Browne, 2020)
	1.46	0.12	(Kim & Xu, 2017)
	1.55	0.49	(Roger Atkinson, 1991)
	2.60	2.3 – 2.9	(Safron et al., 2015)
	2.46	2.2 – 2.74	(Xiao et al., 2015)
<p style="text-align: center;">D6</p> 	2.44	0.92	(Kim & Xu, 2017)
	2.80	2.5 – 3.2	(Safron et al., 2015)

Bernard et al. (Bernard et al., 2018) suggests that the possible reason the linear VMS react faster with OH than cyclic VMS having the same number of CH₃ groups is the formation of hydrogen-bonded pre-reactive complexes where a hydrogen bond is formed between OH and one of the O atoms in the Si-O-Si bridge.

These studies aid the atmospheric modeling of VMS and their potential contribution to new particle and SOA formation and impacts on the air quality (Yao et al., 2023). However, the chemistry of VMS is not only dependent on reaction with OH but may involve autooxidation reactions which make its transformations more complex to study (Ren & Da Silva, 2020). As for example the reaction of tetramethylsilane ((CH₃)₃SiCH₂) with O₂ leads to peroxy radical ((CH₃)₃SiCH₂O₂) which in turn makes the alkoxy radical ((CH₃)₃SiCH₂O). This alkoxy radical can undergo isomerization processes forming alkyl radicals ((CH₃)₃SiOCH₂) which enable a second oxidation step, forming trimethylsilyl formate ((CH₃)₃SiOCHO) that contribute to the formation of secondary organic aerosols.

1.2. Measurement of HO_x and RO_x radicals in the atmosphere

The measurement of ambient radical concentration is extremely challenging due to their quite low concentration which highly depends on the atmospheric chemical composition and the photolysis processes.

The OH concentration is the balance between the rate of production and consumption.

$$\frac{d([OH])}{dt} = P(OH) - L(OH) \quad \text{Equation 1}$$

$$P(OH) = k_{HO_2+O_3}[HO_2][O_3] + k_{HO_2+NO}[HO_2][NO] + \sum v_i J_i [i] + P' \quad \text{Equation 2}$$

$$L(OH) = \sum k_{OH+X}[X][OH] \quad \text{Equation 3}$$

where P(OH) refers to the total production rate of OH from different sources including production of OH by HO₂ reacting with O₃ or NO, by photolytic sources ($\sum v_i J_i [i]$) such as the photolysis of O₃, HONO, H₂O₂ and CH₃OOH (where v_i refers to the OH yield, J_i the photolysis frequency in s⁻¹ and [i] the concentration of the precursor in molecule.cm⁻³), and by additional processes (P') such as ozonolysis of alkenes.

L(OH) encompass all the different losses of OH such as the consumption with all the reactive species (X) in the atmosphere such as NO, NO₂, CO, CH₄ and VOCs. Due to the short lifetime of OH in the atmosphere, its concentration is not affected by transportation and a steady state can be assumed. The approximation d[OH]/dt = 0 can be considered so the OH concentration is given as the ratio between its production sources and consumption pathways. However, this approximation provides only a rough estimation of the OH concentration. Thus, for real measurements of HO_x and RO_x concentrations an appropriate sensitive technique is needed. Thanks to the availability of plenty of instruments worldwide it is now possible to improve the understanding of the oxidation mechanisms in the gas phase involving HO_x radicals in the atmosphere and indoors. An article from [Heard & Pilling, \(2003\)](#) reviews most of the various techniques used by different groups in the world for OH and HO₂ radical detection. In this section, a brief summary about the most common instruments used to measure the OH, HO₂ and RO₂ radical concentrations in the field is presented.

1.2.1. Quantification of OH radicals in the atmosphere

Different instruments have long been used for the quantification of tropospheric OH radicals. The most widely used instruments in the field are either based on optical spectroscopic techniques: laser-induced fluorescence spectroscopy at low pressure (FAGE), or mass spectroscopic technique: chemical ionization mass spectrometry (CIMS) whereby OH is converted chemically into H₂SO₄. The principle of operation, advantages and disadvantages of each of these techniques is described below. Long-path differential optical absorption spectroscopy (DOAS) is no longer used for field campaign.

1.2.1.1. *The FAGE technique*

The FAGE (Fluorescence Assay by Gas Expansion) instrument used in this work is based on the direct LIF (Laser Induced Fluorescence) detection of OH at low pressure after a gas expansion, hence the name FAGE. LIF involves the electronic excitation of a molecule or radical, which absorb in the ultraviolet region, from the ground electronic state to excited electronic state. The subsequent relaxation of the excited species to a lower energy level can be accompanied by the spontaneous emission of light: fluorescence. Excited species can additionally relax through nonradiative processes: intersystem crossing, collisional quenching by transferring excess energy to another molecule (i.e. N₂ or O₂). At constant laser power the collected fluorescence is directly proportional to the OH concentration.

The LIF technique was first applied for measuring OH in the atmosphere by Hard et al. (Hard et al., 1979). For these first measurement, the OH was excited at $\lambda=282$ nm in the $A^2\Sigma^+ v'=1 \leftarrow X^2\Pi v''=0$ transition band and the fluorescence was collected at $\lambda\sim 310$ nm in the $A^2\Sigma^+ v'=0 \rightarrow X^2\Pi v''=0$ transition band, thus allowing the separation of the fluorescence light from scattered laser light (Baardsen & Terhune, 1972). However, due to the presence of ozone, the excitation at $\lambda=282$ nm is not well adapted because the photolysis of ozone at 282 nm generates excited O atoms that will react with water vapor to produce OH. Therefore, to strongly reduce this interference (by about a factor 30), the next instruments developed in different research groups used the excitation of OH at $\lambda=308$ nm in the $A^2\Sigma^+ v'=0 \leftarrow X^2\Pi v''=0$ transition band and detection of the fluorescence occurring on the same band in the same wavelength range than the excitation. The main drawback of this excitation/collection scheme is the difficulty in separating the fluorescence from the excitation. For this reason, in the FAGE instruments, a temporal separation between the scattered laser light and the fluorescence emission is required: the fluorescence lifetime of OH is increased (reducing quenching) by detecting OH after expansion of ambient air to low pressure. The FAGE instruments are generally calibrated with a known source of HO_x radicals. The results of some field campaigns (Mao et al., 2012;

Dusanter et al., 2009; Tan et al., 2018; Whalley et al., 2018) point to potential interferences in the measurements of the FAGE instrument. These interferences will be discussed later.

The FAGE technique, first pioneered by Hard et al (Hard et al., 1984) for tropospheric HO_x radical measurement is nowadays one of the most widely used techniques for OH field measurements. Several groups worldwide are using such type of instrument (Amedro et al., 2012; Chan et al., 1990; Dusanter et al., 2009; Faloon et al., 2004; Hard et al., 1984; Martinez et al., 2010; Stevens et al., 1994; Whalley et al., 2018). The UL-FAGE instrument is described in details in the following chapter dedicated to the experimental setup.

1.2.1.2. The DOAS technique

The DOAS (Differential Optical Absorption Spectroscopy) technique is a spectroscopic technique for making measurements of tropospheric OH radicals (Brandenburger et al., 1998) and other trace gases such as CH₂O, HNO₂, O₃, NO₂, SO₂, NO₃, BrO, and IO (Platt and Perner, 1980; Platt and Hausmann, 1994). It is based on the extinction of UV light passing through a gas mixture by absorption of OH over a long absorption path according to the Beer-Lambert law represented below:

$$\ln\left(\frac{I_0}{I}\right) = \sigma_{OH} \times [OH] \times L \quad \text{Equation 4}$$

where I₀ and I are respectively received light intensities before and after transmission through the sample, σ_{OH} = absorption cross section (in cm²), [OH] = concentration of OH (in molecule.cm⁻³) and L = light path length (in cm). The absolute accuracy of the DOAS technique is limited by the precision of the σ_{OH} and L.

The DOAS instrument consists of four elements: (1) a light source with a sufficiently high luminance due to the long absorption path length and a homogeneous spectral profile in order to be selective. (2) a 1 mirror configuration or multi-path reflection cell configuration that improve the spatial resolution with mirrors separated by 10-40 m, between which the laser light passes several hundred times (3) A high-resolution spectrometer to detect the different OH absorption lines. (4) A cooled photodiode for the light detection.

The DOAS technique provides inherently absolute and calibration-free in-situ measurements. The sensitivity of this technique is not as good as that for other techniques (LIF and CIMS) due to the interferences from other absorbers that must be subtracted from the complex absorption spectrum to extract the OH concentration. The unique Jülich DOAS instrument was deployed in previous field experiments (Brandenburger et al., 1998; Brauers et al., 2001) and has currently been installed permanently in the SAPHIR chamber.

1.2.1.3. The CIMS technique

The CIMS technique is based on the measurement of OH indirectly after it is chemically converted in a reactor at atmospheric pressure into a molecule that can be readily ionized and then detected by a mass spectrometer (Berresheim et al., 2000; Eisele and Tanner, 1991; Kukui et al., 2008). This technique is based on the titration of OH radicals by $^{34}\text{SO}_2$ after sampling to produce isotopically labeled $\text{H}_2^{34}\text{SO}_2$ via the following mechanism:



The $\text{H}_2^{34}\text{SO}_3$ is then ionized into $\text{H}^{34}\text{SO}_4^-$ by charge transfer reaction (R 28) with NO_3^- ion which is produced separately in a sheath gas containing HNO_3 (nitric acid) by a corona discharge. The $\text{H}^{34}\text{SO}_4^-$ ions are then detected using a quadrupole mass spectrometer. The determination of the OH concentration requires knowledge of the $\text{H}^{34}\text{SO}_4^-/\text{NO}_3^-$ ratio, the reaction time and the rate coefficient of reaction (R 28). However, the rate coefficient is not well known, and so an accurate calibration of the CIMS instrument is required using H_2O photolysis calibration system similar to those used for the FAGE instrument (details in the following chapter).



The CIMS technique is considered as the most sensitive among all the techniques used for measuring OH, with a detection limit below 10^5 molecule cm^{-3} for 5 min average (Eisele et al., 1996). As the measurement is not instantaneous, the atmospheric HO_2 may be converted into OH at high NO concentration which causes an interference. In order to minimize this interference, the conversion time of OH into H_2SO_4 must be reduced (Kukui et al., 2008). Also, high purity propane is regularly added to quantify the interferences.

1.2.2. Detection of tropospheric HO_2 and RO_2

Several measurement techniques allow the quantification of HO_2 and RO_2 in the atmosphere. The MIESR (Matrix Insulation Electron Spin Resonance) technique can measure simultaneously and selectively different types of radicals such as HO_2 , the sum of RO_2 , $\text{CH}_3\text{C}(\text{O})\text{O}_2$, NO_2 and NO_3 using the method of Electron Spin Resonance (ESR) after the collection of the radicals on a cold matrix, but it is not instantaneous and not very sensitive, limiting its use for atmospheric measurements. In this section, only the currently deployed techniques for field measurements FAGE, PERCA (Peroxy Radical Chemical Amplification) and PeRCIMS (Peroxy Radical Chemical Ionization Mass Spectrometry) will be mentioned with their advantages and disadvantages.

1.2.2.1. The FAGE technique

The FAGE technique allows the indirect measurement of HO₂ and RO₂ radicals. The HO₂ radicals are converted into OH by adding NO within the HO₂ FAGE cell following the reaction HO₂ + NO → OH + NO₂ and the produced OH radicals are then detected by LIF. This technique is adapted to the selective measurement of HO₂ only when low NO concentration is injected into the HO₂ FAGE cell. Indeed, it has been shown that certain RO₂, those containing double bonds, can efficiently be converted into HO₂ and subsequently HO₂ into OH when the NO level is high in the HO₂ FAGE cell (Fuchs et al., 2011). This potential interference can be used as an advantage to detect some RO₂ radicals in the HO₂ FAGE cell.

In addition, RO₂ radicals can be detected by using a setup consisting of a conversion flow-tube on top of a FAGE cell where RO₂ is converted into OH by a two-step process: first, the atmospheric radicals (RO₂, RO and OH) are converted into HO₂ by adding CO and NO into the flow-tube:



Then HO₂ are converted into OH in the FAGE cell, by adding NO, so it can be detected by LIF. The principle of operation of the FAGE instrument for HO₂ and RO₂ detection is described in detail in chapter 2.

1.2.2.2. The PERCA technique

The PERCA technique allows the indirect measurement of the total concentration of peroxy (RO_x) radicals, which is the sum of HO₂ and sum of RO₂ radicals (Cantrell & Stedman, 1982). In this technique, as the ambient air containing the radicals is drawn into a reaction chamber, it is converted into NO₂ via the amplification chemistry that takes place close to the sampling point by adding two reagent gases (CO + NO). It is the same chemistry as in the RO_x-FAGE instrument (mentioned above).

Finally, the NO₂ formed in reaction R 22 can be detected by different techniques such as LIF (Miyazaki et al., 2010), cavity ring-down spectroscopy (CRDS) (Liu et al., 2009), chemiluminescence detector with luminol (Parker et al., 2009), cavity attenuated phase-shift spectroscopy (CAPS) (Wood & Charest, 2014) or incoherent broadband cavity-enhanced absorption spectroscopy (IBBCEAS) (Chen et al., 2016). The peroxy radical concentration is

determined from the chain length of the chain reaction, which defines the number of NO₂ produced by one initial HO₂ or RO₂ radical and ΔNO₂, which corresponds to the difference between the signal due to NO₂ concentration produced in the amplification process and the signal due to the NO₂ present in ambient air and NO₂ produced by other reactions (such as O₃ with NO).

$$[HO_2 + \Sigma RO_2] = \frac{\Delta NO_2}{\text{chain length}} \quad \text{Equation 5}$$

The PERCA instrument is used by various groups for field measurements (Kartal et al., 2010; Kundu et al., 2019; Liu et al., 2009; Wood & Charest, 2014; Duncianu et al., 2020; Kundu et al., 2019) due to its portability, its low cost, and its low level of complexity. However, the dependence of the chain length, and therefore the sensitivity of the instrument, on the water vapor content in the sampled air is considered as main disadvantage. Due to the high variability of the ambient humidity, an accurate characterization of the chain length and instrument calibration (similar to those used for the generation of HO_x radicals based on H₂O photolysis) is therefore necessary to perform reliable measurements of RO_x radicals with PERCA instrument. Recent studies have shown improvements to minimize the impact of water vapor on the chain length through using a Nafion dryer reactor (Yang et al., 2019).

An attempt to use a PERCA instrument for the selective quantification of HO₂ has also been proposed by Miyazaki et al. (Miyazaki et al., 2010).

1.2.2.3. The PeRCIMS technique

As for measuring OH, the CIMS technique can be used also for the measurement of HO₂ and RO_x radicals based on the chemical conversion of RO_x radicals into HO₂ that is converted into OH in presence of NO followed by the reaction of OH with SO₂ to form H₂SO₄ and its subsequent detection by chemical ionization mass spectrometry. Hornbrook et al. reported a method to speciate between HO₂ and ΣRO₂ radical on CIMS instrument based on the variation of the conversion efficiency of RO₂ into HO₂ under different ratio of concentrations of NO and O₂ ([NO]/[O₂]) (Hornbrook et al., 2011). Therefore, at low [NO]/[O₂] the conversion of RO into HO₂ (R 12, R 13) is more favorable and HO₂ + ΣRO₂ will be quantified, while at higher [NO]/[O₂] the conversion of RO into RONO (R 16) is more favorable and thus only HO₂ will be quantified.

1.2.3. Field measurements of HO_x and RO_x radicals in the troposphere and modeling

Tropospheric measurements of OH, HO₂ and RO_x (HO₂+RO₂) radicals have been performed in the atmosphere during the last decades by a number of groups since the development of the measurement techniques described above. Plenty of studies have been devoted to a better understanding of the tropospheric oxidation of VOCs by comparing field measurements in a specific environment (marine, forest, urban) to atmospheric models based on the most advanced chemical mechanisms published in the literature, including the Master Chemical Mechanism (MCM) (Whalley et al., 2018), the Regional Atmospheric Chemistry Mechanism (RACM) (Griffith et al., 2013), the Leuven Isoprene Mechanism (LIM) (Peeters et al., 2009) and others. Some of these studies have highlighted gaps between measured and modeled radicals under different sites and under a wide range of various atmospheric conditions. These differences could be due to incomplete understanding of radical chemistry. Even with the latest improvements of the isoprene mechanism (previously mentioned in Figure 2), it is difficult to reproduce some field measurements performed in low NO_x environments rich in biogenic VOCs (BVOCs) (Whalley et al., 2011). The potential interferences (as mentioned below for the FAGE technique) in the measurements could be another reason for the discrepancies. However, these interferences fail to account for all the differences between the measured and modeled levels of HO_x radicals found in numerous field campaigns. Underestimations of OH and HO₂ concentrations have been recorded in urban areas (Dusanter, et al., 2009; Sheehy et al., 2010; Tan et al., 2018; Whalley et al., 2018; Zhang et al., 2022), suburban (Lu et al., 2013; Tan et al., 2019; Yang et al., 2021) and rural environments (Tan et al., 2017; Bottorff et al., 2023). As concluded by previous reviews (Rohrer et al., 2014; Lu et al., 2019) and as shown in Figure 5, the discrepancy between the HO₂/OH ratio measured and modeled is strongly dependent on the NO level with a strong overestimation of the model at low NO which suggests a need for a better understanding of the radical chemistry at low NO levels for which radical + radical reactions will be more important.

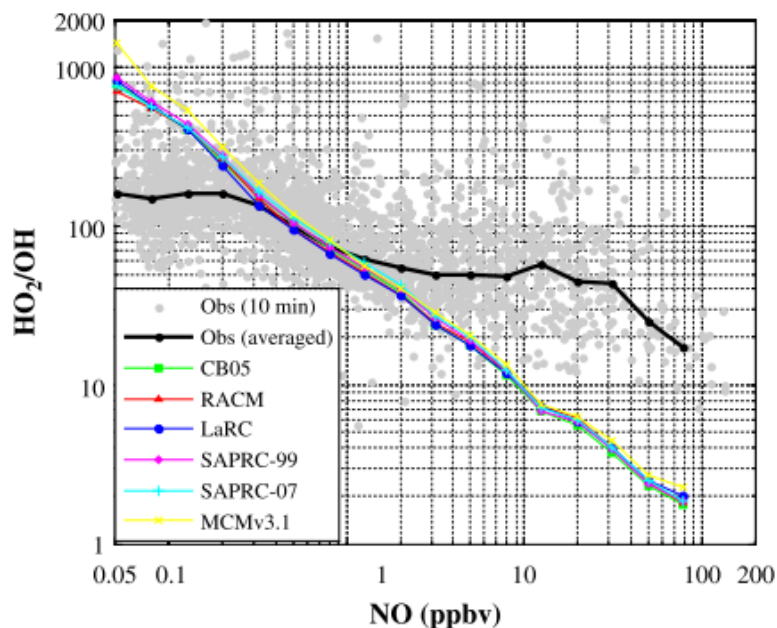


Figure 5: HO_2/OH measured (during the TRAMP campaign) and modeled as function of NO concentration (Chen et al., 2010)

Field campaign measurements, carried out at the ground level or using aircraft, dedicated for the understanding of HO_x role in the atmosphere presents notable challenges. This complexity arises from the dependence of the radical production or loss processes on many parameters including the photolysis rate of precursors (such as O_3 and HONO) or the concentration of numerous species with which they interact (Clemmitshaw, 2004).

1.2.4. Interferences on HO_x measurements

As discussed above, different instruments with high sensitivity and appropriate limits of detections are involved for the measurement of the OH and HO_2 (HO_x) concentration in the atmosphere. In the last few years, the overestimation of OH and HO_2 concentration by models compared to measurements highlighted different types of OH and HO_2 interference. This section is dedicated to the presentation of known interferences for the HO_x measurement using the FAGE technique.

1.2.4.1. Interferences on OH measurements using FAGE technique

Two different types of OH interferences using the FAGE technique have been reported in the literature: spectral and chemical interference.

Spectral interference occurs when other species are fluorescing at the same wavelength as OH such as naphthalene, sulfur dioxide and formaldehyde (Ren et al., 2004). Studies have shown that only naphthalene has an excitation spectrum with defined lines in the wavelength region near 308 nm. However, this contribution can be easily eliminated by well selecting the laser wavelength and by alternating the measurement at a wavelength corresponding to OH line

(on resonance) and out of OH line (off resonance) and subtracting the OH fluorescence signal off resonance from the on resonance, this measurement mode is called OHwave.

Chemical interferences can occur due to the photolysis of chemical species producing OH at the wavelength used to excite OH (308 nm). When using high repetition rate lasers (few kHz), care should be taken to refresh the gas mixture in the detection volume between each laser pulse in order to limit this type of OH interference. Extensive chemical interference tests were made by (Ren et al., 2004) for different atmospheric species in different concentration ranges: ozone (up to 4 ppm), hydrogen peroxide (up to 120 ppb), nitrous acid (up to 5 ppb), formaldehyde (up to 250 ppb), nitric acid (up to 50 ppb) and acetone (up to 200 ppm). Except for ozone, none of the chemical species showed a noticeable interference signal under ambient conditions. However, other studies assumed this interference to be eliminated in current atmospheric OH measurements (Schlosser et al., 2009).

Additional non-photolytic chemical interferences can occur via the generation of OH radicals within the low-pressure FAGE cell from dark reactions. Holland et al. (Holland et al., 1995) showed that the O₃ interference signal was linear with respect to the laser power for a given O₃ concentration. This interference was attributed to possible heterogeneous reactions within the detection cell in the gaseous mixture or on the walls of the cell. Lu et al. (Lu et al., 2012) have reported during the PRIDE campaign that O₃ interference is only dependent on the concentration of O₃ entering the cell. Fuchs et al (Fuchs et al., 2016) did not observe any instrumental interferences under typical ambient ozone concentration and BVOCs. However, a measurable OH interference is detected when high ozone concentration is reacted with high concentration of BVOCs. The observed interference has been well characterized and confirmed to be negligible under atmospheric conditions.

The chemical interferences can also involve species other than O₃ that could decompose and produce OH radicals in the FAGE cell. This type of interference was made following the overestimation of OH concentration by models compared to field measurements in forestry environment (Mao et al., 2012; Whalley et al., 2011), even after improvements in oxidation mechanisms such as the isoprene one. This hypothesis has been tested by the FAGE instrument of PennState University during campaign in forest (Mao et al., 2012) using a pre-injector on top of the instrument to inject intermittently an OH scavenger (C₃F₆). The results obtained by Mao et al. showed significant OH interference of up to 50 %. The analysis of the interferences as a function of the conditions exhibit a dependence of the interference on the low NO chemistry which favors RO₂ reactions (from BVOCs such as isoprene) with other radicals whose product could be dissociated in the FAGE cell. This measurement mode alternating fluorescence signal

without and with scavenger is called OHchem and is used by different groups to eliminate this interference (Fuchs et al., 2011; Whalley et al., 2013).

Recently, from the kinetic studies done on the reaction of different $\text{RO}_2 + \text{OH}$ leading to the formation of different products (Fittschen, 2019) and the results showing a strong decrease in the HO_2 yield with the increase of the alkyl group, a hypothesis that trioxide ROOOH could be a source of interference in the FAGE instrument was emitted by our group. Indeed, when increasing the alkyl group, the pathway leading to HO_2 becomes very minor at the profit of the ROOOH stabilization pathway. This hypothesis has been confirmed performing a series of experiments with the FAGE instrument at Lille University in its reactivity configuration (Fittschen et al., 2019). The experimental results showed a significant interference for conditions in favor of ROOOH formation and supported by a modelling study done at the university of Cambridge. The model simulations predict high ROOOH concentrations in pristine environments which would be high enough to generate within the Lille FAGE an interference at the same order as the OH concentrations that have been observed in field campaigns in pristine environments.

1.2.4.2. Interferences on HO_2 measurements using FAGE technique

In order to detect HO_2 by LIF, it should be converted into OH by the rapid reaction with NO . It has been demonstrated that RO_2 species produced during the oxidation of VOCs such as alkenes, aromatics and long-chain alkanes can be a source of HO_2 interference in FAGE instruments (Fuchs et al., 2011; Whalley et al., 2013) due to the reaction with NO . Long alkyl chain RO_2 can also produce an interference owing to isomerization of the RO_2 species giving HO_2 . Other functionalized RO_2 could also interfere. The level of this interference may vary depending on the type of RO_2 and the probing conditions. Different tests have been performed to adjust the operating conditions to either minimize the interferences for measuring HO_2 or optimize the conversion and determine the conversion efficiency of RO_2 into HO_2 to measure HO_2^* , which represents the sum of HO_2 and the interference due to RO_2 converted.

These interferences on HO_x measurements could explain a part of the discrepancies between measured and modeled HO_x radicals. However, measuring HO_x radicals in field campaigns is still considered challenging and techniques need to be improved and tested in atmospheric simulation chambers (Fuchs et al., 2013; Novelli et al., 2020). A better understanding of the atmospheric chemistry can be obtained by simultaneous quantification of these radicals and the so called “OH reactivity” (inverse of OH lifetime).

1.2.5. Principle of the OH reactivity

OH reactivity, which represents the sum of OH losses, is considered as another important parameter to measure to better describe the radical balance. It provides global information about the different species present in the atmosphere reacting with OH. The OH reactivity is proportional to the species concentration multiplied by their respective rate constant. The total OH reactivity represented below is expressed in s^{-1} :

$$k_{air} = \sum_i k_{X_i+OH}[X_i] \quad \text{Equation 6}$$

where X_i is the reactive species, k_{X_i} represents the rate constant of $OH + X_i$ and $[X_i]$ the concentration of the reactive species.

The measured OH reactivity can be compared to the calculated reactivity based on the simultaneously measured concentrations of OH reactive species in the same volume and their corresponding well known rate coefficients (Di Carlo et al., 2004; Mogensen et al., 2011; Bsaibes et al., 2020; Cho et al., 2023; Whalley et al., 2016). A possible difference between measured and calculated reactivity describes the OH sinks due to the presence of unmeasured reactive species in the atmosphere. This difference is known as the missing reactivity.

$$k_{missing} = k_{measured} - k_{calculated} \quad \text{Equation 7}$$

The OH missing reactivity change as function of the atmospheric conditions (period of the day: day or night, temperature, wind direction and others), which allows to make assumptions concerning the unmeasured but critical species in the OH budget.

1.2.5.1. Measurement techniques of tropospheric OH reactivity

Different methods for measuring the tropospheric OH reactivity have been developed and applied in a wide range of studies. In this section a brief discussion about the main techniques used to measure OH reactivity, including one techniques using FAGE detection: the laser flash photolysis (LP) technique (Sadanaga et al., 2004; Stone et al., 2016), which directly measures OH decay rates. The comparative reactive method (CRM) technique measures the variation of the concentration of a reagent molecule detected with either mass spectrometry (MS) or gas chromatography (GC) techniques (Sinha et al., 2008; Hansen et al., 2015).

1.2.5.1.1. The laser flash photolysis technique coupled to a FAGE/LIF detection (LP-LIF)

The laser flash photolysis technique is based on generating OH in a reactor (photolysis cell) through the photolysis of O_3 at 266 nm by a pulsed laser and subsequent reaction with H_2O . The decay of the OH radical concentration can subsequently be followed by time-resolved LIF technique through coupling the reactor to a FAGE cell. The time scale of the reaction to be studied is determined by the duration of the photolysis pulse which must be short (in

nanosecond) compared to the reaction time. This technique is a real time measurement technique allowing the measurement of short lifetime atmospheric species such as OH. The OH radical detection system that is connected at the end of the reactor enables the measurement of the time-resolved concentration profiles under pseudo-first order conditions (one of the reactants is in large excess over the second reactant and thus its concentration can be considered constant during the reaction). Another advantage of this technique is the production of the reactants from well-mixed precursors (if the photolysis is homogeneous), so there is no mixing time impacting the time resolution. Also, since the reactants are produced and monitored at the center of the coated photolysis cell (with an unreactive substance), the wall chemistry is generally minimized. The main drawback is the possible simultaneous co-generation of different radicals and secondary co-photolysis products may lead to complicated secondary reactions. This is the technique used in this work and it will be described in detail in Chapter 2.

1.2.5.1.2. The comparative reactive method (CRM)

This method is based on competitive reactions of OH with the reactive species present in ambient air and with a selected reagent molecule quantified by a suitable detector at the output of the reactor. The reagent molecule, such as pyrrole (C_4H_5N), must satisfy some general criteria as capable of being well measured (have physical and chemical properties for easy and accurate detection) and the rate constant for its reaction with OH should be well established. Also, it should not be present in ambient air under normal circumstances.

The CRM apparatus consists of two components: the first one is a reactor where the OH is mixed with the tracer and alternately with either zero air (without reactive species) or with ambient air. The second component is an appropriate detector that enables the measurement of the tracer concentration. Typically, this detector is a Proton Transfer Reaction-Mass Spectrometer (PTR-MS) or a Gas Chromatography-Flame Ionization Detector (GC-FID) (Nölscher et al., 2012; Sinha et al., 2008). The OH reactivity is measured by monitoring the pyrrole concentration in different conditions as shown in Figure 6.

The initial step involves introducing solely pyrrole and dry zero air to measure C_1 , which corresponds to the pyrrole concentration in absence of OH. Subsequently, humid zero air is introduced to generate OH through the photolysis of water vapor using a mercury lamp emitting light at 185 nm, the pyrrole concentration C_2 is then measured. The C_2 has a lower value than C_1 due to pyrrole reacting with OH. In the last step, zero air is substituted with ambient air. This triggers a competition between the reaction of OH with pyrrole and OH with reactive species present in the ambient air. The measured concentration labeled as C_3 , higher than C_2 , is measured.

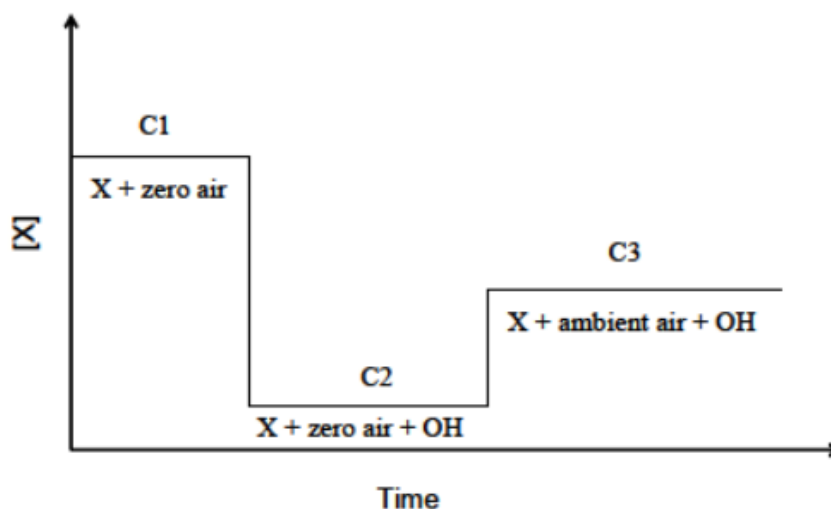


Figure 6: Schematic representation of the CRM concept

The value of the OH reactivity can be obtained using the following equation:

$$k_{OH} = \frac{C3 - C2}{C1 - C3} k_{pyrrole+OH} \cdot C1 \quad \text{Equation 8}$$

where $k_{pyrrole+OH} = 1.28 \times 10^{-10} \text{ cm}^3 \text{ molecule}^{-1} \text{ s}^{-1}$ (Dillon et al., 2012)

However, this calculation is subject to different types of adjustments depending on the operational parameters of the instrument (including dilution and pseudo first order corrections) and the environmental conditions, particularly the concentration of NO_x (Michoud et al., 2015). In cases where the concentration of ambient NO is high, the HO_2 radical generated from the water photolysis can be rapidly converted into OH radicals within the reactor. These additional OH can react with pyrrole, subsequently altering the pyrrole concentration and thereby introducing an error in the determination of the reactivity value, necessitating correction.

The advantage of this method is that absolute concentrations are not needed. The disadvantages are the presence of unknown secondary reactions and the uncertainty on the rate constant of the reference reaction.

1.2.5.2. Field measurements of OH reactivity in the troposphere and modeling

Around 40 field campaigns involving OH reactivity have been carried out in different environments under various atmospheric conditions, including clean air (marine boundary layer), continental low- NO_x regions influenced by biogenic emissions (forests and rural areas) and polluted urban areas. The ranges of reactivities as function of NO_x concentration in the different types of environments are reported in Figure 7.

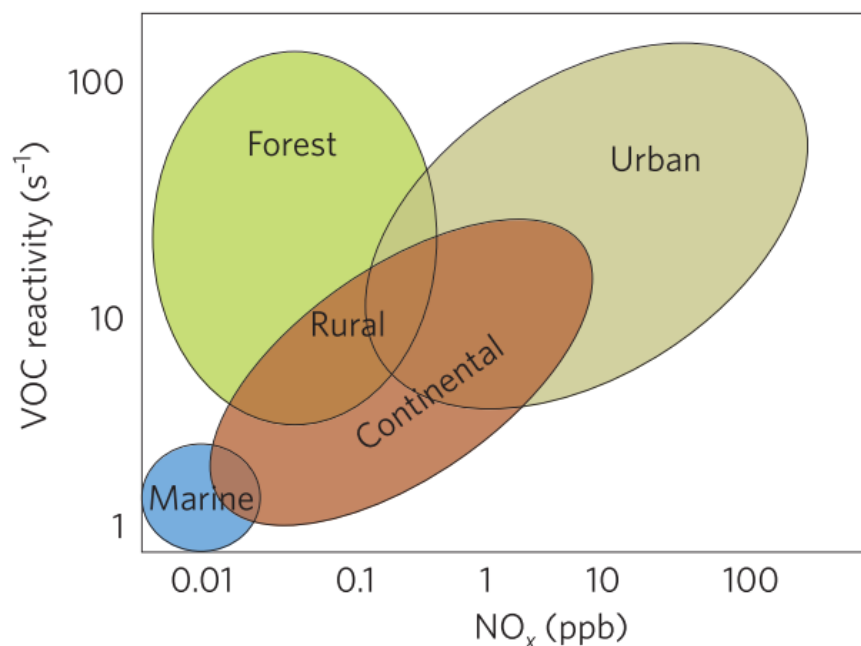


Figure 7: Classification of different types of environments depending on the VOCs reactivities and NO_x concentration (Rohrer et al., 2014)

Field measurements have shown that the OH reactivity in urban areas is higher than in rural areas due to the presence of a quite large number of anthropogenic species in high concentrations such as NO_2 , alkenes and aromatics, as has been observed in Tokyo (reactivity up to 100 s^{-1}) (Yoshino et al., 2006, 2012), with a missing reactivity on the order of 30 %. They found a good correlation between missing OH reactivity and measured oxygenated VOCs (OVOCs) in summer, spring and autumn, assuming that the missing reactivity is due to an unmeasured secondary OVOCs. A similar missing OH reactivity was observed in London (Whalley et al., 2016). In Beijing (Yang et al., 2017), a missing reactivity of 21 % was observed, mainly attributed to unmeasured primary species, such as branched alkenes. High reactivities were reached during a campaign in India (Kumar & Sinha, 2014) at a suburban site influenced by both urban and agricultural emission sources.

On the other hand, lower reactivities (order of 10 s^{-1}) were observed in forest environments (dominated with BVOCs) and poor agreement between calculated and measured OH reactivity was also obtained. During the PROPHET (Program for Research on Oxidants: Photochemistry, Emissions, and Transport) campaign, investigations showed that the missing reactivity (33-50 %) increased significantly with temperature and concentration of BVOCs (Di Carlo et al., 2004). This behavior could be explained by the presence of unknown BVOCs in the site. During the LANDEX (LANDes EXperiment) campaign (Bsaibes et al., 2020), an average missing OH reactivity of 22 % and 33 % was observed inside and above the canopy, respectively. The nighttime missing OH reactivity was higher than during the day for stable and

warm conditions, which promotes the accumulation of long-lived primary and secondary compounds. The missing OH reactivity during the day is dependent on temperature, though it is unclear whether it is due to an increase of primary or secondary compounds. Similar to LANDEX, in North China Plain (Wangdu) (Fuchs et al., 2017), the highest missing OH reactivity (approximately 25 %) was observed during the nighttime. Only one study of OH reactivity conducted in a forested environment (Ren et al., 2006) does not report significant missing OH reactivity. The measurements were conducted in a forest in eastern New York State, which could be influenced by nearby urban air masses. It remains unclear why there was no significant missing OH reactivity at this site, despite the fact that isoprene only contributed around 14 % to OH reactivity.

Reactivities are very high in tropical rainforest. For example, during the campaign done in April 2008 within a tropical rainforest on Borneo (Edwards et al., 2013), the OH reactivity reached a maximum around 84 s^{-1} . The missing reactivity during these measurements was approximately 30 %, with oxidized intermediates considered as potential contributors. Reactivities up to 72 s^{-1} were also measured during a campaign in the Suriname forest (Sinha et al., 2008) with 35 % of the total reactivity being attributed to isoprene, MVK+MACR, acetone, acetaldehyde and methane (Kubistin et al., 2010). Campaigns in boreal forests have determined significant missing reactivity from 58 to 89 % attributed to unmeasured primary species and secondary products derived from the oxidation of VOCs (Nölscher et al., 2012).

These different field campaigns in most of the environments have demonstrated a lack of atmospheric chemistry understanding. Even with some assumptions and improvements in the atmospheric chemical mechanism there is still remaining a large gap between models and atmospheric measurements. Therefore, it is necessary to continue field measurements under different atmospheric conditions in different environments. Also, in order to better understand these discrepancies between measurements and models and determine more accurate chemical mechanisms, laboratory measurements under controlled conditions are useful.

1.3. Conclusion

This chapter has described the troposphere which is highly variable in chemical composition and physical conditions. HO_x and RO_x radicals are present in a very low concentration and involved in oxidation processes in the gas phase. The understanding of these oxidation processes, which is still challenging, allows to better identify the products generated in the atmosphere. For this reason, laboratory measurements under controlled conditions and field measurements have been performed using different types of instruments. During this work, the FAGE technique (presented in chapter 2) was improved and deployed for the quantification of OH, HO_2 and RO_2 radicals and OH reactivity measurements during the ACROSS field campaign (Chapter 5) and measurements at the SAPHIR simulation chamber (Chapter 4). It was also used in the laboratory (reactivity configuration) to study oxidation mechanisms of importance for indoor and outdoor chemistry involving HO_x and RO_x radicals (Chapter 3).

Chapter 2: Experimental Set-up

The UL-FAGE instrument used during this work enables the measurement of the following parameters: quantification of the OH, HO₂ and HO₂* (sum of HO₂ + RO₂ converted such as RO₂ from double bond precursors such as β-hydroxyalkylperoxy, long alkyl chain RO₂), RO_x quantification when the UL-FAGE is coupled to a conversion flow-tube (RO_x-FAGE) and OH reactivity measurement when coupled to a photolysis cell. This chapter provides a detailed description of the UL-FAGE instrument in the 3 configurations (OH, HO₂, HO₂* setup, RO_x-FAGE setup and OH reactivity setup) to be used in the field, in simulation chambers and in laboratory (OH reactivity configuration to perform kinetic studies).

As a part of my work was dedicated to the optimization of the new RO_x-FAGE setup, a focus on it will be presented in this chapter.

2.1. The UL-FAGE Technique

The UL (university of Lille)-FAGE (Fluorescence Assay by Gas Expansion) instrument is based on the LIF (Laser Induced Fluorescence) detection of OH at low pressure after a gas expansion. The UL-FAGE instrument was first developed for the quantification of OH and HO₂ in the atmosphere and then it was adapted for the measurement of the total OH reactivity in ambient air and later to RO₂ measurements. The OH reactivity set-up can also be used to perform kinetic studies involving OH in the laboratory.

The instrument is constituted of different parts, some common between the different configurations:

- the excitation laser used as a high repetition rate UV light source for the excitation of OH in order to average the fluorescence signal while keeping a high time resolution (details in section 2.3).
- the FAGE cell for the detection of the fluorescence of OH, directly from OH or after conversion of HO₂ or RO₂ to OH (details in section 2.2).
- the pump for the expansion of the gas mixture
- the reference cell to lock the laser on an OH excitation peak (OH resonance) (details in section 2.4)

and some specific parts:

- the photolysis cell for the OH reactivity where OH is generated by a pulsed photolysis laser (details in section 2.6.1)
- the conversion cell for the RO_x-FAGE instrument (details in section 2.5.2)

During this work the FAGE technique has been used in different measurement

configurations for both laboratory and atmospheric measurements. A summary of these configurations is presented in this section.

2.1.1.1. Measurement Configuration used during Atmospheric Measurements

The UL-FAGE participated in two different campaigns:

- The ACROSS campaign to perform atmospheric measurements. These measurements allow to better understand the atmospheric chemistry of a particular environment.
- The RO₂ intercomparison campaign: measurements done at the SAPHIR chamber under controlled conditions. This type of intercomparison exercise allows to test the reliability of different instruments by quantifying radicals in the same air mass.

2.1.1.1.1. ACROSS campaign

During the ACROSS campaign, the UL-FAGE instrument was used in the configuration shown in Figure 8 including the complete set of UL-FAGE instruments:

- OH and HO₂ cells (described in 2.5.1)
- RO_x-FAGE (described in 2.5.2)
- OH reactivity (described in 2.6)

More details about this configuration will be presented in Chapter 5.

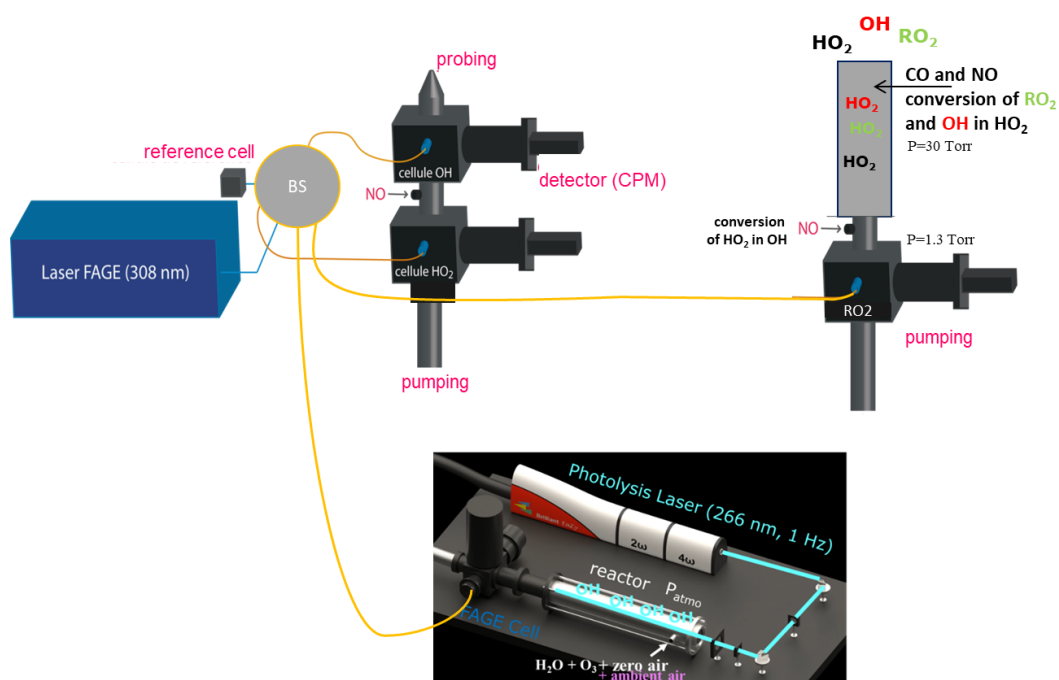


Figure 8: Measurement configuration used during ACROSS campaign

2.1.1.2. RO_2 intercomparison campaign : SAPHIR chamber

During the RO_2 intercomparison campaign, the UL-FAGE instrument was only used in its quantification mode (as shown in Figure 9) to measure OH, HO_2 and RO_2 radicals. This measuring configuration will be explained in detail in Chapter 4.

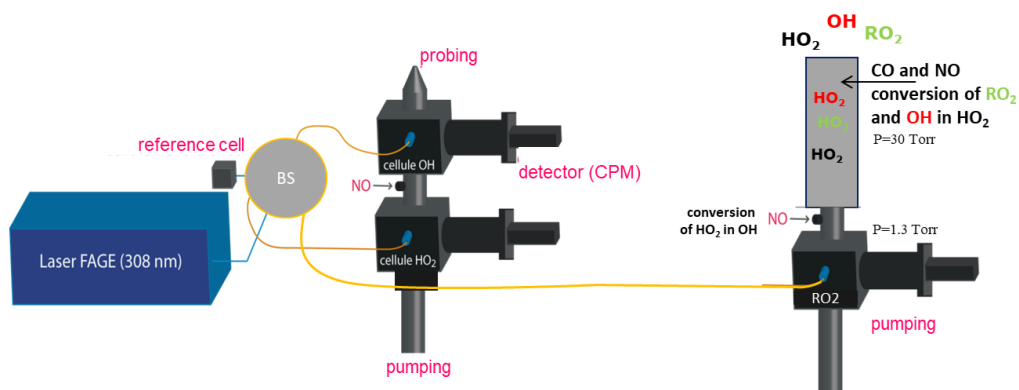


Figure 9: Measurement configuration used during the RO_2 intercomparison campaign

2.1.2. Measurement Configuration used during Laboratory Studies

Laboratory measurements have been done using the reactivity set-up for two different topics:

- Studying the chemistry of organosiloxanes through determining the rate constant of the reaction of siloxanes with OH using one photolysis laser.
- Studying the influence of humidity on the $RO_2 + OH$ reaction through determining the HO_2 yield of this reaction at different humidity levels using two photolysis lasers.

2.1.2.1. Influence of humidity on radical + radical reaction

Studying the influence of humidity on the HO_2 yield of the $RO_2 + OH$ reaction has been done using the OH reactivity setup (Figure 10) using two different photolysis lasers to generate separately the two different radicals in the photolysis cell. In the first part of the Chapter 3, more details will be discussed about this measurement configuration.

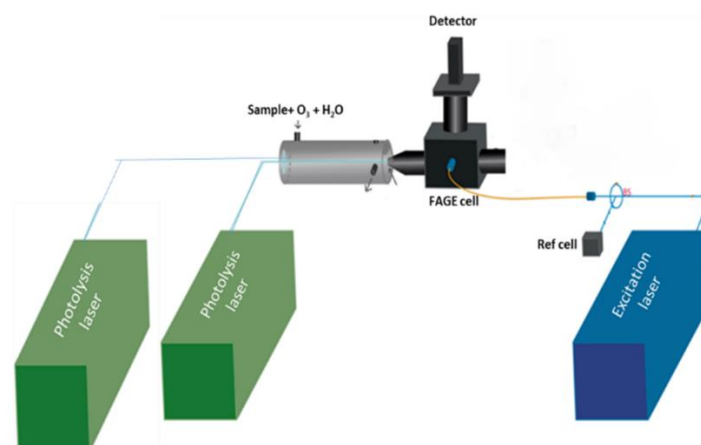


Figure 10: Measurement configuration used during the study of humidity effect on $RO_2 + OH$ reaction

2.1.2.2. Chemistry of Siloxanes

Studying the chemistry of organosiloxanes has been done under controlled conditions using the OH reactivity setup shown in Figure 11. During this study only one photolysis laser was used to generate the OH radical and a known concentration of the studied organosiloxane compound has been injected into the photolysis cell to determine the rate constant of the reaction of OH + organosiloxanes. More details of these measurements will be discussed in the second part of Chapter 3.

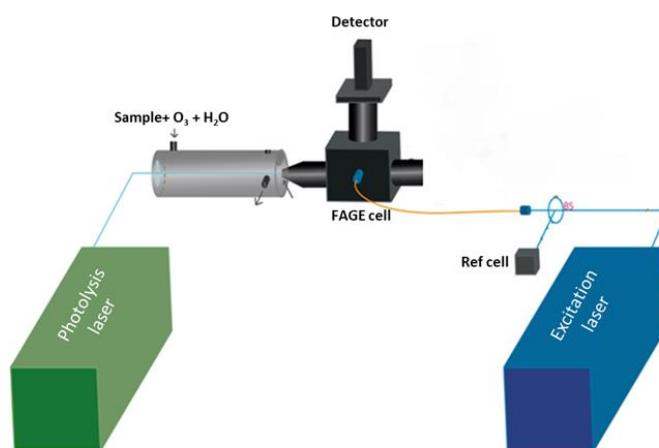


Figure 11: Measurement configuration used during the siloxanes kinetic studies

2.2. Description of the FAGE cells used in the different configurations

The FAGE cells are composed of 4 parts: the excitation laser injection, the probing, the cell where OH is excited and the collection of the fluorescence.

All the FAGE cells used in the UL-FAGE instruments are White type multi-pass cells (Figure 12) based on the PennState design (Faloona et al., 2004). Each one is composed of three concave mirrors: one front mirror, cut out on edges, through which the laser beam enters and exits the cell and two back mirrors. Usually, the cell is aligned so that the total number of passes of the laser beam in the cell is between 24 and 40 (Parker et al., 2011). The use of a multi-pass cell is considered as an advantage compared to the single pass cells because it allows to limit the laser density and increases the sensitivity. The disadvantage of the multi-pass cell compared to single pass cell is the increase in the background signal due to scattered laser light thus reducing the sensitivity to a certain extent. The laser beam exiting the White cell is sent on a photodiode to continuously monitor the laser power stability and to enable normalization of fluorescence signals for laser power fluctuations.

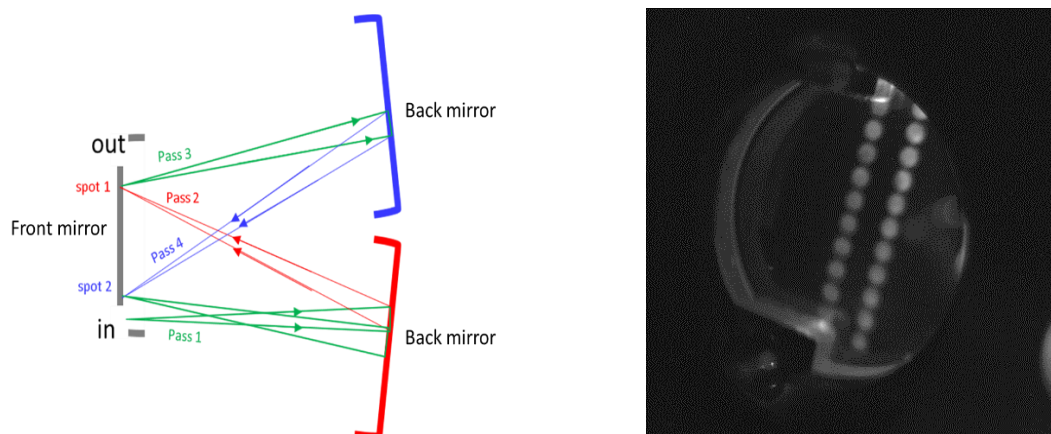


Figure 12: Representative schemes of the multi-pass cell

The fluorescence is collected at 90° with respect to the laser beam through a system of two lenses. An interference filter at 308 nm can be added (used for the OH cell) to limit the ambient light contribution. The fluorescence is detected by a CPM (Channel Photon Multiplier, Perkin Elmer or Proxivision), made of 3 components: a photocathode which converts the photons into electrons, the tube where the electrons are multiplied on the walls and an anode where the electrons are collected. An electronic card allows the shaping of each peak/photon. The signal is collected by an acquisition card (National Instrument) to perform photon counting. As mentioned previously, the excitation and the detection are in the same wavelength range but the lifetime of the OH fluorescence is extended (several hundreds of nanoseconds) through the reduced pressure, therefore the use of gated detectors is essential in order to discriminate between the OH fluorescence and scattered laser light. The gated CPMs are switched off during the laser pulse and rapidly switched on to collect the fluorescence signal after the laser pulse varying the voltage of the cathode using a delay generator connected to the power supply. For that, the voltage applied to the photocathode is modulated using an external power supply. When a high voltage is applied to the photocathode with respect to the voltage at the channel entrance, the detector is turned off. On the contrary if a lower voltage is applied to the photocathode with respect to the channel entrance, the photoelectrons will enter the electron multiplier tube and, hence, the detector is turned on. Two types of CPM are used: a negative CPM on the OH cell and a positive one on the HO₂ cell, RO_x cell and reactivity cell (Figure 13).

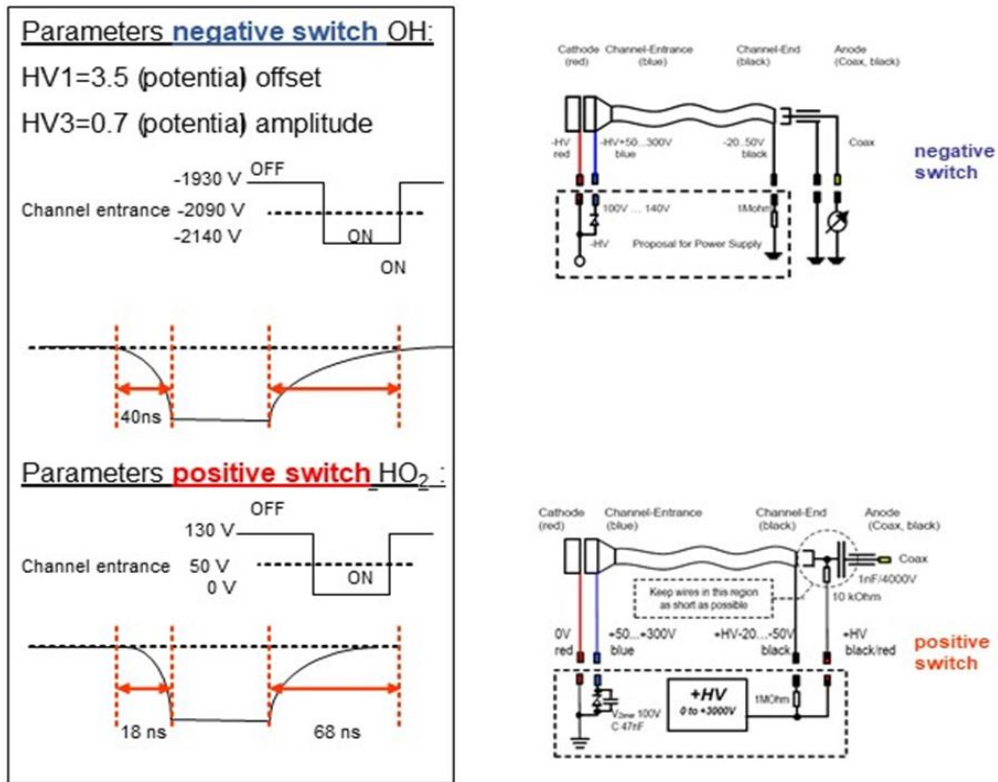


Figure 13: Schematic representation of a CPM (Perkin Elmer) connected to a negative and positive switch

Figure 14 shows the synchronization diagram to collect the fluorescence with a positive CPM as an example. The main drawback of the gated CPM is the presence of parasite peaks as the switch is turned on, which increases the noise level. Therefore, to avoid this increase in the noise level, the counting of the photons must be delayed after the CPM parasite peaks. In the quantification mode, the CPM is gated a second time for the measurement of the background signal since it is essential to subtract the background signal generated due to the remaining ambient light. The data acquisition is controlled by a delay generator, which is triggered internally at 5 kHz and starts the YAG, the detector switches and the acquisition card.

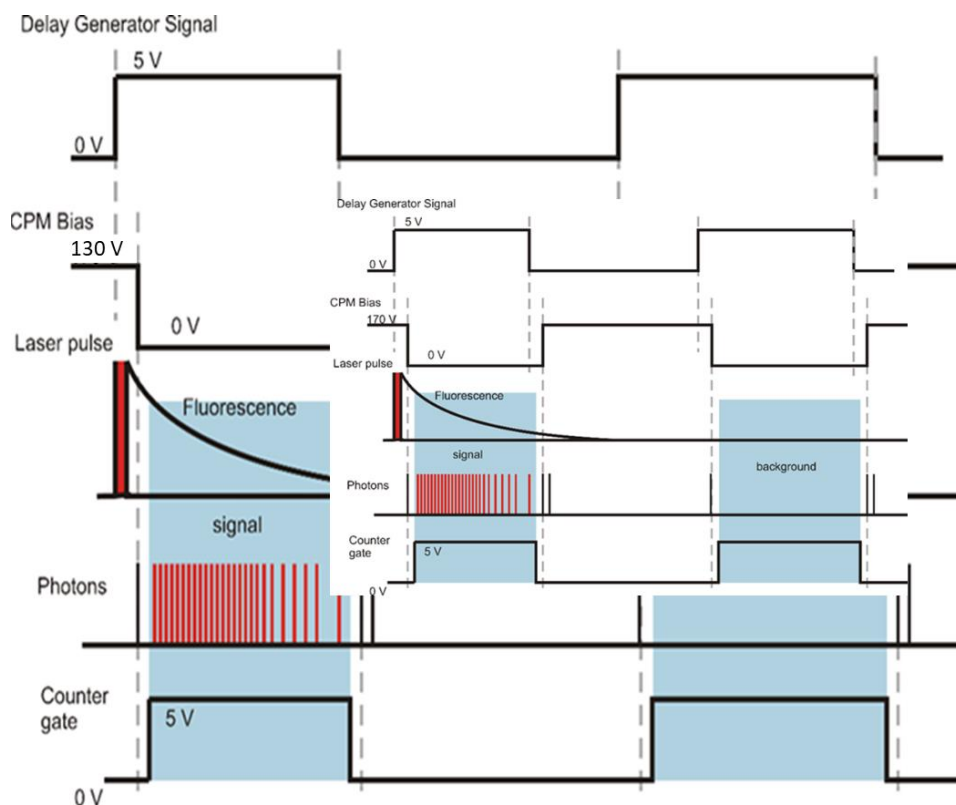


Figure 14: Diagram to illustrate the detection of the OH fluorescence controlled by the gate timing of the CPM detector and the photon counting card (Amedro, 2012)

Four different FAGE cells, presented in Table 4, have been used during this work. OH cell to quantify OH radicals, HO₂ cell to quantify HO₂ and HO₂^{*} radicals (section 2.5.1), RO_x cell to quantify HO₂^{*} and RO₂ radical concentration (section 2.5.2) and OH_{reactivity} cell to measure the OH reactivity. These cells are used in different operating configurations to perform measurements in the laboratory and during field campaigns.

Table 4: The different FAGE cells used for different measurements and the CPM used on each cell

Cell	Use	CPM
OH _{reactivity}	Reactivity measurement	PE – positive switch
OH	OH quantification	PE – negative switch
HO ₂	HO ₂ and HO ₂ [*] quantification	PE – positive switch
RO _x	HO ₂ [*] and RO ₂ quantification	Proxivision – positive switch

2.3. The Excitation Laser

Two different excitation laser systems have been used during my thesis to excite the OH radicals in the FAGE cells.

The Q₁(3) transition, A–X 0–0 at 308.05 nm is chosen (Figure 15) since the Q₁(3), Q₂(1),

$P_1(1)$ triplet is easily identified and this transition corresponds to one of the most intense peaks around 308 nm.

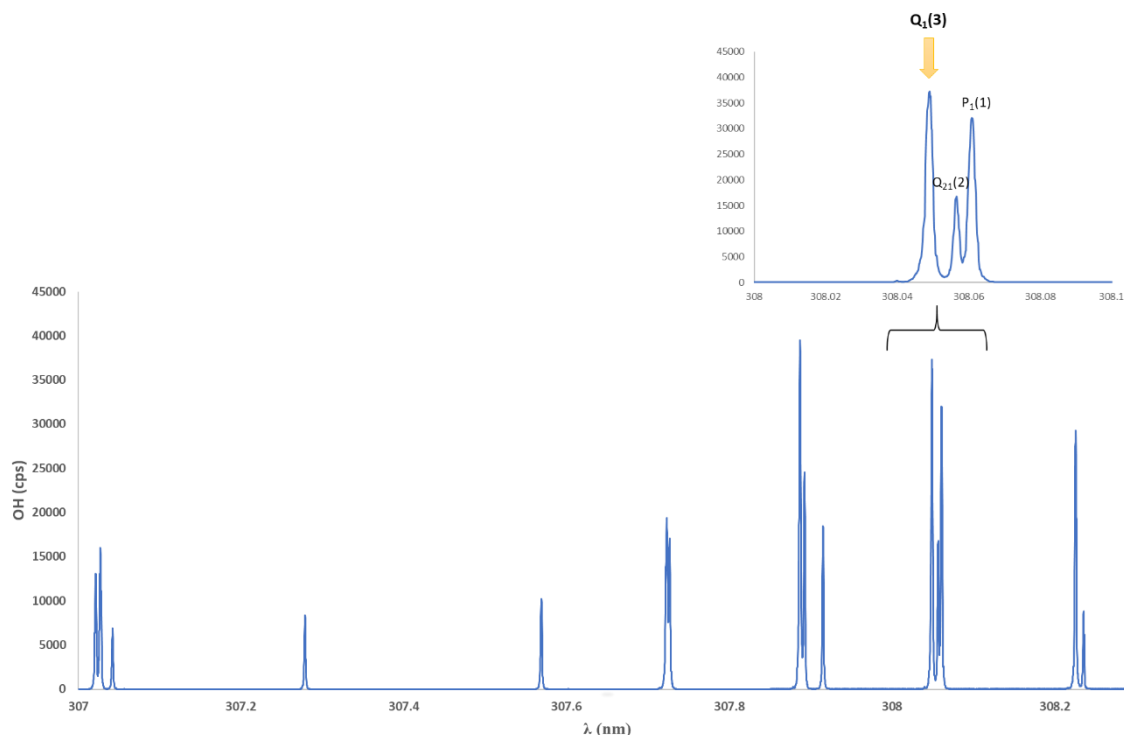


Figure 15: Excitation spectrum of OH at the spectral range 307 - 308 nm

The first excitation laser, used at the beginning, is a tunable frequency doubled dye laser (Sirah Laser PrecisionScan) pumped by the frequency doubled output of a Nd: YVO₄ laser (Spectra Physics Navigator). The laser beam ($\lambda=1064$ nm) produced by the diode pumped Nd: YVO₄ laser is converted into green light ($\lambda=532$ nm) through the doubling crystal. The produced green light is used to pump a tunable single stage dye laser using a mixture of Rhodamine 610 also called Rhodamine B and Rhodamine 640 diluted in ethanol. The red shifted laser output beam exiting the dye cell ($\lambda=616$ nm) is focused onto a BBO doubling crystal to produce a laser emission around 308 nm. By using four Pellin-Broca prisms, the UV light is separated from the remaining fundamental (red) light. The output power of the laser beam at $\lambda=308$ nm ranges between 30 to 40 mW with a high repetition rate of 5 kHz and a pulse width of 20 ns. The diagram of the system is shown in Figure 16. This laser has a too low output power to be used with the complete set of FAGE instruments requesting 5 beams for the OH, HO₂, ROx and reactivity cells and the reference cell.

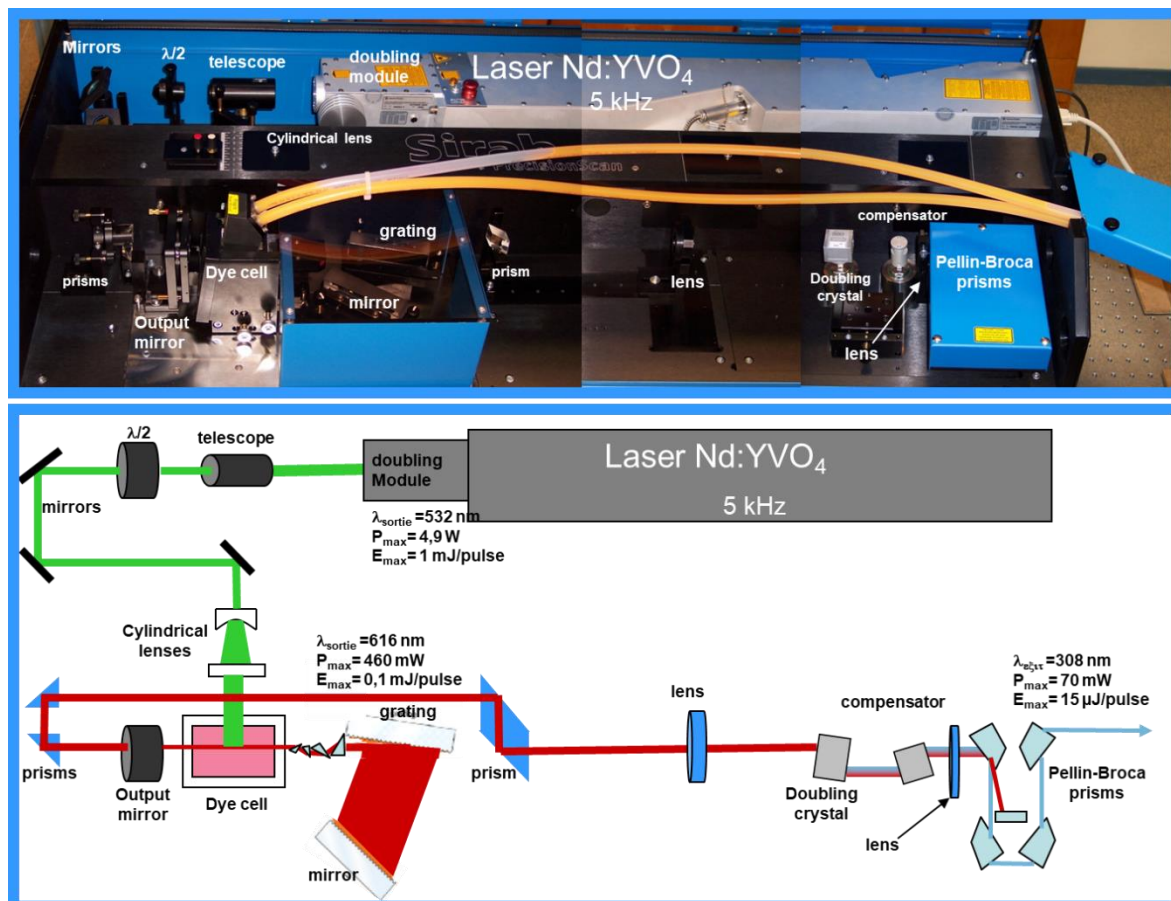


Figure 16: Diagram of the Sirah dye laser pumped by Spectra Physics high speed Vanadate laser

A new, 10 times more powerful laser (Sirah CREDO dye laser pumped by an Edgewave YAG laser) using DCM special dye has been tested in order to replace the old dye laser with the goal to be able to inject enough laser energy simultaneously into all the four different FAGE cells and the reference cell during field campaigns. The maximum output laser power is about 400 mW at 308 nm and around 3 W at 532 nm at 5 kHz. To check the power and wavelength stability of this laser, several tests have been done in the frame of my thesis (mentioned in section 2.7.1).

The laser beam at the output of the excitation laser is injected into the FAGE cells (OH, HO₂, RO_x and reactivity cell) through fibers. Different configurations can be used depending on the number of cells used (different fibered and non-fibered splitters). Most of my thesis results have been obtained using a 5 arms fibered beam splitter, where the beam exiting the excitation laser directly pass through a collimator that is connected to a fibered splitter with 5 branches connected to the four different FAGE cells (OH, HO₂, RO_x and OH reactivity) and the reference cell. The loss of laser power between the exit of the laser and the fibered splitter is lower using this configuration then with previous ones.

2.4. The Reference Cell

The excitation laser must be tuned on the wavelength corresponding to the maximum excitation of OH radicals ($Q_1(3)$, Figure 15). The laser wavelength may drift with time due to changing ambient conditions. Therefore, about 20% of the laser power is sent to a reference cell which is used to check the wavelength stability of the excitation laser and to move from ON resonance (at the peak) and OFF resonance (out of an OH peak) and *vice versa*.

A high and stable concentration of OH radicals is produced through thermolysis of water vapor on a heated coiled filament in the reference cell (Figure 17): for this purpose, ambient air is drawn through the cell made of a stainless-steel cube with a pressure inside kept at approximately 2 Torr using a vacuum pump. Contrarily to the detectors used in the FAGE cells, a non-gated CPM (Perkin Elmer) is used to collect the OH fluorescence signal perpendicular to the laser beam because the high OH concentration in the cell allows to observe easily the fluorescence signal on top of the signal due to scattered laser light.

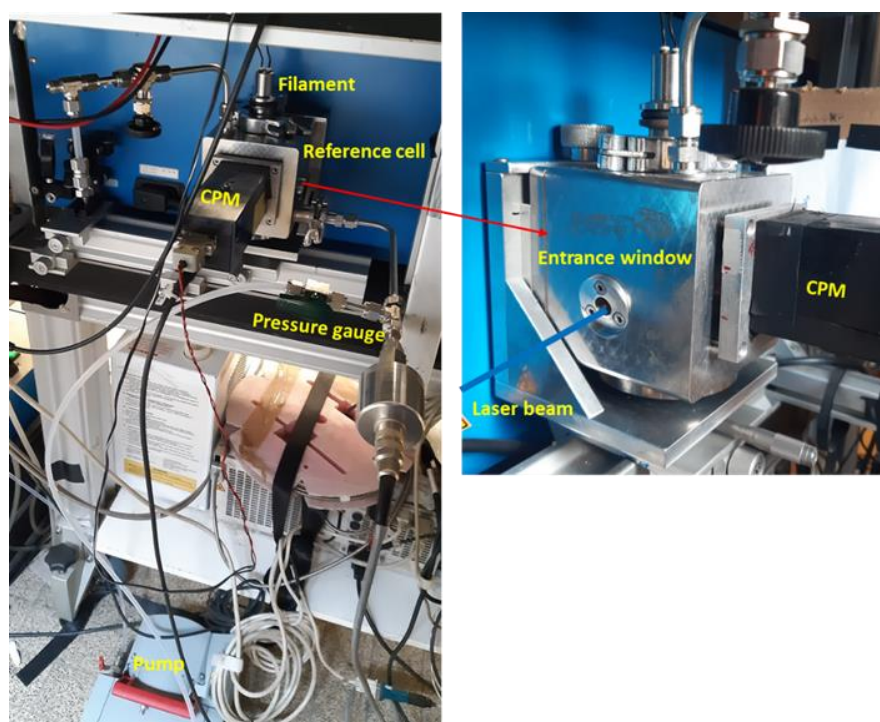


Figure 17: The reference cell used to select and stabilize the OH excitation laser wavelength

During the experiment, a laser wavelength scan is performed periodically over a small wavelength range (about 0.03 nm) in order to find the laser wavelength at which the $Q_1(3)$ transition occurs, as shown in Figure 18. The laser wavelength is automatically fixed on the OH excitation peak thanks to the Labview program used to control the laser, collect and analyse the signals.

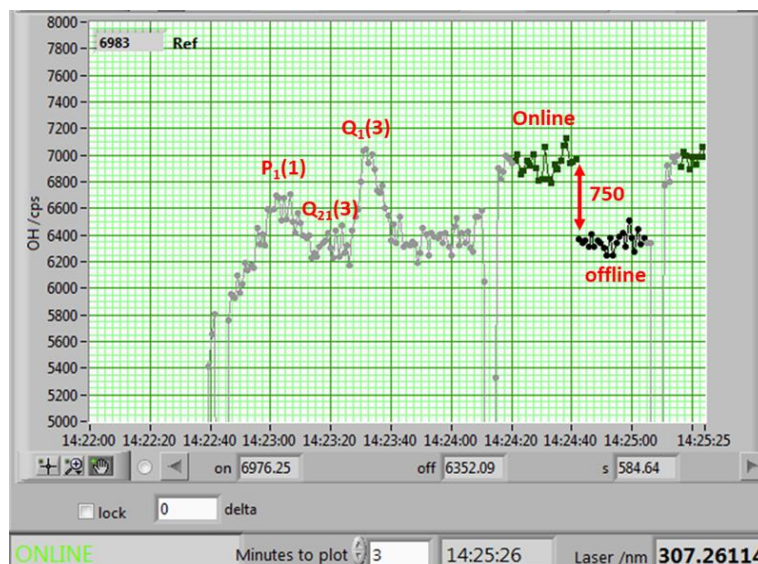


Figure 18: Typical reference cell signal for FAGE measurement sequence

The measurement sequence is generally alternating between online measurements (ON resonance) for 20 s and then the laser wavelength is shifted to a wavelength where OH does not absorb and the offline measurement (OFF resonance) takes place for 20 s.

2.5. Description of the UL-FAGE in the Quantification Mode

2.5.1. FAGE instrument for HO_x quantification

The UL-FAGE instrument used for the quantification of HO_x (OH and HO₂) radicals is based on the PennState design (Faloona et al., 2004). As shown schematically in Figure 19, it is composed of the excitation laser (pumping system), the FAGE cells (OH and HO₂) and the reference cell.

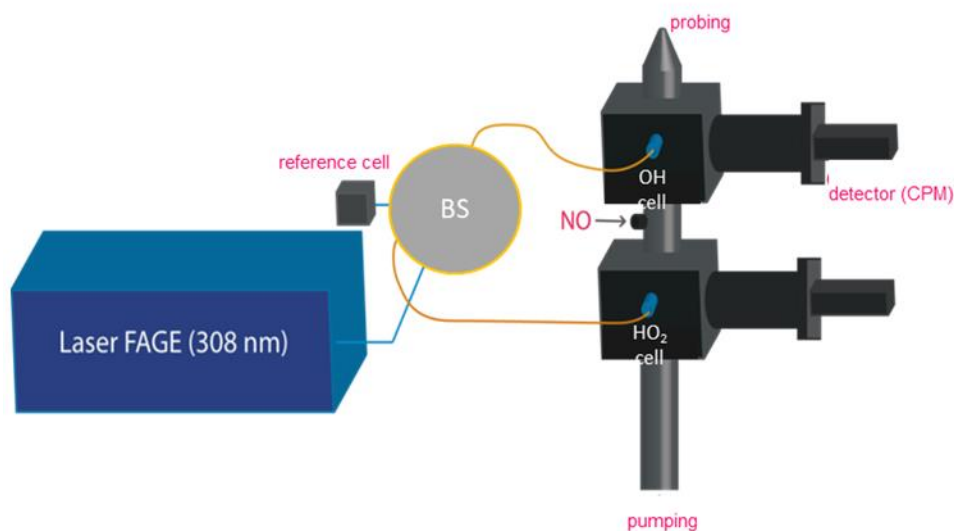


Figure 19: Scheme of the UL-FAGE instrument for OH and HO₂ radical quantification (CPM: Channel Photon Multiplier)

To sample the ambient air, a pumping system (Edwards XL 600 or iLX1000 connected also to the reactivity cell depending on the measurement needs) with a pumping rate of 8 to 9.2 L/min is used to draw the air through a small orifice (1 mm) into the two-low pressure (1.5 – 2 Torr) detection cells. The first cell (OH cell) is dedicated to the measurement of OH radicals and the second cell, placed downstream of the OH cell, is used for the quantification of HO₂ radicals after injection of NO to convert HO₂ into OH.

Thanks to the reference cell and the automation LabVIEW program, we can determine the net signal produced by the OH fluorescence ($S_{\text{OH fluorescence}}$), proportional to the OH concentration. It corresponds to the difference in the average of the S_{online} (ON resonance) and the average of the S_{offline} (OFF resonance). As the ambient light level might change between the online period and the offline period, a background signal ($S_{\text{background}}$), associated with the ambient light, must be recorded after a short delay (about 1.3 μs) after the fluorescence peak to derive $S_{\text{OH fluorescence}}$.

$$S_{\text{OH fluorescence}} = (S_{\text{online}} - S_{\text{background-online}}) - (S_{\text{offline}} - S_{\text{background-offline}}) \quad \text{Equation 9}$$

HO₂ radicals are measured indirectly in the second FAGE detection cell. NO is injected to the ambient airflow between the two detection cells to convert HO₂ into OH, leading to the quantification of the sum of ambient OH and HO₂. The HO₂ signal is obtained by subtracting the contribution of OH to the signal measured in the second cell. However, this signal may also contain some contributions due to RO₂ from VOCs containing double bonds (Fuchs et al., 2011; Lew et al., 2018) and/or long chain alkane (Whalley et al., 2013) depending on the pure NO concentration used (low [NO] = 1.24×10^{10} molecule cm⁻³: contribution considered as negligible, high [NO] = 2.48×10^{11} molecule cm⁻³: contribution considered as high). In conditions with significant RO₂ contribution, we consider that we measure the HO₂* signal: sum of HO₂ and a RO₂ contribution.

The FAGE is a very sensitive technique, but it is not absolute, thus, the calibration of the signal with a well characterized HO_x source is essential to convert the signal into concentration (see 2.5.3).

2.5.2. RO_x-FAGE instrument for RO₂ quantification

The FAGE technique can be expanded to the measurement of RO₂ radicals. This is done by coupling a RO₂-to-HO₂ conversion flow tube on top of the FAGE cell nozzle. This configuration is often called RO_x-LIF (Fuchs et al., 2008). In our case, we prefer to call it RO_x-FAGE because it well describes the coupling of a RO_x conversion tube to a FAGE cell (specific case of a LIF detection). Figure 20 shows that as the sampled air is pumped into the conversion

flow-tube, all HO_x and RO_x radicals can be continuously converted into OH by a two-step process. First, within the conversion tube the RO₂, RO and OH radicals are converted into HO₂ radicals by adding CO and well-chosen, low concentrations of NO. Then, HO₂ radicals are converted into OH through injection of pure NO above the FAGE cell. Two individual pumping systems are connected to the conversion flow-tube and the FAGE detection cell to independently adjust the pressure in both (P = 30 Torr in flow-tube and P = 1.3 Torr in FAGE cell).

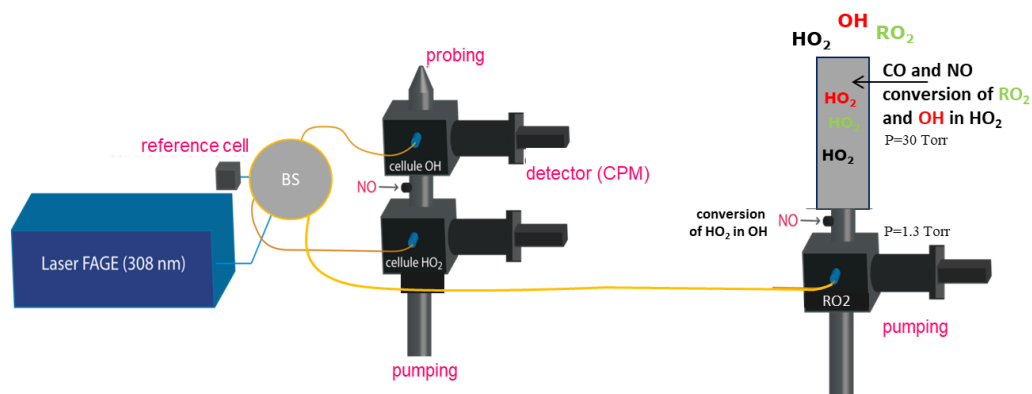
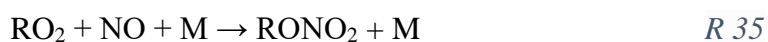


Figure 20: Scheme of the UL-FAGE instrument for OH, HO₂ and RO₂ measurement

2.5.2.1. Conversion principle

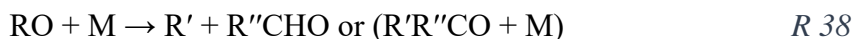
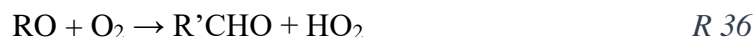
The chemical mechanism in the RO_x conversion tube consists of the RO₂ conversion propagating reactions which lead to the HO_x cycle and radical chain terminating reactions.

In the first step, the RO₂ radicals are converted into RO radicals through their reaction with NO which dominates the entire gas phase reactions of RO₂ radicals due to the high concentration of NO added. This reaction may lead either to the formation of alkoxy radicals (RO) and NO₂ (*R 34*) or nitrates (RONO₂) (*R 35*). Both channels share a common critical intermediate, the peroxy nitrite (ROONO) (Zhang et al., 2004), whose subsequent decomposition lead to *R 34* and collision stabilization gives *R 35*. The alkyl nitrate yield increases with the size of the alkyl group of the peroxy radical (Atkinson et al., 1982).



In a second step, the alkoxy radicals (RO) which are formed during the first step react further with oxygen forming HO₂ radicals and oxidized organic compounds (*R 36*). Due to the high NO concentration added to the conversion tube, this reaction is in competition with the alkoxy radical combination reaction with NO (*R 37*) forming nitrites. In addition, alkoxy radicals can undergo other loss reaction sequences including unimolecular decomposition (*R*

38) and intramolecular isomerization (R 39). These loss reactions can be suppressed by reducing the pressure in the conversion tube.



In the third step, HO₂ formed in turn reacts with NO to be converted to OH. This is followed by a rapid backreaction of OH with CO to reform HO₂, much less reactive than OH.



Due to the very high concentration of NO (1.7×10^{12} molecule cm⁻³) added into the conversion tube, the formation of HONO reaction (R 43) competes the gas phase reactions:



These conditions correspond to the RO_x mode in the conversion tube. The concentration of RO₂ can be determined from the determination of a calibration factor and the contribution of HO₂ to the signal (see in details in 2.5.3.2.3).

This system can be operated alternately in two different modes: HO_x and RO_x mode (Figure 22) in order to distinguish between RO₂ and HO_x (in practice HO₂ or HO₂* measurement depending on NO injected in the FAGE cell and considering that OH contribution is negligible in the sampled air). In the HO_x mode, only CO is added, leading only to the conversion of OH into HO₂. In the RO_x mode, NO and CO are added into the flow-tube leading also to the conversion of RO₂ radicals into HO₂ (Figure 21). The species detected in the FAGE cell will depend on the NO injected above the FAGE cell.

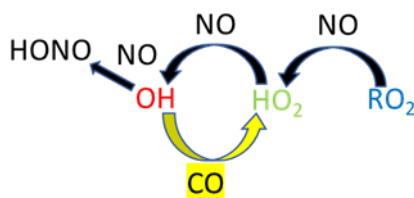


Figure 21: General scheme of the radical chemistry in the RO_x conversion tube

In practice, in order to keep a constant flow, in the HO_x mode, NO is replaced by a non-reactive gas as described in the following paragraph (section 2.5.2.2). The RO₂ radical concentration can be obtained by two different ways; both based on the subtraction of the HO₂ contribution to the RO_x mode signal of the RO_x-FAGE instrument but with the concentration

of HO₂ obtained from different measurements:

- The HO₂ concentration obtained in the HO₂ FAGE cell at low NO to avoid the interferences due to RO₂ (Fuchs et al., 2011; Lew et al., 2018).
- The HO₂ concentration obtained in the HO_x mode (of the RO_x FAGE cell). In our case, due to a low sensitivity of the RO_x-FAGE instrument, this option has not been chosen but the HO_x mode (using high NO) can be compared to the HO₂* mode of the HO₂ FAGE cell to validate the RO_x-FAGE instrument.

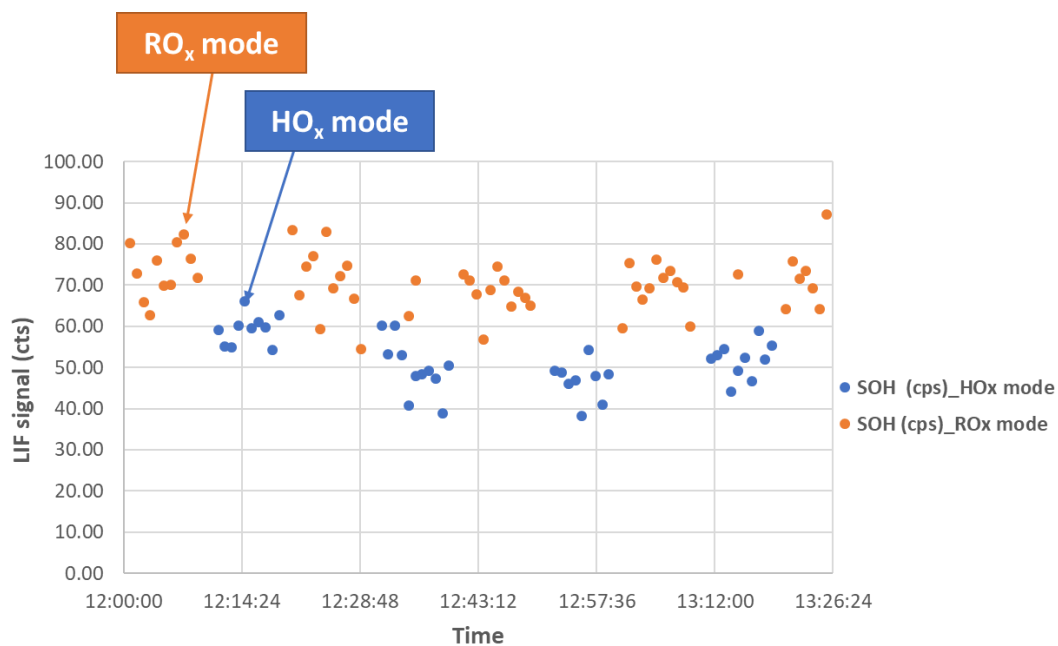


Figure 22: Alternating measurement in different modes (HO_x and RO_x mode) during the calibration of the RO_x-FAGE instrument

2.5.2.2. Experimental Setup

The RO_x conversion tube is made of an aluminum tube (diameter = 6 cm) covered internally with a Teflon layer. In the conversion flow-tube, which is kept at a pressure of 25 Torr (to limit the formation of RONO₂ and RONO), the NO and CO are added 2 cm downstream of the flat sampling nozzle through a Teflon loop (diameter: 0.25 cm) designed with holes to homogenize the mixture. In the RO_x mode, NO and CO are added into the flow-tube leading to the conversion of RO₂ radicals. In the HO_x mode, NO is replaced by a non-reactive gas (N₂, 99.99% purity). The ambient air is sampled at 3 L/min through a 0.635 mm pinhole, NO and CO are added to the ambient flow in the conversion tube to obtain a mixing ratio of 1.82 ppmv and 0.61 %, respectively: these concentrations allow to keep the conversion of OH to HO₂ faster than the reverse. At the exit of the flow-tube, the mixture is sampled into the FAGE detection cell (pressure = 1.5 Torr) through an inlet nozzle (diameter: 3 mm). Additional NO is injected to convert constant portion (around 90 %) of HO₂ radicals into OH, detected further

downstream by LIF at 308 nm as in the other FAGE cells dedicated for the OH, HO₂ and HO₂* radical measurement. All the added gas flows are controlled by calibrated mass flow controllers and an automatic valve, controlled by a LabVIEW software, that can close the NO arrival.

The conversion efficiency of the radicals in this setup is highly related to the residence time of the gases inside the flow-tube, which is an important parameter to adjust (details in section 2.7.2).

2.5.3. Calibration of the FAGE instrument

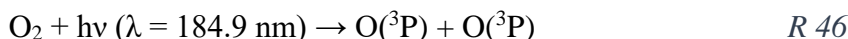
The calibration method used for the FAGE setup in quantification mode is based on the generation of a well-defined concentration of OH and HO₂ (HO_x) radicals in a calibration cell by the photolysis of water in air at 184.9 nm with a mercury lamp, placed over the sampling nozzle. As shown in *R 44* an equal amount of OH radicals and H-atoms is generated, in which the latter rapidly reacts with O₂ to form HO₂ (*R 45*).



The OH and HO₂ concentrations are directly proportional to the concentration of H₂O ([H₂O] in molecule.cm⁻³), the H₂O absorption cross section at 184.9 nm ($\sigma_{\text{H}_2\text{O}}$ in cm².molecule⁻¹), the lamp flux (F in photons.cm⁻². s⁻¹), the quantum yield ($\phi = 1$ (Atkinson et al., 2004)) and the irradiation time of the mixture (t in s).

$$[\text{OH}] = [\text{HO}_2] = [\text{H}_2\text{O}] \times F \times \sigma_{\text{H}_2\text{O}} \times \phi \times t \quad \text{Equation 10}$$

The lamp flux is determined indirectly by O₃ actinometry method: O₃ is formed simultaneously to OH and HO₂ in the calibration cell through the recombination of oxygen atoms in their electronic ground state (O(³P)), produced by the photolysis of O₂ at 184.9 nm, with O₂.



The concentration of O₃ generated in the cell is used for the calculation of the lamp flux at 184.9 nm using the known O₂ absorption cross section (σ_{O_2} in cm².molecule⁻¹), irradiation time (t in s) and having a quantum yield ϕ' equal to 2.

$$F = \frac{[\text{O}_3]}{2 \times [\text{O}_2] \times \sigma_{\text{O}_2} \times t} \quad \text{Equation 11}$$

Hence, as can be seen in Equation 12, the concentrations of OH and HO₂ radicals generated in the calibration cell can be calculated from the concentrations of H₂O and O₃ which are constantly monitored with two commercial analyzers (Thermo Scientific model 49i for ozone

and a dew point hygrometer, Michell Instruments, S8000, for water vapor), throughout the calibration procedure:

$$[OH] = [HO_2] = \frac{[O_3] \times [H_2O] \times \sigma_{H_2O}}{2 \times [O_2] \times \sigma_{O_2}} \quad \text{Equation 12}$$

2.5.3.1. Calibration cell setup

The calibrator, shown in Figure 23, consists of a rectangular aluminum tube ($1.2 \times 1.5 \times 50$ cm) equipped with 5 quartz windows of 6 cm height. The Hg lamp is placed in an aluminum housing fixed to the calibration cell that is continuously purged with a nitrogen flow N_2 (50 sccm) to avoid absorption by O_2 which would reduce the lamp flux. An interference filter (Melles Griot 185NB20) is placed inside the lamp housing to avoid the photolysis of O_3 by the strong light emission at $\lambda = 254$ nm and thus the generation of additional OH radicals.

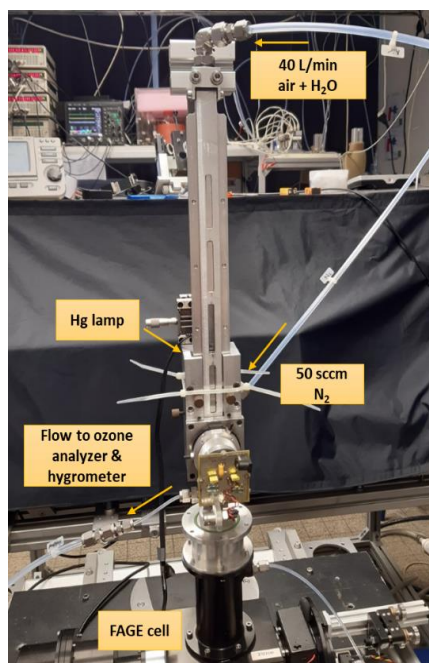
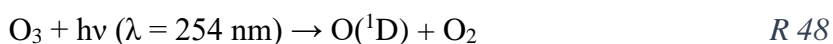


Figure 23: FAGE calibration cell

Synthetic air mixed with water vapor (produced either by the bubbler or Controlled Evaporator Mixer system, CEM) is flown through the calibration cell at a flow rate of 40 $L \cdot min^{-1}$ allowing a turbulent flow in the cell. The OH and HO_2 concentration generated in our system range between 1×10^8 and 1×10^{10} $molecule \cdot cm^{-3}$.

2.5.3.2. Determination of calibration parameters

2.5.3.2.1. OH cell

The fluorescence signal detected in the OH cell during the calibration procedure ($S_{OH \text{ calibration}}$ in count. s^{-1}) relates to the concentration of OH radicals ($[OH]$ in molecule. cm^{-3}) generated in the calibration cell (calculated as mentioned in section 2.5.3), the laser power at the entrance of the OH cell (P_{OH} in mW), the OH losses between the sampling and OH detection in the 1st cell (L_{OH}) and the OH calibration factor (C_{OH} in count. s^{-1} . molecule $^{-1}$. cm^3 . mW $^{-1}$).

$$S_{OH \text{ calibration}} = [OH]_{generated} \times K_{OH} \times P_{OH} = [OH]_{generated} \times C_{OH} \times (1 - L_{OH}) \times P_{OH} \quad \text{Equation 13}$$

where $K_{OH} = (1 - L_{OH}) \times C_{OH}$ in count. s^{-1} . molecule $^{-1}$. cm^3 . mW $^{-1}$ is the effective OH calibration factor for the cell.

From the measured $S_{OH\text{-calibration}}$ (after background subtraction) divided by the laser power and calculated $[OH]_{generated}$, K_{OH} can be determined. Therefore, after the determination of the effective calibration factor (K_{OH}) it is possible to determine the absolute concentration of OH from the total fluorescence signals ($S_{OH \text{ measured}}$) recorded by the quantification OH FAGE cell using the following equation:

$$[OH]_{measured} = \frac{S_{OH \text{ measured}}}{K_{OH} \times P_{OH}} \quad \text{Equation 14}$$

2.5.3.2.2. HO₂ cell

Calibration of $[HO_2]$ for the HO₂ cell requires two steps: the determination of the calibration factor $C_{HO_2,1}$ for the detection of OH in the HO₂ cell without NO addition and a calibration factor $C_{HO_2,2}$, determined in presence of NO converting HO₂ into OH.

First step:

$$\begin{aligned} S_{HO_2-1\text{-calibration}} &= [OH]_{generated} \times K_{HO_2} \times P_{HO_2} \\ &= [OH]_{generated} \times C_{HO_2,1} \times (1 - L_{OH,2}) \times P_{HO_2} \end{aligned} \quad \text{Equation 15}$$

where $[OH]_{generated}$ represents the concentration of OH generated in the calibration cell, P_{HO_2} (mW) is the laser power entering the HO₂ cell, C_{HO_2} (count. s^{-1} . molecule $^{-1}$. cm^3 . mW $^{-1}$) is the calibration factor for HO₂ cell and $L_{OH,2}$ represents the OH losses between the sampling and the detection in the HO₂ cell. K_{HO_2} (count. s^{-1} . molecule $^{-1}$. cm^3 . mW $^{-1}$) is the effective OH calibration factor for the HO₂ cell which is determined as described above (K_{OH}).

Second step:

The resulting fluorescence signal $S_{OH+HO_2\text{-calibration}}$ (count. s^{-1}), after the addition of NO and conversion of HO₂ into OH, consists of a contribution due to OH radicals

($S_{HO_2-1-calibration}$) and a contribution due to OH radicals generated from HO_2 ($S_{HO_2-2-calibration}$).

$$\begin{aligned} S_{OH+HO_2-calibration} &= S_{HO_2-1-calibration} + S_{HO_2-2-calibration} & \text{Equation 16} \\ &= S_{HO_2-1-calibration} + [OH]_{generated} \times C_{HO_2,2} \times P_{HO_2} \end{aligned}$$

As for OH in the OH cell, the calibration factors K_{HO_2} and $C_{HO_2,2}$ can be determined by varying the $[OH]_{generated}$ in the calibration cell and recording the fluorescence signal without NO ($S_{HO_2-1-calibration}$) and with NO ($S_{OH+HO_2-calibration}$). Unlike for OH, wall loss of HO_2 is considered negligible due to the significantly lower reactivity of HO_2 compared to OH. It must be kept in mind that a variation of the concentration of NO added to the gas flows affects the conversion of HO_2 into OH, hence affecting the $S_{OH+HO_2-calibration}$ and, ultimately, the resulting calibration factor for HO_2 , $C_{HO_2,2}$.

The absolute HO_2 concentration is calculated from the total fluorescence signals ($S_{HO_2-measured}$) measured by the quantification FAGE (HO_2 cell), the calibration factors are applied as follows:

$$S_{HO_2-measured} = [OH]_{measured} \times K_{HO_2} \times P_{HO_2} + [HO_2]_{measured} \times C_{HO_2,2} \times P_{HO_2} \quad \text{Equation 17}$$

$$[HO_2]_{measured} = (S_{HO_2-measured} - [OH]_{measured} \times K_{HO_2} \times P_{HO_2}) / (C_{HO_2,2} \times P_{HO_2}) \quad \text{Equation 18}$$

Table 5: Sensitivities measured for OH and HO_2^* radicals in the UL_x -FAGE instrument

FAGE Cell	NO level	Sensitivity measured ($\text{count} \cdot \text{s}^{-1} \cdot \text{molecule}^{-1} \cdot \text{cm}^3 \cdot \text{mW}^{-1}$)
OH	–	4.47×10^{-7}
HO_2	Low	3.11×10^{-8}
HO_2	High	1.95×10^{-7}

2.5.3.2.3. RO_x cell

For the RO_x -FAGE setup, the detection sensitivity for HO_2 and RO_2 is determined by generating known concentrations of these radicals in the calibration cell, based on the photolysis of H_2O to generate equal amounts of OH and HO_2 radicals and the conversion of OH into a specific RO_2 adding the corresponding hydrocarbon RH. These radicals are detected in the two operation modes (HO_x and RO_x modes) of the instrument. In order to get the sensitivity of RO_2 , the calibration procedure is based on different steps to determine the sensitivity of the different

radicals contributing to the signal such as: (Table 6)

$C_{OH,HO_x \text{ mode}}$: sensitivity for OH radicals in the HO_x mode

$C_{HO_2,HO_x \text{ mode}}$: sensitivity for HO_2 radicals in the HO_x mode

$C_{OH,RO_x \text{ mode}}$: sensitivity for OH radicals in the RO_x mode

$C_{HO_2,RO_x \text{ mode}}$: sensitivity for HO_2 radicals in the RO_x mode

$C_{RO_2,RO_x \text{ mode}}$: sensitivity for RO_2 radicals in the RO_x mode

Table 6: Gas flows in the calibration cell, RO_x conversion tube and FAGE cell at each step

Step	calib cell	Gas in RO_x tube		Mode	Gas in FAGE NO	Species present out calib cell
		CO	NO			
1	Air + water	x		HO_x	x	OH + HO_2
2	Air + water	x	x	RO_x	x	OH + HO_2
3	Air + water + CO	x		HO_x	x	HO_2
4	Air + water + CO	x	x	RO_x	x	HO_2
5	Air + water + Ethane	x	x	RO_x	x	$HO_2 + C_2H_5O_2$

The sensitivity of OH ($C_{OH,HO_x \text{ mode}}$) and HO_2 ($C_{HO_2,HO_x \text{ mode}}$) radicals determined in the HO_x mode requires two steps (Table 6):

Step 1: Generating OH and HO_2 radicals in the calibrator and injecting CO in the RO_x conversion tube to convert all OH into HO_2 radicals which are less reactive.

Step 3: Same as step one with adding CO in the calibrator to quickly convert OH into HO_2 , so the latter is the only radical species existing in the calibrator.

$$C_{OH,HO_x\text{-mode}} = (S_{OH+HO_2,HO_x \text{ mode}} (step 1) - S_{HO_2,HO_x\text{-mode}} (step 3) / 2) / ([OH]_{\text{generated}} \times P_{RO_x\text{-cell}}) \quad \text{Equation 19}$$

$$C_{HO_2,HO_x\text{-mode}} = S_{HO_2,HO_x \text{ mode}} (step 3) / 2 / ([HO_2]_{\text{generated}} \times P_{RO_x\text{-cell}}) \quad \text{Equation 20}$$

where $[OH]$ and $[HO_2]_{\text{generated}}$ represents the concentration of OH and HO_2 generated in the calibration cell, $P_{RO_x\text{-cell}}$ (mW) is the laser power entering the RO_x -FAGE cell, $S_{OH+HO_2,HO_x \text{ mode}}$ and $S_{HO_2,HO_x \text{ mode}}$ are the LIF signal (cts) obtained during both steps, and $C_{OH,HO_x\text{-mode}}$ and $C_{HO_2,HO_x \text{ mode}}$ ($\text{count} \cdot \text{s}^{-1} \cdot \text{molecule}^{-1} \cdot \text{cm}^3 \cdot \text{mW}^{-1}$) are the calibration factors for OH and HO_2 , respectively, in the RO_x -FAGE cell in the HO_x mode.

The OH and HO_2 detection sensitivity is determined in the RO_x mode following both steps mentioned above but then in the RO_x mode adding NO (steps 2 and 4 in Table 6) in the conversion tube during both steps (to change from HO_x to RO_x mode).

$$C_{OH,RO_x\text{-mode}} = (S_{OH+HO_2,RO_x \text{ mode}} (step 2) - S_{HO_2,RO_x \text{ mode}} (step 4) / 2) / ([OH]_{\text{generated}} \times P_{RO_x\text{-cell}}) \quad \text{Equation 21}$$

$$C_{HO_2,RO_x\text{-mode}} = S_{HO_2,RO_x \text{ mode}} (step 4) / 2 / ([HO_2]_{\text{generated}} \times P_{RO_x\text{-cell}}) \quad \text{Equation 22}$$

where $S_{OH+HO_2,ROx\ mode}$ and $S_{HO_2,ROx\ mode}$ are the LIF signal obtained during both steps and $C_{OH, ROx-mode}$ and $C_{HO_2,ROx\ mode}$ ($\text{count}\cdot\text{s}^{-1}\cdot\text{molecule}^{-1}\cdot\text{cm}^3\cdot\text{mW}^{-1}$) are the calibration factors for OH and HO_2 , respectively, in the RO_x -FAGE cell in the RO_x mode.

Also, the RO_2 detection sensitivity in the RO_x mode is determined following a similar procedure. Two steps are required (Table 6):

Step 4: Adding CO in the calibrator to generate only HO_2 radicals and injecting CO and NO in the RO_x conversion tube.

Step 5: CO is replaced by ethane in the calibration cell to generate a mixture of HO_2 and $C_2H_5O_2$ radicals (RO_x). Ethane concentration is adjusted to convert all OH quickly so that the concentration of $C_2H_5O_2$ is estimated to be equal to the initial OH concentration.

$$C_{RO_2,ROx-mode} = (S_{RO_x, ROx-mode\ (step5)} - S_{HO_2,ROx-mode\ (step4)}/2) / ([RO_x]_{generated} \times P_{ROx-cell}) \quad \text{Equation 23}$$

where $S_{RO_x,ROx-mode}$ is the LIF signal obtained during step 5 and $C_{RO_2,ROx-mode}$ ($\text{count}\cdot\text{s}^{-1}\cdot\text{molecule}^{-1}\cdot\text{cm}^3\cdot\text{mW}^{-1}$) is the calibration factor for RO_2 in the RO_x -FAGE cell in the RO_x mode.

The RO_2 concentration measured in the ambient air ($[RO_2]_{measured}$) can be calculated using this sensitivity and subtracting the contribution of HO_2 using the concentration of HO_2 measured in the HO_2 cell simultaneously, the sensitivity of HO_2 in the RO_x mode of the RO_x -FAGE cell and the sensitivity of RO_x in the RO_x -FAGE cell.

$$[RO_2]_{measured} = (S_{RO_x, ROx-FAGE} - ([HO_2]_{measured\ in\ HO_2\ cell} \times C_{HO_2,ROx-mode} \times P_{ROx-cell})) / (C_{RO_2,ROx-mode} \times P_{ROx-cell}) \quad \text{Equation 24}$$

The sensitivities for the OH, HO_2 and RO_2 radicals measured in both HO_x and RO_x mode of the UL- RO_x -FAGE system during the intercomparison in the SAPHIR chamber are summarized in Table 7.

Table 7: Sensitivities measured for different radicals in the RO_x-FAGE instrument (HO_x and RO_x mode)

	Sensitivity measured (count.s ⁻¹ .molecule ⁻¹ .cm ³ .mW ⁻¹)
C_{OH,HOX-mode}	5.55 × 10 ⁻⁸
C_{HO₂,HOX-mode}	8.68 × 10 ⁻⁸
C_{OH,ROX-mode}	5.61 × 10 ⁻⁸
C_{HO₂,ROX-mode}	5.99 × 10 ⁻⁸
C_{RO₂,ROX-mode}	6.81 × 10 ⁻⁸

After the optimization of the RO_x-FAGE instrument (section 2.7.2), it was used during field campaigns next to the other two FAGE detection cells (OH and HO₂) to quantify RO₂ radicals present in the ambient air.

2.5.3.3. Calibration uncertainties

The calibration uncertainty is due to the fluorescence signal to noise ratio, laser power fluctuations and OH and HO₂ concentration calculation as shown in Equation 25.

$$DC = C \times \sqrt{\left(\frac{SD \text{ signal}}{\text{signal}}\right)^2 + \left(\frac{SD \text{ laser power}}{\text{laser power}}\right)^2 + \left(\frac{OH \text{ error}}{[OH] \text{ and } [HO_2]}\right)^2} \quad \text{Equation 25}$$

where (SD) is the standard deviation of the signal. The uncertainty coming from the OH and HO₂ concentration calculation is related to the uncertainty on absorption cross section of O₂ and H₂O, the concentration of water and ozone.

$$\left(\frac{\delta[OH]}{[OH]}\right)^2 = \left(\frac{\delta[O_3]}{[O_3]}\right)^2 + \left(\frac{\delta[H_2O]}{[H_2O]}\right)^2 + \left(\frac{\delta \sigma_{H_2O}}{\sigma_{H_2O}}\right)^2 + \left(\frac{\delta \sigma_{O_2}}{\sigma_{O_2}}\right)^2 \quad \text{Equation 26}$$

Table 8 gives the uncertainty of the parameters used for the calculation of the OH and HO₂ concentration. On this basis, the uncertainty for the OH calculation for the UL-FAGE was estimated to be around 30 %.

Table 8: Uncertainty on the parameters used to determine the UL-FAGE sensitivity (Amedro, 2012)

Parameters	Range	Percentage
[O ₃]	3 – 10 ppb	10 – 33 %
[H ₂ O]	150 – 3000 ppm	5 %
$\sigma_{\text{H}_2\text{O}}$ (Cantrell et al., 1997)	$7.14 \times 10^{-20} \text{ cm}^2$	3 %
σ_{O_2}	$1.20 \times 10^{-20} \text{ cm}^2$	20 %*
Total		23 - 41 %

*Hofzumahaus et al. (Hofzumahaus et al., 1997) measured in their calibration conditions a variation of the O₂ absorption cross section depending on different Hg lamps. The O₂ absorption cross section varied from 1.1 to $1.4 \times 10^{-20} \text{ cm}^2$. We did not measure the absorption cross section of O₂ in our conditions and assume it to be of $1.20 \times 10^{-20} \text{ cm}^2$.

In the usual condition of work of the UL-FAGE, DC/C=32 % for OH, and 40 to 32 % for HO₂ (1 σ) depending on the NO level.

2.5.3.4. Radical losses in the calibration cell

The radical losses between the generation and the exit of the calibration cell has been quantified previously (Amedro, 2012) changing the lamp position and corresponds to 10% at the usual lamp position.

Another type of losses has been studied as a function of the humidity in the calibration cell (Amedro, 2012). It was at the origin to test the sensitivity of the UL-FAGE instrument dependence on water vapor content. This investigation involved measuring the sensitivity of OH and HO₂ over a large humidity range, ranging from 0 to 2.5% of mixing ratio in the calibration cell. However, our calibration cell does not have a system to decrease the lamp flux and increasing the humidity involves to increase the radical concentration. The results (Figure 24) indicate an apparent instrument sensitivity decrease to [H₂O] following a polynomial pattern, for both OH and HO₂ (in their respective OH cell and HO₂ cell), more important than the expected decrease due to the water quenching.

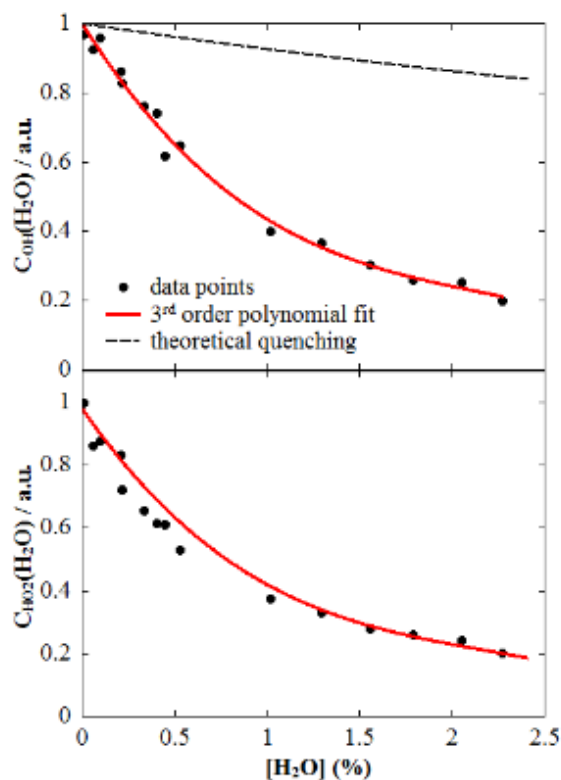


Figure 24: Evolution of the UL-FAGE sensitivity as function of H_2O . Bottom: HO_2 cell and Top: OH cell

It has been checked that it is a calibration artifact and not a decrease in sensitivity instrument during the first intercomparison performed in the SAPHIR chamber in 2011. It could be due to radical-radical reactions in the calibration cell when increasing the concentration. It is why, up to this point, the UL-FAGE calibrations have been conducted only at low humidity levels to limit the HO_x concentration and the correction. But, for the deployment of the UL- RO_x -LIF, there was a need to calibrate at high humidity due to the low sensitivity of the new RO_x FAGE cell. For this reason, calibration tests on the UL-FAGE (OH and HO_2 cell) were done again at high humidity.

Before the campaigns a test checking the signal-noise/laser power (measured in the OH cell) as a function of OH concentration generated in the calibrator have been performed. In Figure 25 we can observe an increase in the OH signal with the increase of the OH concentration generated in the calibrator ($[H_2O]$ increased from 0.19 to 2.23 %). These results contradict with Amedro (2012) results.

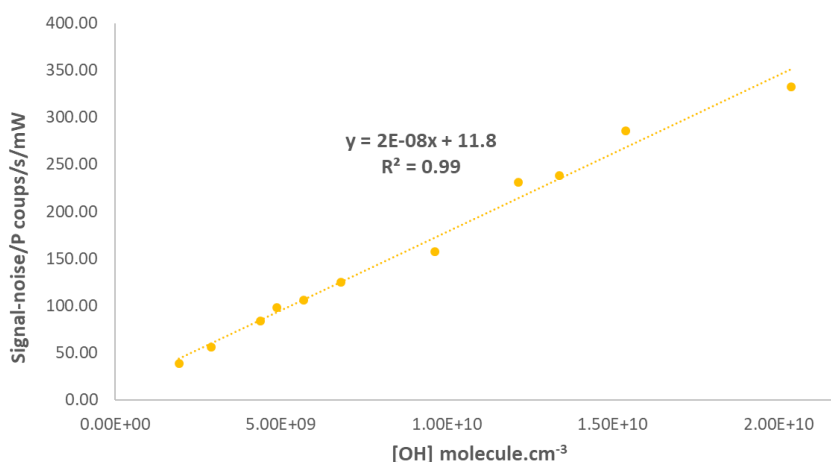


Figure 25: Signal-noise/P as a function of the [OH] generate in the calibration cell

During and after the RO_xComp campaign, calibration tests varying the humidity were repeated. For that, 3 experiments have been performed: a calibration of the OH/HO₂ instrument at low humidity and a measurement of OH/HO₂ concentration at high humidity using the calibration factor determined at low humidity. Any difference between the measured radical concentration and the calculated radical concentration (expected to be generated in the calibration cell) at high humidity corresponds to a loss of radicals at high humidity. The third experiment was similar but injecting CO in the cell to convert all the radicals into HO₂. During these test measurements were done on OH and HO₂ cells.

Table 9: [OH] and [HO₂] measured at high H₂O concentration ([H₂O] = 0.4 %) using the sensitivity determined at low H₂O concentration ([H₂O] = 0.06 %), the radical concentration generated in the calibrator and the ratio

Cell	CO	[OH] and [HO ₂] measured (× 10 ⁹ cm ⁻³)	[OH] and [HO ₂] calculated in the calibrator (× 10 ⁹ cm ⁻³)	[OH] and [HO ₂] measured/calculated
OH		2.61	4.52	0.58
HO ₂		2.47	4.84	0.51
HO ₂		2.57	5.23	0.49
HO ₂	x	2.71	4.50	0.60
HO ₂	x	2.68	4.53	0.59

The results in Table 9 have shown 40-50 % radical losses at high humidity. These results contradict the results obtained in Figure 25 and in agreement with Amedro (2012) results. These radical losses observed at high humidity were not considered while determining the RO₂ concentration during the RO_xComp and ACROSS campaigns. Further investigations have to be performed to better understand these radical losses observed at high humidity. More results

concerning the cross-calibration results done during the RO_xComp campaign (Lille and Julich) are mentioned in Chapter 4.

2.5.4. H₂O dependence of the FAGE instrument sensitivity

A change in the sensitivity of the FAGE instrument is expected with the variation of the water vapor concentration due to changing quenching phenomena (Creasey et al., 1997; Hofzumahaus et al., 1996) as water is a more efficient quencher than Oxygen or Nitrogen. Fluorescence quenching refers to a non-radiative deactivation of the excited OH molecule with molecules such as H₂O and results in the reduction in the fluorescence lifetime of OH. This reliance on water vapor can be adjusted by determining the quenching as a function of the concentration of water vapor. Subsequently, the measurements done by the UL-FAGE instrument can be corrected for this quenching impact as a function of the measured water concentration, knowing the quenching constant for the main gas present in ambient air and the pressure in the FAGE cell (method described in Fuchs, 2006). For simplification, the quenching correction is expressed as a polynomial of order 2 obtained after fitting the quenching calculated following the equation (P = 1.3 Torr and T = 298 K):

$$C(H_2O) = 0.0046 \times [H_2O]^2 - 0.075 \times [H_2O] + 1 \quad \text{Equation 27}$$

2.5.5. O₃ interferences

O₃ is a significant source of interference in the FAGE cell as it undergoes photolysis within the FAGE cells at the excitation wavelength for OH (308 nm). This photolysis process generates OH through the reaction between O(¹D) and water vapor. The OH produced within the FAGE cell can then be detected by a second laser pulse if the sampled volume is not entirely refreshed between two laser pulses. Through years, one of the reasons for switching the laser excitation wavelength from 282 nm to 308 nm was to reduce the O₃ interference. This is because the O₃ absorption cross-section is about 25 times lower at 308 nm compared to 282 nm. On the other hand, all FAGE instruments use high repetition rate lasers to enhance sensitivity. For the UL-FAGE, the repetition rate is maintained at 5 kHz, implying that to limit interference from the photolysis of species that produce OH, the sampled volume would need to be refreshed every 200 μs. Characterizing the O₃ interference in a laboratory work is relatively straightforward. It involves introducing a known quantity of O₃ and water through the calibrator and observe the change in the OH concentration with the increase of the O₃ concentration. Amedro (2012) observed a linear increase with a slope equal to $(1.7 \pm 0.3) \times 10^3 \text{ cm}^{-3} [\text{OH}]$ per ppb of O₃, corresponding to a weak interference. In addition, they investigated the O₃ interference in ambient air that can be corrected by considering factors such as laser power, repetition rate, O₃

and H₂O concentrations. Amedro (2012) determined additional information for the O₃ interference from experiments done in the SAPHIR chamber in dark conditions. They measured for OH an interference of $1.15 (\pm 0.72) \times 10^3 \text{ cm}^{-3}$ per ppb of O₃ (in agreement with their laboratory experiments) and $1.99 (\pm 0.16) \times 10^5 \text{ cm}^{-3}$ per ppb of O₃ for HO₂.

2.6. Description of the UL-FAGE technique for OH reactivity and kinetic studies

The UL-FAGE instrument for the measurement of the OH reactivity is comprised of five main components: an excitation laser, a photolysis laser, a photolysis cell, a FAGE cell with its OH fluorescence detection system and a reference cell (used to check the wavelength of the excitation laser and retrieve the OH peak).

All different parts except the photolysis laser and the photolysis cell have been described above.

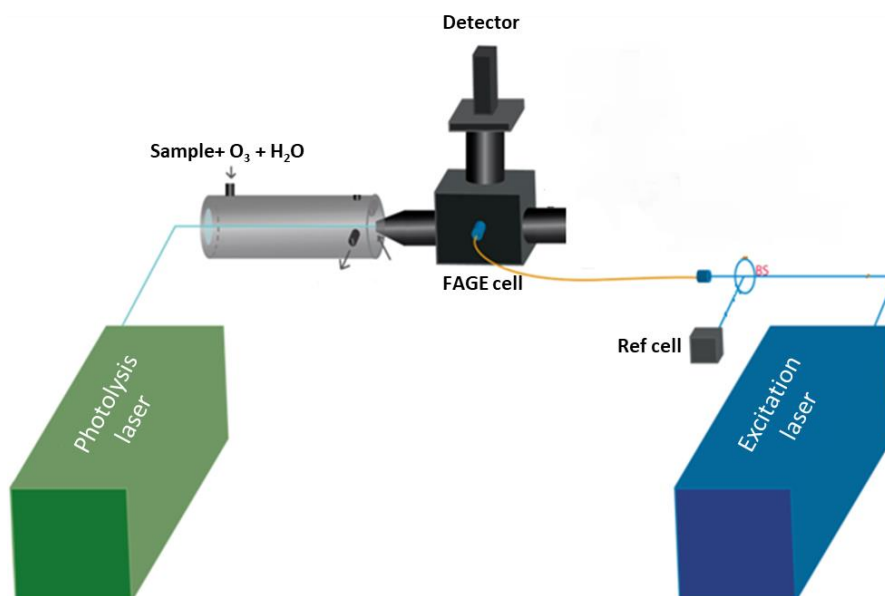


Figure 26: Schematic diagram of the UL-FAGE for the OH reactivity setup

As shown in Figure 26, the OH radicals are generated in the photolysis cell by pulsed laser photolysis of ozone in the presence of water vapor and then these radicals are detected in the FAGE cell connected to the photolysis cell by a gated CPM (Perkin-Elmer) after being excited by the excitation laser. The decay of OH can be expressed by the following equation:

$$r = -d[OH]/dt = k_{obs} [OH] = (\sum_i k_i \times [reactive\ species]_i + k_{zero}) \times [OH] \quad \text{Equation 28}$$

where k_{zero} is measured using zero air (air with reduced amount of impurities) and represents the losses of OH radicals due to heterogeneous reactions on the cell walls or due to diffusion. The value of k_{zero} is influenced by the quality of the zero-air and the cleanliness of the photolysis cell.

The integration of *Equation 28* is:

$$[OH] = [OH]_0 \times e^{-k_{\text{obs}} \times t} \quad \text{Equation 29}$$

where $[OH]_0$ corresponds to the initial concentration of the OH radicals produced by the photolysis laser at time t_0 . k_{obs} is obtained from the time resolved detection of OH in the FAGE cell by performing an exponential fit of the decay over an appropriate range of time (Figure 27).

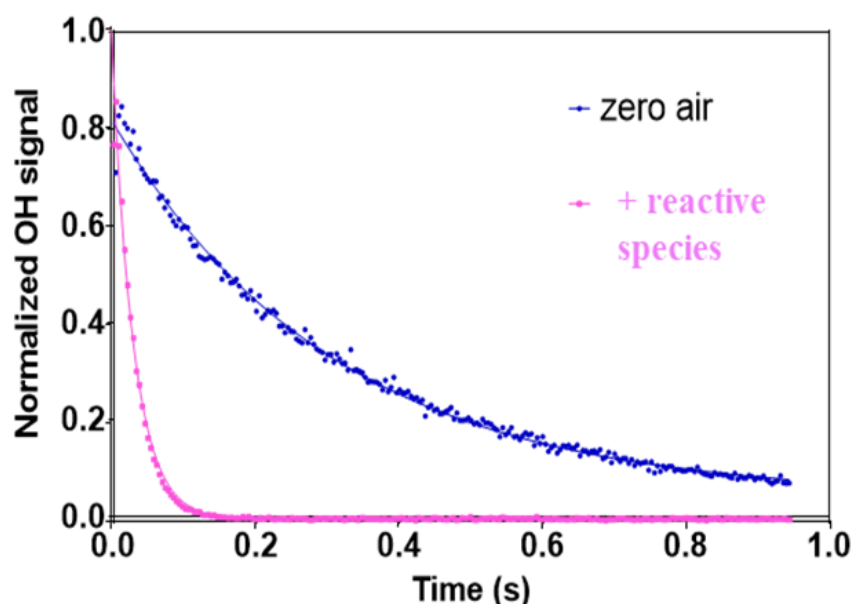


Figure 27: OH decays obtained in the absence (blue) and presence of reactive species (pink)

2.6.1. The photolysis cell and photolysis laser

The photolysis cell used in this work is a stainless-steel cylinder with an internal diameter of 5 cm and a length of 48 cm. It has two openings, one for the entrance of the sampled air and the other one is connected to a pressure gauge (Keller PAA-41) to measure the pressure inside the cell.

The photolysis laser used to generate OH radicals in the photolysis cell is a YAG laser operating at 1 Hz, with maximum pulse energy of 40 mJ at 266 nm after frequency quadrupling with a QUANTEL Brilliant EaZy or a Q-Smart laser. The photolysis laser beam is aligned by two prisms in the center of the photolysis cell entrance window and is expanded by two cylindrical lenses (a concave and a convex lens) in order to increase the photolysis volume and thus limit the diffusion effect in the photolysis cell. The laser beam entering the cell is slightly

divergent with a diameter of 3.5 cm. To ensure a mono-exponential decay of OH LIF, the beam is aligned along the axis of the reactor. Part of the laser beam is reflected at its exit by a tilted window and stirred onto a photodiode to measure continuously the laser power.

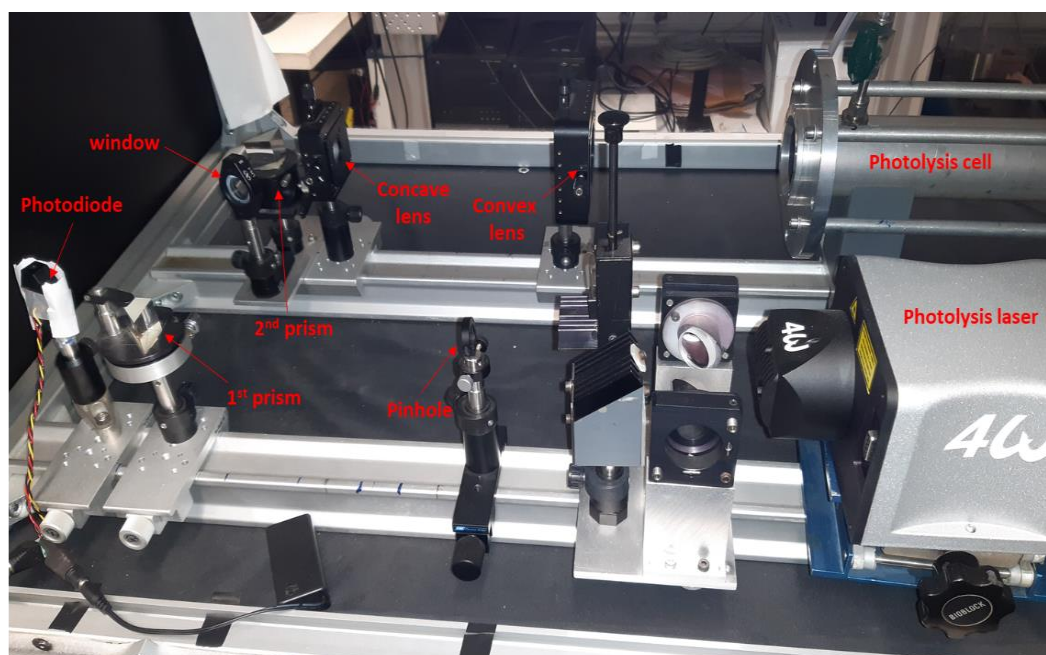


Figure 28: Optical setup used for the photolysis laser beam alignment

2.6.2. The Gas Flow

The gas flow is introduced into the photolysis cell at around 8.5 L/min to maintain an atmospheric pressure in the cell. It is composed of either ambient air (for reactivity measurements) or a mixture of zero dry or humid air and known amount of trace gases for kinetic measurements. A small flow of zero air (around 60 sccm) passing through an ozone generator is continuously added in the photolysis cell to generate enough OH to have a good signal/noise ratio (S/N), corresponding to an ozone concentration around 120 ppb. The ozone and water vapor concentrations inside the photolysis cell are monitored regularly by an ozone analyzer (Thermo Scientific model 49i) and a dew point hygrometer (Michell Instruments, S8000), respectively. The different gas flows are introduced into the photolysis cell using calibrated mass flow controllers (MFC) as shown in Figure 29.

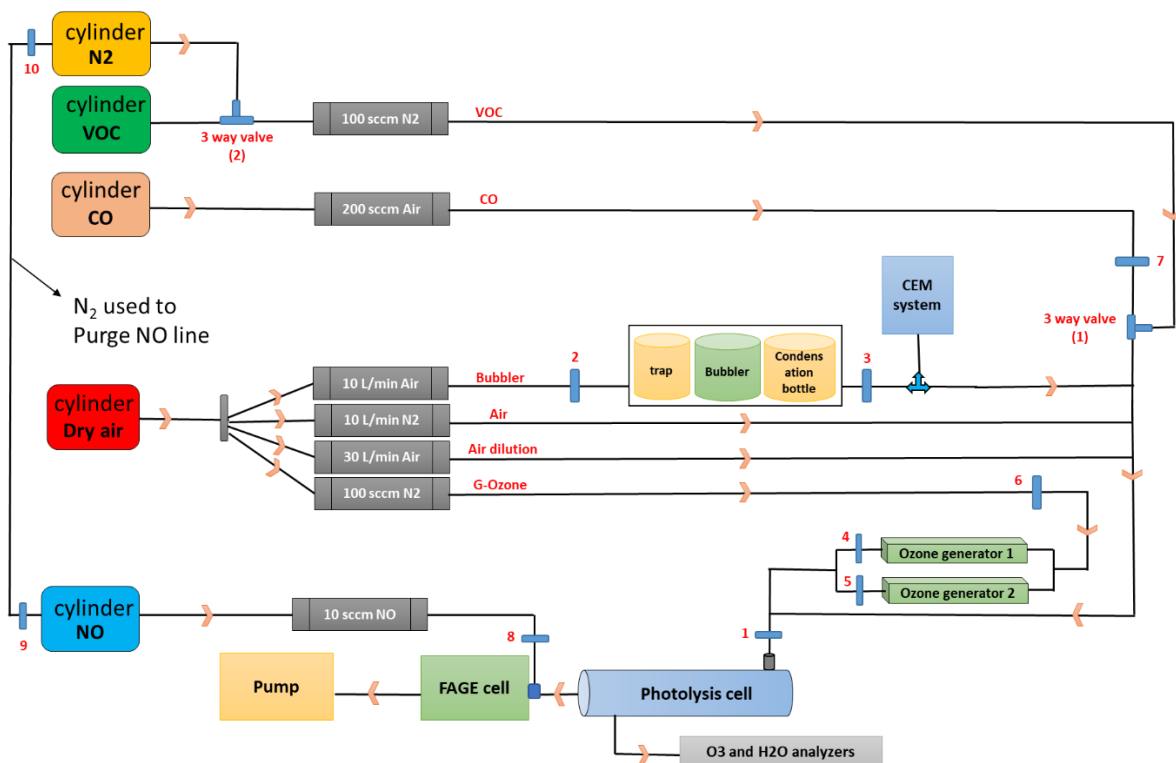


Figure 29: Diagram of the gas flow distribution in the photolysis cell (numbers correspond to the different valves)

The humid air is either produced by a bubbler system where dry zero air is passed through a water bubbler or by using a CEM system (Bronkhorst) (Controlled Evaporator Mixer) allowing to reach higher water vapor concentrations. As shown in Figure 30, in the CEM, the water quantity is controlled by a liquid mass flow meter and a MFC is used for the carrier gas (air). Afterwards, the formed mixture is led into the evaporator at controlled temperature to achieve total evaporation.

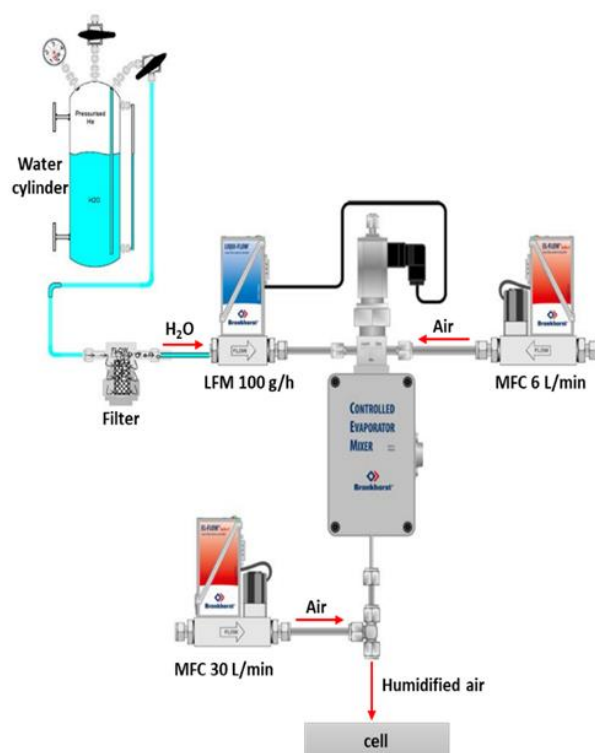


Figure 30: CEM system (Bronkhorst, 2015)

Several tests have been done to check the stability and reliability of the CEM system. In addition, the CEM allows to reach a maximum RH of up to 90%, compared to only around 67% reached by the bubbler system at room temperature.

The gas within the photolysis cell is drawn into the FAGE cell with a conical nozzle with an aperture of 1 mm thanks to a high-volume dry pump (Edwards iXL 1000 or Edward IGX 600 depending on the configuration). The pressure in the FAGE cell is at 1.5 – 2 Torr.

2.6.3. Validation of the reactivity setup

The validation of the reactivity experimental setup is essential before starting any measurements. This is done by regularly measuring the rate constant of the reaction $\text{CO} + \text{OH}$ which is well known and reported in the literature. As mentioned previously (2.1), the decay of OH resulting from the reaction of CO with OH at different CO concentration entering the photolysis cell can be expressed as follows:

$$r = -d[\text{OH}]/dt = (k_{\text{CO+OH}} \times [\text{CO}] + k_{\text{zero}}) \times [\text{OH}] \quad \text{Equation 30}$$

As

$$[\text{OH}] \ll [\text{CO}] \quad d[\text{OH}]/dt = (k' + k_{\text{zero}}) \times [\text{OH}] = k_{\text{obs}} \times [\text{OH}] \quad \text{Equation 31}$$

where $k' = k_{\text{CO+OH}} \times [\text{CO}]$

An example of the rate constant measured in one of this control tests is showed in Figure 31. $k_{\text{CO}+\text{OH}} = (2.36 \pm 0.04) \times 10^{-13} \text{ cm}^3 \text{ molecule}^{-1} \text{ s}^{-1}$ has been measured close to the recommended value ($k_{\text{CO}+\text{OH}} = 2.31 \times 10^{-13} \text{ cm}^3 \text{ molecule}^{-1} \text{ s}^{-1}$).

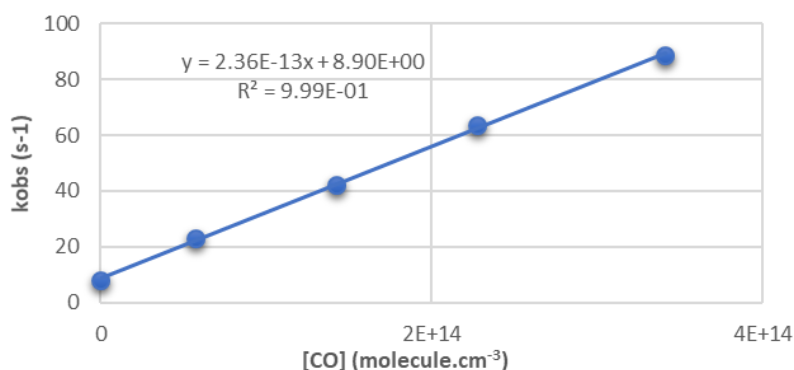


Figure 31: Determination of the rate constant of CO + OH reaction

2.7. Improvements and validation of the different instruments

2.7.1. Validation of the Sirah CREDO dye laser

The new Sirah Credo dye laser pumped by an Edgewave YAG has been tested (power, wavelength stability) to validate its use as the new excitation laser to replace the previous one, too weak in power to supply all the cells. To check the stability of the output laser power, measurements were done consecutively at the exit of the **dye** ($\lambda = 308 \text{ nm}$) and at the exit of the **YAG** laser ($\lambda = 532 \text{ nm}$) at varying diode currents (between 31.8 A and 49 A, maximum current).

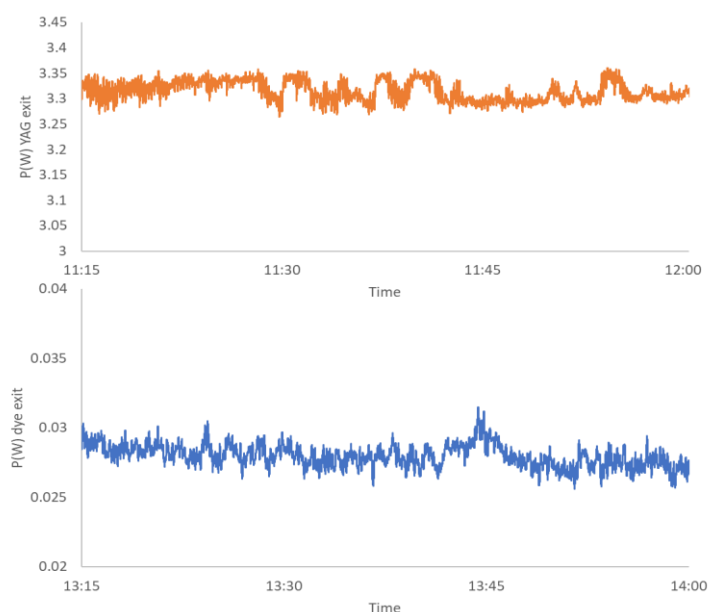


Figure 32: Variation of the laser power at the **YAG laser** ($\lambda = 532 \text{ nm}$, upper graph) and exit of the **dye** ($\lambda = 308 \text{ nm}$, lower graph) and ($C = 31.8 \text{ A}$)

The results presented in Figure 32 and Table 10 have shown that the instability of the output laser power at the exit of the **dye** ($\lambda = 308 \text{ nm}$) is higher than that at the exit of the **YAG** laser ($\lambda = 532 \text{ nm}$) and this can be explained by the variation of the room temperature. Also, the variation in the laser power exiting the dye ($\lambda = 308 \text{ nm}$) of the new laser is like that of the old laser.

Table 10: Power stability at the exit of the dye and YAG laser (old and new laser)

	New laser				Old laser
	$\lambda = 308 \text{ nm}$ (C = 31.8 A)	$\lambda = 532 \text{ nm}$ (C = 31.8 A)	$\lambda = 308 \text{ nm}$ (C = 49 A)	$\lambda = 532 \text{ nm}$ (C = 49 A)	$\lambda = 308 \text{ nm}$ (C = 38 A)
Standard deviation	0.0008	0.02	0.003	0.01	0.0002
Average Power (W)	0.028	3.31	0.48	16.34	0.028
Max	0.031	3.36	0.49	16.37	0.03
Min	0.025	3.26	0.48	16.31	0.026
% st dev	2.87	0.60	0.61	0.07	0.66

Another test was performed to compare the wavelength stability of the new dye laser to the old laser. For that, the laser beam of the new dye laser was sent to the OH FAGE cell and a laser beam of the old dye laser was sent to the HO₂ FAGE cell in order to compare the variation of the OH fluorescence signal in both cells OH and HO₂ respectively with each laser with the same OH source. The laser power stability is checked for both by measuring the laser power using two separate photodiodes (PhD). A mercury lamp placed over the sampling nozzle of the OH cell is used to photolyze ambient water in the air at 184.9 nm to generate OH radicals pumped into both cells (OH and HO₂ cell without the addition of NO, measuring OH in both cells). The result of this test, done for one hour (Figure 33), shows that the OH fluorescence signal, normalized by the laser power, decreased at the same time in both cells, implying a decrease in the produced OH concentration. A constant ratio of the OH fluorescence signal obtained using the new laser to that using the old laser for the first half hour (~2), then a decrease from 2 to 1.4 is observed, this drift can be explained by a stronger wavelength shift of the new laser compared to the old laser. This test was performed three times giving similar results, where the wavelength stability is confirmed to be enough for FAGE measurements. Therefore, the new Sirah CREDO dye laser pumped by an Edgewave YAG was used during the field campaigns performed in this thesis.

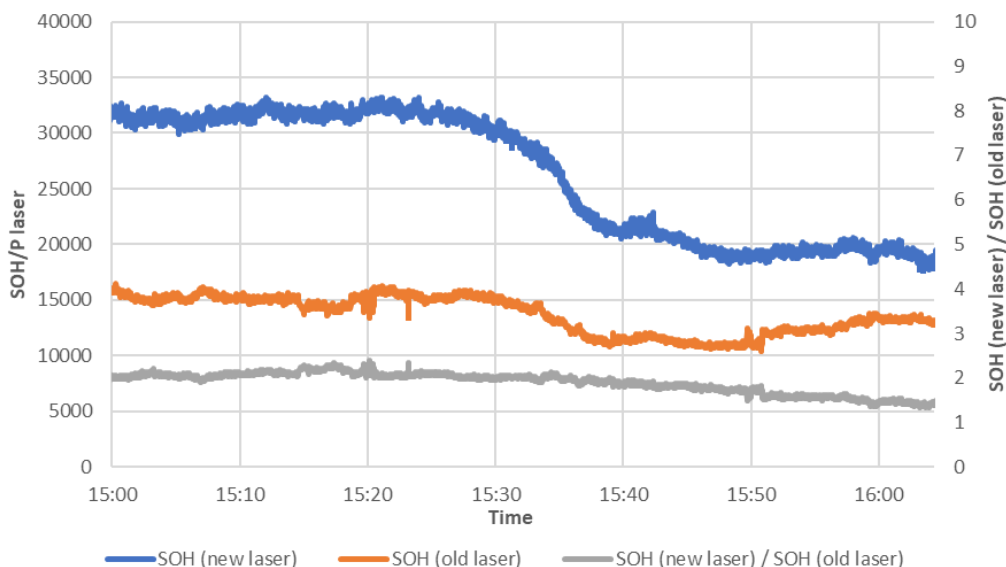


Figure 33: OH fluorescence signals measured using the two different excitation dye lasers (old and new)

2.7.2. Optimization of the UL-RO_x-FAGE setup: (for RO₂ measurement)

A set of experiments was performed with the newly implemented UL-RO_x-FAGE instrument to identify the operating conditions at which the RO₂-to-HO₂ conversion is optimized. It concerns the reaction time, the conversion flow-tube pressure and the NO and CO flow.

2.7.2.1. Reaction time and Pressure dependence

There are 3 other groups in the world having RO_x-LIF instrument: Julich ([Fuchs et al., 2008](#)), Leeds ([Woodward-massey, 2018](#)), and Indiana ([Lahib, 2019](#)). In their RO_x tube the pressure is reduced (18-30 Torr) to reduce the radical loss through reactions like the formation of nitrites (*R 37*), nitrates (*R 35*) and HONO (*R 43*). However, decreasing the pressure slows down the RO₂ conversion and increases the amount of HO₂ lost on the walls. For these reasons compromised conditions have to be selected. A comparison of the three different RO_x-FAGE instrumental conditions is present in Table 11.

Table 11 : Experimental conditions of the Julich RO_x-FAGE, Indiana RO_x-FAGE (Lahib, 2019), Leeds-RO_x-FAGE (Whalley et al., 2013; Woodward-massey, 2018) instrument and the UL-RO_x-FAGE instrument (*this work*)

	Parameter	Value – Julich	Value-Leeds	Value – Indiana	Value – UL
Conversion flow-tube	Inlet nozzle orifice	1.0 mm	–	0.635 mm	0.635 mm
	Sample flow rate	7 L/min	–	2.1 L/min	3 L/min
	Length × diameter	83 × 6.6 cm	–	45 × 5.1 cm	47.9 × 6 cm
	Pressure	18.75 Torr	30 Torr	28 Torr	28 Torr
	Flow residence time	0.62 s	1 s	1 s	0.88 s
	Reagent mixing ratio	0.7 ppmv NO, 0.17% CO	–	0.8 ppmv NO, 0.4% CO	1.82 ppmv NO, 0.61% CO
Fluorescence cell	Transfer nozzle orifice	4.0 mm	1.0 mm	2.0 mm	3.0 mm
	Sample flow rate	3.5 L/min	7 L/min	1.5 L/min	8 L/min
	Pressure	2.25 Torr	1.5 Torr	2 Torr	1.3 Torr

In order to better identify the relevant parameters to test and the expected behavior of the radicals in the conversion tube, we first referred to the literature. A model of the conversion flow-tube chemistry based on reaction kinetics of the conversion of CH₃O₂ radicals in pure synthetic air was made by Fuchs et al. (Fuchs et al., 2008) in order to better predict the RO_x detection sensitivity. Using this model and comparing it to their experimental measurements, they were able to choose the required conditions to get an optimum conversion of RO₂ radicals in the conversion tube (Table 11) reporting the evolution of the sensitivity of HO₂ and CH₃O₂ as a function of the reaction time:

$$\text{Reaction time} = V \times (P/760) \times F$$

where V represents the volume of the conversion tube, P is the tube pressure and F is the flow in the tube.

The results of the simulations show a decrease in the CH₃O₂ concentration from 100 % to about 30 % changing the reaction time in the conversion tube from 1s to 0.1s. The HO₂ radical concentration slightly decreases with reaction time due to the increase of the losses in the gas phase and wall losses. Similar trends are observed experimentally, within the specified measurement errors due to the reproducibility of the measurements, changing the reaction time varying only the length of the conversion flow-tube.

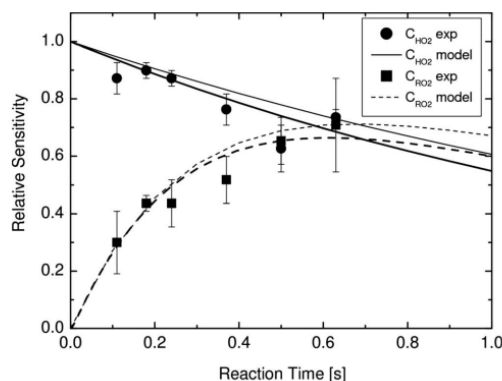


Figure 34: Experimental measurements of the sensitivity of HO_2 and CH_3O_2 radicals as function of the reaction time (symbols). Model simulations of the concentration of the HO_2 and CH_3O_2 radicals (solid and dashed lines) (Fuchs et al., 2008)

For optimizing the UL-RO_x-FAGE instrument, we first studied the detection sensitivity of HO_2 radicals experimentally as a function of the reaction time in the flow-tube. The measurements were done at the conditions mentioned in Table 11, varying only the pressure inside the RO_x conversion tube by changing the pinhole size and not the conversion flow-tube length like Fuchs. This test was done by placing a mercury lamp above the nozzle of the conversion tube and producing an equal amount of OH and HO_2 radicals which are all converted into HO_2 radicals as NO and CO are injected into the conversion tube. The calibration cell was not used at that time because we wanted to produce a large number of radicals because of the low sensitivity of the UL-RO_x-FAGE during this test. The results of this test (Table 12) shows that decreasing the pressure inside the conversion tube from 41 to 27 Torr (involving a slight decrease in the FAGE cell pressure) increases the HO_2 signal from 20800 cts to 29000 cts, respectively, which can be explained by the reduction of the loss reactions.

Table 12: Experimental measurements of the HO_2 signal at different conversion tube pressure

$P_{\text{ROX tube}}$ (Torr)	Reaction time (s)	HO_2 signal (cts)
41	1.33	20800
31	1.01	24800
27	0.88	29000

Therefore, the optimum reaction time 0.88 s corresponding to a pressure of 27 Torr was chosen during the optimization of the UL-RO_x-FAGE instrument.

The reagent gas concentrations are also a significant operating condition to test. The concentration of NO and CO should be adjusted in a way to get the conversion of OH in HO_2 due to its reaction with CO is significantly faster than HO_2 in OH due to its reaction with NO. These conditions are checked by calculating the ratio $(k_{(\text{NO}+\text{HO}_2)} \cdot [\text{NO}] / k_{(\text{CO}+\text{HO}_2)} \cdot [\text{CO}])$.

2.7.2.2. NO dependence

The optimal conversion of the RO₂ into HO₂ highly depends on the concentration of the reagent gases (both NO and CO). Model and experimental NO dependence of the detection sensitivity of CH₃O₂ and HO₂ was tested by Fuchs et al (2008). The measurements were obtained at the conditions shown in Table 11 by varying only the NO mixing ratio. As shown in Figure 35, both model and experimental measurements showed a weak dependence of the HO₂ sensitivity on NO concentration. The HO₂ sensitivity decreases with the increase of the NO concentration due to gas phase losses. This behavior was nearly the same with the measurements of the HO₂ sensitivity as function of NO flow (sccm) using the UL-RO_x-FAGE instrument (Figure 36). These measurements were done using a mercury lamp placed at the top of the conversion flow-tube (2.5 cm above the nozzle) to generate OH and HO₂ at the optimum conditions (Table 11) varying only NO concentration added into the flow-tube.

In the case of RO₂ represented by CH₃O₂ in Fuchs experiment, the conversion efficiency increases with the increase of the NO concentration to reach a maximum at NO mixing ratio above 0.8 ppmv and decreases with further increase of the NO concentration due to HONO formation or HO_x radical losses (more reactive than RO₂ radicals). For the UL-FAGE, tests were done to measure RO_x conversion efficiency dependence on NO. This was done by generating OH and HO₂ radicals in the calibration cell and adding C₂H₆ in the calibrator to convert all the OH into RO₂. The optimum conditions were set during these measurements, with a constant CO flow (20 sccm) and varying the NO flow. Figure 36 shows a similar trend to what is expected (Fuchs et al., 2008) showing a maximum level reached at a NO flow = 3 sccm. Therefore, the optimum mixing ratio of NO taken as a reference for testing the UL-RO_x-FAGE instrument must be around 1.82 ppmv (NO flow = 3 sccm).

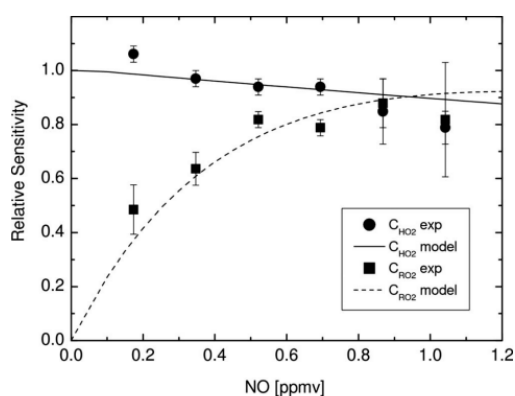


Figure 35: Experimental measurements of the sensitivity of HO₂ and CH₃O₂ radicals as function of the NO mixing ratio (symbols). Model simulations of the concentration of the HO₂ and CH₃O₂ radicals (solid and

dashed lines) (Fuchs et al., 2008)

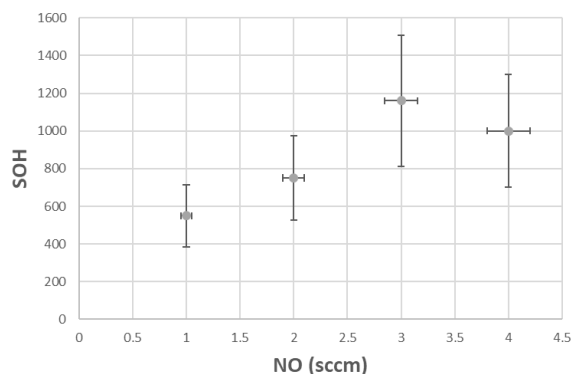


Figure 36: Experimental measurements of the RO_x yield as function of the NO with CO flow = 20 sccm, constant ($[CO] = 6.2 \times 10^{12}$ molecule cm^{-3})

2.7.2.3. CO dependence

Similarly to tests performed to optimize the conversion efficiency as a function of NO, tests changing the concentration of CO in the RO_x instruments have been done. Fuchs et al. (2008) performed simulations to investigate the response of the CH_3O_2 conversion chemistry to CO with all the other parameters set to their optimum values. The results of the model calculations showed an increase of the conversion efficiency for CH_3O_2 radicals and HO_x radicals with the increase of the CO concentration to reach a saturation level at a CO mixing ratio of approximately 0.2 %, where all OH radicals are converted into HO_2 radicals.

Laboratory experiments using UL- RO_x -FAGE were performed to test the OH to HO_2 conversion efficiency dependence on CO using a mercury lamp to generate OH and HO_2 radicals. The optimum conditions were set during these measurements, with a constant NO flow and varying the CO flow. Figure 37 shows a similar trend to what is expected (Fuchs et al., 2008) showing a saturation level at a CO flow = 20 sccm. Therefore, a CO concentration of 6.2×10^{12} molecule cm^{-3} (CO flow = 20 sccm) is enough to convert almost all the OH into HO_2 radicals and avoid significant wall losses of OH.

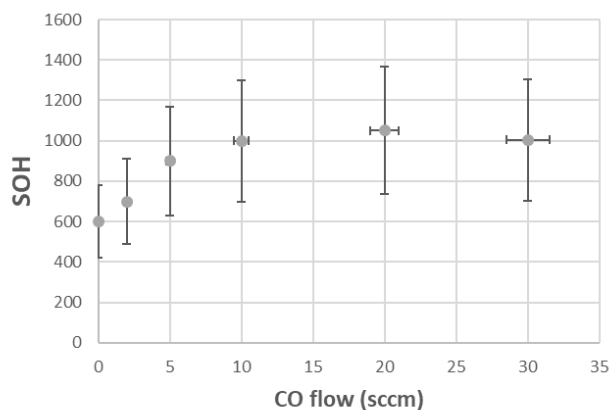


Figure 37: Experimental measurements of the HO_2 yield as function of the CO flow using a mercury lamp to generate OH and HO_2

Using the concentrations mentioned in Table 11, the ratio $(k_{(NO+HO_2)} \cdot [NO]) / k_{(CO+HO_2)} \cdot [CO]$ is 0.023 and 0.016 for Fuchs et al. (Fuchs et al. in 2008) and UL- RO_x -FAGE in this work, respectively.

2.8. Conclusion

During my thesis, a part of the work was dedicated to the optimization of new equipment (new excitation laser, RO_x conversion tube and new FAGE cell for RO_2 radical quantification). Another part of the work was dedicated to laboratory kinetic measurements and campaign measurements. Different measurement configurations were used depending on the type of study. The UL-FAGE technique can be used in the reactivity mode, HO_x quantification mode and RO_x quantification mode having detection limits and temporal resolution in agreement with the requirements for atmospheric measurements.

Concerning the RO_x -FAGE instrument optimization, chemical and physical conditions in the conversion flow-tube were optimized to reach the maximum conversion efficiency. This was achieved relying on the operating conditions used by Fuchs et al. and some laboratory experiments varying the different relevant parameters. The determination of the optimum operating conditions used by the newly developed RO_x -FAGE instrument allowed us to measure the RO_x radical concentration in ambient air during the ACROSS campaign simultaneously to the measurement of OH and HO_2 radicals and the OH reactivity. The RO_x -FAGE instrument participated also in the intercomparison measurements in the SAPHIR chamber to compare its performance with other instruments measuring RO_2 radicals.

Chapter 3: Kinetic Studies in Laboratory

This chapter presents the results obtained from kinetic studies carried out under controlled conditions in the laboratory using the UL-FAGE in its OH reactivity mode in two different configurations. It is divided into two parts:

The first part, written in an article format, is dedicated to the study of the humidity effect on radical + radical reactions, through a specific RO_2 reacting with OH: $\text{C}_2\text{H}_5\text{O}_2$. We first present the questioning leading to this study followed by the description of the measurement configuration used to generate separately two radicals with two photolysis lasers. The preliminary results of this study are then discussed. Missing tests that are needed to be finalized these results are also mentioned.

In the second part, we present the results obtained for studying siloxane chemistry. Siloxanes compounds are common indoor pollutants, and their degradation may lead to the formation of secondary pollutants such as formaldehyde indoors. The goal of this study was to improve the knowledge of their chemical mechanism by combining the experimental results carried out using the UL-FAGE at the University of Lille with theoretical work done by a PhD student at the University of Melbourne. However, due to a lack of time the experimental studies were limited to the study of the reaction of the simplest siloxane molecule (L2) with OH.

3.1. The dependence of humidity on the HO_2 yield in the $\text{RO}_2 + \text{OH}$ reaction

This part is written as an article to be submitted after complementary experiments.

Abstract

Methanol (CH_3OH) is a predominant oxygenated organic component in the lower remote atmosphere but the magnitude of its sources and sinks is highly uncertain and underestimations of the methanol measured by models have been observed, in particular in remote environments. One of its sources is the rapid reaction of methylperoxy radicals (CH_3O_2) with hydroxyl radicals (OH) which has different pathways leading to either the formation of $\text{CH}_3\text{O}/\text{HO}_2$ or CH_3OOOH or methanol/ O_2 . The reaction of CH_3O_2 with OH radicals becomes more important in remote environments due to the low concentration of NO and less competition with the reaction of CH_3O_2 with it. Thus, the reaction of CH_3O_2 with OH could be an important source of methanol under these conditions, for example in the marine boundary layer. Several studies ([Assaf et al., 2017](#); [Yan et al., 2016](#); [Muller et al. 2016](#)) have been published on the branching ratio between the different pathways and it is admitted that the formation of $\text{CH}_3\text{O}/\text{HO}_2$ is the major pathway for this reaction and CH_3OH is only a very minor product. However, the product yield can possibly be influenced by the humidity level. In the presence of high H_2O concentrations as in

the tropical marine boundary layer, a possible complexation of CH_3O_2 and OH radicals might lead to an increased stabilization of CH_3OOOH (Assaf et al. 2018), which could be transformed subsequently into CH_3OH for example in water droplets. Another potential explanation for high methanol level observed in remote environments is a measurement artefact with CH_3OOOH which could decompose into CH_3OH during sampling (Caravan et al., 2018) and thus increase the apparent CH_3OH concentration.

Here, we study the influence of humidity on the HO_2 yield in the $\text{RO}_2 + \text{OH}$ reaction for the reaction $\text{C}_2\text{H}_5\text{O}_2 + \text{OH}$, used as a proxy of the reaction $\text{CH}_3\text{O}_2 + \text{OH}$, by coupling the photolysis reactor of our UL-FAGE instrument in its reactivity mode, with two photolysis lasers for the separate generation of $\text{C}_2\text{H}_5\text{O}_2$ from 355 nm photolysis of Cl_2 in presence of $\text{C}_2\text{H}_6/\text{O}_2$ and OH from 266 nm photolysis of O_3 in presence of H_2O . The detection of OH and HO_2 radicals is then performed by the FAGE cell coupled to the photolysis reactor. The measurements showed no influence of humidity on the HO_2 yield of $\text{C}_2\text{H}_5\text{O}_2 + \text{OH}$ reaction. Preliminary results show an HO_2 yield of $\Phi = 0.64 \pm 0.16$ for this reaction under atmospheric pressure.

3.1.1. Introduction

Methanol is the most abundant non-methane organic compound and an oxygenated volatile organic compound (OVOC) found in the troposphere, and has an important impact on the budgets of ozone (O_3), carbon monoxide (CO) and formaldehyde (HCHO) (Choi et al., 2010; Duncan et al., 2007; Hu et al., 2011; Wells et al., 2014). The global methanol source ranges from 75 to 350 Tgyr^{-1} from different sources (Galbally & Kirstine, 2002; Jacob et al., 2005; Millet et al., 2008; Singh et al., 2000; Stavrakou et al., 2011; Tie et al., 2003) with the largest fluxes arising from direct emissions from terrestrial plant growth (Harley et al., 2007; Hu et al., 2011; MacDonald & Fall, 1993). Additional sources include emissions from oceans (Millet et al., 2008; Williams et al., 2004), biomass burning (Hornbrook et al., 2011; Wentworth et al., 2018), urban and industrial activities (de Gouw et al., 2005; Velasco et al., 2009) and atmospheric production (Madronich & Calvert, 1990; Tyndall et al., 2001). Methanol can also be produced by chemical reactions as discussed below. The methanol removal pathways include gas-phase oxidation by OH (Atkinson et al., 2006; Sander et al., 2006), dry and wet deposition (Karl et al., 2005; Talbot et al., 2005; Wells et al., 2014) and exchange with the ocean (Heikes et al., 2002; Millet et al., 2008). The global atmospheric lifetime for methanol is approximately 5-12 days (Heikes et al., 2002; Tie et al., 2003; Wells et al., 2014). A number of modelling studies attempting to provide estimates of the global methanol budget in the atmosphere exhibit large apparent discrepancies in its total sources and sinks (Bates et al., 2021; Heikes et al., 2002; Jacob et al., 2005; Millet et al., 2008; Singh et al., 2000; Galbally & Kirstine, 2002), particularly

in remote oceanic areas, which highlights the need to better constrain the sources of tropospheric methanol (Bates et al., 2021; Jacob et al., 2005; Müller et al., 2016; Stavrou et al., 2011).

Recently, the reaction of methylperoxy radicals (CH_3O_2) with hydroxyl radicals (OH) was proposed as an additional source of methanol in the remote atmosphere, such as tropical marine boundary layer where low NO concentrations lead to long peroxy radical lifetimes and make this reaction a major sink of peroxy radicals (Fittschen et al., 2014; Archibald et al., 2009):



The methanol production from the $\text{CH}_3\text{O}_2 + \text{OH}$ reaction depends on the overall reaction rate and the branching ratio of $R\ 50.2$. Following the first measurement of the rate constant of $R\ 50$ ($k = (2.8 \pm 1.4) \times 10^{-10} \text{ cm}^3 \text{ molecule}^{-1}$) by Bossolasco et al. (Bossolasco et al., 2014), Muller et al. (Müller et al., 2016) have investigated the reaction products of this reaction by means of high-level *ab-initio* calculations. They showed that the dominant initial product is the singlet trioxide intermediate (CH_3OOOH^*), which can either be stabilized or rapidly converted to a pre-product complex $R\ 50.1$. From applying different product branching scenarios in their global chemical transport model, Muller et al. (Müller et al., 2016) was only able to reconcile the modeled and measured atmospheric methanol concentrations with a yield of CH_3OH up to 30 %. However, their RRKM (Rice–Ramsperger–Kassel–Marcus) calculations predicted only a yield of 7 % for $R\ 50.2$. Furthermore, recent findings indicate that the rate constant of this reaction reported by Bossolasco et al. (Bossolasco et al., 2014) is overestimated by a factor of 3, which leads to an even higher CH_3OH yield (around 80 %) that would be necessary to reconcile models with measurements.

The rate constant of this reaction is now thought to be well known with $(1.0 \pm 0.2) \times 10^{-10} \text{ cm}^3 \text{ molecule}^{-1} \text{ s}^{-1}$ (Assaf et al., 2017; Yan et al., 2016; Fittschen, 2019). Yan et al. provided first experimental insights into the potential product yield of $R\ 50$. By modeling their UV absorption-time profiles to a complex mechanism, they estimated an upper limit of 5% for the formation of the Criegee intermediate which was later confirmed by Assaf et al. (Assaf et al., 2018) using broadband cavity enhanced absorption spectroscopy. The experimental studies of Assaf et al. (Assaf et al., 2018) suggested that at a total pressure of 50 Torr helium the dominant

pathway of *R 50* is $\text{CH}_3\text{O} / \text{HO}_2$ with a yield comprising $90 \pm 10\%$. These experimental results agree with the theoretical predictions of Muller et al. (Müller et al., 2016) with a HO_2 yield of 86%.

A more recent work by Caravan et al. (Caravan et al., 2018) was then intended to a direct measurement of the CH_3OH yield using two different experimental approaches: laser photolysis at either low (30 Torr) or high (760 Torr) pressure coupled to a multiplexed photoionization mass spectrometry (MPIMS) and an atmospheric simulation chamber coupled to proton-transfer reaction time-of-flight mass spectrometry (PTR-ToFMS). The laser photolysis experiments resulted in a CH_3OH yield of $9 \pm 5\%$ and $6 \pm 2\%$ in the low- and high-pressure, respectively. Observation of this small CH_3OH yields is in good agreement with the theoretical value ($\sim 7\%$) from Muller et al. (Müller et al., 2016). This study also detected directly in the high-pressure reactor for the first time the trioxide association product, CH_3OOOH (*R 50.3*), while in the low pressure experiments the trioxide was not detected. This supports the calculations of Muller et al. (Müller et al., 2016) that showed that CH_3OOOH is increasingly stabilized with increasing pressures, predicting a trioxide fraction of approximately 7% at 760 Torr and 0.02% at 30 Torr. However, the CH_3OH fraction obtained in the atmospheric simulation chamber was, with $\Phi_{\text{CH}_3\text{OH}} = 17 \pm 3\%$, higher than in the pulsed photolysis experiments, even accounting for the respective error bars. It was suggested that the trioxide, CH_3OOOH , is detected by the PTR-ToF-MS as CH_3OH , thus increasing the apparent CH_3OH yield. It remains unclear whether the decomposition of CH_3OOOH into CH_3OH^+ occurs during protonisation or if CH_3OOOH is already undergoing heterogeneous decomposition into CH_3OH , either on the Teflon walls of the simulation chamber or on the walls of the sampling tubes. This study highlights the need for additional characterization of potential sources of atmospheric methanol, with a particular focus on understanding the fate of the trioxide (*R 50.3*) in the troposphere, where in the presence of high H_2O concentrations, a possible complexation of CH_3O_2 and OH radicals might lead to an increased yield for *R 50.3* due to an increased stabilization of CH_3OOOH . Such conditions are predominant in the tropical marine boundary layer, where *R 50* is highly important due to low NO concentration. Additionally, Khan et al. (Khan et al., 2015) found that up to 17% of peroxy radicals could form complexes with a single water molecule under atmospheric conditions, and previous studies (Butkovskaya et al., 2009; Vaida, 2011) have shown that the water complexation can influence reaction rate constants and product branching fractions. The near-atmospheric pressure measurements conducted by Caravan et al. (Caravan et al., 2018) were carried out at low relative humidity (RH). Conducting

further investigations at different RH levels could provide insights into whether water influences this type of reactions or not.

Ethanol is an OVOC which is increasingly used as a fuel for motor vehicles (Sharma et al., 2021). It is also known as a minor biogenic volatile organic compound (BVOC) in the atmosphere (Kirstine & Galbally, 2012). Previous studies (Millet et al., 2010; Naik et al., 2010; Singh et al., 2004) showed that the largest atmospheric source of ethanol is from emissions by living plants, with smaller contributions from plant litter, biomass burning, anthropogenic production and atmospheric chemistry. The primary global sink of ethanol is oxidation by OH followed by dry deposition and wet deposition. Current levels of ethanol measured in remote oceanic areas are an order of magnitude larger than those in the model (Naik et al., 2010), suggesting a large missing source of ethanol. Ethanol plays a significant role in the global tropospheric chemistry; its oxidation is an important source of acetaldehyde and peroxyacetyl nitrate (PAN), both of which are highly toxic and contribute to ozone pollution (Naik et al., 2010). Ethanol also act as a potential precursor of secondary aerosols. Therefore, an improved understanding of its atmospheric cycle is important.

In this work, we focused on the reaction of C₂H₅O₂ radicals with OH (*R 51*) rather than on CH₃O₂ + OH due to constrains linked to our radical generation and reaction competition. The peroxy radicals (C₂H₅O₂) are generated in an atmospheric temperature and pressure photolysis cell by pulsed photolysis of Cl₂ at 355 nm in the presence of the respective alkane (C₂H₆) in excess O₂, while OH radicals are produced shortly after by the photolysis of O₃ in the presence of H₂O using a laser at 266 nm. The cell is coupled to a FAGE instrument for the time-resolved measurements of OH and HO₂ radicals.



3.1.2. Experimental description

The experimental setup is based on the OH reactivity instrument described in detail in previous work (Parker et al., 2011). An additional photolysis laser was coupled to the instrument for this work, allowing the separated generation of both radicals: C₂H₅O₂ and OH. Therefore, only a brief description critical for the current experiments is discussed here. The system consists of four main components: two photolysis lasers, a photolysis cell and the OH fluorescence detection system. The first photolysis laser used to generate C₂H₅O₂ is a YAG

laser (Q-Smart 850, QUANTEL) with a doubling and tripling stage providing radiation at 355 nm and operating at 1 Hz. The second photolysis laser used to generate OH is another YAG laser (Brilliant EaZy, QUANTEL) with a doubling and quadrupling stage providing radiation at 266 nm with a repetition rate of 1 Hz. The photolysis beams of both photolysis lasers are superposed and propagate in the center of the photolysis cell. The photolysis cell is a stainless-steel cylinder with an entrance window and two gas opening on opposite sides, one as entrance to put the studied gas mixture in the cell and the other connected to a pressure gauge to measure the pressure inside the cell and to analysers to control water and ozone levels. Time to time, part of the gas is sampled to additional instruments such as the O₃ analyzer for O₃ concentration measurements, and a hygrometer for H₂O measurements. The mixture is pumped through a FAGE cell connected at the back of the photolysis cell

A schematic is shown in Figure 38:

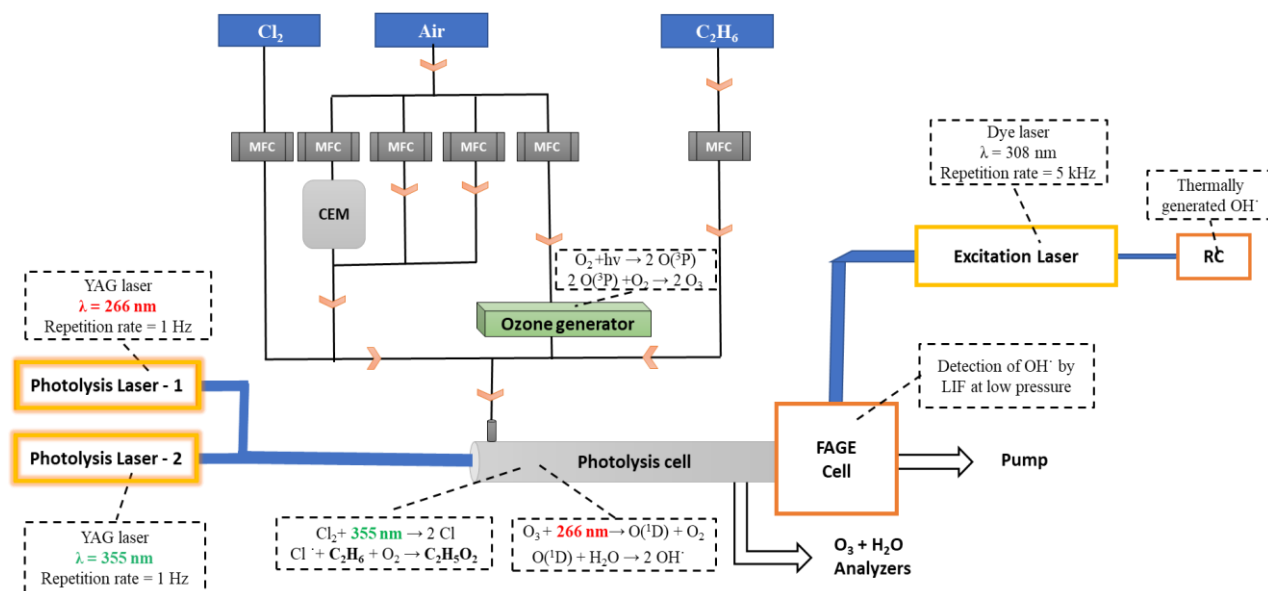
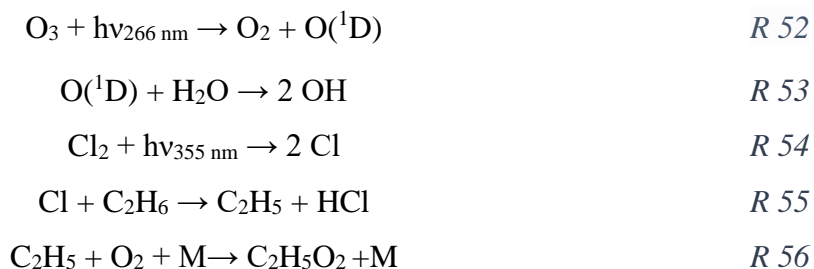


Figure 38: Scheme of the experimental setup occupying two photolysis lasers

To maintain atmospheric pressure (760 Torr) in the photolysis cell against the sampling into the FAGE cell, a total gas flow of 8.56 L/min is introduced into the photolysis cell. O₃ was produced by an ozone generator and mixed with a flow of humid air, generated by a CEM (Controlled Evaporator Mixer), and flows of C₂H₆ and Cl₂ were added directly from cylinders through calibrated mass flow controllers (Bronkhorst). The C₂H₅O₂ radicals are generated in the photolysis cell by pulsed laser photolysis of Cl₂ at 355 nm in the presence of C₂H₆ in excess O₂. OH radicals are generated 10 ms later from ozone photolysis at λ = 266 nm in the presence of water vapor:



The gas from the photolyzed mixture is expanded into the FAGE cell where OH can be detected by LIF (Laser Induced Fluorescence) after being excited at $\lambda = 308\text{ nm}$. The fluorescence signal is collected by a gated CPM (Channel Photon Multiplier, Perkin-Elmer), sent to an acquisition card and recorded via a LabView program. The detection of the OH fluorescence is synchronized with the photolysis laser ($\lambda = 266\text{ nm}$) pulses by means of delay generators. The fluorescence signals are accumulated over several photolysis laser shots with the number of photolysis pulses being determined according to the obtained SNR (signal-to-noise ratio), typically SNR = 4.

A small flow of pure NO can be added at the entrance of the FAGE cell through a Teflon tube (diameter = 0.25 cm) to convert a constant fraction (around 1/3) of HO₂ radicals formed into OH radicals. These OH radicals are generated in addition to OH radicals already present in the FAGE cell; therefore, the signal corresponds to the sum of OH and HO₂ radicals. The HO₂ signal is thus obtained from the difference of two signals: with and without NO. The following section presents in detail the different measurements carried out to obtain the HO₂ concentration time profile.

3.1.3. Method

As the aim of this work is to determine the yield of HO₂ in the reaction C₂H₅O₂ with OH, the first step is to “calibrate” the system with a well-known reaction at different humidity levels. For this purpose, the well-known CO+OH reaction, producing HO₂ with a yield of 1, was chosen. This reaction, requesting only the photolysis laser to generate OH and a flow of diluted CO ($[CO] = 2.27 \times 10^{14}\text{ molecule cm}^{-3}$), is used as a reference reaction to determine the HO₂ yield for the reaction of C₂H₅O₂+OH. From this study we were able to evaluate the fraction of HO₂ radicals lost due to the coupling of the photolysis cell to the FAGE cell and to determine the loss rate of HO₂ due to diffusion within the photolysis cell.

3.1.3.1. Extract of the HO₂ profiles for the reference reaction CO+OH

As shown in Table 13, to extract the HO₂ concentration time profile, four subsequent steps are required:

Table 13: Four different steps required to determine the HO₂ formed concentration time profile

Step	Mixture in photolysis cell	Injection in FAGE cell	Radical Detected	Signal Detected
1	zero air		OH	OH reacting with impurities
2	zero air	NO	OH	OH reacting with impurities + bkg
3	zero air + reactant (CO)		OH	OH reacting with CO
4	zero air + reactant (CO)	NO	HO ₂ + OH	OH reacting with CO + HO ₂ formed + bkg

Step 1: OH not reacting:

OH concentration time profile is obtained by introducing zero air in the absence of any reactant, i.e. OH can only react with the impurities in the photolysis cell or decrease through wall loss and the obtained decay is called ‘‘OH not reacting’’.

Step 2: OH not reacting + bkg

As a second step, NO is injected at the entrance of the FAGE cell also without adding any reactant in the photolysis cell to measure the HO₂ produced due to the reaction of OH with impurities as well as a background signal generated through the addition of NO (possibly from HONO formed in the FAGE cell) and the obtained decay is called ‘‘OH not reacting + bkg’’.

From the subtraction of signal obtained in step 1 to step 2, we can calculate the background linked to the addition of NO:

$$\text{Background} = \text{OH not reacting + bkg} - \text{OH not reacting}$$

As shown in Figure 39 the OH not reacting + bkg decay (step 2) is slower than the OH not reacting decay (step 1) and has also a higher OH concentration. The increase in the initial OH concentration and the slower decay at longer time scales is probably due to a percentage of OH converted to HO₂ through its reaction with the impurities in the zero air and the increase in the OH concentration is due to a stationary HO₂ concentration in the cell after the addition of NO. Figure 39 (right graph) shows the background profile, where an increase in the LIF signal to reach a maximum after 0.25 s can be observed. Then the signal decrease slowly to reach the initial value which could correspond to the presence of stable HO₂ concentration in the photolysis cell. The residence time within the photolysis cell is around 7 sec, i.e. at a photolysis repetition rate of 1 Hz, the gas mixture is photolyzed around 7 times before it enters the FAGE

detection cell. This can explain the presence of a stable HO_2 concentration in the photolysis cell.

The background profile allows to determine the percentage of OH reacting with the impurities in zero air producing HO_2 concentration.

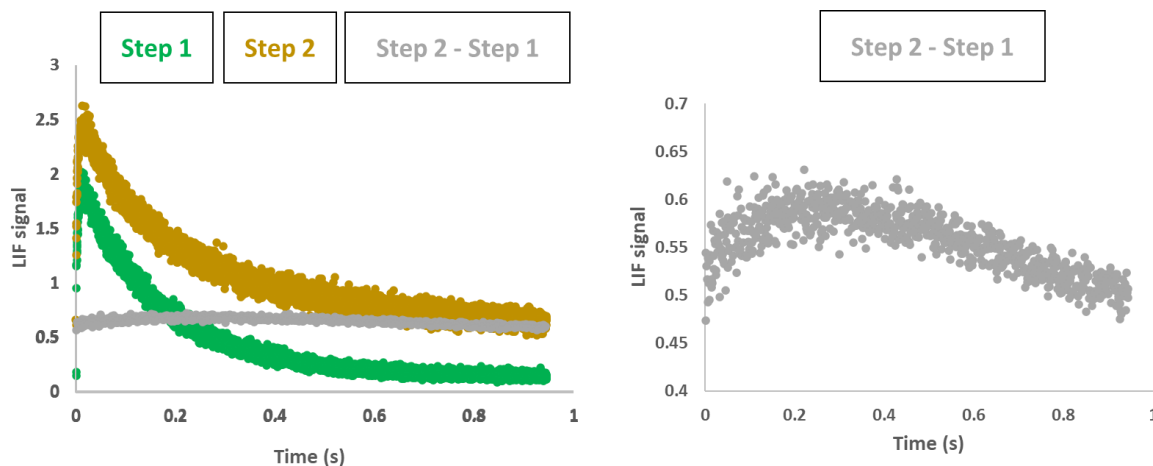


Figure 39: Left graph: The OH concentration time profile obtained during *step 1: OH not reacting profile*, *step 2: OH not reacting + bkg* and background profile. Right graph: background profile with a y-axis scale: 0.3 – 0.7

Step 3: OH reacting

For the third step, a reactive species (CO) is added at the entrance of the photolysis cell without any addition of NO. This decay shown in is called ‘OH reacting’ (Figure 40).

Step 4: HO_2 formed + OH reacting + bkg

The final step is the addition of both, the reactive species (CO) to the photolysis cell and NO to the FAGE cell. The obtained decay (Figure 40) is called ‘ HO_2 formed + OH reacting + bkg’ since it sums up the HO_2 radicals produced from the reaction of OH with the reactants and the impurities and the HO_2 bkg.

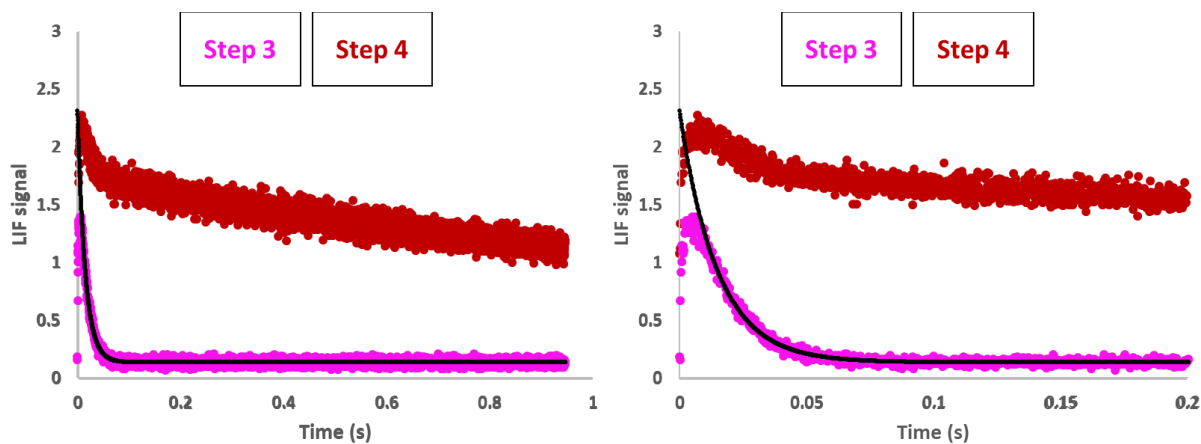


Figure 40: The OH concentration time profile obtained from CO + OH reaction during *step 3: OH reacting* and *step 4: HO_2 formed + OH reacting + bkg* and fit for OH reacting decay. Right graph: zoom with x-axis scale: 0–0.2

The fluorescence signal is summed for around 300 photolysis pulses for each step.

The HO₂ formed concentration time profile (Figure 41) is obtained from the difference of the last two mentioned steps:

$$\begin{aligned} \Rightarrow \text{HO}_2 \text{ formed} &= \text{Step 4} - \text{Step 3} \\ &= (\text{HO}_2 \text{ formed} + \text{OH reacting} + \text{bkg}) - (\text{OH reacting}) \end{aligned}$$

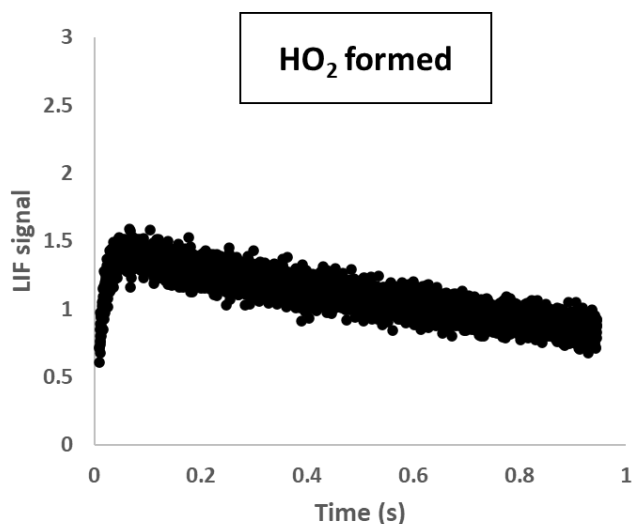


Figure 41: The HO₂ formed concentration time profile obtained from CO + OH reaction

This HO₂ formed has to be normalized by the OH available (ΔOH). For that, we fit to a mono-exponential the OH reacting decay obtained in step 3. $\Delta\text{OH} = \text{OH}_{\text{max}}$ (extrapolated at $t=0$) – OH_{min} (Figure 42).

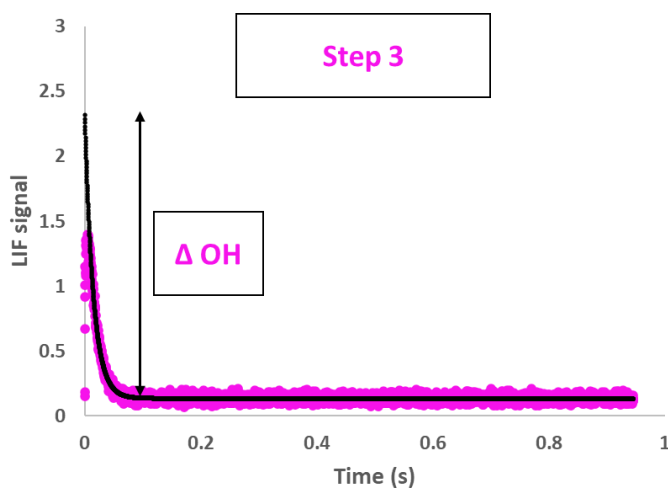


Figure 42: The OH concentration time profile obtained CO+OH reaction during step 3: OH reacting showing ΔOH

Finally, the $\text{HO}_2 \text{ formed}/\Delta\text{OH}$ time profile shown in Figure 43 can be obtained from the fit:

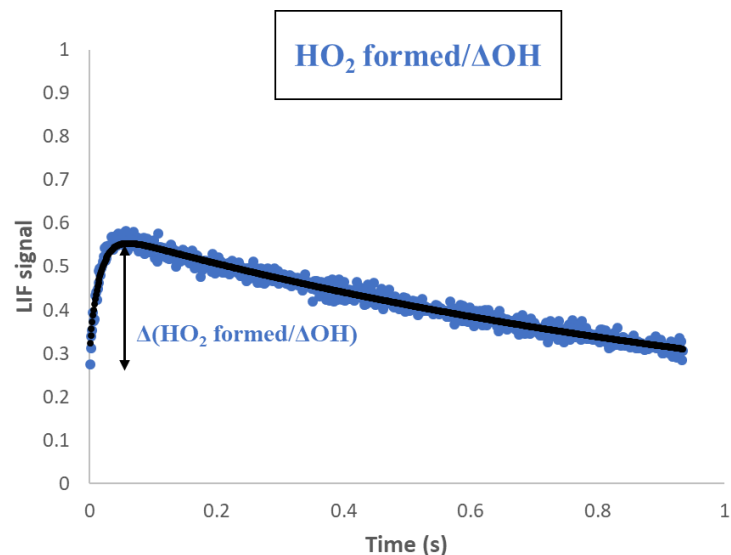


Figure 43 : HO_2 formed/ ΔOH time profile obtained from $CO+OH$ reaction

The ratios ΔHO_2 formed/ ΔOH obtained at different humidities for the reference reaction $CO+OH$ are shown in Figure 44. The average ratio is around 0.27 ± 0.05 . This ratio shows that not all HO_2 radicals are converted into OH injecting an NO flow of 10 sccm at which the maximum conversion of HO_2 to OH occur (as shown in Figure 45).

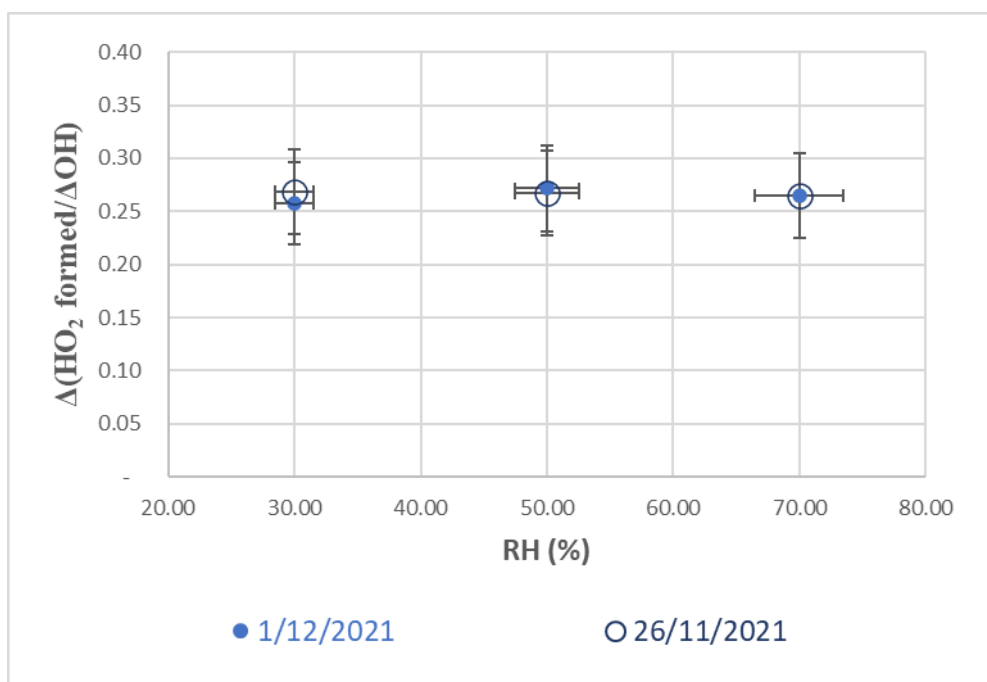


Figure 44: $\Delta(HO_2$ formed/ $\Delta OH)$ obtained at different RH (%) for two days measurement

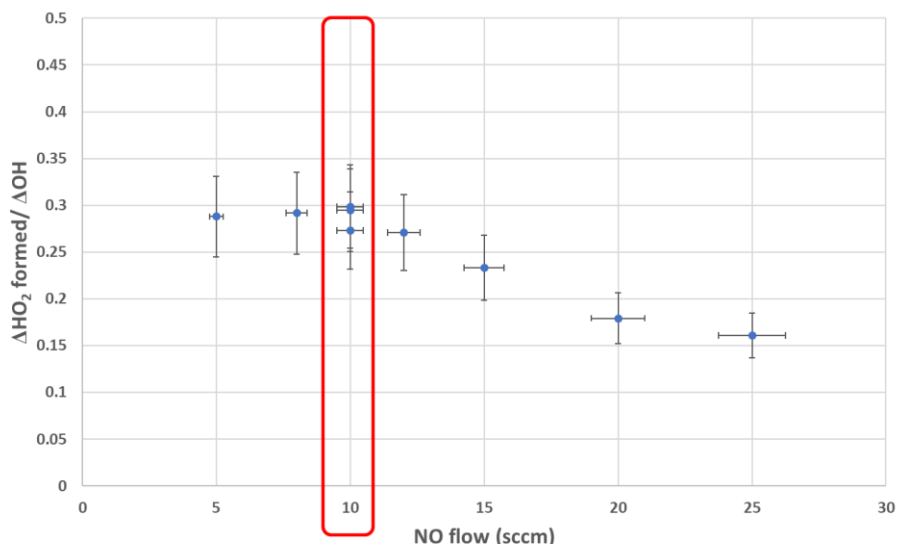


Figure 45: $\Delta\text{HO}_2 \text{ formed} / \Delta\text{OH}$ obtained at different NO level injected into the FAGE cell

In order to use the reference yield of 1 known for the reaction of CO with OH for the reaction of $\text{C}_2\text{H}_5\text{O}_2$ with OH and to take into account the experimental conditions, these experimental results have been compared to simulations using the model shown in Table 14. The losses of OH in zero air condition have been separated in 2 reactions: one leading to the formation of HO_2 (R9), 1 not (R8). To determine the respective rate, the OH decay recorded in step 1 and HO_2 profile obtained from step2-step 1 have been used and the values reported in Table 14 obtained from adjusting the model to reproduce the measured HO_2 profile (shown in Figure 46) taking into account the other reactions involving HO_2 formation such as reaction 3 ($\text{O}_3 = 2.21 \times 10^{13} \text{ molecule.cm}^{-3}$). The diffusion loss of HO_2 was determined by fitting the measured $\Delta\text{HO}_2 \text{ formed} / \Delta\text{OH}$ decay.

Table 14 : Model used for CO + OH reaction, all rate constants have been taken from the preferred IUPAC evaluations

Reaction nb	A	+	B	→	C	+	D	Rate Constant ($\text{cm}^3 \text{ molecule}^{-1} \text{ s}^{-1}$) or Reactivity (s^{-1})
1	CO	+	OH	→	HO_2	+	CO_2	2.31×10^{-13}
2	OH	+	HO_2	→	H_2O	+	O_2	1.10×10^{-10}
3	OH	+	O_3	→	HO_2	+	O_2	7.30×10^{-14}
4	HO_2	+	O_3	→	OH	+	2O_2	2.00×10^{-15}
5	HO_2	+	HO_2	→	H_2O_2	+	O_2	2.35×10^{-12}
6	OH	+	OH	→	H_2O	+	O	1.48×10^{-12}
7	HO_2	+		→	Diff	+		0.5
8	OH	+		→	kzero			5.9
9	OH	+		→	HO_2			0.2

As we observed a HO₂ formation in zero air (step 2), showing a stationary concentration of HO₂ in the photolysis cell.

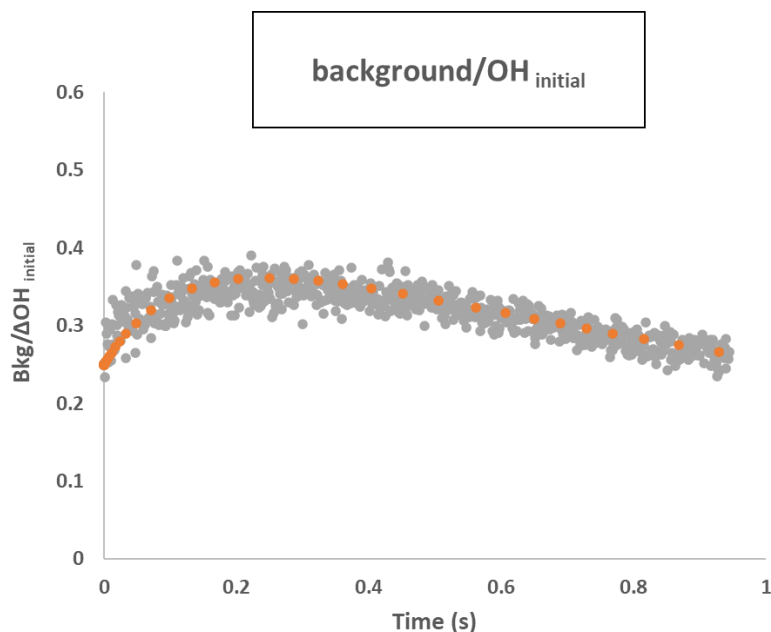


Figure 46: The grey symbols show the background/ $\Delta OH_{initial}$ measured and the orange symbol correspond to model calculations

From this model, and taking into account the experimental diffusions, HO₂ formation in zero air, ozone level, a $\Delta HO_2 \text{ formed}/\Delta OH = 0.82$ was obtained from the model (Figure 47). Comparing it with the experimental results of 0.27, it corresponds to a factor of 3 more. The reasons for this difference can be the limitation of HO₂ conversion in the FAGE (maximum 80% observed) and extra HO₂ losses in the sampling.

Therefore, to compensate the difference of HO₂ radicals produced measured compared to the expected one from the model, a correction factor of 3 is applied to the measured $HO_2 \text{ formed}/\Delta OH$ time profile (Figure 48) to reproduce the modelled profile with a HO₂ yield of 1. This correction factor will be applied to the experimental measurements of the target reaction: $C_2H_5O_2 + OH$ to take into account the differences observed with the reference reaction.

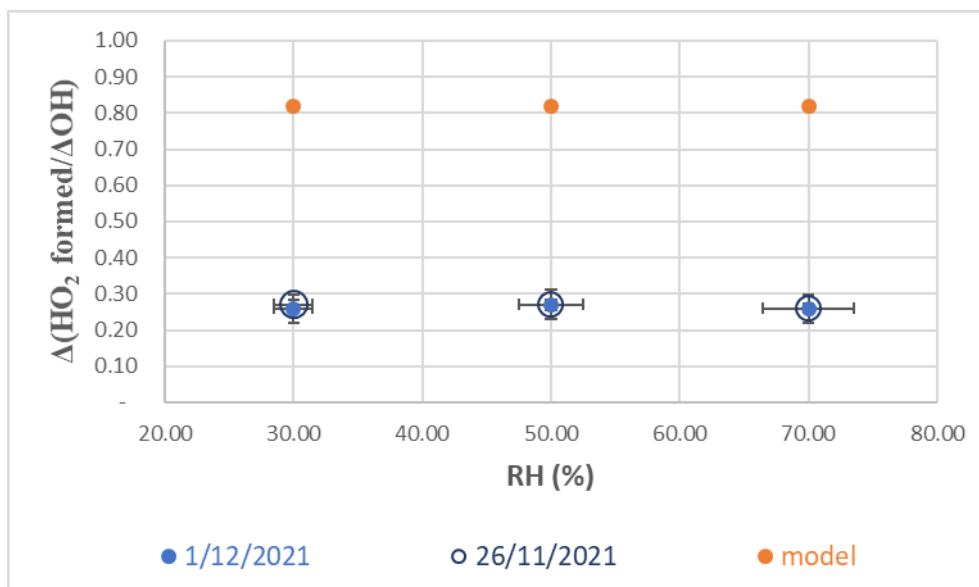


Figure 47: $\Delta\text{HO}_2/\Delta\text{OH}$ obtained at different RH (%) for two days *measurement* and $\Delta\text{HO}_2/\Delta\text{OH}$ obtained from the *model*

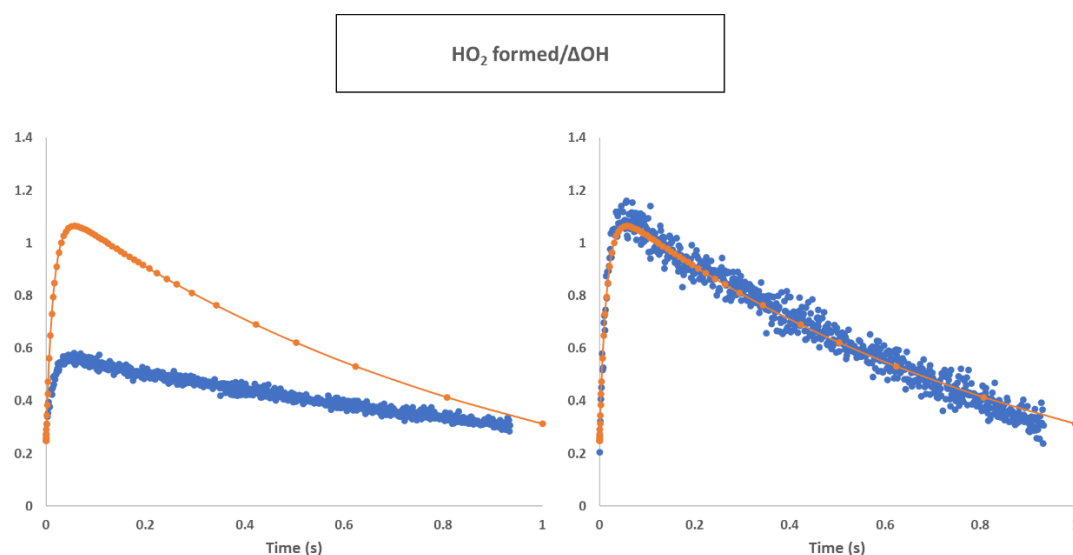


Figure 48: - left graph: the *blue symbols* show the ΔHO_2 formed/ ΔOH measured profile *before correction* and the *orange symbol* correspond to the *model calculations* and right graph: the *blue symbols* show ΔHO_2 formed/ ΔOH measured profile *after correction by a factor of 3* and the *orange symbol* correspond to the *model calculations*

The second part of the work was dedicated to the analysis of the reaction of $\text{C}_2\text{H}_5\text{O}_2$ with OH.

3.1.3.2. Determination of the experimental conditions for $\text{C}_2\text{H}_5\text{O}_2 + \text{OH}$ reaction study

To ensure that the reaction of the peroxy radical with OH is the major fate for OH radicals in the photolysis cell, several constraints due to relative reaction rate constants or experimental limitations must be considered:

- ✓ $\text{C}_2\text{H}_5\text{O}_2 + \text{Cl} \rightarrow \text{CH}_3\text{CHOO} + \text{HCl}$ or $\text{CH}_3\text{CH}_2\text{O} + \text{ClO}$ (< 20 % Cl)
- ✓ $\text{OH} + \text{C}_2\text{H}_6 \rightarrow \text{H}_2\text{O} + \text{C}_2\text{H}_5$ (< 20 %)
- ✓ $\text{OH} + \text{Cl}_2 \rightarrow \text{HOCl} + \text{Cl}$ (< 20 %)

- ✓ $C_2H_5O_2$ must be generated in a large excess over OH
- ✓ Reactivity (OH + $C_2H_5O_2$) in the range from 20 to 100 s^{-1}

Simulations (Table 15) have been performed to determine the precursor concentrations ($[Cl_2]$ and $[C_2H_6]$) that need to be introduced into the photolysis cell to respect these constraints. It should be mentioned that no condition could be found for CH_4 as precursor for CH_3O_2 to fulfil the constraints. Indeed, the reaction of Cl-atoms with CH_4 (which is the precursor for the CH_3O_2 radicals) is only 15 times faster than the reaction of OH radicals with CH_4 , while this ratio is much higher for C_2H_6 (236 times faster). Therefore, during this study the C_2H_6 is used rather than CH_4 to avoid the competition between CH_4 and CH_3O_2 to react with OH radicals.

Table 15: Model used for $C_2H_5O_2 + OH$ reaction, all rate constants have been taken from the preferred IUPAC evaluations

Reaction nb	A	+	B	→	C	+	D	Rate Constant ($\text{cm}^3 \text{ molecule}^{-1} \text{ s}^{-1}$) or k (s^{-1})
1	C_2H_6	+	Cl	→	C_2H_5	+	HCl	5.90×10^{-11}
2	C_2H_5	+	O_2	→	$C_2H_5O_2$	+		4.80×10^{-12}
3	C_2H_5	+	O_2	→	HO_2	+		3.00×10^{-14}
4	$C_2H_5O_2$	+	Cl	→	CH_3CHO	+	HCl	7.69×10^{-11}
5	$C_2H_5O_2$	+	Cl	→	CH_3CH_2O	+	ClO	7.41×10^{-11}
6	$C_2H_5O_2$	+	$C_2H_5O_2$	→	C_2H_5O	+	C_2H_5O	4.7×10^{-14}
7	$C_2H_5O_2$	+	$C_2H_5O_2$	→	MOL	+	MOL	2.80×10^{-14}
8	OH	+	C_2H_6	→	C_2H_5	+	H_2O	2.40×10^{-13}
9	OH	+	ClO	→	pdt	+		2.00×10^{-11}
10	OH	+	Cl_2	→	HOCl	+	Cl	6.50×10^{-14}
11	HO_2	+	HO_2	→	H_2O_2	+	O_2	2.50×10^{-12}
12	HO_2	+	$C_2H_5O_2$	→	O_2	+		6.90×10^{-12}
13	C_2H_5O	+	O_2	→	HO_2	+		9.48×10^{-15}
14	O_3	+	Cl	→	ClO	+	O_2	1.20×10^{-11}
15	OH	+	O_3	→	HO_2	+	O_2	7.30×10^{-14}
16	HO_2	+	O_3	→	OH	+	$2O_2$	2.00×10^{-15}
17	OH	+	HO_2	→	H_2O	+	O_2	1.10×10^{-10}
18	OH	+	OH	→	H_2O	+	O	1.48×10^{-12}
19	HO_2	+		→	Diff	+		0.5
20	OH	+		→	kzero	+		8.3
21	OH	+		→	HO_2	+		0.5
22	OH	+	$C_2H_5O_2$	→	HO_2	+		8.4×10^{-11}
23	OH	+	$C_2H_5O_2$	→	PDT	+		4.6×10^{-11}

Initial experiments were carried out on 12th of January 2022 with a Cl₂ concentration of around 1.7×10^{14} molecule cm⁻³, leading with a photolysis energy of 22 mJcm⁻² to an initial Cl-atom concentration of around 2.5×10^{11} molecule.cm⁻³. In presence of a C₂H₆ concentration of around 1.3×10^{13} molecule.cm⁻³ a C₂H₅O₂ concentration of approximately 2.5×10^{11} molecule.cm⁻³ is generated. Using these concentrations and assuming that all OH is reacting with C₂H₅O₂, we can reach an optimal OH-reactivity of around 30 s⁻¹. However, these conditions were only used during the measurements on 12th of January and 23rd of February 2022 due to some instrument limitations such as the damage of the photolysis cell at high humidity level (70 %) because of high Cl₂ concentration reacting with H₂O and producing HCl, which is corrosive. Therefore, the experimental conditions were modified to limit the loss of Cl₂ and the damage of the photolysis cell. The experiments on 1st of March 2022 were carried out with the Cl₂ concentration lowered by a factor of 10 together with an increased pulse energy (to around 100 mJ cm⁻²), still allowing the generation of a sufficient C₂H₅O₂ concentration.

The C₂H₅O₂ concentration was changing depending on the [Cl₂] entering the photolysis cell. That's why, measurement of the total reactivity before and after adding C₂H₆ and Cl₂ was needed to determine the % of OH reacting with C₂H₅O₂ ($k_{C_2H_5O_2+OH}$). A missing step identified in the data analysis was measuring the reactivity adding all the reactants without the photolysis laser 355 nm. This step is useful to determine the % OH reacting only with C₂H₅O₂ by comparing the profiles with the laser at 355 nm. This step will be done in the coming work at each condition to finalize these results.

Table 16 shows a summary of the experimental conditions for all experiments done at different RH. All experiments were done at atmospheric pressure (760 Torr) with constant [O₃] = 2.21×10^{13} molecule cm⁻³.

To determine the reactivity of C₂H₅O₂ + OH reaction several loss reactions of OH radicals other than *R 50* need to be considered and subtracted:

- $k_{C_2H_5O_2+OH} = k_{total} - (k_{Cl_2,Cl+OH} - k_{C_2H_6+OH} - k_0)$ - with k_{total} corresponding to the total reactivity measured fitting the OH decay, .
 - k_0 representing the reactivity of OH with the impurities in the cell in absence of any other reactive species. It was measured before each step for all conditions and is typically in the order of 10 s⁻¹,
- ⇒ and represents around 20% of the OH consumption,
- $k_{C_2H_6+OH}$ is the reactivity of OH with C₂H₆. The pseudo-first-order rate constant of OH with C₂H₆ ($k_{C_2H_6+OH}$) can be calculated from the known [C₂H₆] = 1.3×10^{13} molecule cm⁻³. It was measured in a separated step adding zero air + C₂H₆ + photolysis

lasers $\lambda = 266$ nm to generate only OH to measure $k_{C_2H_6+OH} = 3.3$ s⁻¹ and represents 6 % of the OH consumption.

The reactivity of C₂H₆ with OH was only measured twice and since it was reproducible this value was used for all the measuring conditions. However, in order to insure the reproducibility of the conditions, future experiments have to be repeated with all the steps at each condition.

- $k_{Cl_2,Cl+OH}$ corresponds to the reactivity of Cl₂ with OH. It is measured in another separated step without C₂H₆, adding Cl₂ to the mixture + photolysis lasers $\lambda = 266$ nm and $\lambda = 355$ nm, we obtain the % of OH reacting with Cl₂ ($k_{Cl_2+OH} = k_{obs} - k_{zero\ air}$). Between 2 to 9% of the OH will react with the precursor Cl₂, this percentage varies depending on the concentration of Cl₂ and C₂H₆ entering the photolysis cell and with the photolysis laser ($\lambda = 355$ nm) energy. It was difficult to obtain reproducible results due to the difficulty of working with Cl₂ because of corrosion problems and cleaning of the cell after each measurement was needed.
- Finally, the fraction of OH having reacted with C₂H₅O₂ can be estimated in a first approximation for each experiment as the ratio of $k_{total} - (k_{Cl_2,Cl+OH} - k_{C_2H_6+OH} - k_0)/k_{total}$. Under our conditions, between 50 and 63% of all OH reacted with RO₂ (last column in Table 16).

Table 16: Experimental conditions for all experiments, *measured and calculated values*

Date	RH (%)	C ₂ H ₆ × 10 ¹³ (cm ⁻³)	Cl ₂ × 10 ¹³ (cm ⁻³)	k _{zero} (s ⁻¹)	k _{C₂H₆+OH} (s ⁻¹)	k _{Cl₂+OH} (s ⁻¹)	k _{total} (s ⁻¹)	k _{C₂H₅O₂+OH} (s ⁻¹)	% OH reacting with C ₂ H ₅ O ₂
12/1/2022	30	1.3	7.5	9.7	3.3	4.9	48.7	30.8	63
	70	1.3	13	10.6	3.3	8.5	60.6	36.4	63
23/2/2022	30	1.3	11.5	9.2	3.3	7.3	41.3	21.4	52
	50	1.3	13	8.6	3.3	9.6	44.8	23.3	52
1/3/2022	50	1.3	3.5	7.4	3.3	2.3	29.4	16.4	56
	70	1.3	2.3	7.5	3.3	1.5	24.9	12.7	51

Same experimental steps than mentioned above for the reference reaction: CO + OH were followed to determine the ΔHO_2 formed/ ΔOH for the reaction C₂H₅O₂ + OH reaction. The ΔHO_2 formed/ ΔOH must be corrected by the ratio $k_{C_2H_5O_2+OH}/k_{total}$. Also, a correction factor (CF) of 3 on the $\Delta HO_2/\Delta OH$ measured as the one determined comparing the ΔHO_2

formed/ ΔOH obtained from the reaction $\text{CO} + \text{OH}$ has been applied (ΔHO_2 formed/ $\Delta\text{OH}_{\text{corrected}}$).

$$\rightarrow \Delta\text{HO}_2 \text{ formed}/\Delta\text{OH}_{\text{corrected}} = \Delta\text{HO}_2 \text{ formed}/\Delta\text{OH}_{\text{measured}} \times k_{\text{C}_2\text{H}_5\text{O}_2+\text{OH}}/k_{\text{total}} \times \text{CF}_{\text{HO}_2 \text{ losses}}$$

3.1.4. Experimental results and discussion

Figure 49 presents the measurements of the ΔHO_2 formed/ $\Delta\text{OH}_{\text{corrected}}$ obtained during the experiments presented in Table 16.

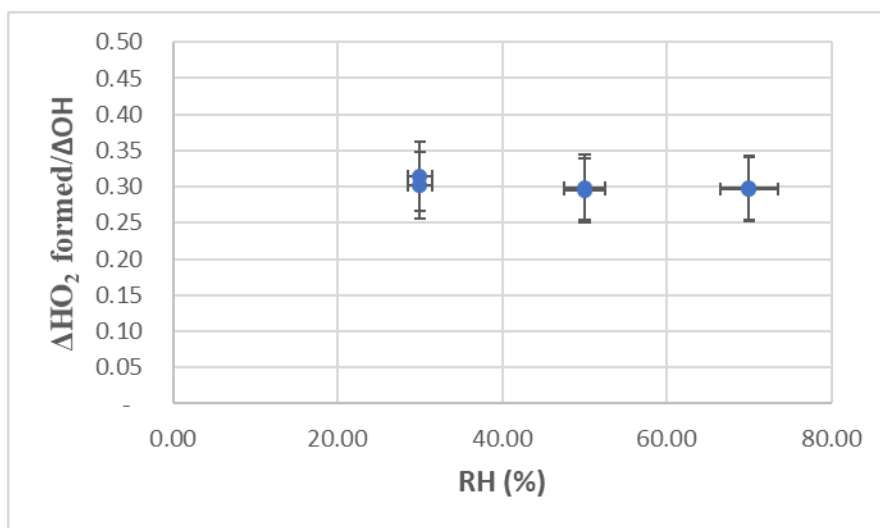


Figure 49: ΔHO_2 formed/ ΔOH for the reaction $\text{C}_2\text{H}_5\text{O}_2 + \text{OH}$ obtained under all experimental conditions given in Table 16

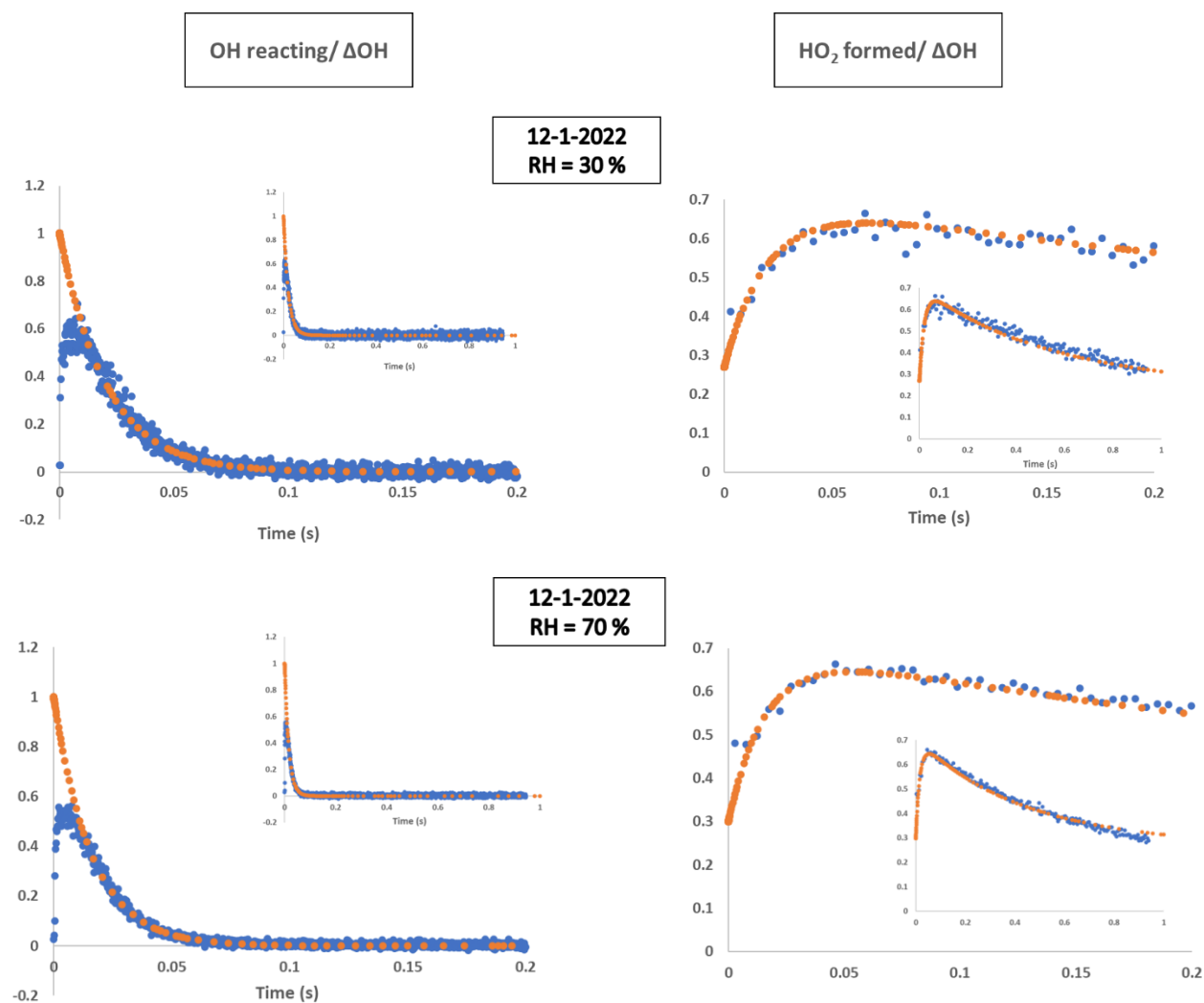
The observed results show a stable and reproducible ΔHO_2 formed/ ΔOH with a value around 0.3 ± 0.07 at different relative humidity levels (RH= 30, 50 and 70%). Therefore, no effect on the ΔHO_2 formed/ ΔOH with increasing relative humidity is observed in our series of experiments assuming stable conditions between the series. This tends to show that there is no impact of the water complexation on the product branching fractions of $\text{C}_2\text{H}_5\text{O}_2 + \text{OH}$ reaction under atmospheric pressure. However, as mentioned above, some assumptions on the stability of conditions have been done and should be checked to confirm this result

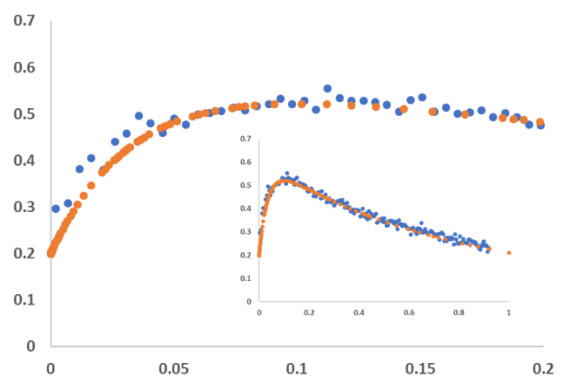
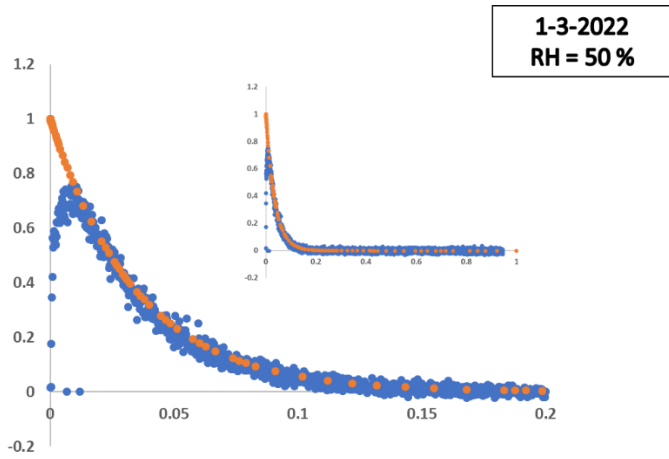
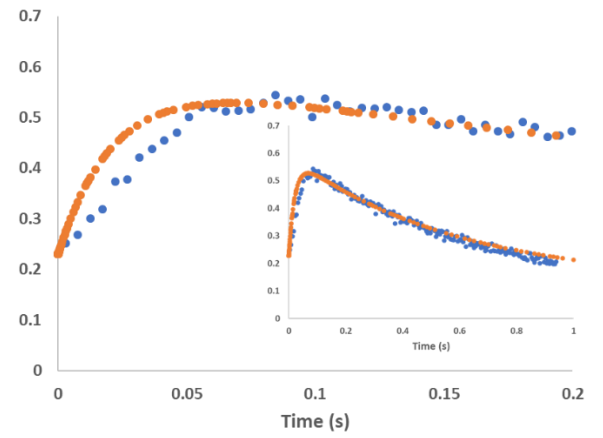
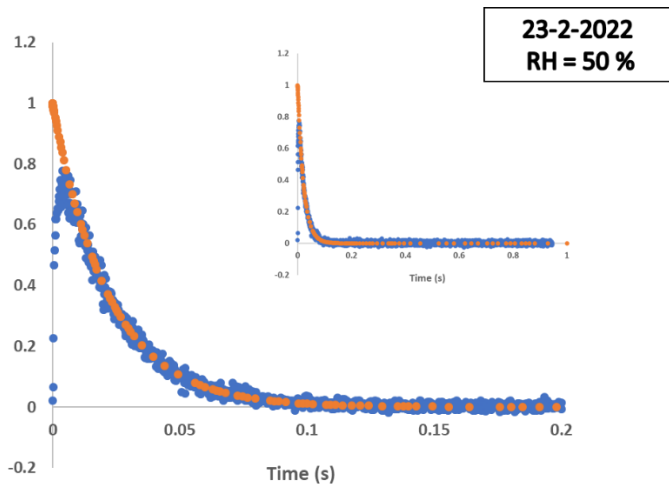
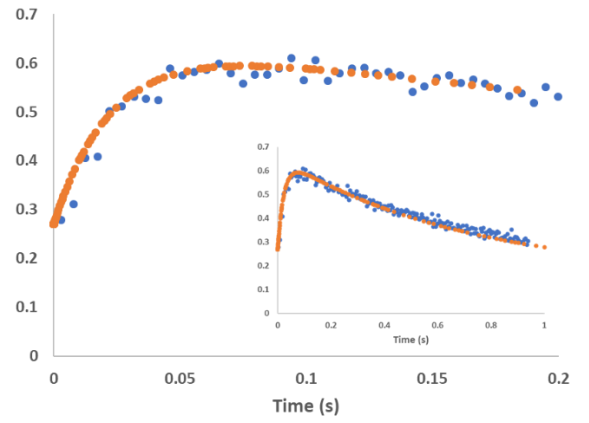
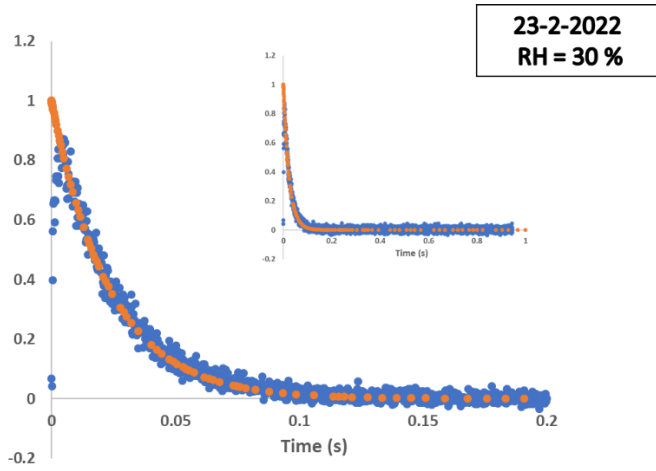
The HO_2 yield in the $\text{C}_2\text{H}_5\text{O}_2 + \text{OH}$ reaction has also been determined by modeling the experimental traces. The model, summarized in Table 15, has been generated by considering the sinks and sources of OH and HO_2 , other than R1. Initial conditions have been chosen as discussed previously in section 3.1.3.2 and reported in Table 16. An initial concentration of HO_2 of $2.7 \times 10^9 \text{ molecule}^1 \text{ cm}^{-3}$ is added to the model to consider the stationary HO_2 concentration generated in the photolysis cell. Only the ratio of the rate constants for the channel leading to HO_2 and $\text{C}_2\text{H}_5\text{O}$ or to the other products (PDT) has been adjusted such that the profiles of OH reacting/ ΔOH and HO_2 formed/ ΔOH are well reproduced by keeping the total rate constant for R51 at $1.3 \pm 0.3 \times 10^{-10} \text{ cm}^3 \text{ molecule}^{-1} \text{ s}^{-1}$. Figure 50 presents the result for

the 3 different relative humidities. (This rate constant has been measured recently by Assaf et al. (Assaf et al., 2017) and showed a very good agreement with the value of Yan et al ($1.2 \pm 0.3 \times 10^{-10} \text{ cm}^3 \text{ molecule}^{-1} \text{ s}^{-1}$).

The HO₂ yield obtained from these experimental measurements performed at atmospheric pressure (760 Torr) is 0.64 ± 0.16 and consistent under all RH levels. Assaf et al. (Assaf et al., 2018) determined experimentally an HO₂ yield of 0.75 ± 0.15 for this reaction under low pressure (50 Torr) and found to agree with our results, within the expected uncertainties. Our experimentally determined yield exhibits substantial unexplained disagreement when compared to the theoretical predictions, HO₂ yield = 0.21 (Assaf et al., 2018).

The uncertainties on the HO₂ yield determined by our work have been estimated to 25%. Errors in the absolute rate constant of the C₂H₅O₂ + OH reaction would have an influence on the retrieved HO₂ yield that has been determined using its well-known rate constant. Another error source is the variation in the water and O₃ concentration that were measured before and after each series.





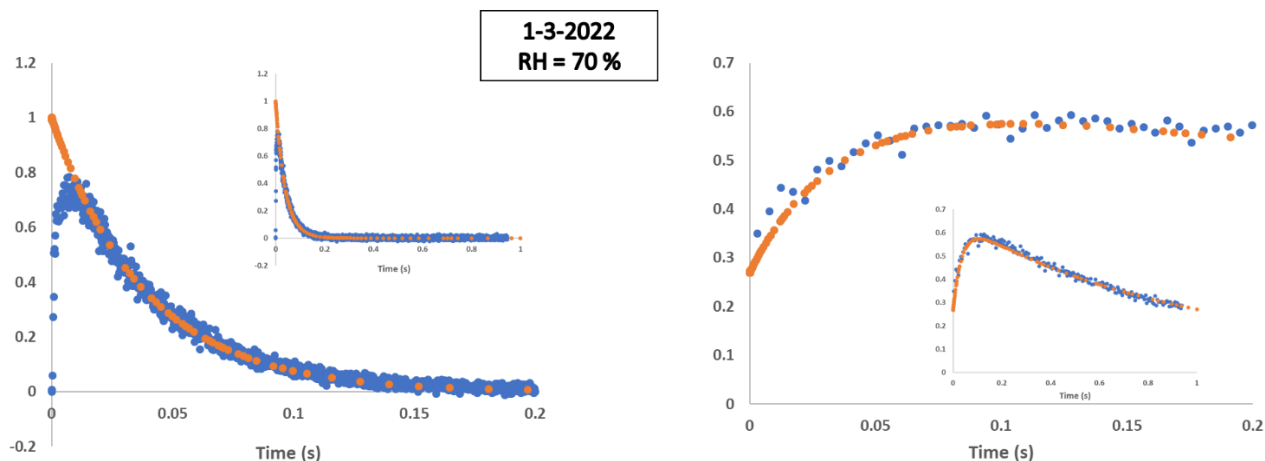


Figure 50: OH reacting/ ΔOH (left) and ΔHO_2 formed/ ΔOH (right) profiles for all experimental conditions given in Table 16 (except for the profiles in the absence of C_2H_6). The blue symbols show the measured profile, and the orange symbols correspond to model calculations using rate constants such as given in Table 15

3.1.5. Conclusion and Perspective of the work on $RO_2 + OH$

This aim of this work was to study the influence of humidity on the HO_2 yield in the $RO_2 + OH$ reaction, working with $C_2H_5O_2$ using the UL-FAGE instrument in the reactivity configuration. The HO_2 yield obtained for the $C_2H_5O_2 + OH$ reaction is 0.64 ± 0.16 at different relative humidity levels. It was suggested that in the atmosphere, at high pressure of 760 Torr and with more efficient N_2 and O_2 colliders, an increased yield of stabilized $ROOOH$ can occur. However, our results show an agreement with the HO_2 yield measured at low pressure (Assaf et al. 2018).

These are preliminary results since we did some assumptions and did not systematically reproduce all the intermediate steps between experiments. Due to time limitations because of the preparation of the field campaigns, we were not able to check the reproducibility of these measurements except once. Additional measurements under different conditions will be performed such as measuring the reactivity of the OH with all the reactant with and without the 355 nm photolysis laser. Also, performing these measurements with a photolysis laser operating at different repetition rates will help refresh the mixture and better understand the stable HO_2 concentration observed during this work.

This work highlights the complexity of studying peroxy + OH reaction and the necessity for further measurements of the HO_2 yield for the reaction of larger peroxy radicals with OH as well as direct measurements of CH_3OH yield carried out at high RH. Further investigations of CH_3OH yield as function of RH may help to support the conclusion of no impact of water on this type of reactions and might determine unexplored functionalized peroxy radical cross-reactions could account for the unidentified source of atmospheric methanol.

3.2. Chemistry of Siloxanes

One of the well-known VMS (volatile methyl siloxanes) oxidation products is formaldehyde (CH_2O) with a high yield (Fu et al., 2020). Formaldehyde causes eye, nose and throat irritation and it is likely to pose a carcinogenic risk to humans (Gupta et al., 1982). In addition, the other products that may be formed, such as silanol ($\text{Si}(\text{OR})_2(\text{CH}_3)(\text{OH})$), formate ester ($\text{Si}(\text{OR})_2(\text{CH}_3)(\text{OC}(\text{O})\text{H})$) and silyl methanol ($\text{Si}(\text{OR})_2(\text{CH}_3)(\text{CH}_2\text{OH})$), have a lower vapor pressure and higher water solubility than the parent VMS. Recently, studies have indicated that these products may be present in new particles and contribute to secondary organic aerosol (SOA) with potential impacts on air quality and human health (Wu & Johnston, 2017).

The aim of this work was to study the role of VMS oxidation and their potential role in indoor environments or in the atmosphere. To achieve our goal, kinetic studies on the reactions between VMS and OH radicals using the Laser Induced Fluorescence Assay by Gas Expansion (LIF-FAGE) technique in its reactivity configuration (detailed in Chapter 2, section 2.6) have been carried out at the university of Lille in the PC2A laboratory. As a first step to study the reactivity of siloxanes with OH, we have chosen to remeasure the rate constant of a well-known siloxane: L2. L2 is the simplest molecular structure corresponding linear siloxanes and rate constant value is available in the literature, it can facilitate the comparison and the validation of experimental results and theoretical model.

3.2.1. Preliminary tests on Siloxanes

During this work, L2 has been prepared as diluted mixture in stainless steel canisters by injecting liquid L2 with a micro-syringe and filling the canister with nitrogen (N_2) to 1.7 bar total pressure. Before adding any siloxanes into the canister, OH reactivity measurements are performed with the canister filled with only N_2 to check its cleanliness. The mixture in the canister is added to the main flow through a calibrated mass flow controller (MFC). Figure 51 shows the pseudo-first order rate constants as a function of L2 concentration for the three measurements (done with the same prepared canister) ($k_{1-\text{L2}+\text{OH}}$, $k_{2-\text{L2}+\text{OH}}$ and $k_{3-\text{L2}+\text{OH}}$). The obtained rate constants, which is the slope of the linear regression, were reproducible within around 3%. The average of the three rate constants resulted $k_{\text{OH}+\text{L2}} = (0.95 \pm 0.25) \times 10^{-12} \text{ cm}^3 \text{ molecule}^{-1} \text{ s}^{-1}$ and is in agreement with the results of Bernard et al., 2018 (slightly slower) using a similar technique: PLP-LIF (Pulsed Laser Photolysis-Laser Induced Fluorescence). The concentration of the L2 introduced into the photolysis cell is calculated based on the volume of L2 liquid injected into the canister (adjusted in a way to reach an OH reactivity of about

100 s⁻¹), the filling time of the canister with N₂ using a MFC, the flow from the canister containing L2 and the total gas flow (8.56 L/min to reach atmospheric pressure in the photolysis cell).

The main uncertainty in the determination of the rate constant is linked to the concentration of L2 and the preparation method (estimated to 15 %). To reduce this uncertainty, it would be useful to perform absolute measurements of the L2 concentration in the canister using the proton transfer reaction-mass spectrometry (PTR-MS).

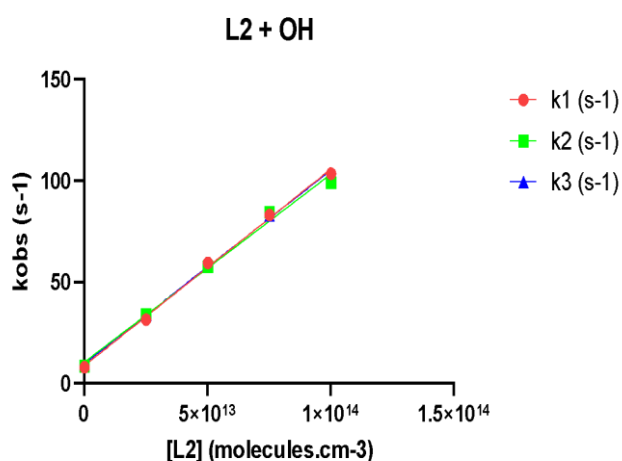


Figure 51: Pseudo first order rate constant as a function of [L2] for 3 different measurements

This preliminary rate constant determined experimentally at the university of Lille was compared with the value determined theoretically at the University of Melbourne and with the literature (Bernard et al 2018).

The theoretical work done by a PhD student (Nguyen Thuy Dung Thi) at the university of Melbourne is based on a model composed of two main calculations: the electronic structure properties and the temperature-dependent rate constants. All the electronic structure calculations were performed using Gaussian 16 package (Frisch et al. 2019). In details, M06-2X/aug-cc-pVTZ (Zhao et al. 2007) was used to obtain the optimized geometries, frequencies, and zero-point energies (ZPE) of all species in the reaction. The intrinsic reaction coordinate (IRC) calculations were then carried out to confirm the connection of transition state with pre-reaction complex and bimolecular product through the minimum energy pathway. The final single point energy was calculated at higher level of theory, DSD-PBEP86-D3BJ/def2-TZVPP, to achieve more accurate energies. These results help to construct the potential energy surface of the L2 + OH reaction (Figure 52), which represents the chemical transformation from L2 and OH to the radical and water.

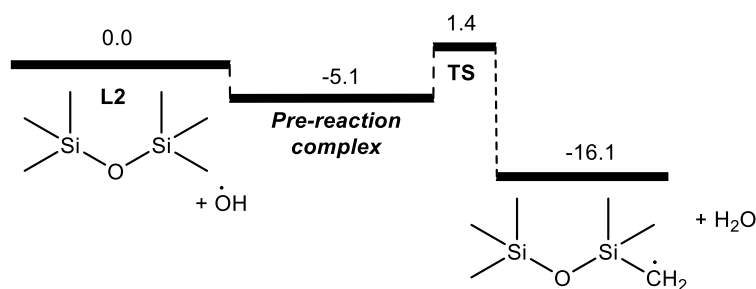


Figure 52 : The potential energy surface of L2 + OH reaction. Numbers (in kcal/mol) are the 0-K energies relative to reactants.

From the obtained electronic structure properties, the canonical transition state theory was applied to calculate the rate constant of L2 + OH in the temperature range of 200 – 500 K, 1 atm (Figure 53). All calculations in this step were carried out with the MultiWell 2021 program suite (Barker et al. 2020; 2001; 2009).

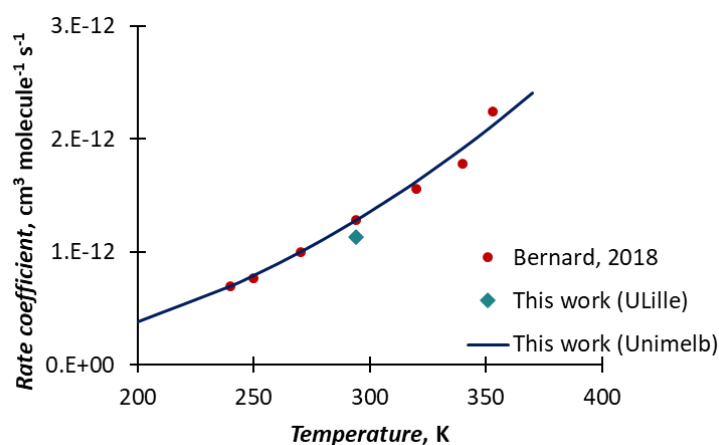


Figure 53 : Rate coefficient of L2+OH reaction as function of temperature (K) determined experimentally (at 298 K at university of Lille) and theoretically (at university of Melbourne) and compared to the literature (Bernard et al. 2018)

Based on the chemistry model from university of Melbourne, the calculated rate coefficient of the L2 + OH reaction at 298 K and 1 atm is $1.22 \times 10^{-12} \text{ cm}^3 \text{ molecule}^{-1} \text{ s}^{-1}$ (Figure 53). This value is 1.3 times larger than the experimental value ($(0.95 \pm 0.25) \times 10^{-12} \text{ cm}^3 \text{ molecule}^{-1} \text{ s}^{-1}$) from the university of Lille using the FAGE technique and in a very good agreement with the literature data value, $k_{\text{L2+OH}} = 1.28 \times 10^{-12} \text{ cm}^3 \text{ molecule}^{-1} \text{ s}^{-1}$ (Bernard et al. 2018). In the range temperatures of 200 - 400 K, the calculated rate coefficients exhibit a positive dependence on temperature. They obtained the same trend as the experimental results of Bernard et al. (Bernard et al. 2018).

3.2.2. Conclusion and Perspective of the work on siloxane reactivity

The experimental and theoretical obtained rate coefficients agree with the literature. It shows that the L2 are short-lived in the atmosphere with approximate lifetimes of 11 days for a representative OH radical concentration of 1×10^6 molecule cm^{-3} . If this reaction is too slow to have an impact indoors, it could affect the outdoor air quality. Therefore, it is important to continue studying the transformation of their primary and secondary oxidation products after the oxidation initiated by OH. In addition, more complex studies such as autooxidation reactions of VMS should be done to better understand the impact of these compounds in indoor environments or in the atmosphere (Ren & Da Silva, 2020).

This work validates the FAGE experimental setup at the university of Lille and the theoretical model at the university of Melbourne to study the oxidation of siloxanes. The future experimental work will focus on measuring the L2 + OH rate constant varying the temperature and studying other indoor chemical species that impact the air quality. After the validation of the L2 + OH reaction theoretical model, the theoretical studies continued to explore the oxidation of other more complex siloxanes such as: trimethylsilanol (TMSOH), pentamethylsiloxane (L5), Decamethylcyclopentasiloxan (D5) and others.

To study more in detail the oxidation processes and products resulting from siloxanes oxidation, measurements of reactivity change following the aging of siloxane mixture in presence of OH would be useful. For this the coupling of the reactivity instrument with a reaction chamber where siloxanes can be oxidized would be of great interest.

Chapter 4: SAPHIR Intercomparison Campaign

This chapter reports the analysis of an intercomparison campaign (ROxComp) held at the Forschungszentrum Jülich in Germany in August 2022. The UL-FAGE instrument in its quantification mode to measure OH, HO₂, HO₂* and the sum of RO₂, described in chapter 2 (section 2.3), next to eight other instruments dedicated to RO₂ quantification, was coupled to the SAPHIR chamber. All the instruments measured peroxy radical concentration simultaneously during several oxidation experiments done under controlled conditions. Some instruments measured also OH and HO₂ radicals. For the analysis of the results, we used the FAGE instrument of the Jülich group (Forschungszentrum: FZJ-FAGE) as a reference. Indeed, this instrument was intercompared previously with inherently calibration-free-techniques such as MIESR for HO₂ (Fuchs et al., 2009) and DOAS for OH (Schlosser et al., 2009) and showed good correlation in all these intercomparison measurements.

In this chapter, we first describe the SAPHIR chamber, and the different experiments done during this campaign. The radical measurements (OH, HO₂, HO₂* and RO₂) done by the UL-FAGE are then compared to the radical concentration measured by FZJ-FAGE.

4.1. State of the art of intercomparison measurements for radicals

The intercomparison provides an important process for the development and validation of the analytical instruments and measurement techniques. Most of the intercomparison measurements for radical quantification (such as: OH, HO₂, or [HO₂] + [RO₂]) are made in ambient conditions during intensive field campaigns (Beck et al., 1987; Brauers et al., 1996; F. Eisele et al., 2001, 2003; Hall, 1995; Mount et al., 1997; Platt et al., 2002). In general, these measurements have shown relatively good agreement. However, due to the high temporal and local variation of the atmospheric radicals, they were subject to discrepancies that could be explained by the sampling inhomogeneities (Fuchs et al., 2010; Schlosser et al., 2009). This problem could be excluded in large atmospheric simulation chambers where the air masses are homogeneously mixed to investigate the instruments performance and determine potential interferences of measurements under well-controlled conditions were few intercomparisons took place (Schlosser et al., 2007; Fuchs et al., 2012).

4.1.1. OH intercomparison measurements

In the recent years, few ambient and chamber intercomparison exercises have been conducted for OH measurement techniques. Among the intercomparison field campaigns dedicated to the study of different environments is the POPCORN 1994 campaign (Brauers et al., 1996). It is an intercomparison of OH measurements between the FZJ-FAGE and DOAS

technique carried out in clean rural environment in North-East Germany. Most of the days, measurements performed with DOAS and FZJ-FAGE instruments agreed well except when the wind came from the north-west sector, where the DOAS data exceeded systematically the LIF measurements.

Schlosser et al. (Schlosser et al., 2007) presented the first OH intercomparison measurement between the FZJ-FAGE and DOAS techniques at the SAPHIR chamber in Forschungszentrum Jülich (Germany). A series of experiments was carried out in standard conditions where no trace gases were added and some other experiments where HCHO, NO, NO₂, O₃, CO and H₂O were added in different combinations. Six valid measurement days have shown a good agreement between the two instruments with regression slope around 0.99. Three measurement days were discarded from the analysis because of the poor correlation between the two instruments. Higher NO_x concentration was present in the chamber during these three days however, no instrumental interference from NO_x is known or expected. The disagreement between the instruments could be explained by the instability of the FAGE instrument calibration, interferences with other molecules and photochemical or chemical gradient inside the chamber.

In 2005, Schlosser et al. (Schlosser et al., 2009) performed the first formal blind intercomparison for OH measurements involving three FAGE instruments and one DOAS during the HO_xComp campaign in ambient air and in the SAPHIR chamber. Over the nine measurement days, six experiments were carried out in the SAPHIR chamber (oxidation of various hydrocarbons and ozonolysis of alkenes) and instruments sampled ambient air during three days. Excellent agreement was observed for the instruments during the measurements performed inside the chamber with regression slope in the range of 1.01 to 1.13. The ambient results revealed some discrepancies between instruments with regression slopes ranging between 1.06 to 1.69, which can partly be explained by the stated instrumental accuracies, sampling inhomogeneities and calibration problems. Taking the DOAS technique as the reference measurement, no relevant interferences with respect to ozone, water vapor, NO_x and peroxy radicals could be observed with the LIF system.

In 2010, the UL-FAGE underwent an intercomparison with the FZJ-FAGE instrument in the SAPHIR simulation chamber. The experimental conditions (H₂O, O₃ and NO_x concentration levels) have been varied similarly to those during the HO_xComp intercomparison campaign carried in the SAPHIR chamber. They studied the chemistry of CO, phenol and isoprene under different conditions of O₃ and NO_x. In addition, the Jülich FAGE instrument (OH and HO₂) was calibrated using the Lille calibration source and an agreement within 12 % has been found

with a systematic overestimation using Lille calibration cell. The measurement of the OH concentration during all the experiments (9 days) showed a good agreement between both instruments (FZJ-FAGE and UL-FAGE) with a slope of 0.86 ($r^2 = 0.93$) and a small intercept of $1.42 \pm 0.24 \times 10^5$ molecule cm^{-3} .

In 2011, a series of intercomparison measurements was carried out in the SAPHIR chamber between the FZJ-FAGE and DOAS technique, in order to investigate the photochemical degradation of isoprene, methyl vinyl ketone (MVK), methacrolein (MACR) and aromatic compounds by OH. The goal of these experiments was to reproduce the conditions experienced during the PRIDE-PRD2006 campaign in China, where a large difference between OH measurements and model was found (Fuchs et al., 2012). The analysis of twenty measurement days showed good agreement. The regression slope equaled 1.02 and a correlation coefficient of $r^2 = 0.86$. This good agreement between the DOAS and FZJ-FAGE instrument indicates that the sensitivity of the LIF instrument is well defined by the calibration procedure and reduces the possibility of an artifact in the OH measurements during the PRIDE-PRD2006 campaign. However, discrepancies were observed for measurement days of MVK and toluene, where the LIF measurements of OH concentration, for both experiments, were approximately 30-40 % larger than those by DOAS showing potential interferences from these species on FAGE instruments. It should be also mentioned that it is not possible to reproduce in the chamber conditions at very low concentration of NO due to desorption from the chamber walls. This could lead to underestimate the potential interference due to trioxides such as identified in the UL-FAGE instrument (Fittschen et al., 2019).

4.1.2. HO₂ and RO₂ intercomparison measurements

Contrary to OH, intercomparison measurements for HO₂ and RO₂ are fewer. An old HO₂ intercomparison of ambient HO₂ measurements was performed in 2003 at a rural site in the US between the Penn State LIF-FAGE and NCAR/University of Colorado PerCIMS instrument (Ren et al., 2003). An excellent agreement was observed between both instruments' measurements with a regression slope close to unity. In addition, a very good agreement from cross-calibration has been reported during this campaign.

During the HOxComp, three LIF instruments participated in the formal blind intercomparison HO₂ measurements (Fuchs et al., 2010). No absolute reference measurements (MIESR) were available during this intercomparison campaign. The analysis of the entire data set of ambient measurements revealed significant discrepancies between instruments with regression slopes ranging between 0.56 and 1.46. A better agreement was observed for the measurements performed in the SAPHIR chamber with regression slopes ranging from 0.69 to

1.26. While these results indicate differences that lie within measurement uncertainties, the quality of the fit parameters improves significantly when the data were grouped into subsets of similar water vapor concentrations, suggesting an unknown artifact related to water-vapor.

The intercomparison done in 2010 between the UL-FAGE and FZJ-FAGE at the SAPHIR chamber included HO₂ measurements also. The analysis of all the experiments showed significant difference between both instruments with a regression slope of 1.5 ($r^2 = 0.93$) with a small intercept of $1.48 \pm 0.12 \times 10^7$ molecule cm⁻³ (FZJ-FAGE concentration vs UL-FAGE). However, it is not representative of the contrasted results for analysis day by day that have showed good agreements except when double bound reactants were injected. These results are in linked to the recently discovered RO₂ interference. Indeed, due to technical problems with the NO Mass Flow Controller of the UL-FAGE, the NO concentration in the UL-FAGE was much lower than in the FZJ-FAGE leading to a lower interference on the HO₂ measurements and thus lower concentration.

Similarly, only few intercomparison measurements have been reported for total peroxy radicals ($[HO_2] + [RO_2]$). There was only one attempt to intercompare the instruments measuring peroxy radicals inside a simulation chamber, that has been carried out in 2006 in the SAPHIR chamber between the Jülich RO_x-LIF (FZJ-FAGE) and MIESR instruments (Fuchs et al., 2009). Two experiments were made, the OH-oxidation of methane and 1-butene, indicating an excellent agreement, with a regression slope of 0.96 and r^2 of 0.85. An ambient intercomparison field study for the total peroxy radicals involved a PERCA and MIESR instrument during the BERLIOZ field campaign (Platt et al., 2002) in a rural semi-polluted site near Berlin, Germany. Results of the two days of measurement indicated a good agreement with a slope of 1.07 and r^2 of 0.91.

More instruments measuring RO₂ radicals have been developed recently and intercomparison experiments involving more types of instruments need to be performed. Therefore, in August 2022, an intercomparison campaign took place at the SAPHIR chamber (Jülich, Germany). This campaign allowed to test the reliability of the different instruments detecting peroxy radicals at very low concentrations in the atmosphere. Among these instruments was the UL-FAGE from the PC2A laboratory.

4.2. The atmosphere simulation chamber SAPHIR

4.2.1. Description of the SAPHIR chamber

The atmosphere simulation chamber SAPHIR (Simulation of Atmospheric Photochemistry In a large Reaction chamber), shown in Figure 54, is designed to investigate photochemistry

processes under controlled conditions at ambient temperature, pressure, and natural irradiation with small amounts of trace gases as typically present in the atmosphere. Unlike field measurements, the chemical conditions are thoroughly defined. A detailed description of the chamber can be found in previous works such as (Bohn et al., 2005; Rohrer et al., 2005). The reaction chamber has a volume of 270 m³ (inner diameter 5 m, length 18 m). It consists of a double-walled FEP (DuPont, per-fluoro-ethylene-propylene foil) cylinder held by a steel-frame. The foil is chemically inert and has 85 % transmission to UV-A and UV-B. The pressure is held at 50 Pa above ambient pressure to avoid ambient air contaminating the chamber during the experiments. Two fans are installed inside the chamber to ensure the homogeneous mixing of the gases. Rohrer et al. (Rohrer et al., 2005) showed that HONO and HCHO from the walls are the major sources of radicals in the chamber.

Previous intercomparative measurements using different techniques to measure OH (Fuchs et al., 2012; Nehr et al., 2014), HO₂ (Fuchs et al., 2010), NO₃ (Dorn et al., 2013), HCHO (Wisthaler et al., 2008), OVOC (Apel et al., 2008) and OH reactivity (Fuchs et al., 2017) have already been done at the SAPHIR chamber.



Figure 54: Photos of the SAPHIR chamber in 2 measurement mode

4.2.2. Measurement Protocol at the SAPHIR chamber

One chamber experiment was performed per day (8-14, 16-20, 22-26 August 2022). Before each experiment, the chamber was flushed with synthetic air until the concentration of the residual trace gases from former experiments are below the detection limit of the measuring instruments. Then water vapor is added to the purge flow to adjust the humidity in the chamber. Water vapor is needed to generate HONO, as OH precursor, in the chamber (Rohrer et al., 2005). After complete gas mixing, intercomparison measurements at the SAPHIR chamber were started. During the experiments, photochemistry inside the chamber was controlled by its shutter system which allowed the chamber either to be exposed to or shielded from the solar

radiation. Compounds were introduced into the chamber either by injecting a known volume of a gas mixture or by vaporizing a known amount of the liquid chemical in a zero-air flow using a syringe. Daily measurements at the SAPHIR chamber were typically done from 6:00 to 15:00 (UTC). The fans were operated throughout the entire duration of the experiments to ensure well mixing of the air in the chamber.

4.2.3. Instruments coupled to the SAPHIR chamber

Several instruments sampled from the SAPHIR chamber for the measurement of trace gases and meteorological parameters, including PTR-ToF-MS (proton transfer reaction-time-of-flight mass spectrometer), CIMS (Chemical Ionization Mass Spectrometry) monitors for CO, O₃ and NO_x. In addition, to the spectroradiometer and several temperature and pressure probes.

Seven different groups using different instruments sampled from the SAPHIR chamber for radical intercomparison measurements, as shown in Table 17.

Table 17: Different groups involved in the RO_x intercomparison campaign and different instruments used

Institute	Type of instrument
Forschungszentrum Jülich	FAGE
University of Leeds	FAGE
Lille Université	FAGE
Universität Bremen	PERCA
IMT Lille Douai	PERCA
AIOFM Anhui	PERCA
Deutscher Wetterdienst	CIMS

The FAGE technique used by our group (PC2A laboratory at the University of Lille), during this campaign is shown in Figure 55. Three FAGE cells were used during this campaign for the separate measurement of HO_x radicals (OH, HO₂ and HO₂^{*}) radicals using the UL-FAGE setup where the HO₂ FAGE cell is placed downstream the OH cell and peroxy radicals (RO₂ and HO₂^{*}) using a newly implemented setup called UL-RO_x-FAGE.

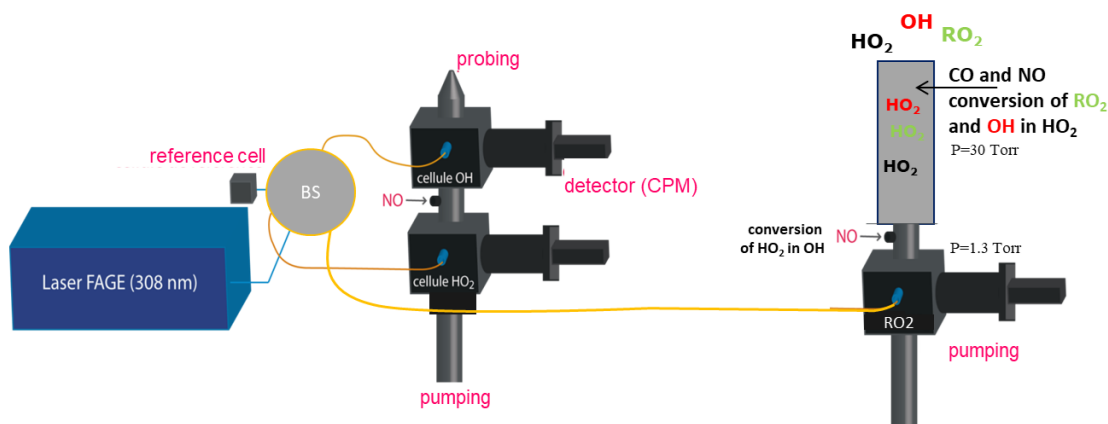


Figure 55 : Scheme of the three UL-FAGE cells (OH, HO₂ and RO₂ cells) used for the measurement of OH, HO₂, HO₂* and RO₂ radicals during the intercomparison campaign at the SAPHIR chamber

In the following sections, only the comparison of measurements of HO_x radicals between the UL-FAGE and FZJ-FAGE and peroxy radicals between UL-RO_x-FAGE and FZJ-RO_x-FAGE will be presented.

4.2.3.1. FAGE instruments for HO_x radical measurements

HO_x radicals were measured during this campaign using the FAGE technique by both the PC2A (UL-FAGE) and Jülich groups (FZJ-FAGE). The UL-FAGE technique and its principle have been detailed in chapter 2 and in previous reports (Ajami, 2018; Amedro, 2012). In Table 18 the main characteristics of both FAGE instruments are summarized. The main difference between the two instruments is the type of the detection cell used: in case of the UL-FAGE, a multi-pass cell is used while the FZJ-FAGE uses a single pass cell. Another difference is the separation of the OH and HO₂ FAGE cells for FZJ-FAGE whereas for the UL-FAGE, the HO₂ cell is downstream of the OH cell and pressure in each cell is around 1.5 Torr, while the FZJ-FAGE the pressure is 2.8 Torr. An OH scavenger (C₃F₆) was added above the OH FZJ-FAGE cell to measure which fraction of the OH LIF signal is coming from spurious OH compared to OH present in the sampling air. Indeed, OH in the sampled air will react with C₃F₆ and if any OH signal is still detected it corresponds to artificial OH generated within the FAGE cell. No OH scavenger was used for the OH UL-FAGE instrument during this campaign. For the UL-FAGE, the signal of OH was corrected for the water quenching.

Table 18 : Characteristics and performance of the UL-FAGE and FZJ-FAGE instruments during the intercomparison campaign

FAGE Cell	Parameter	Value – UL	Value – Jülich
	Cell assembly	HO ₂ cell downstream of OH cell	Separate cells
	Inlet nozzle orifice	0.8 mm	0.4 mm
	Sample flow rate	9.5 L/min	1 L/min
	Pressure	1.5 Torr	2.8 Torr
	Laser beam shape (cell)	Multi-pass (White type)	Round: 8 mm diameter
	Time resolution	40 s	270 s for OH 47 for HO ₂ and HO ₂ [*]
OH	Laser power	3-3.5 mW	35-40 mW
	Accuracy	32 % (due to calibration)	18% (1σ)
	LOD (S/N=2)	$9.6 \times 10^5 \text{ cm}^{-3}$	$0.5 \times 10^6 \text{ cm}^{-3}$
	OH Sensitivity	$4.47 \times 10^{-7} \text{ counts/s/cm}^{-3}/\text{mW}$	$4.36 \times 10^{-7} \text{ C V}^{-1} \text{ s}^{-1}$
HO ₂	Laser power	2-2.5 mW	35-40 mW
	Conversion efficiency	10 % (NO low) 95 % (NO high)	90 %
	Accuracy	32 to 40 % (due to calibration)	18% (1σ)
	LOD (S/N=2)	$6.7 \times 10^7 \text{ cm}^{-3}$ (NO low) $1.1 \times 10^7 \text{ cm}^{-3}$ (NO high)	$1 \times 10^6 \text{ cm}^{-3}$ $5 \times 10^6 \text{ cm}^{-3}$
	HO ₂ Sensitivity	$3.11 \times 10^{-8} \text{ counts/s/cm}^{-3}/\text{mW}$	$2.23 \times 10^{-8} \text{ C V}^{-1} \text{ s}^{-1}$
	HO ₂ [*] Sensitivity	$1.95 \times 10^{-7} \text{ counts/s/cm}^{-3}/\text{mW}$	$1.24 \times 10^{-7} \text{ C V}^{-1} \text{ s}^{-1}$

We have chosen to do a measurement cycle between the HO₂ and HO₂^{*} (HO₂ + some RO₂ from alkenes and some aromatics converted in the detection cell) in the HO₂ cell. Indeed, even if only the HO₂ concentration is needed, we wanted to take the opportunity of the intercomparison to test the HO₂^{*} measurement protocol. Therefore, the HO₂ FAGE cell was used to sequentially measure HO₂ (low NO concentration of $1.24 \times 10^{10} \text{ molecule cm}^{-3}$ added in the detection cell, 0.5 sccm) and HO₂^{*} (high NO concentration of $2.5 \times 10^{11} \text{ molecule cm}^{-3}$ added in the detection cell, 10 sccm). The measurement mode was switched every 10 min. The HO₂ and HO₂^{*} concentrations are determined for each condition from the signal measured at different NO flows, the laser power and the measured calibration factor (details in chapter 2, section 2.5.3).

For the UL-FAGE, the signal of HO₂ was corrected for the water quenching and the NO background was determined from experiment in zero air in the chamber.

For the FZJ-FAGE, the signal of HO₂ was corrected for the NO background ($\sim 1 \times 10^7 \text{ cm}^{-3}$) and for the O₃ interference ($\sim 1.5 \times 10^7 \text{ cm}^{-3}$, for 60 ppbv of O₃ and $\sim 1.2 \%$ absolute water. Even if an NO₃ interference has been identified, it was not considered as the NO₃ concentration has not been measured.

4.2.3.2. FAGE instruments for RO_x radical measurements

Next to the OH and HO₂ FAGE cells, a setup consisting of a conversion flow-tube placed at the top of a FAGE cell (RO_x-FAGE) was used to measure the peroxy radicals. The UL-RO_x-FAGE and its principle have been detailed in chapter 2. A comparison between the UL-RO_x-FAGE and FZJ-RO_x-FAGE setup have been presented in Table 20.

Table 19 : Experimental conditions of the Julich RO_x-FAGE (Fuchs et al., 2008) and UL-RO_x-FAGE instrument (this work)

	Parameter	Value – Julich	Value – UL
Conversion flow-tube	Inlet nozzle orifice	1.0 mm	0.635 mm
	Sample flow rate	7 L/min	3 L/min
	Length × diameter	83 × 6.6 cm	47.9 × 6 cm
	Pressure	18.75 Torr	28 Torr
	Flow residence time	0.62 s	0.88 s
	Reagent mixing ratio	0.7 ppmv NO, 0.17% CO	1.82 ppmv NO, 0.67% CO
Fluorescence cell	Transfer nozzle orifice	4.0 mm	3.0 mm
	Sample flow rate	3.5 L/min	8 L/min
	Pressure	2.25 Torr	1.3 Torr
	Laser power	2-2.5 mW	35-40 mW
	Accuracy	32 % (due to calibration)	18% (1σ)
	LOD (S/N = 2)	$5.7 \times 10^7 \text{ cm}^{-3}$	$2 \times 10^7 \text{ cm}^{-3}$
	Time Resolution	40 s	47 s
	RO ₂ sensitivity	$6.81 \times 10^{-8} \text{ counts/s/cm}^{-3}/\text{mW}$	$2.23 \times 10^{-8} \text{ C V}^{-1} \text{ s}^{-1}$

A measurement cycle between the RO_x and HO_x mode in the RO_x cell was done. As for the HO₂ cell, it was an opportunity to test the HO_x mode and its meaning.

As shown in Figure 56, the HO₂ radicals are measured in the HO₂ cell simultaneously with the RO_x radicals (RO₂ + HO₂^{*}) during the RO_x mode (with NO flow in the conversion tube,) in the RO_x cell. The concentration of RO₂ radicals is obtained as the difference between both measurements by subtracting the contribution of HO₂ from the sum of HO₂ + RO₂. After 10 min, the RO_x cell measurements is changed into the HO_x mode (no NO flow in the RO_x conversion tube) where HO₂^{*} radicals in the RO_x cell are measured simultaneously with the HO₂^{*} radicals in the HO₂ cell. Measurements in the RO_x and HO_x mode are both at high NO

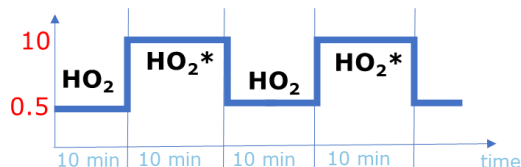
injected in the FAGE cell coupled to the RO_x tube in order to obtain a sensitivity level requested for the ambient measurements.

This step was done to compare the HO₂* measured in the different FAGE cells (HO₂ and RO_x), to check if the measurements of the UL-RO_x-FAGE instrument were compatible with the UL-FAGE measurements.

HO₂ cell:

NO injected in HO₂ FAGE cell

(sccm)



RO_x cell: NO injected in RO_x FAGE cell (10 sccm)

NO injected in conversion tube

(sccm)

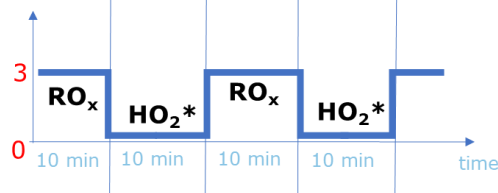


Figure 56 : Measurement cycle between HO₂ and HO₂* in the HO₂ FAGE cell and between HO₂* and RO₂ radicals in the RO_x FAGE cell

The UL-FAGE instrument and the calibration processes were described in chapter 2. The data treatment includes the correction of water quenching.

For the FZJ-FAGE, the signal of RO₂ was corrected for the NO background ($\sim 3 \times 10^7 \text{ cm}^{-3}$) and for the O₃ interference ($\sim 1 \times 10^7 \text{ cm}^{-3}$, for 60 ppbv of O₃ and $\sim 1.2 \%$ absolute water. Even if an NO₃ interference has been identified, it was not considered as the NO₃ concentration has not been measured.

4.3. Experiments performed at the SAPHIR chamber

During the campaign period from 1st to 31st of August, sixteen different experiments (Table 20) were performed in the light (chamber shutter open) and in the dark (chamber shutter closed). Different chemical system were studied in each experiment in order to different identify potential interferences. In order to analyse the data, we classified the experiments into five groups depending on the chemistry taking place in the chamber:

- Simple chemistry
- Nighttime chemistry
- BVOC chemistry
- Anthropogenic chemistry
- Ambient chemistry

The experiments that will be discussed in detail in the following sub-sections are shown in green in the following table.

Table 20: List of the different experiments performed during the intercomparison campaign

Date	Chamber roof	Gas injected	Experiment	Group of experiments
8/8/2022	Open	CO/CH ₄	CO/CH ₄ oxidation by OH	Simple chemistry
9/8/2022	Open	Isoprene	Isoprene OH oxidation	BVOC chemistry
10/8/2022	Open	Isoprene/O ₃	Isoprene OH oxidation: O ₃ change	BVOC chemistry
11/8/2022	Open	Isoprene/O ₃ /NO	Isoprene OH oxidation : NO _x change	BVOC chemistry
12/8/2022	Open	Isopentane/n-hexane/NO	1-pentane and n-hexane photooxidation	Anthropogenic chemistry
13/8/2022	Closed/Open	α-pinene/O ₃ /NO	α-pinene ozonolysis dark photooxidation /ozonolysis	BVOC chemistry
14/8/2022	Open	Mesitylene	Mesitylene photooxidation (high NO)	Anthropogenic chemistry
16/8/2022	Open	β-pinene	β-pinene photooxidation	BVOC chemistry
17/8/2022	Closed	Isoprene/O ₃ /NO ₂	Isoprene NO ₃ oxidation (dry)	BVOC chemistry
19/8/2022	Closed	Hexene/O ₃	Hexene ozonolysis: humidity change	Anthropogenic chemistry
20/8/2022	Open	CO/CH ₄ /NO	CO/CH ₄ : humidity change, NO change	Simple chemistry
22/8/2022	Closed	β-pinene/O ₃ /NO ₂	β-pinene NO ₃ oxidation	BVOC chemistry
23/8/2022	Open	-	Ambient air	Ambient chemistry

24/8/2022	Open	MVK/O ₃	MVK oxidation	BVOC chemistry
25/8/2022	Open	Cl ₂ /Isoprene	Cl chemistry with isoprene	BVOC chemistry
26/8/2022	Closed/open	Isoprene/O ₃ /TME	Isoprene, TME ozonolysis + photooxidation	BVOC chemistry

The comparison between the FAGE instrument from the Lille group and the Jülich group is discussed for each experiment and a general conclusion summarizing all results is presented to provide an overall picture of the comparison exercise. The scatter plots for each experiment was done using the Jülich time base as the reference and interpolation of our data.

4.3.1. Simple chemistry: CO and CH₄ oxidation by OH

Methane (CH₄) is the second most important greenhouse gas. It is emitted from wetlands, biomass burning and anthropogenic activities (Rigby et al., 2008). The predominant sink of atmospheric CH₄ is the reaction with OH radical leading to the formation of CH₃O₂ radicals which serves as an oxidant for the NO and NO₂ recycling (Golomb & Fay, 1989).

CO is one of the main sink of OH radicals in the atmosphere (Ravishankara & Thompson, 1983; Atkinson, 1976). This reaction form HO₂ radicals as shown in chapter 1 (R 7 and R 8).

Beside the significance of the reaction of methane/CO with OH for atmospheric chemistry, this experiment was chosen to investigate the response of the different instruments to two of the simplest and most abundant peroxy radicals in the atmosphere, HO₂ and CH₃O₂. The CH₄ and CO with OH experiment was carried out on two days in different conditions:

- The first experiment was done on August 8 but some problems occurred and the CO concentration was much higher than planned.
- It was repeated on August 20 with addition of NO and humidity increase to check their impact on this reaction.

4.3.1.1. CO and CH₄ oxidation by OH experiment done on August 8

4.3.1.1.1. Experimental Conditions

During the first experiment, the chamber was humidified to 60 % RH before the chamber opening. The chamber shutters were opened at 8:07 h, OH radicals were generated by the photolysis of HONO. CO (around 12 ppmv) was injected into the chamber at 9:40 h. Then, CH₄ was introduced into the chamber through two consecutive injections at 13:30 h and at 13:35 h to reach 25 ppm. The shutter system was closed after 15:15 h. To observe the evolution of the radical profiles in the absence of sunlight, the UL-FAGE measurements were stopped 60 min later. The injection sequence of the trace gases during this experiment is shown on Figure 57 and the OH, HO₂, HO₂^{*} and RO₂ radical measurements of both Lille and Jülich instruments. In addition, the measured NO mixing ratio (ppb), the O₃ (ppb) produced, the H₂O (%), and the injected CO and CH₄ (ppm) are plotted.

4.3.1.1.2. Experimental Results

As shown in Figure 57, a rapid increase in the OH concentration reaching about 8×10^6 molecule cm⁻³ is observed as the chamber shutters are opened and HONO photolysis started producing OH and additional NO (0.6 ppb) in the chamber. After the CO addition, the concentration of OH decreased sharply down to 2×10^6 molecule cm⁻³, while the HO₂ concentration was doubled reaching around 6×10^8 molecule cm⁻³ with no change of the RO₂ concentration. This is expected because only HO₂ is formed from the reaction of OH with CO. The unexpected decrease in the HO₂ and RO₂ concentration at 11:15 h is probably due to the flushing of 250 m³/h because of the release of high CO concentrations in the chamber from one of the PERCA instruments during this experiment. After the two CH₄ injections, the HO₂ and RO₂ slightly increase to reach 6×10^8 molecule cm⁻³ and 8×10^8 molecule cm⁻³, respectively, where OH radicals should react with CH₄ leading to the formation of CH₃O₂ radicals. The produced CH₃O₂ radicals reacts rapidly with NO to form HO₂ radicals which in turn reacts with NO and O₃ to reform OH. No production of HO₂^{*} radicals is expected during this experiment.

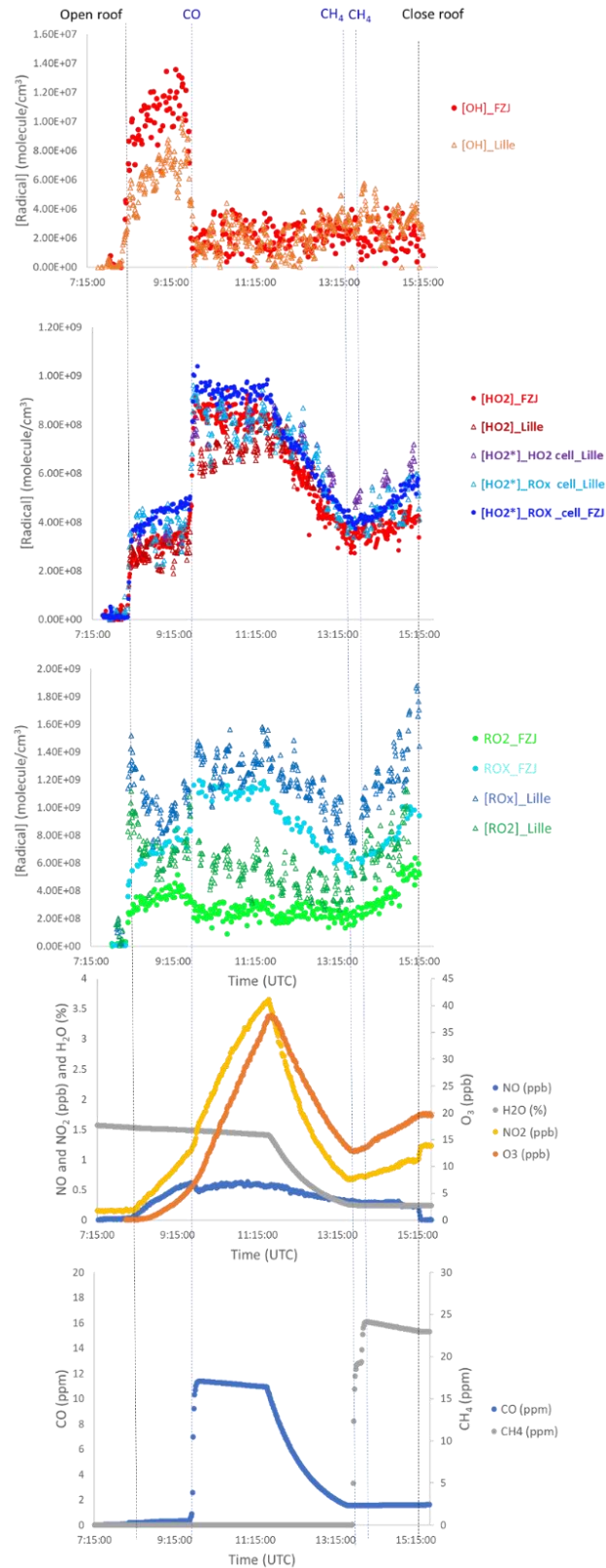


Figure 57: Measurement profiles for August 8 experiment, from bottom to top:
 CO (ppm) and CH₄ (ppm)
 NO (ppb), O₃ (ppb) and H₂O (%) concentration
 RO_x and RO₂ concentrations (molecule/cm³) measured by both instruments
 HO₂ and HO₂^{*} concentrations (molecule/cm³) measured by both instruments
 OH concentrations (molecule/cm³) measured by both instruments

4.3.1.1.3. Comparison between Lille and Jülich measurements

As the shutter system is opened the UL-FAGE measured systematically 30 % higher OH concentration than the FZJ-FAGE. After the first CO injection, the OH and HO₂ concentrations measured by both instruments were identical. The HO₂^{*} measured by the UL-FAGE instrument was the same in both FAGE cells (RO_x and HO₂) and was also in good agreement with the HO₂^{*} measured by the FZJ-FAGE. In addition, the HO₂^{*} concentration is close to the HO₂ concentration. This is what is expected because only HO₂ is produced but even so, we observe a slightly higher HO₂^{*} than HO₂, maybe due to some impurities in the chamber.

Differences are observed in the response of instruments measuring RO₂ radicals: as the shutter system is opened, the UL-RO_x-FAGE observed a faster and higher increase than the FZJ-RO_x-FAGE, then a slight decrease in the RO₂ concentration, while a slight increase is observed by the FZJ-RO_x-FAGE. Even though this behavior, at the opening of the shutter, before any injection, was observed for other experiments, but no clear reason can explain it except that the UL-RO_x-FAGE is possibly sensitive to some impurities present in the chamber. After around 10 mins of the chamber opening, both instruments measured the same range of RO₂ concentration within their respective uncertainties. After the CH₄ injection we observe a more pronounced increase in the RO₂ concentration measured by the UL-RO_x-FAGE than by the FZJ-RO_x-FAGE.

The scatter plots (Figure 58) shows a good linearity for HO₂ and HO₂^{*} whereas it is more scattered for OH. We can observe a low slope and a more scattered trend for OH, probably due to the higher concentration observed by the FZJ instrument before the injections and a low concentration level, close to the LOD after. This disagreement, which is still within the respective uncertainties of the instruments is higher than during the intercomparison done by [Amedro \(2012\)](#), who observed a good agreement between the two instruments after the opening of the chamber during such simple experiment.

The slopes for HO₂ and HO₂^{*} are in the range 0.7-0.9, within the uncertainties of the instruments with a good r². The agreement between both instruments for the HO₂ measurements was also observed during the measurements of [Amedro \(2012\)](#) for similar type of experiments.

The results on RO₂ are affected by the strong disagreement at the opening of the roof. Removing this period (8:00 – 9:30 h), the slope obtained is 1.3 (r² = 0.5) with an intercept equal to 2 × 10⁸ molecule cm⁻³.

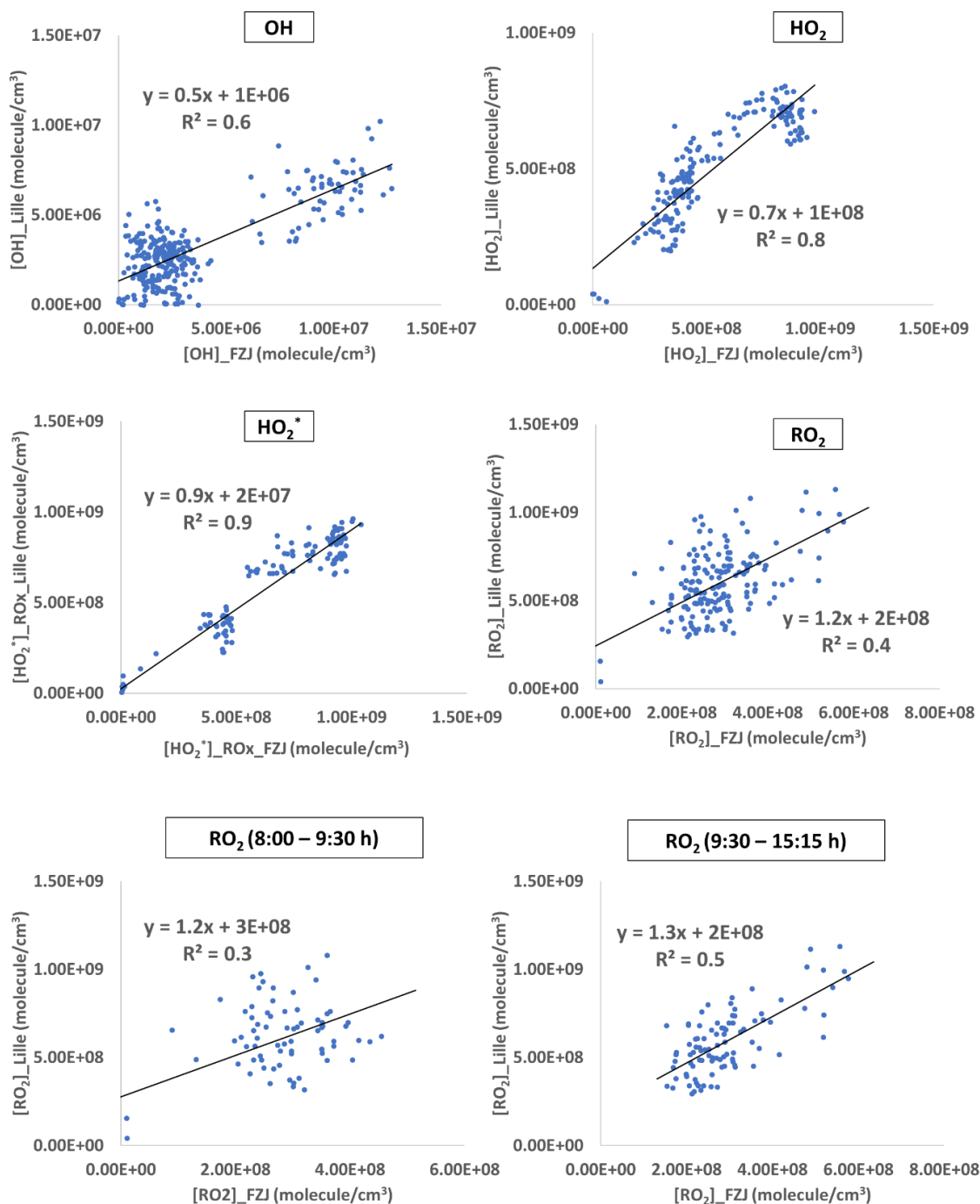


Figure 58: Scatter plot between Lille and Jülich OH, HO₂, HO₂^{*} and RO₂ measurements for August 8 experiment

4.3.1.2. CO and CH₄ oxidation by OH experiment done on August 20

A second experiment for studying CO/CH₄ oxidation by OH was performed on August 20. The aim of this experiment is to confirm the results, but with lower CO concentration and without the contamination problem, of the previous experiment and test the influence of H₂O and NO on the chemistry.

4.3.1.2.1. Experimental conditions

On 20th of August, the chamber was humidified before chamber opening and reached $[\text{H}_2\text{O}] = 0.2\%$ (RH = 10 %). The chamber shutters opened at 6:36 h. First, 1 ppmv of CO was injected at 7:30 h followed by an injection of CH₄ at a mixing ratio of 70 ppmv at 9:03 h. At 13:04, 2 ppbv of NO was injected into the chamber where the NO₂ concentration increased up to approximately 6 ppbv. The chamber shutter system closed at 15:00 h. The injection sequence of the reactants inside the chamber is reported on Figure 59.

4.3.1.2.2. Experimental results

OH, HO₂, HO₂^{*} and RO₂ radical measurements of Lille and Jülich systems are shown in Figure 59 with the measured mixing ratio of NO (ppb), NO₂ (ppb), O₃ (ppb), H₂O (%), CO (ppm) and CH₄ (ppm).

For Lille measurements, as the chamber shutters open, the OH, HO₂ and RO₂ radical concentrations slightly increased. This small increase in the radical concentration compared to the previous CO/CH₄ experiment (August 8) might be due to the low humidity level in the chamber ($[\text{H}_2\text{O}] = 0.2\%$) that induces low concentration of OH precursor (HONO) in the chamber. HO₂ concentration increases as CO is injected into the chamber, followed by a continuous increase as the CH₄ is injected to reach 3×10^8 molecule cm⁻³. As the humidity level was increased up to an RH of 40 % ($[\text{H}_2\text{O}] = 1.5\%$), the HO₂ concentration increased to reach 6×10^8 molecule cm⁻³. We can make the same observation for RO₂ radical concentration that increased up to 6×10^8 molecule cm⁻³. When NO was added, both HO₂ and RO₂ radical concentrations decreased due to their reaction with NO, and OH concentration increased due to the recycling, reaching 6×10^6 molecule cm⁻³. Same than in the previous experiment, no production of HO₂^{*} radicals is expected, but we observe a slightly higher concentration of HO₂^{*} (measured in RO_x cell) than the HO₂ radical, maybe due to some RO₂ from the impurities present in the chamber.

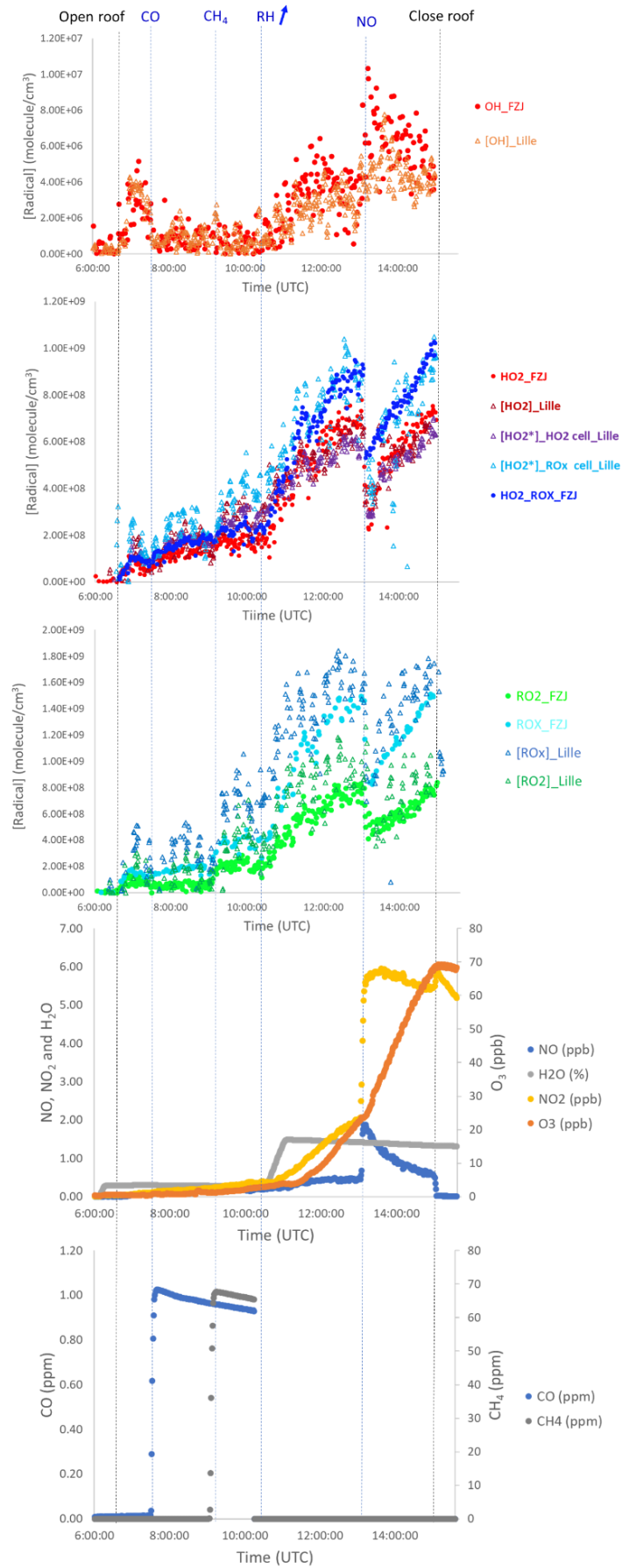


Figure 59: Measurement profiles for August 20 experiment, caption: same as Figure 57

4.3.1.2.3. Comparison between Lille and Jülich measurements

A good agreement between the OH, HO₂, HO₂^{*} and RO₂ radical measurements of both instruments was found in the scatter plots shown in Figure 60. The slopes for OH, HO₂, HO₂^{*} and RO₂ concentration are respectively of 0.5, 0.8, 0.9 and 1.1, within the uncertainties of the instruments. The r² is in the range of 0.8 for HO₂, HO₂^{*} and RO₂ and we can observe a more scattered trend for OH, probably due to the low concentration level, close to the LOD.

From the two CO/CH₄ oxidation by OH experiments, the good agreement between the two instruments tends to validate the measurements done by the UL-FAGE under simple conditions with the assumptions taken for the concentration determination. More complex experiments have been performed in the SAPHIR chamber to identify if more complex chemistry could highlight different behaviors.

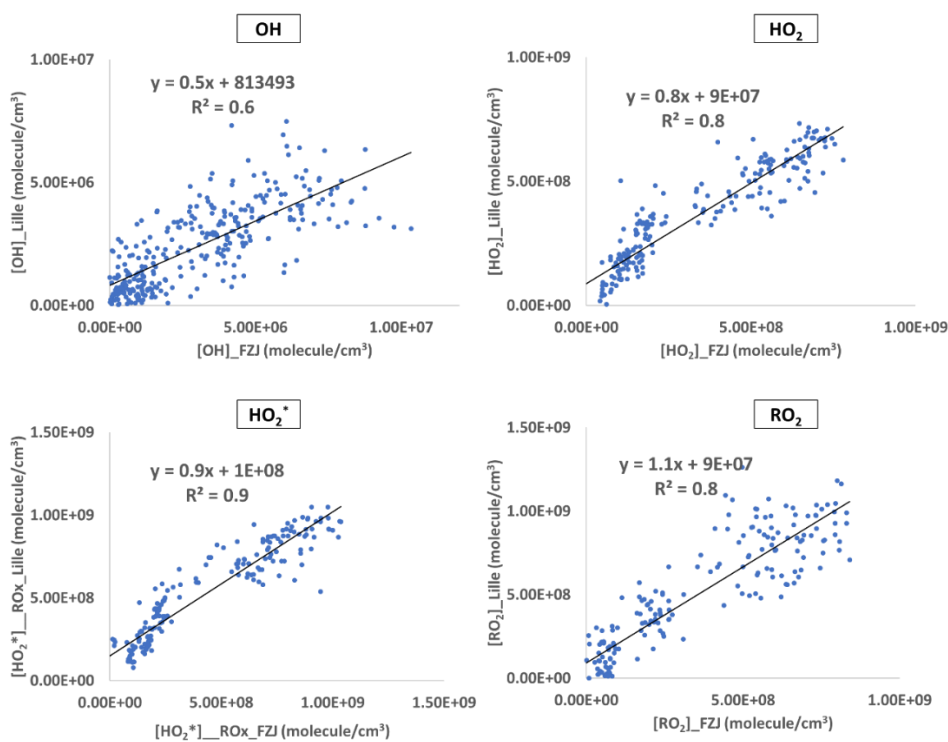


Figure 60: Scatter plot between Lille and Jülich OH, HO₂, HO₂^{*} and RO₂ measurements for August 20 experiment

Comparing the RO_x measurements done by Lille and Jülich FAGE instruments to the measurements of other instruments (graph in Annex), such as PERCA-IMT and FAGE-Leeds; a similar trend and concentration level for the four measurements can be observed for the CO/CH₄ oxidation by OH experiment.

4.3.2. Night-time chemistry

A second group of experiments under dark conditions was designed to investigate the the night-time chemistry. As described in chapter 1, the important initiators of the night-time chemistry are O₃ and NO₃. Ozonolysis experiments of alkenes were performed during the

intercomparison campaign, such as the ozonolysis of trans-2-hexene done on August 19. In addition, the oxidation chemistry of β -pinene with NO_3 was also investigated on August 22. The results of both experiments are discussed in the following.

4.3.2.1. *Trans-2-hexene ozonolysis done on August 19*

The ozonolysis reactions of alkenes, described in Chapter 1, section 1.1.2.2, generates ozonide, which decompose into a carbonyl compound and a Criegee intermediate. This excited Criegee biradical can undergo two paths: it can be decomposed into radicals and stable products or become collisionally stabilized forming a stabilized Criegee intermediate. This stabilized form then gradually decomposes into OH or reacts with water-vapor. This type of chemistry was studied during the intercomparison campaign with the ozonolysis of trans-2-hexene.

4.3.2.1.1. *Experimental conditions*

This experiment was conducted with the chamber shutter system closed. The experiment started at 6:00 h prior the injection of reactants to probe the background reactivity inside the chamber (zero air and background trace gases). The injection sequence initially started with 10 ppbv of O_3 at 6:30 h followed by 1 ppbv of trans-2-hexene at 6:35 h to initiate the ozonolysis reaction. Further injections of ozone and slightly later injection trans-2-hexene were performed in seven steps approximately each 60 or 120 min throughout the experiment. Ozone concentration was increased (from 10 to 45 ppbv). The chamber was humidified in 3 steps in between these injections. The injection time sequence of the reactants into the chamber is reported on Figure 61.

4.3.2.1.2. *Experimental results*

OH, HO_2 , HO_2^* and RO_2 radical measured by both instruments are shown in Figure 61, with the measured NO mixing ratio (ppb), O_3 (ppb) and the H_2O (%), and hexene for this experiment.

After the first injection of O_3 and trans-2-hexene, both instruments quickly responded showing an increase in the radical concentrations. The concentration of OH, HO_2 and RO_2 measured by Lille instruments reached around 1×10^6 , 1×10^8 , 3×10^8 molecule cm^{-3} , respectively. In addition, each time O_3 and trans-2-hexene was reinjected in the chamber, an increase in the HO_2 , HO_2^* and RO_2 concentration was observed by both instruments. The results do not show any effect of the H_2O variation on the radical concentration; therefore, the instruments do not suffer from any significant artifacts due to H_2O variation.

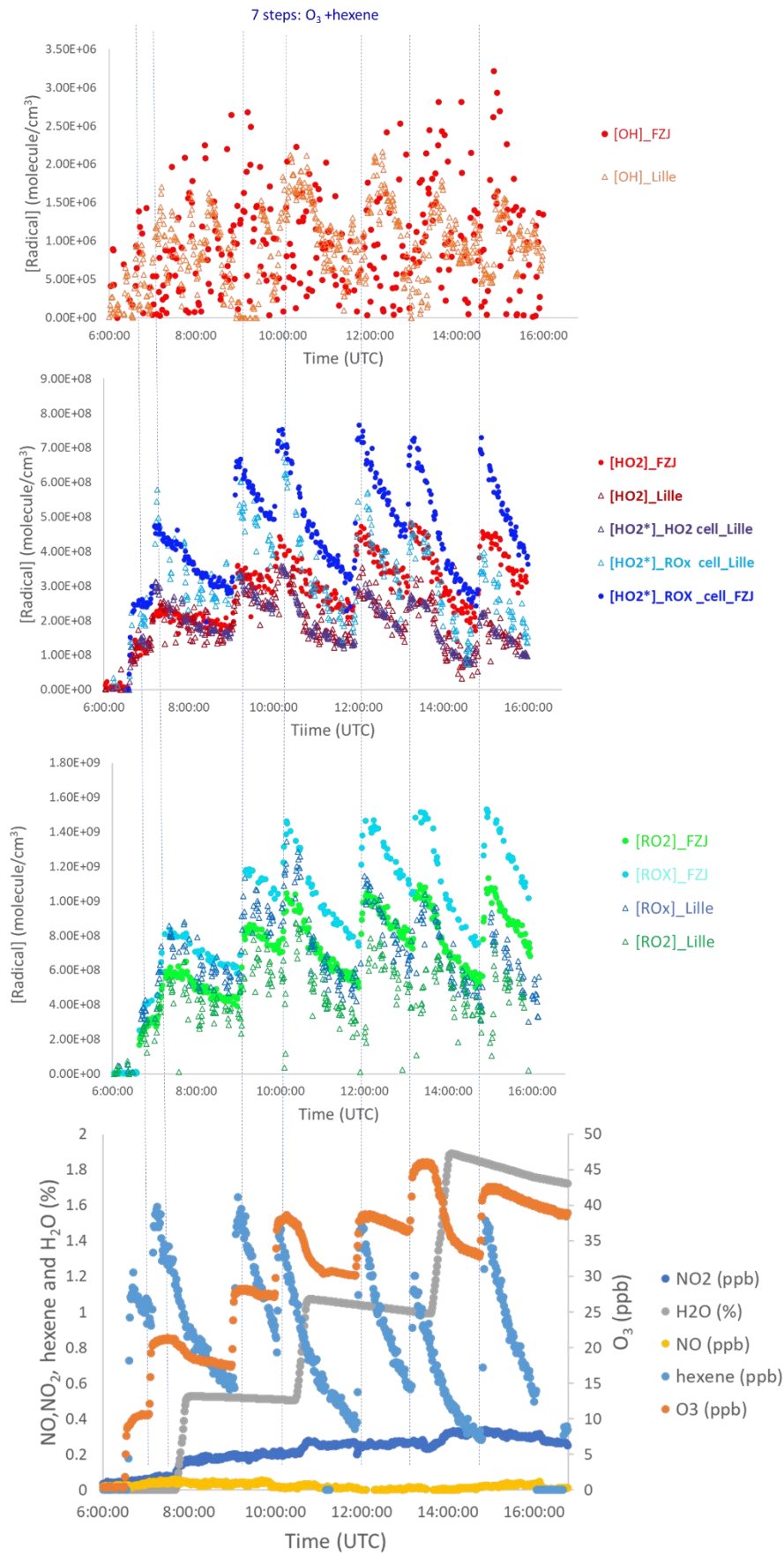


Figure 61: Measurement profiles for August 19 experiment, caption: same as Figure 57

4.3.2.1.3. Comparison between Lille and Jülich measurements

During this experiment, both instruments measured the same HO₂ and RO₂ radical concentrations within their respective uncertainties until 10:00 h. After the injection and the peak at 10:00, we observe a faster decrease in the radical concentration measured by the Lille instrument without clear reason. The dynamic observed by the instruments is similar but the Lille instrument concentrations stay lower. The scatter plots of Lille vs Jülich measurements (Figure 62) give a slope of 0.6 ($r^2 = 0.5$) and an intercept of 3×10^7 molecule cm⁻³ for HO₂ concentration and a slope of 0.6 ($r^2 = 0.7$) and an intercept equal to 6×10^7 molecule cm⁻³ for RO₂. Concerning the OH measurements, the FZJ-FAGE seems to have problems during this experiment where a scattered profile was obtained.

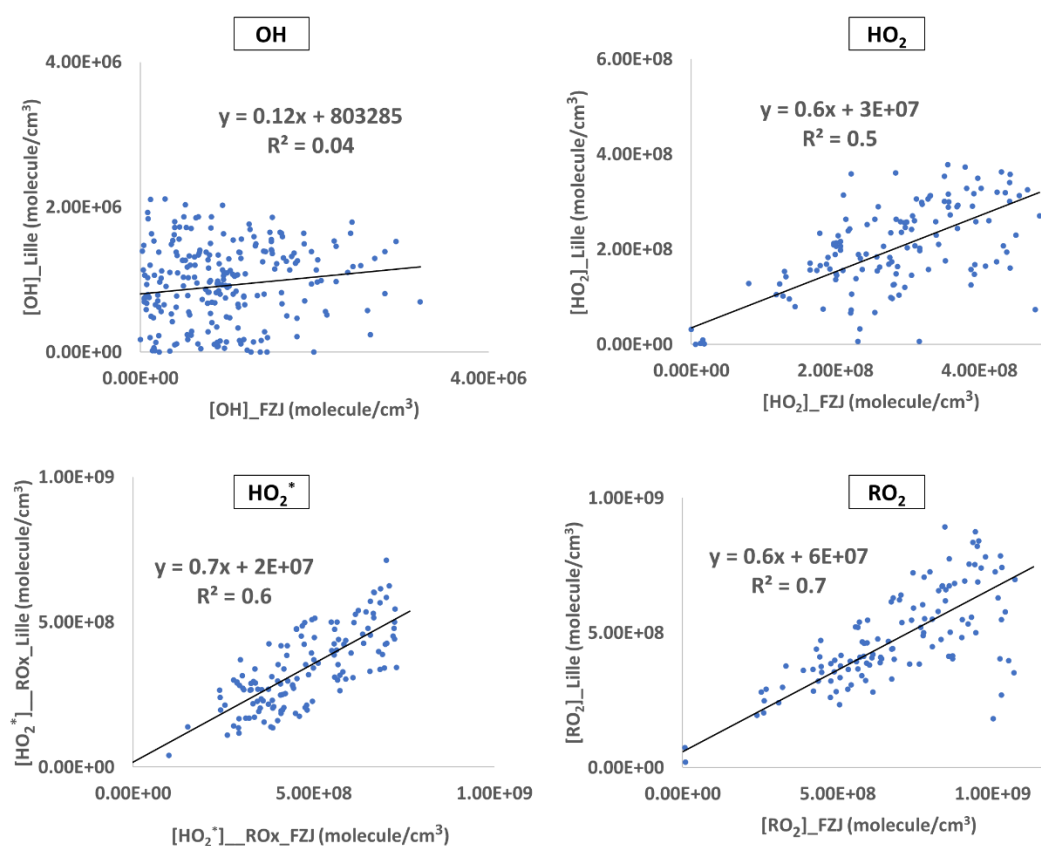


Figure 62: Scatter plot between Lille and Jülich OH, HO₂, HO₂^{*} and RO₂ measurements for August 19 experiment

4.3.2.2. *β -pinene NO₃ oxidation experiment done on August 22*

The reaction of NO₃ with alkenes is another important nighttime source of peroxy radicals and contributes to the entire degradation of alkenes in the dark (Geyer et al., 2003; Moo et al., 2024). A second experiment performed in the dark was done on August 22 using β -pinene.

4.3.2.2.1. Experimental conditions

Similarly to the ozonolysis of trans-2-hexene experiment, the oxidation chemistry of β -pinene with NO₃ was investigated under dark conditions with the chamber shutter system closed. During this experiment, the O₃ was injected stepwise 3 times with a concentration of 50 ppb at 6:00 h, 30 ppb at 7:26 h and 20 ppb at 11:05 h. Every step was followed by a NO₂ injection (around 3 ppbv each time) with an additional NO₂ injection at 9:24 h. β -pinene injection of 2, 1, and 0.8 ppbv were injected into the chamber at 7:00 h, 10:31 h and 12:37 h, respectively. The chamber shutter system was opened at 13:28 h and closed at 15:31 h. The time sequence of the additions of all the compounds is shown in Figure 63. Some technical problems on the RO_x cell, in particular with the sequencer to manage the opening of the valves make the results on the RO_x-FAGE to take with precaution for that day.

4.3.2.2.2. Experimental results

During this experiment, as O₃ and NO₂ is injected into the chamber and NO₃ radicals are produced, a slight increase in the concentration of the RO₂ radicals is observed which may be obtained from the reaction of NO₃ with some impurities on the chamber walls. For Lille measurements, the concentration of HO₂ and RO₂ increases to 2×10^8 molecule.cm⁻³ and 4×10^8 molecule.cm⁻³, respectively. After the first injection of β -pinene took place, the radical concentration slightly decreased until the 2nd injection of O₃ and NO₂ where we observe an increase in the radical concentrations. Same behavior is observed after each injection step of the reactants. When the chamber shutter system was opened, the OH concentration increased up to 5×10^6 molecule.cm⁻³ with HO₂ concentration decreasing from 3×10^8 molecule cm⁻³ to 1.5×10^8 molecule.cm⁻³ and RO₂ concentration from 4×10^8 molecule.cm⁻³ to 2×10^8 molecule.cm⁻³. This decrease is due to the photolysis of NO₃ thus limiting the HO₂ and RO₂ production. The HO₂^{*} measured in the UL-RO_x-FAGE is significantly higher than HO₂ indicating that the RO₂ radicals produced from this chemistry in the chamber can be detected by the RO_x FAGE cells in the HO_x mode.

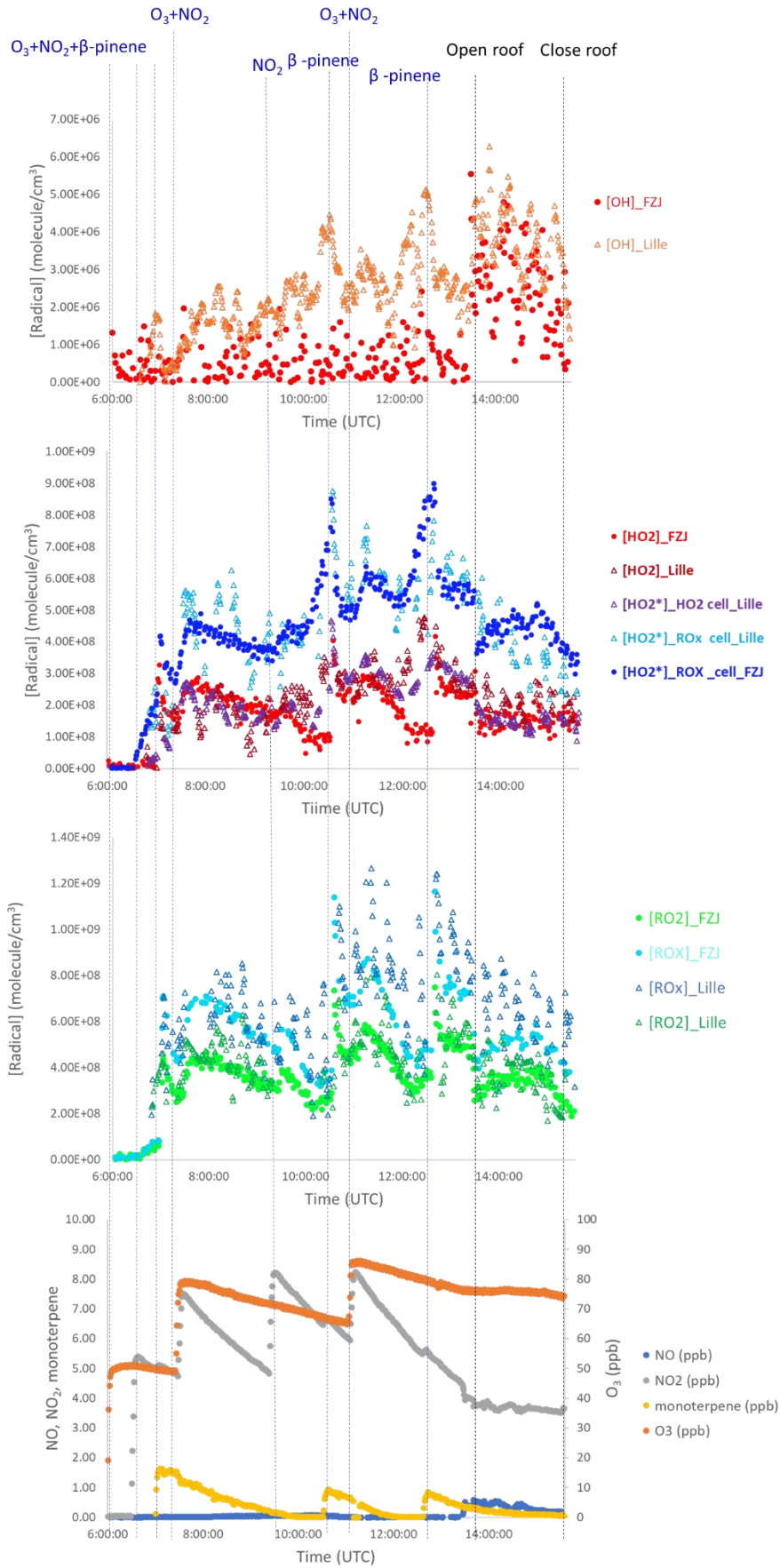


Figure 63: Measurement profiles for August 22 experiment, caption: same as Figure 57

4.3.2.2.3. Comparison between Lille and Jülich measurements

During the dark period, the OH concentration measured by the UL-FAGE was systematically higher than the one measured by the FZJ-FAGE which was close the limit of detection. These measurements suggest that these discrepancies can be due to an interference in the UL-FAGE instrument associated with the NO₃ radical chemistry and the products. Fuchs et al. (Fuchs et al., 2016) reported this kind of interference in their LIF-FAGE, although the exact mechanism of the interference remains unknown. The agreement between the two instruments for OH measurements improved after opening the chamber roof highlighting an interference linked to the dark chemistry. For HO₂, if the same behavior is observed at the beginning, we see a change after the extra addition of NO₂, where the concentration measured by the FZJ-FAGE decreases and not the one measured by the UL-FAGE. The same phenomenon was observed before 13:00 h and explains the bad correlation. On the contrary, both instruments measured the same, HO₂* (RO_x cell) and RO₂ concentration within their respective uncertainties. The good agreement between measurements of both instruments can also be seen in the correlation plot (Figure 64) with a slope close to 1 ($r^2 = 0.7$) and an intercept 1.0×10^7 molecule.cm⁻³ for HO₂* and 1.5×10^7 molecule.cm⁻³ for RO₂.

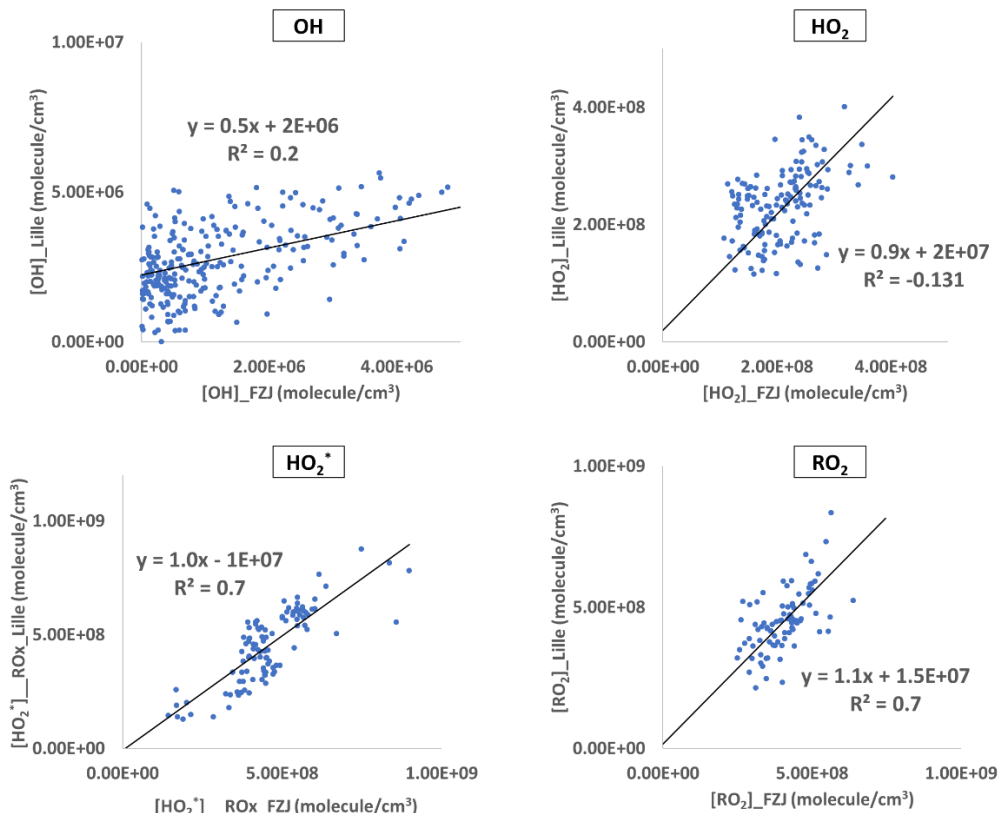


Figure 64: Scatter plot between Lille and Jülich OH, HO₂, HO₂* and RO₂ measurements for August 22 experiment

4.3.3. BVOCs oxidation by OH

Terrestrial vegetation is by far a dominant source of biogenic VOCs (BVOCs) with a global total flux of about 1000 Tg (Guenther et al., 2012). Some of these emitted BVOCs, such as isoprene (C_5H_8), which comprises about half of the total global BVOCs (Guenther, 1995), and others such as monoterpenes (like pinenes or limonene) and sesquiterpenes (Caryophyllene) (Atkinson & Arey, 2003; Sindelarova et al., 2014), have a significant influence on global and local atmospheric chemistry. The role of these BVOCs in the atmospheric chemistry is important because they react rapidly with OH and ozone, it is why their atmospheric lifetime is short, ranging from minutes to hours. They have a dominant role among the OC species in ozone formation and are possibly a source of OH. Their oxidation leads to the formation of different, relatively stable compounds which are transported and thus impacting the tropospheric chemistry on wider scales. These oxidation products can also lead to the formation of secondary organic aerosols (SOA) (Holzinger et al., 2005).

Thus, a third group of experiments at the SAPHIR chamber was designed to investigate the complicated chemistry of BVOCs with OH under different controlled conditions. On the second day of the campaign, August 9, we studied the isoprene oxidation by OH.

4.3.3.1. *Experimental conditions*

During this experiment, the chamber roof was opened at 7:30 h followed by 4 injections of isoprene (around 3.5 ppbv), at 9:01, 11:00, 13:01 and 13:23 h. The injection pattern of isoprene in the chamber is reported on Figure 65. During this experiment one of the fans was switched off for 30 mins at 12:15 and 13:51 h to evaluate the influence of it on the CIMS instrument, which was located close to it. The chamber roof was closed at 15:22 h.

4.3.3.2. *Experimental results*

As the chamber shutter system is opened and before any injections the radical concentrations measured by the Lille instruments increased rapidly to reach 6×10^6 molecule cm^{-3} for OH, 3×10^8 molecule cm^{-3} for HO_2 and 5×10^8 molecule cm^{-3} for RO_2 , respectively, consistent with the photolysis of precursors such as HONO. After the first isoprene injection, the OH concentration decreases rapidly to 3×10^6 molecule cm^{-3} and then starts to slightly increase to reach a concentration of approximately 6×10^6 molecule cm^{-3} after two hours. This OH behavior was observed after each isoprene injection. In the case of HO_2 and RO_2 an increase in their concentration is observed after each isoprene injection.

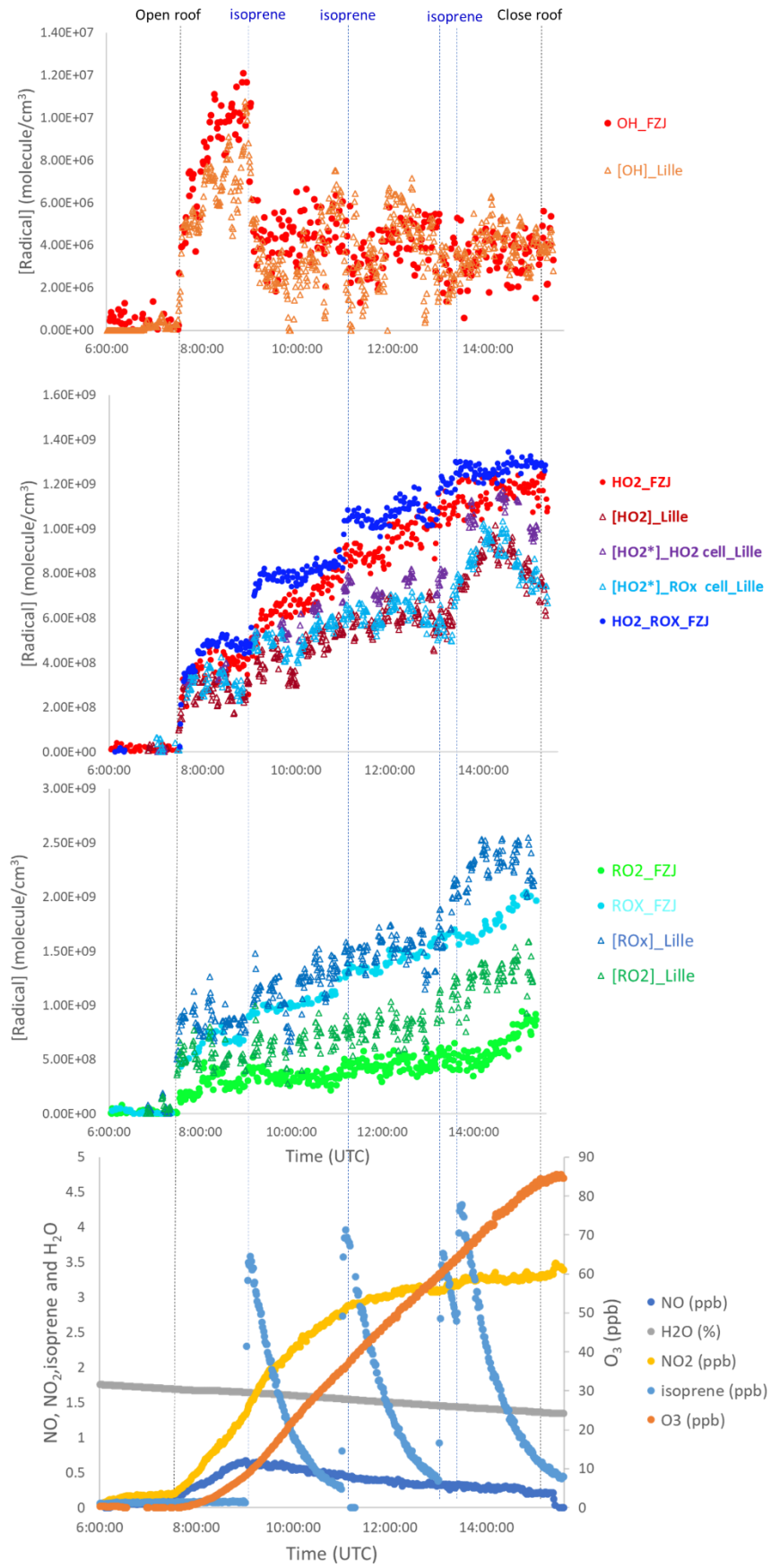


Figure 65: Measurement profiles for August 9 experiment, caption: same as Figure 57

4.3.3.3. Comparison between Lille and Jülich measurements

For OH, a lower concentration was measured by the UL-FAGE at the opening of the shutter, similarly to what has been observed the 8th (CO/CH₄ experiment) and good agreement was observed between the two instruments after the first injection of isoprene giving a slope equal to 0.9 ($r^2 = 0.7$). For HO₂, after the 2nd isoprene injection we observed the same trend between the UL-FAGE and FZJ-FAGE but a disagreement concerning the level with a lower concentration measured by the UL-FAGE. The difference between the HO₂ measurements decreased toward the end of the measurement. Similar behavior is observed for HO₂^{*} measurements with a measurement lower by about 40 %. This disagreement between the instruments can be shown in the correlation plot for HO₂ and HO₂^{*} with a slope of 0.6 and insignificant intercepts. The correlation coefficients obtained were approximately $r^2 = 0.9$. The HO₂^{*} measured by UL-RO_x-FAGE and FZJ-RO_x-FAGE are equal to the HO₂ concentration measured for each instrument. For RO₂, a slope of approximately 1.4 ($r^2 = 0.7$) and an intercept of 2×10^8 molecule cm⁻³. This might hide some differences as the HO₂ subtracted was lower for the UL-FAGE.

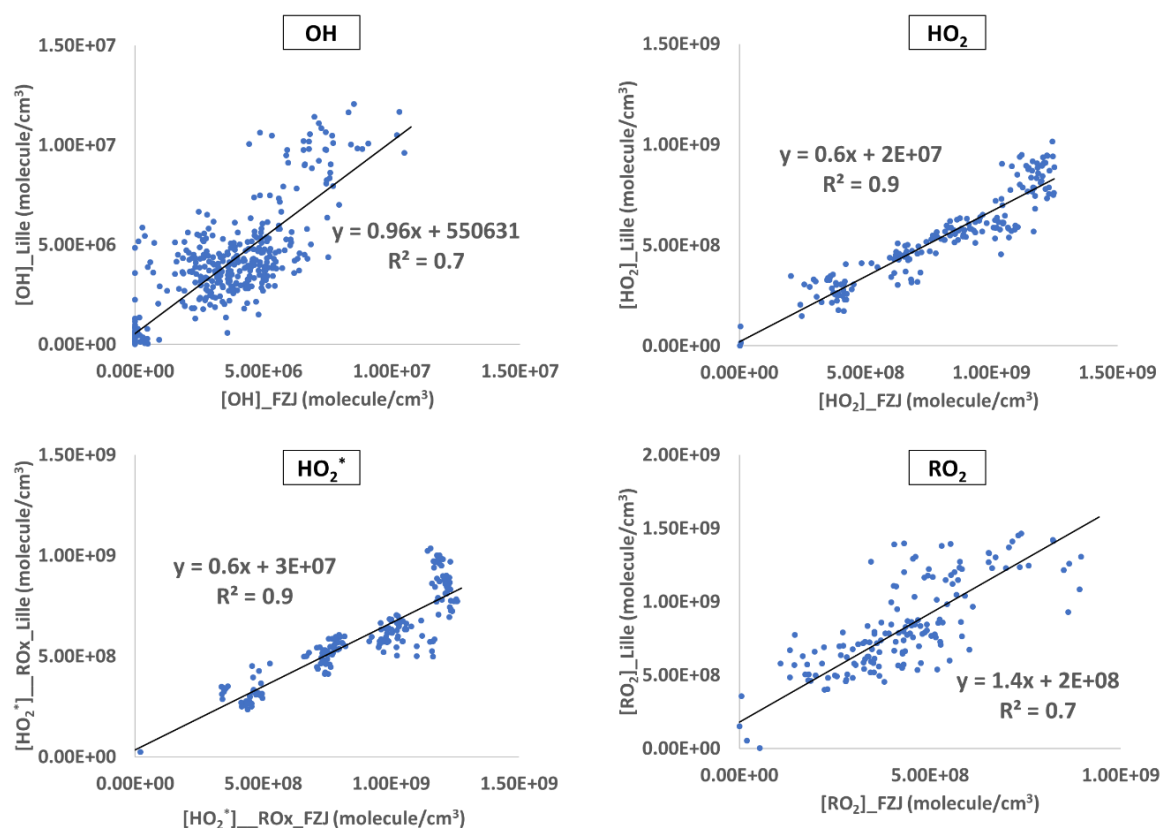


Figure 66: Scatter plot between Lille and Jülich OH, HO₂, HO₂^{*} and RO₂ measurements for August 9 experiment

4.3.4. Anthropogenic chemistry

Another set of experiments is linked to the photooxidation of anthropogenic species in polluted air (high NO levels). One experiment performed during the intercomparison campaign was the photooxidation of isopentane and n-hexane with the chamber roof open on August 12.

4.3.4.1. *Experimental conditions*

The experiment started at 6:00 h prior the injection of any reactant to probe the background reactivity inside the chamber under dark conditions. After one hour, the chamber roof was opened. The injection procedure started with 9 ppbv of NO (7:53 h), followed by 90 μL of isopentane (7:56 h). 45 μL of isopentane was then injected at 8:10 h. Approximately three hours later, a second dose of NO was introduced into the chamber at 11:23 h, followed by an injection of 140 μL of n-hexane at 11:26 h. the chamber roof was closed at 14:57 h. The time sequence of the instrumental additions is shown in Figure 67.

4.3.4.2. *Experimental results*

As the chamber roof was open, the OH concentration increases rapidly to reach 1.2×10^7 molecule cm^{-3} measured by the UL-FAGE. The concentration of HO_2 and RO_2 is increased to reach an equal value of 2×10^8 molecule cm^{-3} . After the first large injection of NO (9 ppbv), the radicals concentrations decrease sharply. The HO_2 and RO_2 concentration starts to increase after the addition of isopentane with a decrease in the OH concentration corresponding to the initiation of oxidation process of isopentane by OH. After the second injection of NO (3 ppbv) followed by the n-hexane injection, the OH concentration continued to decrease to reach 3×10^6 molecule cm^{-3} and the HO_2 and RO_2 radicals continue to increase with an equal concentration to reach 6×10^8 molecule cm^{-3} just before the roof chamber was closed.

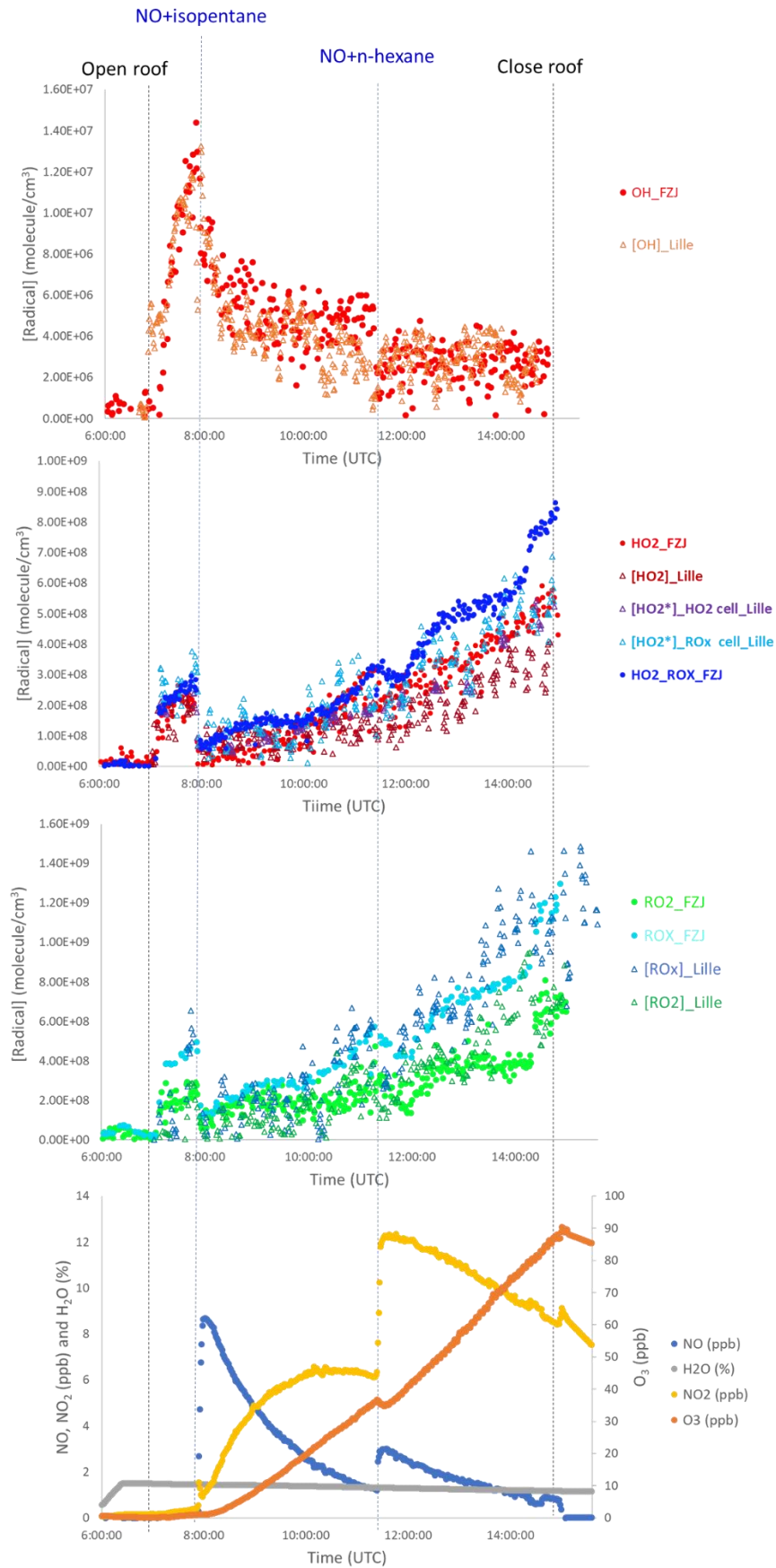


Figure 67: Measurement profiles for August 12 experiment, caption: same as Figure 57

4.3.4.3. Comparison between Lille and Jülich measurements

A slight difference between the OH, HO₂ and HO₂^{*} measurements by both instruments can be seen in Figure 67. The scatter plots (Figure 68) obtained for OH, HO₂, and HO₂^{*} gave a slope in the range 0.6-0.8 ($r^2 = 0.6-0.9$) and an insignificant intercept. The HO₂^{*} concentration measured by both instruments is slightly higher than the HO₂ concentration indicating that an interference from long chain alkyl precursors such as pentane can contribute to the HO₂^{*}, as observed in (Whalley et al., 2013). The good agreement in the RO₂ concentration between both instruments can be also seen in the scatter plots giving a slope equal to 0.9 ($r^2 = 0.7$) and an insignificant intercept.

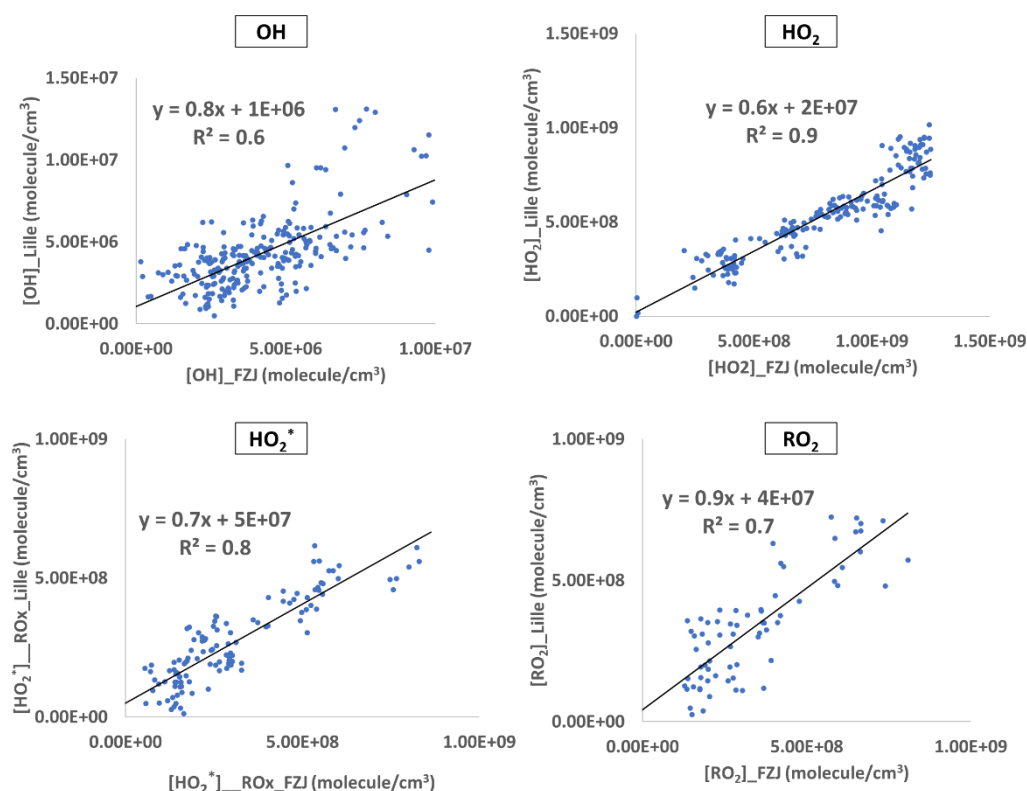


Figure 68 : Scatter plot between Lille and Jülich OH, HO₂, HO₂^{*} and RO₂ measurements for August 12 experiment

4.3.5. Ambient chemistry

The detection of the ambient OH, HO₂ and RO₂ radicals took place during this intercomparison campaign by directly sampling air from the research center Jülich area into the SAPHIR chamber. The research center is surrounded by a forest and located in a region dominated by agricultural and strip mining. The goal of this experiment was to study the aging of the Jülich ambient air inside the chamber and thus investigate the response of the instruments to additional interferences that may be caused from the complex chemical composition of ambient air.

4.3.5.1. *Experimental Conditions*

This experiment was conducted on August 23. The measurement principle includes continuous sampling of ambient air with the chamber shutter system open to allow photooxidation processes. The roof was opened at 6:30 h and closed at 15:01 h. A flow of 250 m³/h of ambient air is pumped into chamber during the measuring period.

4.3.5.2. *Experimental results*

As shown in Figure 69 for Lille measurements, a generally good correlation of the measured OH concentrations and $j(\text{O}^1\text{D})$, representative of the solar radiation, can be observed for this measuring day. The OH concentration exhibited a rapid increase as the roof was opened and a maximum OH concentrations of 8×10^6 molecule cm⁻³ reached around 12:00 h corresponding to the maximum of solar radiation.

A high NO level is observed as the roof is open. Relatively high concentration of NO (2.7 ppbv) reacts with HO₂ and RO₂ radicals to shift the equilibrium between OH and peroxy radicals toward OH. The ratio of HO₂ to OH radical concentration, shown in Figure 70, exhibits a clear dependence on the NO mixing ratio. At low NO mixing ratio (about 0.1 ppbv), HO₂ concentrations are about a factor of 140 higher than OH concentrations. However, this ratio reduces to a factor of 20 for higher NO mixing ratios, around 3 ppbv. This trend can be understood qualitatively considering that the photochemical cycling between OH and HO₂ dominates the overall production and consumption of radicals. High levels of NO cause a shift of HO₂ towards OH, resulting in lower HO₂ concentrations. In contrast, lower NO mixing ratios allow HO₂ concentrations to attain higher values. This behavior has also been found in other campaign such as HO_xComp campaign (Ren et al., 2005) and Pacific Campaign (Cantrell et al., 2003).

In contrast to OH and HO₂ radical concentrations, HO₂ and RO₂ are highly correlated with a ratio RO₂/HO₂ that vary from 0.6 to 1.2 which is nearly independent of the NO mixing ratio since both HO₂ and RO₂ are destroyed in the reaction with NO with similar rate constants, Similar ratios have also been found in the literature (Mihelcic et al., 2003; Ren et al., 2005).

Various VOCs of both primary and secondary origins were quantified in the chamber. The most abundant ones are the acetaldehyde, methacrolein (MACR) + methylvinylketone (MVK), butanone, isoprene and toluene. The concentration of these VOCs reach their maximum during the morning, between 7 and 10 h, to decrease later due to their reaction with OH producing RO₂ radicals.

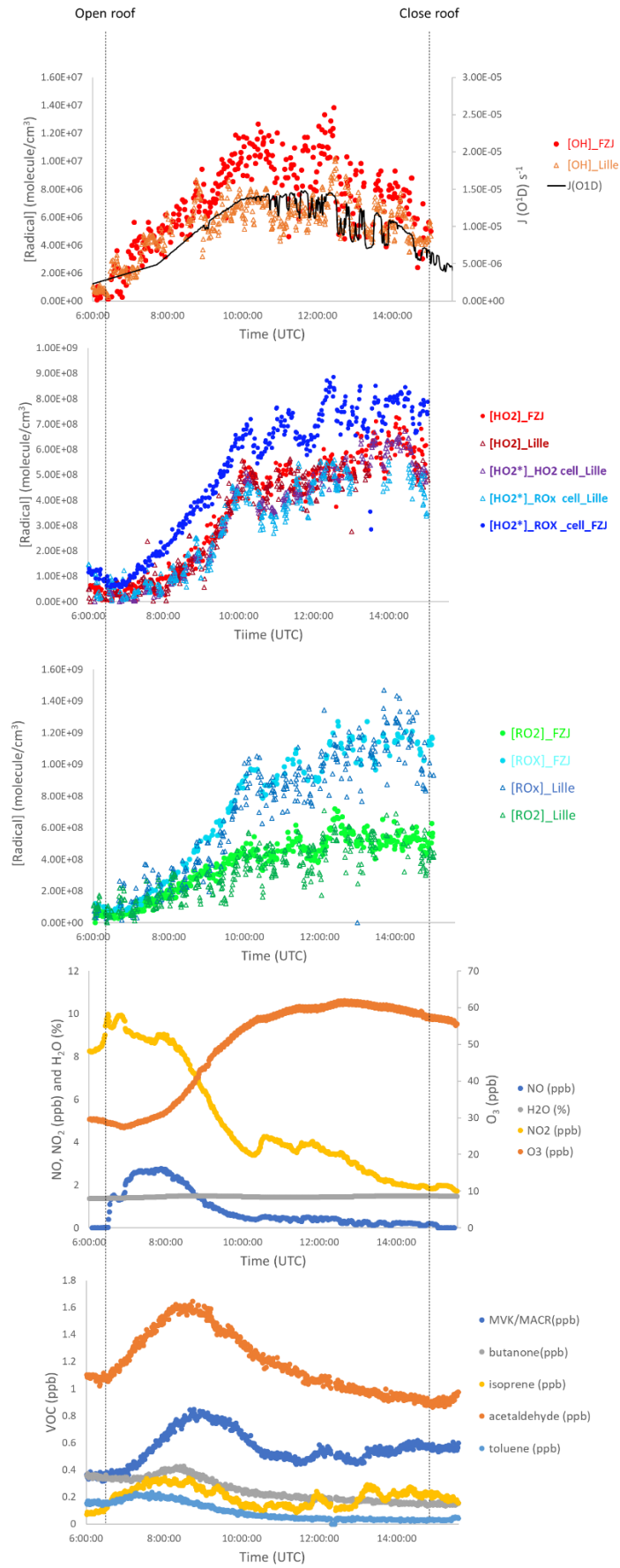


Figure 69: Measurement profiles for August 23 experiment, caption: same as Figure 57

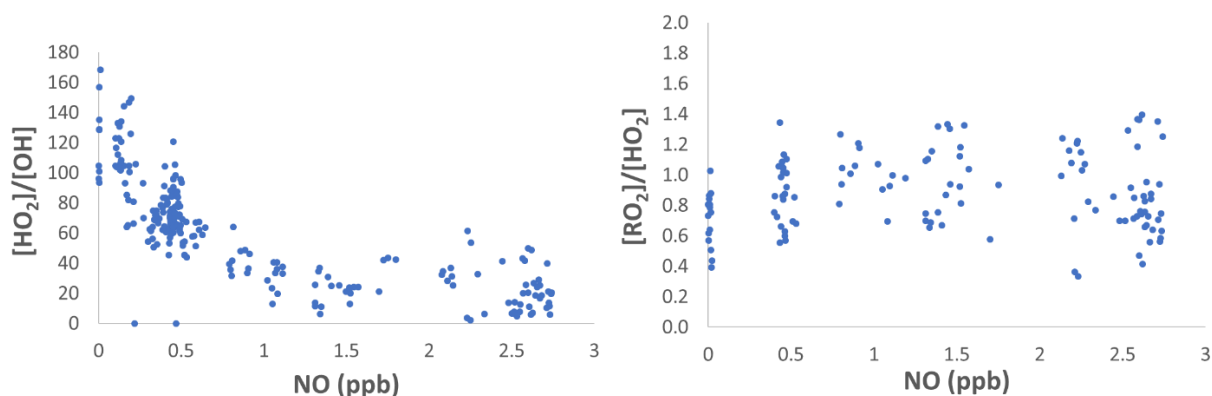


Figure 70: Ratio between measured radical concentration depending on the NO concentration during experiment done on August 23

4.3.5.3. Comparison between Lille and Jülich measurements

The concentration of OH measured by the UL-FAGE was compared to that measured by the FZJ-FAGE and a scatter plot gives a slope of 0.6 ($r^2 = 0.7$) and insignificant intercept. A good agreement is shown in Figure 69 for the HO_2 , HO_2^* and RO_2 concentrations and in the correlation plot (

Figure 71) of the two data sets. The discrepancies between measurements of both instruments is within their respective uncertainties. The HO_2^* measured by the FZJ instrument is higher than that measured by the UL-FAGE indicating a higher sensitivity of the FZJ-FAGE for ambient RO_2 produced from double bonding alkene or aromatics.

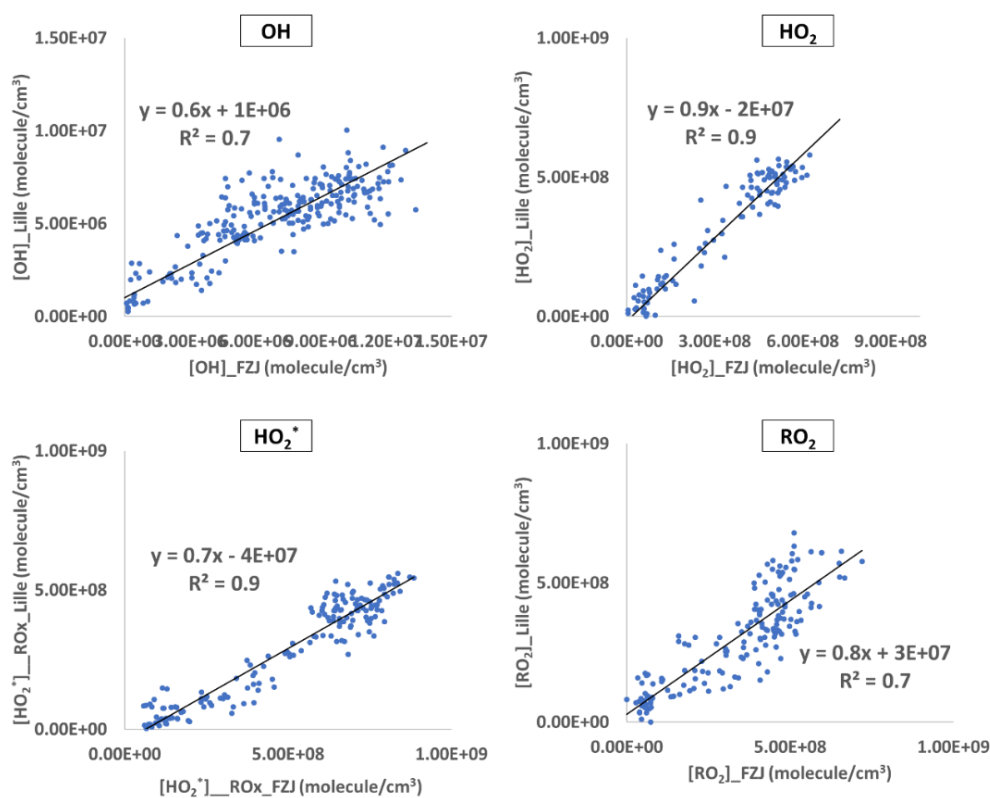


Figure 71: Scatter plot between Lille and Jülich OH, HO_2 , HO_2^* and RO_2 measurements for August 23 experiment

4.3.6. Summary of the intercomparison results of all experiments

The results of some of the experiments that have been conducted during the intercomparison campaign have been discussed in the previous section with an intercomparison between the measurements of the Lille and Jülich group. The results of all the intercomparative measurements are reported in Table 21, where the radical concentration measured by the Lille instruments was considered in agreement with the measurements of the Jülich instruments if it is equal (**green**) to the Jülich measurements within their respective uncertainties (30 and 18%) with $0.7 < \text{slope} < 1.3$. For slight disagreement ($1.3 < \text{slope} < 1.5$) we used **yellow** for higher Lille measurements and **orange** for lower Lille measurements compared to the Jülich measurements ($0.5 < \text{slope} < 0.7$). Such disagreements are slightly above the instrument's combined uncertainties. For significant disagreement (higher than 50 %, where $\text{slope} > 1.5$ or $\text{slope} < 0.5$) we used the **red** color. RO₂ results are shown with (w) and without (wo) considering the radical losses observed at high humidity during cross calibration that will be discussed in section 4.3.7. These results show a relatively good agreement for the radical measurements (OH, HO₂, HO₂^{*} and RO₂ wo considering radical losses at high humidity) for most of the days. This good agreement tends to eliminate several possible explanations for the observed strong differences observed on August 14, such as: inhomogeneous sampled air, high systematic error in the calibration (see also next paragraph), lack of reproducibility of the instrument's sensitivities.

Table 21: Summary of the comparison between the measurements done by the Lille and Jülich instruments with the slopes of the scatter plots for each OH, HO₂, HO₂^{*} and RO₂ (with: w and without: wo considering the radical losses observed at high humidity) measurement

		Lille = Jülich 0.7<slope<1.3	Lille >Jülich 1.3<slope<1.5	Lille <Jülich 0.5<slope<0.7	Lille ≠ Jülich 1.5<slope or <0.5	
Date	Experiment	OH	HO ₂	HO ₂ [*] (RO _x cell)	RO ₂ (wo losses)	RO ₂ (w losses)
8/8/2022	CO/CH ₄ oxidation by OH	0.5	0.7	0.9	1.3	0.5
9/8/2022	Isoprene OH oxidation	0.9	0.6	0.6	1.4	0.5
10/8/2022	Isoprene OH oxidation : O ₃ change	0.5	0.8	0.9	1.4	0.5
11/8/2022	Isoprene OH oxidation : NO _x change	0.7	0.6	0.7	1.9	0.7
12/8/2022	i-pentane and n-hexane photooxidation	0.8	0.6	0.7	0.9	0.3
13/8/2022	α-pinene ozonolysis	0.7	0.8	0.8	0.7	0.3
14/8/2022	Mesitylene photooxidation	0.7	0.7	0.9	1.2	0.4
16/8/2022	β-pinene photooxidation	0.8	0.9	0.8	0.8	0.3
17/8/2022	Isoprene NO ₃ oxidation (dry)	0.6	1.4	0.8	1.5	0.5
19/8/2022	Hexene ozonolysis: humidity change		0.6	0.7	0.6	0.2
20/8/2022	CO/CH ₄ : humidity change, NO change	0.5	0.8	0.9	1.1	0.4
22/8/2022	β-pinene NO ₃ oxidation	0.5	0.9	1.0	1.1	0.4
23/8/2022	Ambient air	0.6	0.9	0.7	0.8	0.2
24/8/2022	MVK oxidation	0.6	0.8	0.8	1.5	0.6
25/8/2022	Cl chemistry isoprene	0.5	0.9	0.7	0.9	0.4
26/8/2022	Isoprene, TME ozonolysis + photooxidation		1.5	0.7	0.8	0.3

For OH, the discrepancies between the UL-FAGE and FZJ-FAGE measurements are due to the lower concentration of OH measured by the UL-FAGE as the chamber shutter system was opened. But in general, both instruments agreed over most of the campaign measurements within the instrument uncertainties except during the experiments performed on August 19 and 26. The higher OH concentration measured by the UL-FAGE during the hexene and isoprene ozonolysis experiment, done on August 19 and 26, correspond to the interferences on the OH measurements of the UL-FAGE instrument under dark conditions and as mentioned previously that neither interference from NO₃ has been considered nor OH scavenger was added for the UL-FAGE during this campaign.

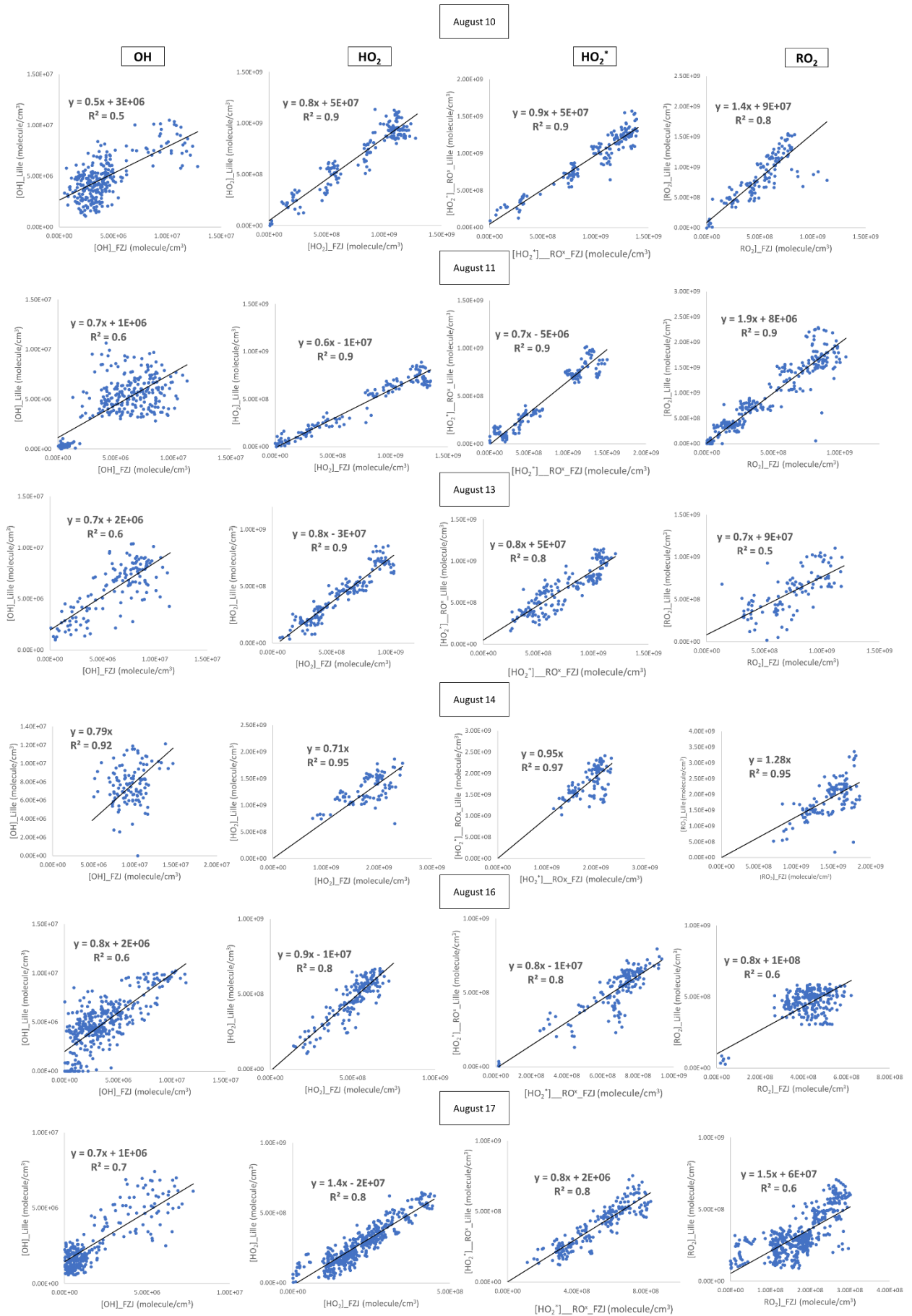
For HO₂, we also had a good agreement between both instruments for most of the intercomparison exercises. Slight disagreement was shown during experiments conducted to study the isoprene chemistry under sunlight and dark conditions. These discrepancies can be explained by the complexity of the isoprene chemistry and potential interferences. Some of the

isoprene experiments (done on August 9, 11, 17 and 26) confirmed the high potential of this alkene to produce RO₂ radicals that can recycle OH inside the FAGE cell after the addition of high NO concentration. The HO₂^{*} concentration measured by both Lille FAGE cells (HO₂ and RO₂) show a slightly lower concentration than that measured by the FZJ-RO_x-FAGE instrument during most of the experiments and this can be due to the low sensitivity of the Lille instruments (UL-FAGE cell with high NO injected in the HO₂ FAGE cell and UL-RO_x-FAGE in the HO_x mode) for RO₂ radicals produced from alkene or aromatics precursors.

For RO₂, without considering any radical losses observed during the RO_x cell calibration at high humidity, a good agreement between the measurements of both instruments has been observed during most of the experiments. These results tend to validate the data of the new UL-RO_x-FAGE instrument for RO₂ measurements even if some further analysis have to be done (calibration issues). While considering the 40 % radical losses on the RO₂ measurements of the UL-RO_x-FAGE, it was found that the UL-RO_x-FAGE always measures a lower peroxy radical concentrations than FZJ-FAGE. This point needs to be further investigated by performing additional laboratory tests to confirm or not the radical losses in the calibrator observed at high humidity.

Concerning the RO_x measurements performed by other instruments such as the IMT-PERCA, they observed a good agreement within 30 % with FZJ-RO_x-FAGE for most of the experiments (Abichou, 2023).

Figure 72 shows the scatter plots for OH, HO₂, HO₂^{*} and RO₂ for the experiments that were not discussed in this chapter (concentration profiles available in Annex).



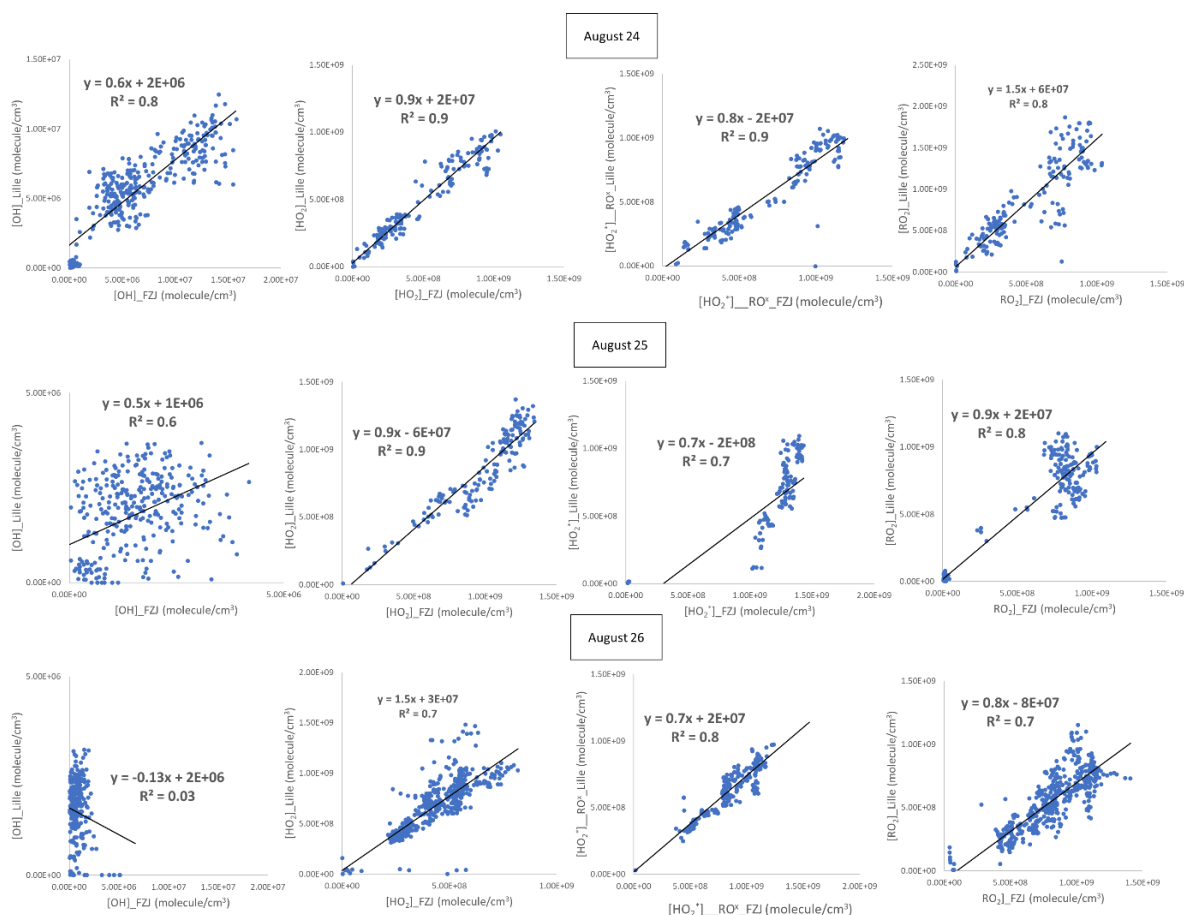


Figure 72: Scatter plots for Lille and Jülich OH, HO₂, HO₂* and RO₂ measurements for the experiments that were not discussed in this chapter

4.3.7. Calibration source exchange

As a key point of the measurements is the calibration, which may lead to systematic differences. A cross calibration, exchanging the calibration sources has been performed at the end of the campaign to check out potential systematic errors hidden by day to day variations. For this purpose, an exchange of the calibration cells between Lille and Jülich groups was conducted on the last day of the campaign and other exchanges have been done between Leeds and Jülich and Douai and Jülich (data not yet available). The characteristic of the calibration source used by our UL-FAGE (Lille group) are given in chapter 2 whereas the FZJ (Jülich group) calibration source is described in detail by (Fuchs et al., 2011; Holland et al., 2003). For both calibration sources, the radicals are produced by the photolysis water in air at 1 atm using 184.9 nm radiation of a mercury lamp (Heard & Pilling, 2003; Schultz et al., 1995). The UL-FAGE calibration source is flushed with N₂ in front of the lamp in order to avoid the absorption of the lamp flux by ambient O₂. Same for the Jülich group but they use N₂O rather than N₂ in order to reduce the intensity of the radiation and produce small radical concentration at a humidity within the range usually found in the troposphere (mixing ration of H₂O about 1 %),

thus, can avoid errors in the calibration caused by performing measurements under artificial conditions.

At first, we placed the FZJ-FAGE calibration source on the UL-FAGE and UL-RO_x-FAGE. Different conditions were used in the calibration cell in order to generate mixtures of OH/HO₂ (humid air) and HO₂ (humid air + CO) and HO₂/RO₂ by adding ethane (C₂H₆) at different humidity. The calculated concentrations provided by the Jülich group were compared to the measured concentrations with the UL-FAGE and UL-RO_x-FAGE obtained converting the signal obtained into an OH, HO₂ or RO₂ concentration using our calibration factors. The calculation of the sensitivity for each FAGE cell to the different radicals is described in details in chapter 2. In Table 22, Table 23 and Table 24 are listed the calibration points made for the UL-FAGE and UL-RO_x-FAGE at two different RH levels. The concentrations are shown with their uncertainties on Figure 73 (the uncertainty for the UL-FAGE is of 32 % for OH and RO₂ and 40 % for HO₂ and 18 % for the FZJ-FAGE) and in Table 22, Table 23, Table 24.

Table 22: Lille OH concentration measured and Jülich calculated for the calibration source exchange

OH	[H ₂ O] %	[OH] _{Lille} measured /10 ⁹ cm ⁻³	[OH] _{FZJ} calculated /10 ⁹ cm ⁻³	[OH] _{FZJ} /[OH] _{Lille}
Point 1	0.25	2.50 ± 0.75	1.79 ± 0.32	0.72
Point 2	0.25	2.50 ± 0.75	1.79 ± 0.32	0.72
Point 3	1	3.73 ± 1.11	3.43 ± 0.61	0.92

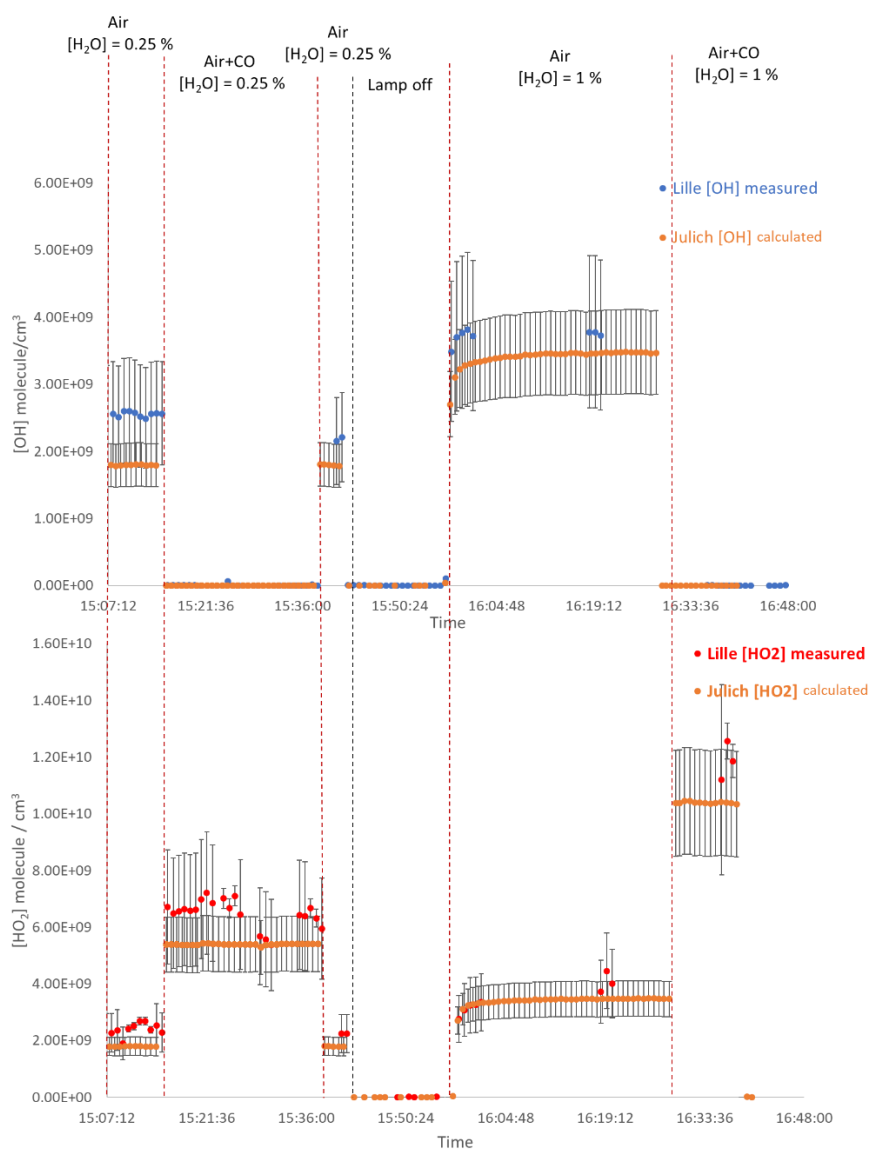
Table 23: Lille HO₂ concentration measured and Jülich calculated for the calibration source exchange

HO₂	[H ₂ O] %	CO (in calibrator)	[HO ₂] _{Lille} measured /10 ⁹ cm ⁻³	[HO ₂] _{FZJ} calculated /10 ⁹ cm ⁻³	[HO ₂] _{FZJ} /[HO ₂] _{Lille}
Point 1	0.25		2.54 ± 0.76	1.79 ± 0.32	0.75
Point 2	0.25	x	6.87 ± 2.06	5.39 ± 0.97	0.82
Point 3	0.25		2.3 ± 0.69	1.79 ± 0.32	0.77
Point 4	1		4.24 ± 1.27	3.41 ± 0.61	0.91
Point 5	1	x	1.12 ± 0.33	1.04 ± 0.18	0.93

Table 24: Lille RO₂ concentration measured and Jülich calculated for the calibration source exchange

RO ₂	[H ₂ O] %	C ₂ H ₆ (in calibrator)	[RO ₂] _{Lille} measured /10 ⁹ cm ⁻³	[RO ₂] _{FZJ} calculated /10 ⁹ cm ⁻³	[RO ₂] _{FZJ} /[RO ₂] _{Lille}
Point 1	0.25	x	4.78 ± 1.43	3.34 ± 0.60	0.7
Point 2	1	x	8.68 ± 2.6	6.91 ± 1.24	0.8

The results show a systematic overestimation of the concentration measured by the Lille instruments (UL-FAGE and UL-RO_x-FAGE) of approximately 10-30 % compared to Jülich concentration provided with a more pronounced difference at low humidity. However, it is most of the time within the uncertainties. These results are consistent with the results obtained in the SAPHIR chamber.



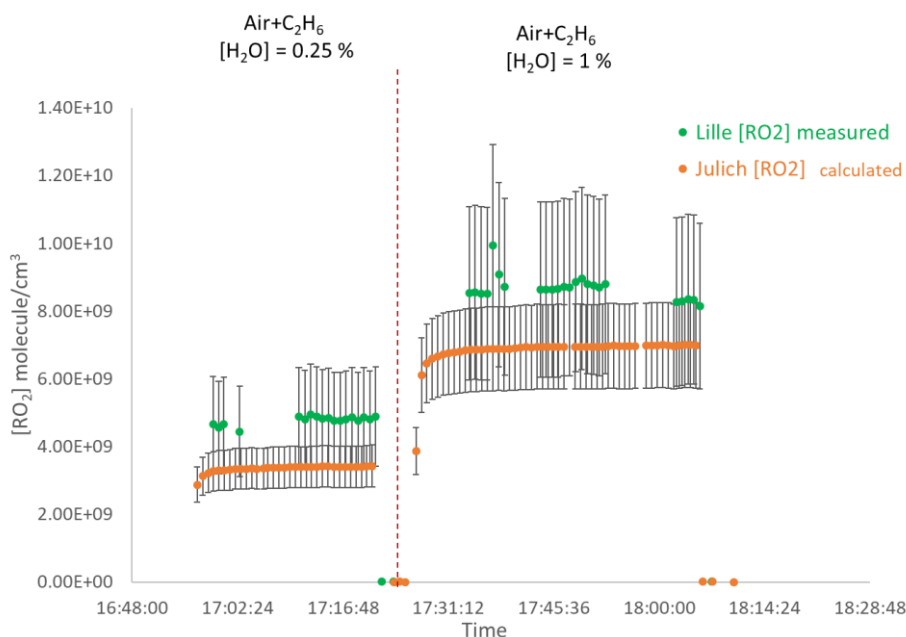


Figure 73: Calibration source exchange. Form bottom to top:

- RO_2 concentration in molecule/cm³
- HO_2 concentration in molecule/cm³
- OH concentration in molecule/cm³

The same steps mentioned above for the calibration of the UL-FAGE using the FZJ-calibrator was done when the UL-FAGE calibration source was placed on the FZJ-FAGE. In Table 25, Table 26 and Table 27 are listed the calibration points for the OH FZJ-cell at 2 different RH level, for HO₂ FZJ-cell at 2 different RH level with and without CO in the calibrator and for RO₂ FZJ-cell at 1 RH level, respectively. The concentrations are given with the uncertainties of each instrument. The calibration source exchange OH, HO₂ and RO₂ measurements are represented in Figure 74.

Table 25: Jülich OH concentration measured and Lille calculated for the calibration source exchange

OH	[H ₂ O] %	RH %	[OH] _{Lille} calculated /10 ⁹ cm ⁻³	[OH] _{FZJ} measured /10 ⁹ cm ⁻³	[OH] _{FZJ} /[OH] _{Lille}
Point 1	0.08	3	0.9 ± 0.27	0.7 ± 0.13	0.77
Point 2	0.3	11	5.3 ± 1.6	3.7 ± 0.66	0.69

Table 26: Jülich HO₂ concentration measured and calculated for the calibration source exchange

HO ₂	[H ₂ O] %	RH %	CO (in calibrator)	[HO ₂] _{Lille} calculated /10 ⁹ cm ⁻³	[HO ₂] _{FZJ} measured /10 ⁹ cm ⁻³	[HO ₂] _{FZJ} /[HO ₂] _{Lille}
Point 1	0.08	3		1.36 ± 0.41	1.17 ± 0.21	0.86
Point 2	0.3	11	x	16.3 ± 4.89	8.5 ± 1.53	0.52
Point 3	0.3	11		5.6 ± 1.68	2.9 ± 0.52	0.51

Table 27: Jülich RO₂ concentration measured and Lille calculated for the calibration source exchange

RO ₂	[H ₂ O] %	RH %	C ₂ H ₆ (in calibrator)	[RO ₂] _{Lille} calculated /10 ⁹ cm ⁻³	[RO ₂] _{FZJ} measured /10 ⁹ cm ⁻³	[RO ₂] _{FZJ} /[RO ₂] _{Lille}
Point 1	0.3	11	x	5.8 ± 1.74	2.85 ± 0.51	0.5

The results show a systematic overestimation of the OH concentration calculated for the calibration source of Lille of approximately 20-30 % compared to FZJ-OH concentration measured with a more pronounced difference at high humidity (RH = 11 %).

For HO₂ concentration, a good agreement between the two groups was found at low humidity (RH = 3 %). However, at high humidity levels we observe an overestimation of approximately 50 % of the HO₂ and RO₂ concentration obtained from our calculations compared to FZJ measurements.

This seems to comfort the observations done with our calibration cell at different humidities showing a loss of radicals of about 40% measured at high humidity using the calibration factor obtained at low humidity. However, this disagreement is more pronounced for HO₂ and RO₂ than for OH, without clear explanation.

Since for this campaign, due to a too low sensitivity, the UL-RO_x-FAGE was calibrated at high humidity, without taking into account losses (see details in chapter 2), and considering the cross calibration, the overestimations of RO₂ concentration observed for different days could be explained. However, it is not the case for all days.

Similarly, the disagreement using the calibration cell of Jülich on the UL-FAGE instruments is less pronounced than when the calibration cell of Lille is used on the FZJ-FAGE instruments.

No clear explanation can be found to explain these disagreements. It could be a combination of different errors (radical losses, laser power variation, ...) and more data analysis and calibration cell tests will be performed.

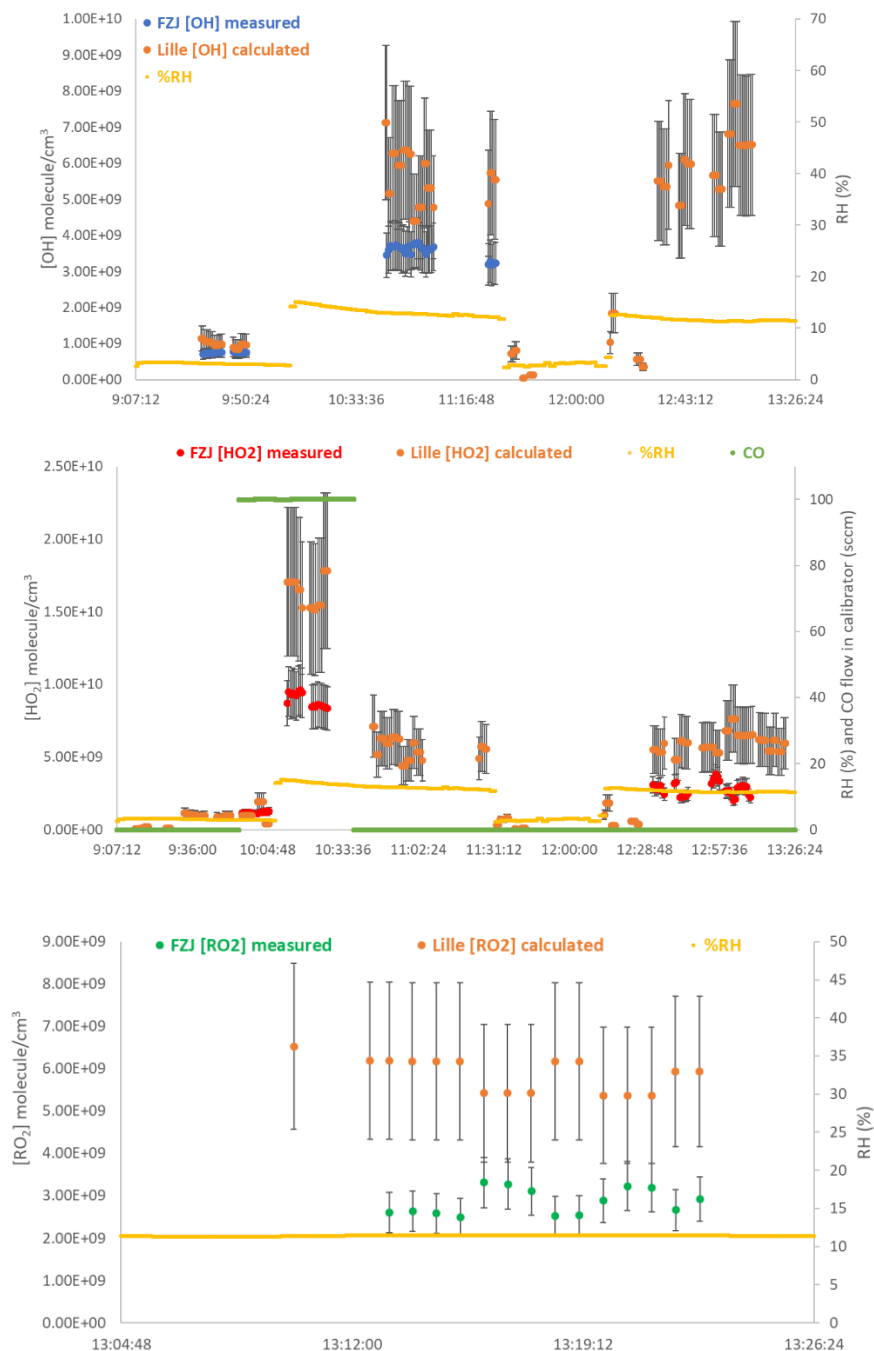


Figure 74: Calibration source exchange. Form bottom to top:

- RO₂ concentration in molecule/cm³ and RH (%)
- HO₂ concentration in molecule/cm³ CO flow and RH (%)
- OH concentration in molecule/cm³ and RH (%)

4.4. Conclusion

A series of intercomparison experiments were conducted in SAPHIR chamber, under sunlight and dark conditions, to investigate the response of eight different instruments to different pools of peroxy radicals generated inside the chamber, starting from the simplest

chemical system to generate only HO₂ and CH₃O₂ and increasing the complexity of the pool step by step by adding peroxy radicals produced by the ozonolysis of alkenes, oxidation by NO₃, isoprene oxidation or under high NO level or in ambient air and varying H₂O, O₃, NO_x and VOC concentrations. Lille and Jülich measurements were compared directly since the Jülich instruments were considered as the reference and both groups measured OH, HO₂, HO₂^{*} and the sum HO₂+RO₂, refers as RO_x from which we can determine the RO₂ concentration.

For OH, the Lille-FAGE and FZJ-FAGE agreed over most of the campaign measurements within the instruments uncertainties except during the experiments performed on August 19 and 26. The reason behind the disagreements on the experiment done under dark conditions (August 19 and 26) might be due the suffering of the UL-FAGE of some interferences on the OH measurements.

During the two experiments performed in the dark, isoprene oxidation by NO₃ (August 17) and isoprene ozonolysis (August 26), higher OH, HO₂, HO₂^{*} and RO₂ concentration were measured by the Lille instruments than by FZJ-RO_x-FAGE.

For HO₂, we also had a very good agreement between both instruments for most of the intercomparison exercises. Slight disagreement was shown during experiments conducted to study the isoprene chemistry under sunlight and dark conditions. These discrepancies can be explained by the complexity of the isoprene chemistry and potential interferences.

For RO₂, a good agreement between the measurements of both instruments have been observed in general for the experiments but contrasted day to day behaviors have been observed.

The cross-calibration results seem to highlight an overestimation of the concentrations by the UL-FAGE, probably due to an overestimation of the concentrations considered to be generated by our calibration cell at high humidity, but some inconsistencies between the different results should be clarified. These results tend to demonstrate that the new UL-RO_x-FAGE instrument has the capacity for RO₂ measurements even if some further analysis have to be done (calibration issues).

In order to better analyze the results of this campaign, the data from other groups have to be considered and a comparison with modelled profiles based on a detailed oxidation mechanism of each VOC species will be performed. In the laboratory, improvements should be done to better correct for laser power variation and more systematic characterizations with different RO₂ will be performed.

Chapter 5: ACROSS Field Campaign

This chapter presents the results obtained from the deployment of the UL-FAGE in the ACROSS campaign. The UL-FAGE was deployed for six weeks in June-July 2022 in one of the measurement sites of the ACROSS (Atmospheric ChemistRy Of the Suburban foreSt) campaign, the site located in the Rambouillet forest, at the south of Paris (France). The aim of this campaign was to study the influence of atmospheric conditions (urban or oceanic air masses movement) on the chemistry of the emitted BVOCs at the Rambouillet forest, in particular on the OH radical cycle. The UL-FAGE was deployed in its full configuration with the quantification part using three FAGE cells: OH, HO₂ and RO_x cell (at the ground level) and the OH reactivity part. The first measurements of RO₂ radicals using the UL-RO_x-LIF instrument were held during this campaign. The OH reactivity was alternatively measured at two different levels: below (ground level) and above the forest canopy (top of a 40 m tower). Comparison between the measured and the calculated OH reactivity allowing to identify the diurnal missing reactivity at both levels is presented in this chapter. An intercomparison between the UL-FAGE and the LPC2E-CIMS for the quantification of OH radical is also shown in this chapter. In addition, a preliminary intercomparison between the 3 instruments measuring RO_x concentration: UL-FAGE, LPC2E-CIMS and IMT-PERCA is also presented.

5.1. Introduction

Several field campaigns involving measurements of OH, HO₂ and RO₂ radicals in biogenic environments have highlighted difficulties to understand the atmospheric chemistry observed (Feiner et al., 2016; Fuchs et al., 2017; Mao et al., 2012; Stone et al., 2012; Whalley et al., 2016; Yang et al., 2017). Concerning the OH reactivity measurements, a missing reactivity have been reported in low NO_x environments such as forests (Nölscher et al., 2016; Whalley et al., 2016; Zannoni et al., 2016). For HO_x measurements, as discussed in chapter 1, discrepancies between measurements and models were reported in the literature for clean environments. Biogenic emissions have a significant influence on the tropospheric chemistry on local and global scales (Dlugi et al., 2010). Therefore, in such type of environments, detailed characterization of both the gas and particle phase is needed. The mixing of anthropogenic and biogenic emissions in the ambient atmosphere can influence the atmospheric chemical processes, as demonstrated by studies such as: Martin et al., 2016; McFiggans et al., 2019; Nascimento et al., 2021; Setyan et al., 2014. Competition for oxidant species such as OH (daytime), O₃ (day and nighttime) and NO₃ (nighttime), between the organic species from biogenic and anthropogenic sources could lead to the formation and growth of SOA with varying yields and properties. Additionally,

elevated NO_x concentration from anthropogenic origin could greatly influence the oxidation pathways of the BVOCs.

Paris, one of the largest European megacities, transports pollution to different surrounding areas depending on the variation of the wind direction associated with specific meteorological conditions. The relatively unique situation of this isolated megacity from other urban areas makes it a suitable location to study the impact of urban emissions on the chemistry of close biogenic environments such as forests and vice versa. Studies of urban-rural air mass interactions over the Paris area were conducted during two large projects: ESQUIF (Etude et Simulation de la QUalite de l'air Ile de France, 1998-2000) (Menut et al., 2000) and MEGAPOLI (Megacities: Emissions, urban, regional and Global Atmospheric POLLution and climate effects, and Integrated tools for assessment and mitigation, 2009-2010) (Baklanov et al., 2010). Although these studies have enhanced the understanding of atmospheric transformation processes for Paris urban outflow, through studying the impacts of megacities on local, regional and global air quality and developing improved predictive tools for urban air quality, many scientific questions remain concerning the oxidation of VOCs, the formation of secondary organic aerosols (SOA) and the budgets of HO_x radicals.

To improve the knowledge of the atmospheric chemical processes that occur in mixed anthropogenic-biogenic air masses and assess their impact on the air quality, the ACROSS (Atmospheric ChemistRy Of the Suburban foreSt) field campaign was performed during the summer 2022, period when photochemistry activity is maximum and biogenic emissions are large.

ACROSS is a large-scale project supported by the “Make Our Planet Great Again” (MOPGA) framework (Cantrell, 2020). The ACROSS field campaign involved more than 20 research groups from France, Europe and the world to perform different activities such as airborne observations, ground-based observations and modelling studies. The measurement of different parameters and chemical species were performed at different locations (Figure 75). The combination of the data provided during this field campaign from different research groups (such as measurements of VOCs, inorganic species, particle concentration and composition, ...) aimed to characterise mixing of anthropogenic urban or oceanic air masses, leading to different NO concentrations, with biogenic forestry emissions to better understand the oxidation of tropospheric VOCs. This will ultimately help improving this chemistry within atmospheric models.

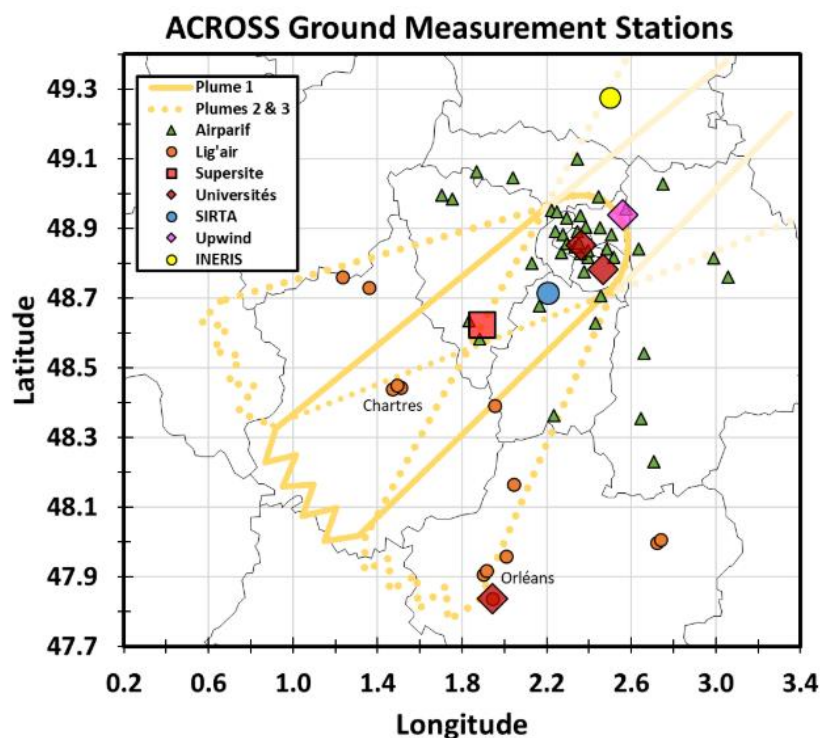


Figure 75: Map of the ACROSS measurement locations in the Paris region. (Cantrell, 2020)

The UL-FAGE instrument was deployed during the ACROSS field campaign, in the measurement site located in the Rambouillet forest with other instruments from different laboratories to characterise the gas phase (see Table 30) to answer scientific questions related to gas phase – free radical chemistry and budget:

- Do we observe conditions with “missing reactivity” (calculated OH reactivity determined from individually measured reactants lower than measured OH reactivity)? What are the potential explanations for any discrepancies?
- Over the range of observed NO levels, what are the HO_x and RO_x radical sources and sinks?
- Do observed radical levels agree with the model constrained values and what are the causes of any differences?

This chapter is mainly focused on the OH reactivity analysis and preliminary results are shown for the quantification. The results of the modeling are not yet available.

5.2. Site description

Part of the ACROSS intensive field campaign was conducted from June 13 to July 25, 2022, at the Rambouillet site for ground-based measurements. The site is in the Rambouillet forest, located southwest of Paris (48°39'0"N, 1°49'59.99"E), in the Île-de-France region. The

dominant tree species at the site are sessile and pedunculate oak. (*Quercus petraea* (Mattus.) Liebl. and *Q. robur* L. respectively) and hornbeam (*Carpinus betulus* L.), with other accompanying deciduous species (i.e. *Populus tremula* L., *Betula pendula* Roth. and *Fagus sylvatica* L.) (Brin et al., 2012). During the campaign period, several distinct weather and pollution patterns occurred such as strong heatwaves with photochemical activities producing secondary pollutants and advection of relatively clean oceanic air masses.

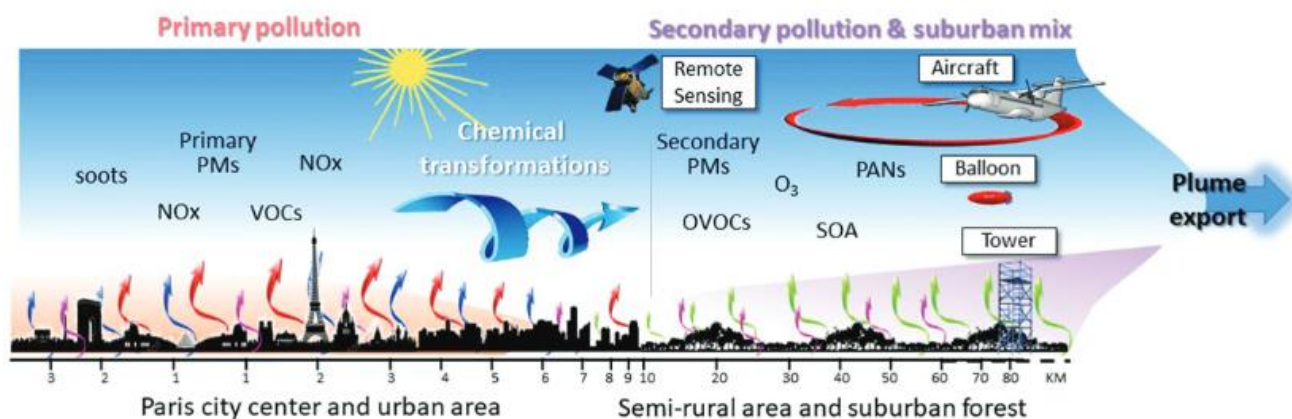


Figure 76: Schematic diagram of the configuration of observation platforms relative to the urban and rural emission areas to be studied during the comprehensive summertime ACROSS project. (Cantrell, 2020)

At the Rambouillet site, several atmospheric observations were performed (Figure 76). These included:

- Aircraft flights to observe the spatial and temporal key species at altitude in the range of about 40 to 300 meters above ground level.
- Tower-based observations at a height of 40 meters to study the chemistry above the canopy level.
- Ground-based measurements where different instruments were setup inside mobile facilities to measure the chemistry below and above the canopy level.

5.3. Deployment of radical measurements in the ACROSS field campaign

5.3.1. Experimental details

The UL-FAGE instrument was deployed at the Rambouillet site for 6 weeks to measure OH, HO₂, HO₂^{*}, RO₂ concentrations and OH reactivity (Figure 77). Most of the components of the FAGE instrument were installed in a shipping container (laser system and part of the electronics) and

- OH reactivity was measured at two levels (ground level and top of the tower), air was sampled by Teflon tubes (details in the following part). It was the only instrument measuring this parameter.
- OH, HO₂, HO₂^{*} and RO₂ radicals were quantified using 5 m above the ground level with the three FAGE cells fixed in a box on top of the container (see chapter 2).

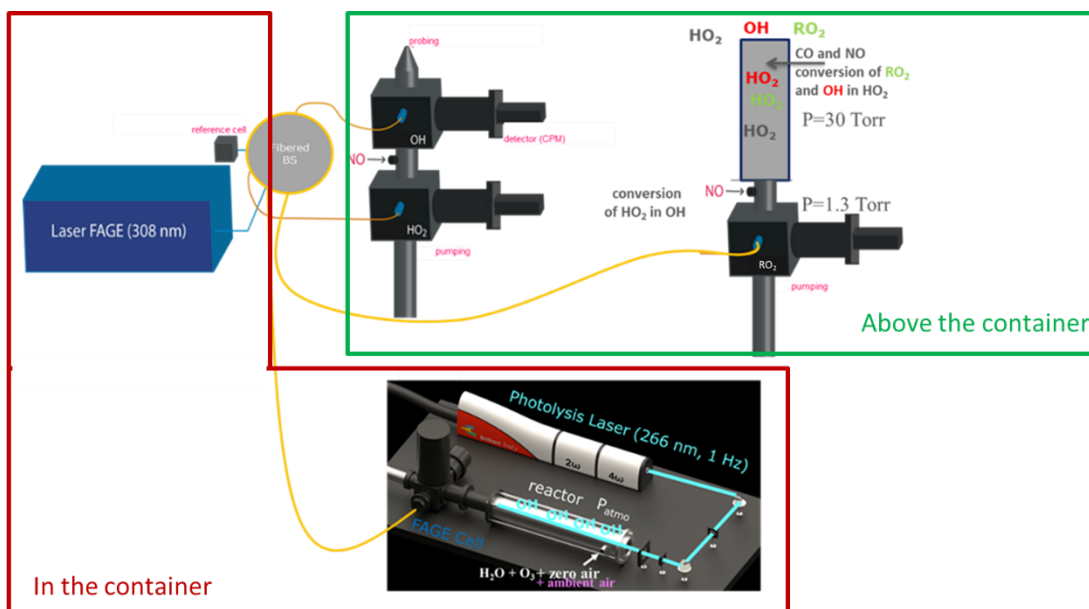


Figure 77: The four FAGE cells used during the ACROSS campaign measurements

Other techniques were deployed by other groups to quantify radicals: CIMS for OH/RO₂ (LPC2E group, technique described in chapter 1, section 1.2.1) and PERCA for RO₂ (IMT group). Both the FAGE and CIMS techniques were measuring at the ground level to perform measurements in the canopy level while the PERCA instrument (technique described in chapter 1, section 1.2.1) was installed on the top of the tower to quantify the radicals above the canopy. Table 28 summarizes the three techniques (FAGE, CIMS and PERCA) that were measuring and intercompared during the ACROSS campaign at the Rambouillet site.

Table 28: The three techniques intercompared for the radical quantification during the ACROSS campaign

Group	Instrument	Level of measurement	Radical	Time resolution	LOD	Uncertainty
PC2A	FAGE (S/N =2)	Ground	OH	40 s	$9.26 \times 10^5 \text{ cm}^{-3}$	32 % (calibration)
			HO ₂	40 s	$6.7 \times 10^7 \text{ cm}^{-3}$	40 % (calibration)
			HO ₂ [*]	40 s	$1.1 \times 10^7 \text{ cm}^{-3}$	32 % (calibration)
			RO _x	40 s	$5.7 \times 10^7 \text{ cm}^{-3}$	32 % (calibration)

LPC2E	CIMS	Ground	OH	12 min	$5 \times 10^4 \text{ cm}^{-3}$	20 % (2σ)
	(S/N = 3)		RO _x	4 min	$1 \times 10^6 \text{ cm}^{-3}$	35 % (2σ)
IMT	PERCA	Tower	RO _x	6 min	0.7 ppt (RH = 10%)	
					1.3 ppt (RH = 50%)	
					3.0 ppt (RH = 80%)	

Concerning the reactivity, the photolysis laser (Brilliant EaSy QUANTEL) providing radiation at 266 nm had suddenly a strong laser power decrease from 30 mW to reach few mW and it was not possible to recover a power high enough for the reactivity measurements. Therefore, it was replaced on July 7 by a Q-Smart 850 laser which could deliver more power and showed more stable behavior. The OH reactivity measurements were stopped for 5 days due to this laser change.

The OH reactivity was measured using the UL-FAGE technique deployed next to the tower region. As shown in Figure 78, air was sampled at two levels: one Teflon tube was connected to a manifold (diameter = 10 cm) installed to connect the main pumped sampling line (using a blower at a flow 2.4-2.5 m³/min) with the probing location at the top of the tower to the different instruments probing the air masses above the canopy measure the total OH reactivity above the canopy (level 2: L2) and another one of 10 m length was placed at the top of our container to measure the total OH reactivity near the sampling area for the radical quantification (level 1: L1). To avoid the sampling of particles and dust, a PFA filter (2.5 μm) was installed at the entrance of the Teflon tube. The pressure in the photolysis cell was approximately 670 Torr during sampling at the tower level and 650 Torr at the ground level. The pressure at both measuring levels was lower than the atmospheric pressure due to restriction of the flow through the Teflon tube. The pressure in the FAGE reactivity cell was around 1.41 Torr.

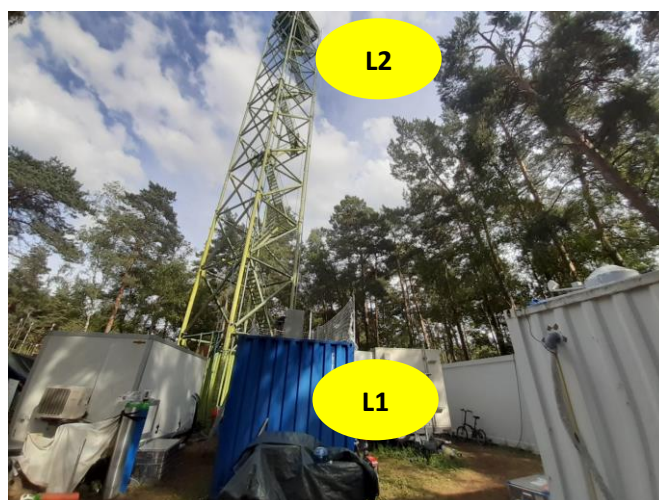


Figure 78: UL-FAGE sampling line for OH reactivity measurement

During ambient measurements, sampled air is introduced into the photolysis cell and mixed with a small flow of synthetic air (60 sccm) passing through an ozone generator to generate an ozone concentration of about 60 ppb in the total flow. Table 29 summarizes the performance of the UL-FAGE instrument in the reactivity mode.

Table 29: Performance of the UL-FAGE instrument measuring OH reactivity during the ACROSS campaign

Instrument	LOD (s ⁻¹)	k _{OH} max (s ⁻¹)	Time resolution (s)	Uncertainty (1 σ)	Level of measurement
UL-FAGE	0.9	150	30-120	15 %	L1 & L2

To check the reliability of the OH reactivity measurements during the campaign, the well-known rate constant of the CO + OH reaction was measured two times (as described in chapter 2). During these tests it was possible to measure reactivities ranging from 10 to 90 s⁻¹ and determine a rate constant of $k_{\text{CO+OH}} = (2.27 \pm 0.04) \times 10^{-13} \text{ cm}^3\text{molecule}^{-1}\text{s}^{-1}$ which is in good agreement with the reference value $k_{\text{CO+OH}} = 2.31 \times 10^{-13} \text{ cm}^3\text{molecule}^{-1}\text{s}^{-1}$ and reproducible.

The zero-air measurement was conducted three times during the campaign, on June 19, 23 and July 14 giving a reactivity of 2 s⁻¹, 2.8 s⁻¹ and 2.5 s⁻¹, respectively. An average value of $2.4 \pm 0.4 \text{ s}^{-1}$ was chosen as k_{zero} for the whole campaign.

$$k_{\text{ambient}} = k_{\text{measured}} - k_{\text{zero}} \quad \text{Equation 32}$$

5.3.2. Complementary measurements

Gas-phase constituents such as anthropogenic and biogenic VOCs and some of their oxidation products were also measured during this campaign by different laboratories (Table 30) using different techniques including Proton Transfer Reaction-Mass Spectrometry (PTR-MS) and Gas Chromatography (GC) coupled to a flame ionization detector (FID) or a mass spectrometer (MS). PTR-MS technique is based on the chemical ionization through proton transfer to simultaneously monitor a suite of VOCs in air. The main problem in PTR-MS applications is the impossibility to specificity compounds with the same mass. The use of the PTR-MS in parallel with a GC-detector (FID) and the comparison of their measurements can provide information on the distribution of compounds that are associated with a given PTR-MS peak (a specific M/Z, mass over charge of the ion) and on possible interferences.

Table 30: List of the instruments measuring VOCs and sampling location; list of species measured available in Table 32

Group	Instrumentation	Level of Measurement (L1/L2)	Time resolution (min)	Data available	Data used
IMT-Lille-NE	PTR-ToFMS	Tower (L2)	0.16 (10 sec)	Y	Y
IMT-Lille-NE	GC/FID	Tower (L2)	60	Y	Y
ICARE	GC/FID/MS	Tower (L2)	40	Y	Y
INREA	PTR-ToFMS	Tower & Ground (L1 & L2)		N	
EPOC	PTR-ToFMS	Ground (L1)	10	Y	N
EPOC	GC/FID	Ground (L1)		N	Y
LISA	PTR-MS	Ground (L1)	10	Y	Y
LISA	GC/FID	Ground (L1)	30	Y	N

Inorganic species such as O₃ and NO_x (NO and NO₂) were measured by commercial analyzers deployed by IMT-Lille-NE (L2 for NO_x), ICARE (L1 for NO_x), LISA (L2 for O₃) and EPOC (L1 for O₃ and NO_x). Carbon monoxide (CO) concentrations were measured by the LISA research group.

The variation of the meteorological parameters such as temperature, relative humidity, global radiation, vertical turbulence, wind speed and wind direction during the campaign period was monitored using sensors. In this work, the data collected at 5 and 40 m height will be used to help with the discussion of results below and above the canopy, respectively.

5.4. Results and discussion

This section reports in the first part the measurements of the OH reactivity performed by the UL-FAGE instrument as well as the comparison with the calculated OH reactivity at the two levels L1 and L2. A second part of the section is dedicated to the radical concentration (OH, HO₂, HO₂^{*} and RO_x) measurements performed by the FAGE instrument from the PC2A laboratory (UL-FAGE and UL-RO_x-LIF) at 5 m height and a comparison with the other radical measurements performed by other groups.

5.4.1. OH reactivity

The OH reactivity measurements were performed by the UL-FAGE from June 20 to July 22 alternatively (20 min at each level) at two sampling levels (L1: below and L2: above the canopy) to study the evolution of the OH reactivity with the height and to determine the level of understanding of the OH losses by comparison with the calculated reactivity. above the canopy allows. First, the variability of the OH reactivity on the vertical scale is studied in

relation to some meteorological parameters. Then, a comparison between the measured and calculated OH reactivity for both heights as well as an analysis of the different VOC contributions are presented. Finally, we discuss the missing OH reactivity observed during this campaign and its possible origin.

5.4.1.1. OH reactivity measured and meteorological parameters

Figure 80 shows the variability of the total OH reactivity measured below and above the canopy by UL-FAGE with the global radiation, temperature and wind speed. Throughout the entire campaign, the OH reactivity measurements at both heights shows a diurnal trend ranging between LOD (1 s^{-1}) and 53 s^{-1} below the canopy and between LOD and 33 s^{-1} above the canopy. The averaged experimental OH reactivity was found to be 7.7 s^{-1} and 5.8 s^{-1} below and above the canopy, respectively.

A higher OH reactivities were recorded during the second part of the campaign (starting July 10) and typically during the nighttime. Four maximum values were recorded during the nighttime, the highest one equal to 53 s^{-1} at 5 m height, 1.6 times higher than that observed above the canopy level at 40 m of height. These OH reactivity values are in with the same range than the other measurements performed in temperate forested environments (Di Carlo et al., 2004; Hansen et al., 2014; Kumar & Sinha, 2014; Mao et al., 2012; Nakashima et al., 2014; Nölscher et al., 2013; Ren et al., 2006), with maximum values higher than that reported for boreal forests (Nölscher et al., 2012; Sinha et al., 2010) and lower than the values reported for tropical (Edwards et al., 2013; Ingham et al., 2009; Sinha et al., 2008) and Mediterranean (Zannoni et al., 2016) forests (Figure 79).

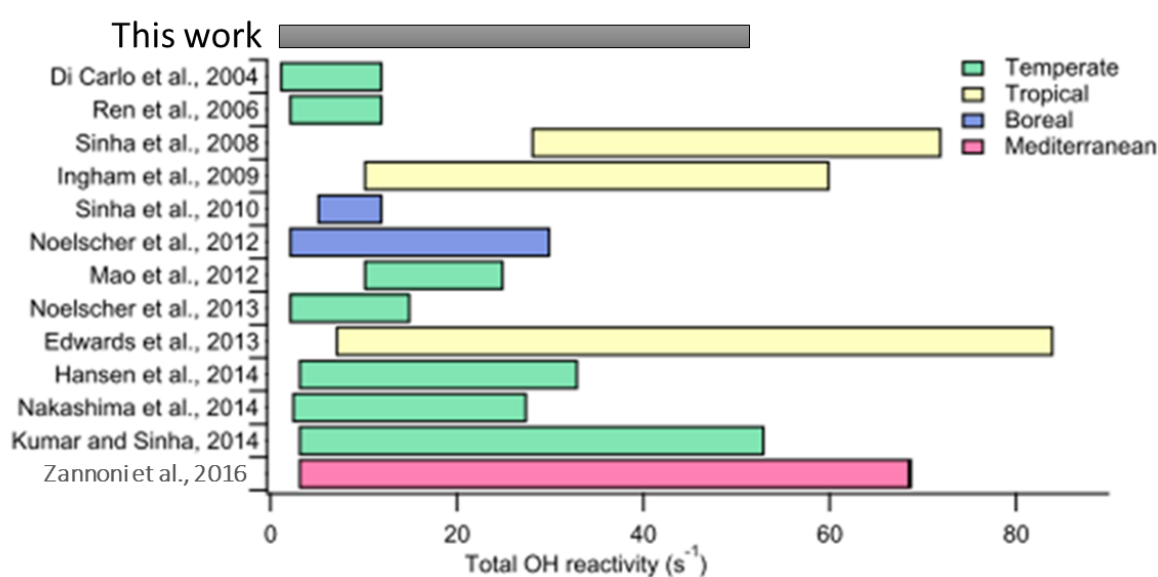


Figure 79: OH reactivity results from published measurements conducted worldwide at forested environments. (Zannoni et al., 2016)

The predominant meteorological parameter that had a role in OH reactivity levels was the ambient temperature which is known to enhance BVOC emissions during the day when the stomata are open and during the night due to permeation, even though the stomata are closed in the dark (Jud et al., 2016; Simon et al., 1994; Zannoni et al., 2016). Figure 81 shows that the OH reactivity increases depending on the temperature. To analyse the OH reactivity, the temperature conditions were divided into 4 subclasses:

- Cd corresponds to daytime (6:00-9:00 h) cool conditions (days with mean $T < 27$ °C)
- Wd include warmer days ($T > 27$ °C)
- Cn includes nighttime (21:00-6:00 h) cool conditions (nights with mean $T < 18$ °C)
- Wn for warmer nights ($T > 18$ °C).

Focusing on the nighttime measurements, it can be seen that the magnitude of the measured OH reactivity was temperature dependent. Indeed, higher OH reactivity values were recorded during the second part of the campaign in Wn conditions, such as during the nights of July 13, 18, 19 and 20 with an average temperature of 20 °C. During the day, the OH reactivity also increased depending on the temperature reaching a maximum of up to 53 s⁻¹ below the canopy and 33 s⁻¹ above the canopy on July 19 associated with the ambient temperature which increased to reach a maximum 37 °C corresponding to the peak of the heatwave period.

When during the day, the reactivity above and below the canopy were similar, a clear stratification (significant difference of the reactivity measured between both levels) was often observed at night during this campaign. These nights correspond to conditions with a wind blowing from the same direction during the night with low speed (Figure 80 (B)). It highlights a low vertical turbulence intensity, which can lead to a lower boundary layer as observed in previous studies (Bsaibes et al., 2020; Fang et al., 2020; Saraiva & Krusche, 2013; Xia et al., 2016) with accumulated biogenic compounds within the canopy. The stratification phenomenon was observed on June 23 (Figure 82), the OH reactivity measured at night above the canopy increased to reach a maximum value of 25 s⁻¹, a factor of 2 higher than that measured above the canopy (6 s⁻¹) while the wind blew from the same direction with low speed suggesting stable meteorological conditions. During the heatwave period corresponding to warm stable nighttime conditions (Figure 83), on July 17, 18 and 19, a similar vertical stratification in the OH reactivity can be observed. On these three days the daytime air temperature was the highest registered over the whole campaign, with also the highest OH reactivity (around 20 s⁻¹) at both levels. As an example, on July 19 (Figure 83), at 6 h when the wind speed started to increase from 4 to 7 m s⁻¹ and wind directions changed, causing unstable atmospheric conditions, equal OH reactivity at both levels was recorded. However, the wind speed and wind directions are not the

only parameters we should consider in order to explain the OH reactivity variation during the day and nighttime and between both levels.

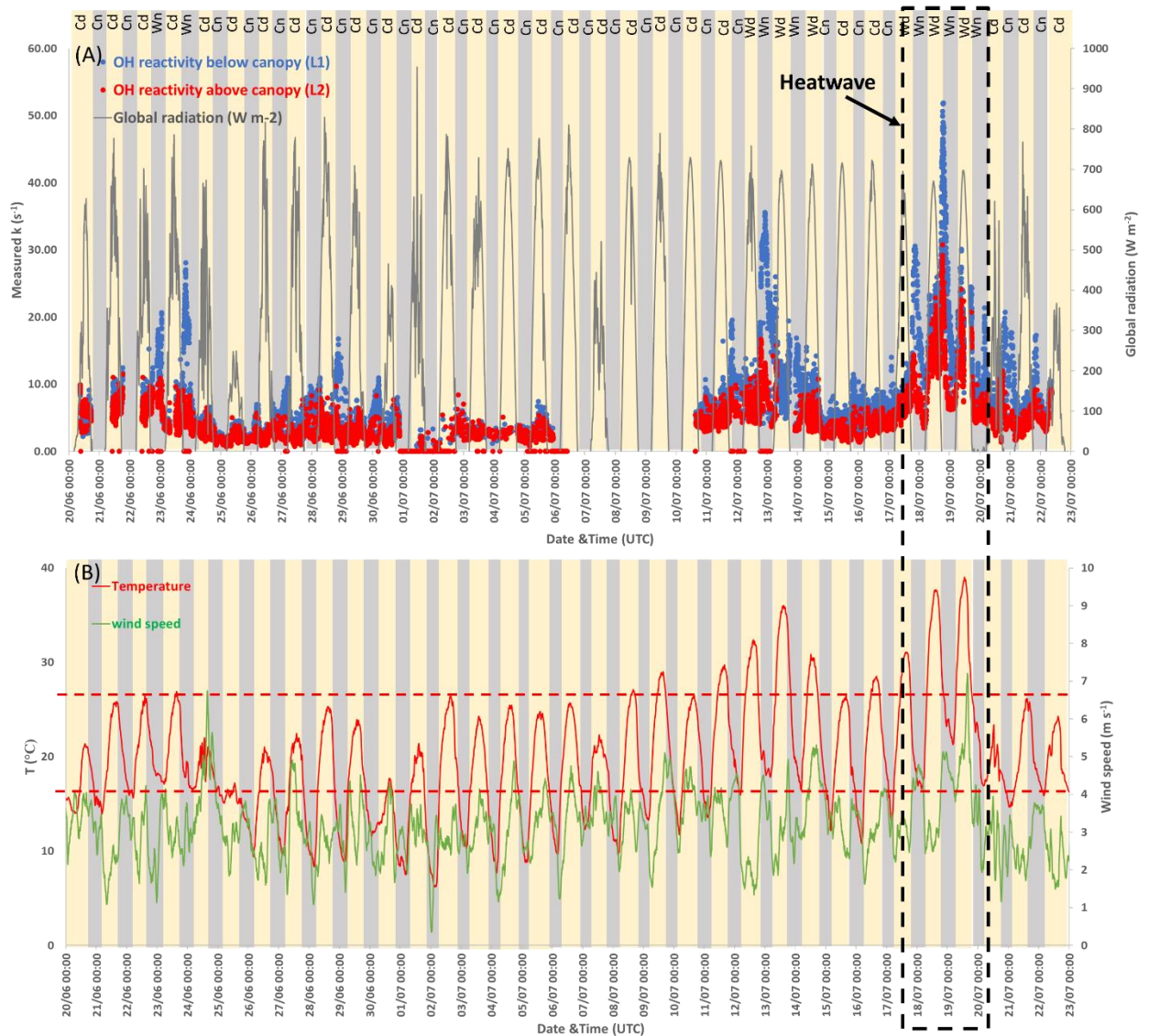


Figure 80: (A) Measured OH reactivity by UL-FAGE below and above the canopy and global radiation, (B) Temperature and friction velocity, red dashes indicate the temperature thresholds to distinguish between warm and cool days and nights. Yellow stripes indicate daytime and grey stripes indicate nighttime. Cn and Cd stand for cooler nights and says, respectively. Wn and Wd stand for warm nights and warm days, respectively

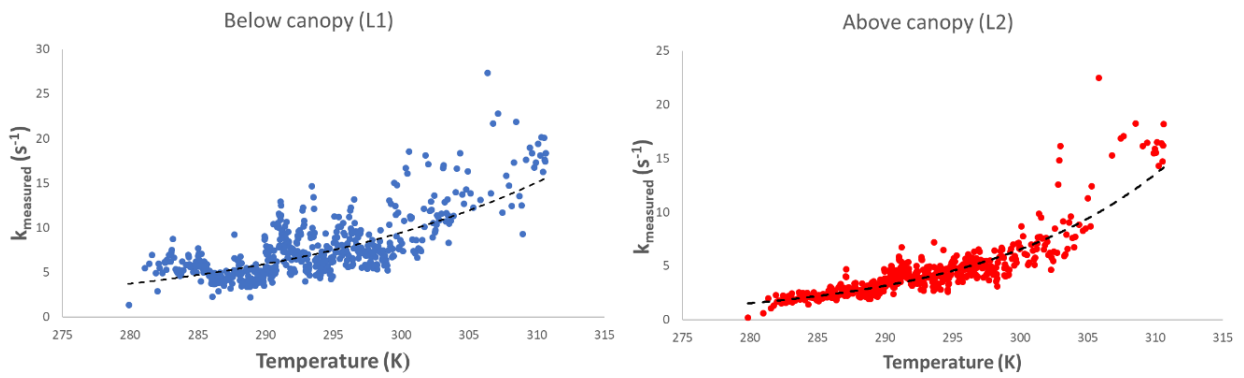


Figure 81: Averaged OH reactivity (s^{-1}) measured below (left figure) and above (right figure) the canopy as function of temperature (K)

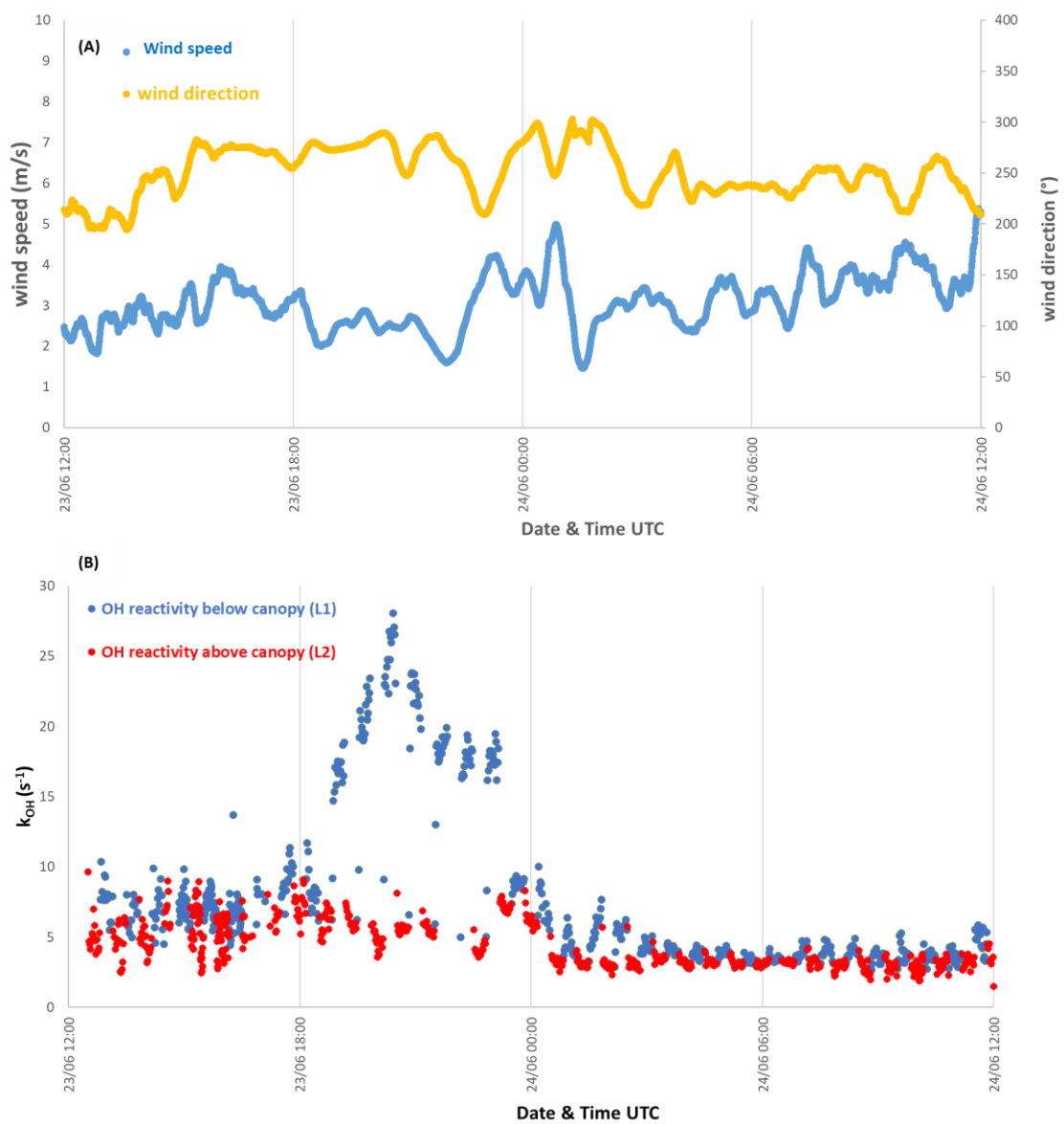


Figure 82: June 23 – 24, (A) wind speed and wind direction data collected at 40 m height, (B) OH reactivity measured below and above the canopy

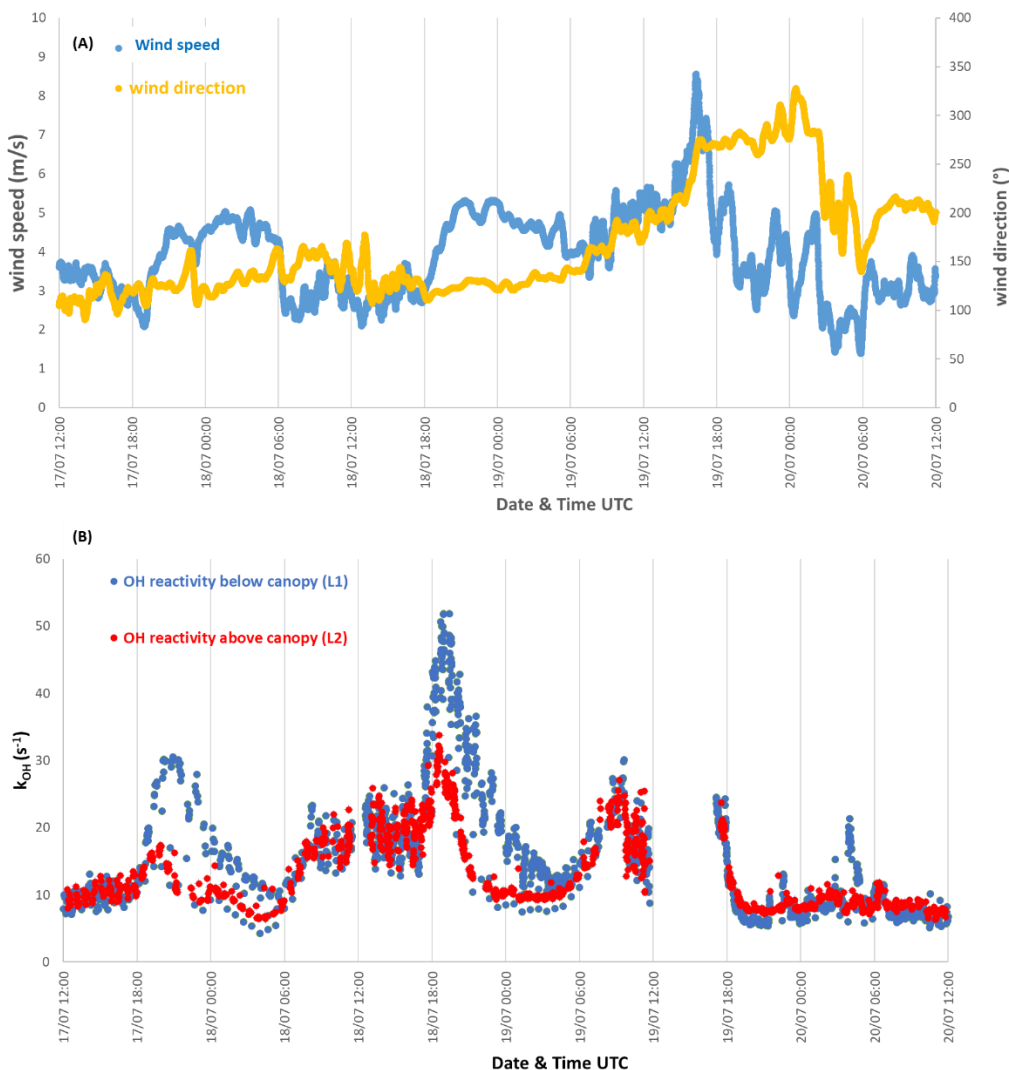


Figure 83: July 17 to 20, (A) wind speed and wind direction data collected at 40 m height, (B) OH reactivity measured below and above the canopy

Examining the primary emitted BVOC profiles (Figure 84) (measured in the second part of the campaign: July 10 to July 23), we can see that isoprene has clear diurnal profiles at both sampling heights with maximum at about 14:00-16:00 h. Monoterpenes reach their maximum during the nighttime below the canopy with a concentration starting to increase at the beginning of the night (20:00-22:00 h) to reach its maximum at midnight and then dropping as soon as the first sunlight broke the stable nocturnal boundary layer. During nighttime, higher monoterpene concentration (by a factor of 10) is observed below the canopy showing a clear vertical stratification consistent with the difference in OH reactivity measured at the two different levels (L1 and L2).

During the daytime, the unstable conditions (higher turbulence) leads for well mixing of the BVOC below and above the canopy, where we observe an isoprene concentration below the canopy higher than the one measured above the canopy only by a factor of 2 (we observed a

decrease in the isoprene measured above the canopy due to the averaging over 10 mins). Considering this homogeneity of the gas mixture composition at a given height and strong reactivity of isoprene with OH, we observed a similar reactivity below and above the canopy than during the night. To analyse more in details the contribution of the different VOCs to the OH reactivity, the measured OH reactivity was compared to the calculated one at both heights.

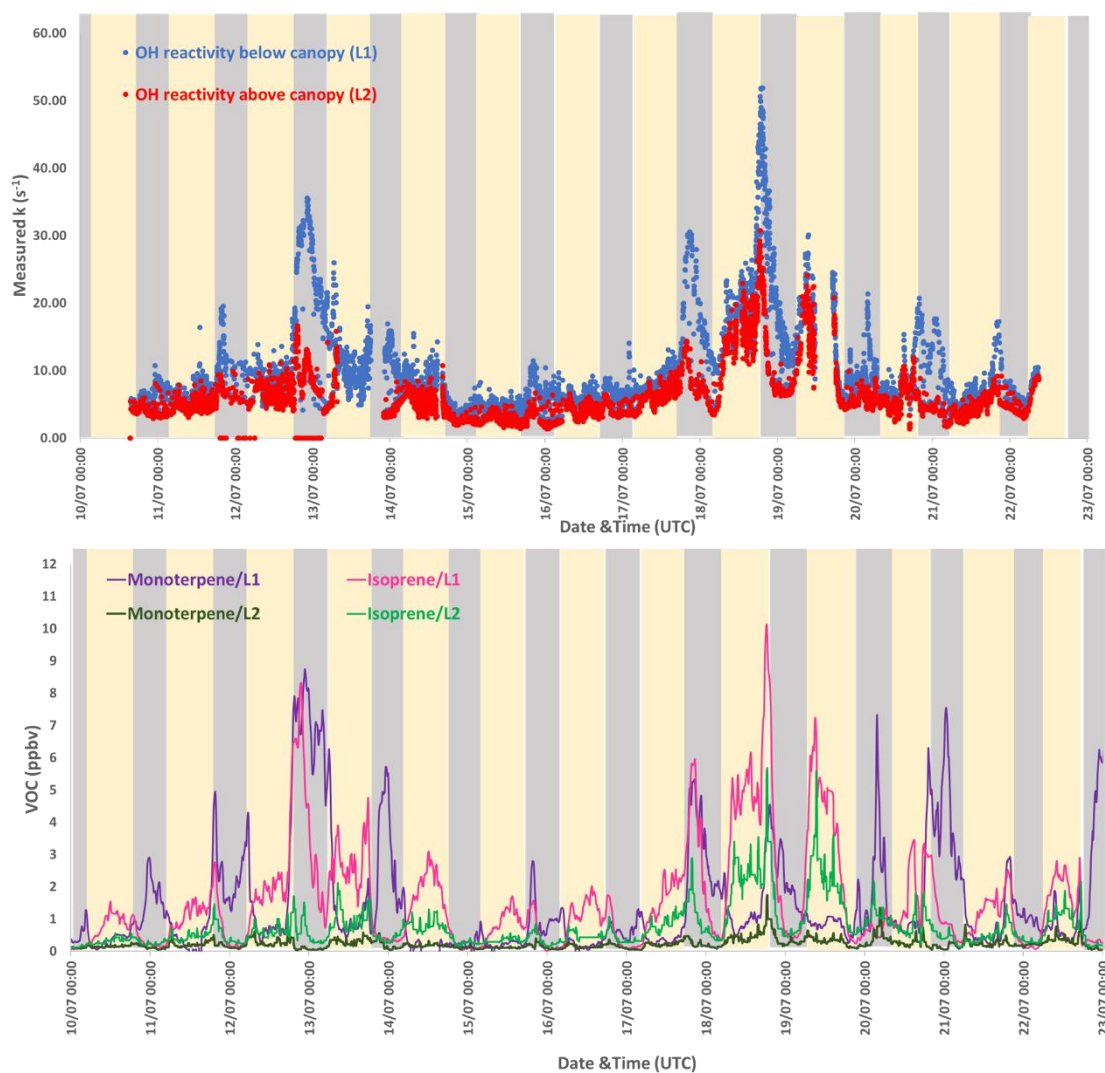


Figure 84: OH reactivity measured above and below canopy (upper graph) and sum of monoterpenes and isoprene mixing ratios (L1: LISA-PTR-MS and L2: IMT-PTR-MS) (lower graph)

Remarkably, the profile of OH reactivity resembled that of isoprene concentration during the day and that of monoterpenes during the night. This behavior was also observed during the LANDEX campaign (Bsaibes et al., 2020). However, the monoterpene concentration measured during the LANDEX campaign was 3 times higher than that measured during this campaign, reaching a maximum of around 30 ppbv, below the canopy, and thus obtaining a higher OH reactivity during the nighttime (99 s^{-1}) compared to this campaign (53 s^{-1}). While the isoprene concentration is in the same range as this campaign (3-10 ppbv).

5.4.1.2. *OH reactivity calculation*

As the aim of comparing measured and calculated reactivity is to identify missing reactivity and potential variation between L1 and L2, we had a pre-analysis of the VOCs data to select the most complete and more adapted data to calculate the reactivity at both levels taking into account the resolution time of the instrument and the species measured (list in Table 32).

Since the measurements from the PTR-MS instruments cover the whole measuring period starting July 28, with a high-resolution time, these measurements were preferred to be used to calculate the OH reactivity. However, these datasets suffer from different limitations such as measuring the total monoterpenes (m/z 137 + m/z 81) that are speciated by the GCs, absence of some species (such as alkanes) and possible interferences on the isoprene measurements (m/z 69) due to the fragmentation of some terpenic species (Kari et al., 2018; Tani, 2013). Therefore, to complete the PTR-MS measurements used to calculate the OH reactivity below and above the canopy, it was necessary to analyse the GCs measurements with the aim of speciating the monoterpenes (similar to Bsaibes et al., 2020) and obtain more VOCs profiles.

When available, we first compared the data of different instruments at the same level but we also compared some VOCs profiles at the two levels, at least in term of range of concentration measured. Indeed, if we expect periods with differences between the two levels, we also expect periods of well mixed air mass between the ground and above the canopy and then agreement between measurements at L1 and L2 during these periods. It is what has been observed on the OH reactivity mainly during the daytime (Figure 84).

The only GCs data available for now is the IMT-GC and ICARE-GC data sets. However, all the GCs measuring at the Rambouillet site suffered from some technical issues and the sum of speciated monoterpenes measured were lower in concentration than that measured by the PTR-MS instruments. A possible reason behind this disagreement would be that monoterpenes adsorbed in the GC trap were reacting with ambient O_3 as none of the GCs implemented an ozone scrubber on their sampling line during the ACROSS campaign. The ICARE-GC measurements (L2) for monoterpene was around zero (Figure 85) and it was not possible to be used to determine the ratio of monoterpenes at L2.

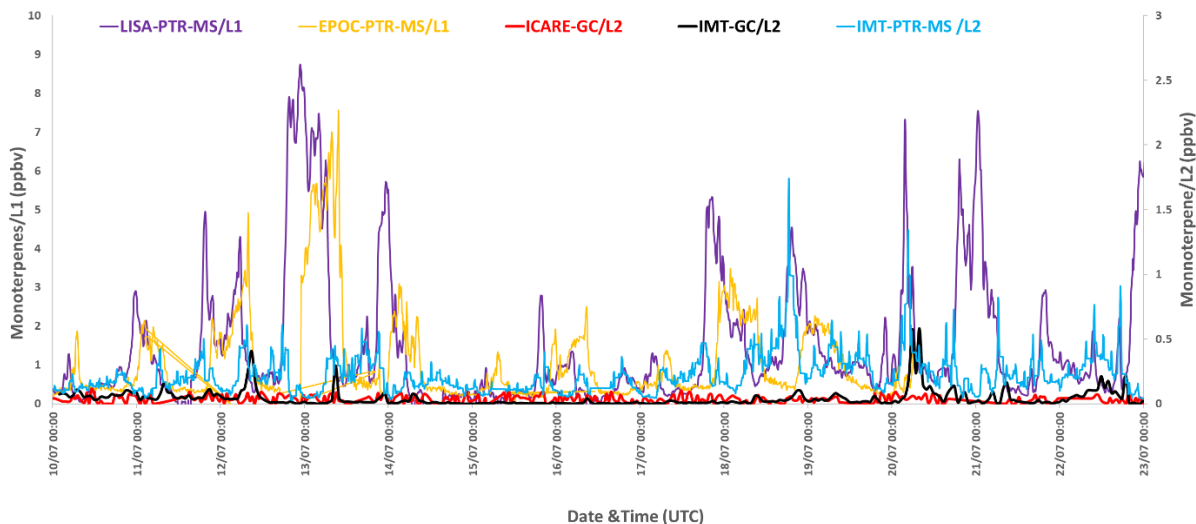


Figure 85: The sum of monoterpenes measured with the IMT-PTR-MS and ICARE-GC above the canopy and with the LISA-PTR-MS and EPOC-PTR-MS below the canopy

Since the only speciated monoterpene concentrations on a limited number of monoterpenes were only measured by the IMT-GC instrument, it will be used as a reference data to determine the ratio of the different monoterpenes. Indeed, each monoterpene has a different rate constant with OH (Table 31). This ratio allows to determine a weighted rate constant to be used (Equation 33) to multiply with the concentration of the sum of monoterpenes measured by the PTR-MS instruments to calculate the OH reactivity. The weighted rate constant is defined as follows:

$$k_{weighted} = \sum_i k_{OH+xi} Xi \quad \text{Equation 33}$$

where Xi represents the ratio of each speciated monoterpene and $k_{OH+xi} Xi$ is the rate constant of the reaction of each monoterpene with OH. The contribution Xi was calculated by dividing the concentration of each individual monoterpene measured by the IMT-GC-MS by the total concentration. As shown in Figure 86, the average $k_{weighted}$ determined from the IMT-GC measurements from July 9 to July 23 was equal to $72 \times 10^{-12} \text{ cm}^3 \text{ molecule}^{-1} \text{ s}^{-1}$.

Table 31 : Rate constant of the reaction of OH with monoterpenes (Atkinson, 2006)

Speciated Monoterpene	Rate constant ($\times 10^{-12} \text{ cm}^3 \text{ molecule}^{-1} \text{ s}^{-1}$)
α -pinene	53.3
β -pinene	78.1
Limonene	167
3-carene	84.5

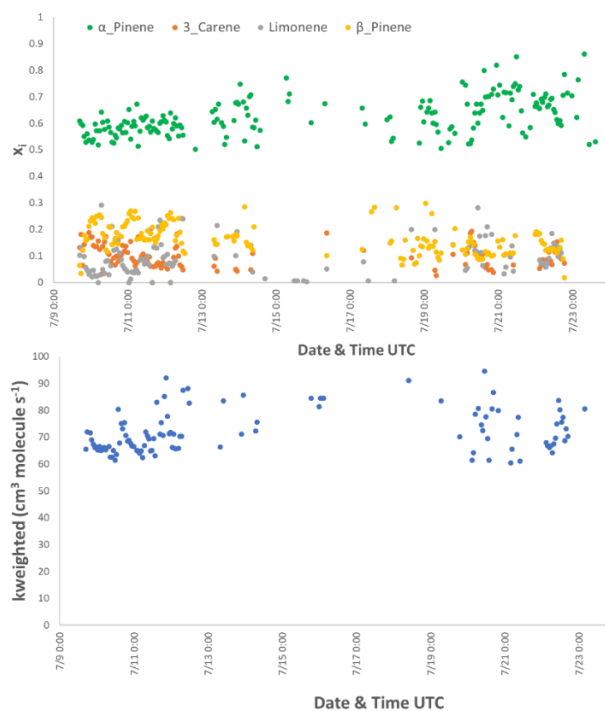


Figure 86: upper graph shows the X_i and lower graph shows the k_{weighted} determined from the speciated monoterpenes measured by the IMT-GC

Since k_{weighted} determined from the IMT-GC is stable over its measuring period and being the only available speciated measurement, it will be used as a reference rate constant for the sum of monoterpenes above and below the canopy.

After the determination of weighted rate constant, the OH reactivity of monoterpenes was calculated using the concentration of the sum of measured by the PTR-MS according to the following equation:

$$k_{OH+monoterpene} = \left[\sum_i k_{OH+xi} X_i \right] \times [Monoterpenes] \quad \text{Equation 34}$$

where $[Monoterpenes]$ represents the total concentration of monoterpenes obtained with the PTR-MS instrument.

The comparison for other species showed that the isoprene measurements of ICARE-GC had a high disagreement with the measurements of IMT-PTR-MS and IMT-GC above the canopy, but also with the measurements of other PTR-MS instruments measuring below the canopy (L1) (Figure 87). Same trends and concentration range were observed even if it seems to have an offset on the EPOC data (for all VOCs, thus we did not include this data in the OH reactivity calculation). Therefore, the measurements of IMT-PTR-MS for isoprene was used for the calculated OH reactivity above the canopy. Interestingly, a scatter plot of the isoprene measurements of the LISA-GC-FID vs the measurements of LISA-PTR-MS showed a very

good correlation (Figure 88) with a slope of 1.06 and $r^2 = 0.92$. Thus, the isoprene measured by the LISA-PTRMS was used for the calculation of the OH reactivity below the canopy.

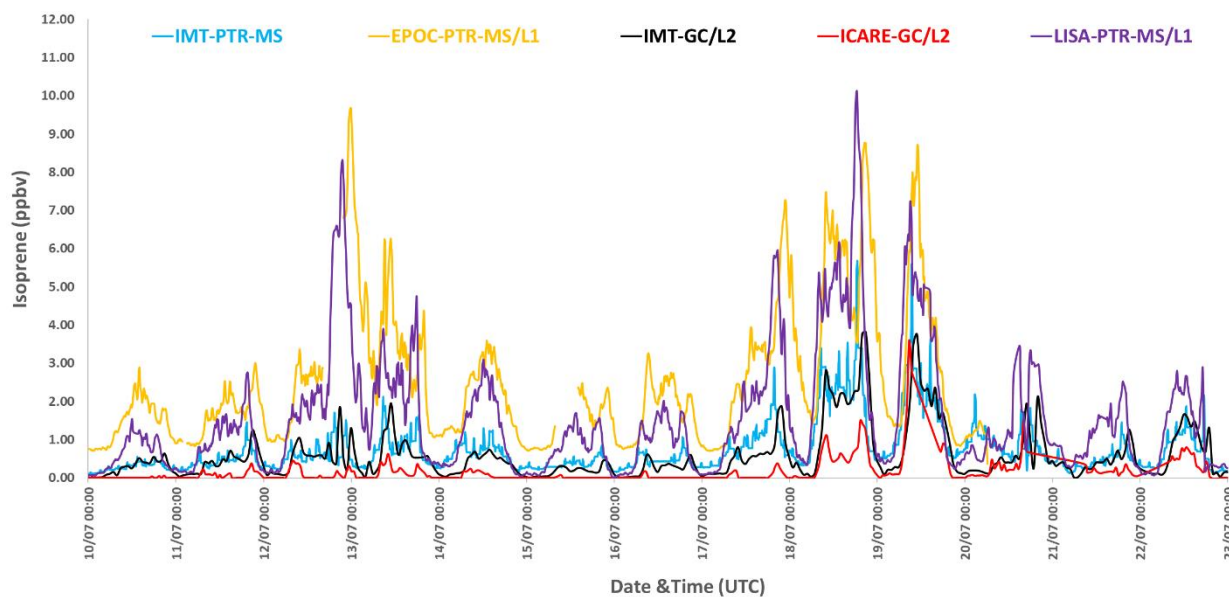


Figure 87: The isoprene measured with the IMT-PTR-MS and ICARE-GC above the canopy and with the LISA-PTR-MS and EPOC-PTR-MS below the canopy

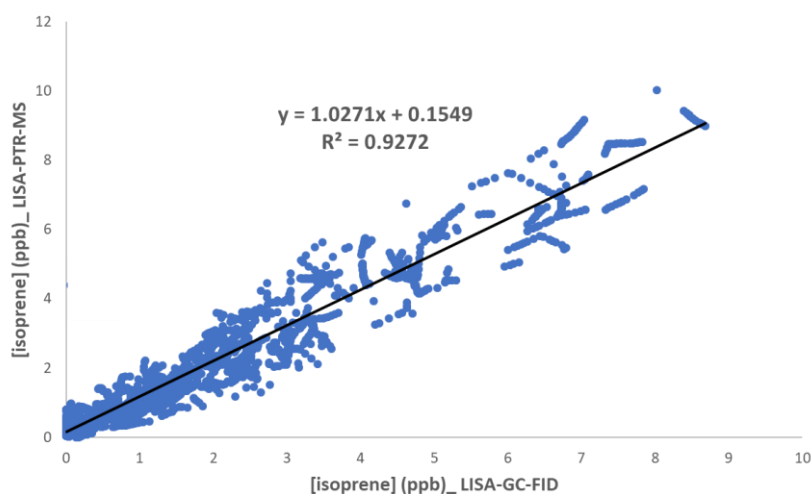


Figure 88 : Scatter plot between the LISA-PTR-MS and LISA-GC-FID isoprene mixing ratio

After checking the consistency between the GC and PTR-MS deployed by the LISA group, the non-methane hydrocarbons (NMHCs), including alkanes and alkenes measured by the LISA-GC-FID below the canopy can be included in the calculation of the OH reactivity. However, the LISA-GC-FID only measured during the second part of the campaign (July 12 to August 23) due to technical problems. Thus, the OH reactivity was only calculated for this period and further work will be done on calculating the OH reactivity for the first part of the campaign below and above the canopy as the data will be available from the other groups.

Concerning the aromatics, PTR-MS cannot speciate the C8-aromatics (m,p,o xylenes) and IMT identified a measurement problem for benzene. Therefore, we used the concentration measured by the ICARE-GC for the aromatics for the calculation of the OH reactivity.

The data used to calculate the OH reactivity below and above the canopy are presented in Table 32. The OH reactivity measured and calculated have been resampled to 10 mins.

Table 32 : Measured species used for calculating OH reactivity below and above the canopy

Measured species	Instrument Level 1	Instrument Level 2	Max k _{OH} (s ⁻¹) Level 1	Max k _{OH} (s ⁻¹) Level 2
isoprene	LISA-PTR-MS	IMT-PTR-MS	23.9	22.7
sum of monoterpene	LISA-PTR-MS	IMT-PTR-MS	16.3	5.5
methacrolein (MAC) + methylvinylketone (MVK) + fragment ISOPOOH	LISA-PTR-MS	IMT-PTR-MS	3.6	2.8
Methanol, acetaldehyde and acetone	LISA-PTR-MS	IMT-PTR-MS	2.1	2.2
toluene and benzene	LISA-PTR-MS	ICARE-GC-FID/MS	0.1	0.1
C8 and C9 aromatics	LISA-PTR-MS	–	1.3	
ethylbenzene, m+p-xylene, o-xylene, 1,3,5-trimethylbenzene (TMB) and 1,2,4-TMB	–	ICARE-GC-FID/MS		0.3
α-pinene, β-pinene, Δ-carene and limonene	–	IMT-GC-FID		0.8
methylglyoxal, formic acid and acetic acid	LISA-PTR-MS	IMT-PTR-MS	0.7	0.3
furan, nopinone and acetonitrile	LISA-PTR-MS	IMT-PTR-MS	0.7	0.5
ethane, propane, propene, i-butane, n-butane, i-pentane, n-pentane, n-hexane	LISA-GC-MS	–	1.5	
trans-2-butene, 1,3-butadiene, i-pentane, n-hexane	–	IMT-GC-MS		0.1
NO _x	EPOC	IMT	5.5	6.4
O ₃ ,	EPOC	LISA	0.1	0.2
CO	LISA	–	0.9	

5.4.1.3. Measured and calculated OH reactivity below and above the canopy

Figure 89 shows the variability of the measured and calculated OH reactivity at 5 and 40 m of height, respectively, and the missing reactivity (data averaged over 2 hours), which represents the difference between OH reactivity measured and calculated at each level. Due to the absence of some BVOCs measurements during the first period of the campaign we focus on the second part of the campaign starting on July 10 to comment on the missing OH reactivity. A good agreement of the measured and calculated OH reactivity below the canopy, considering

the compounds presented in Table 32, can be observed during this period. However, some differences are observed mainly during the nighttime where a missing OH reactivity reached more than 50 %. The negative values in the missing reactivity (mostly during the daytime) can be either due to the underestimation of the OH reactivity measured by the UL-FAGE (loss of the reactive species through the sampling lines) or overestimation of the species measured by the instruments reported in Table 32. Time synchronization between measured and calculated OH reactivity could be also a reason behind these negative values.

The comparison between measured and calculated OH reactivity above the canopy shows a bigger difference compared to below the canopy. These results indicate that the missing OH reactivity above the canopy is more important than below the canopy. A missing OH reactivity of an average of 50 % is determined above the canopy over the whole measuring period considered (day and nighttime). The difference in the oxidation processes contribution can explain part of the difference in the magnitude of the missing OH reactivity between the two different levels where above the canopy there was more time to transform primary species into secondary species. These oxidated species could be an important source of the missing OH reactivity.

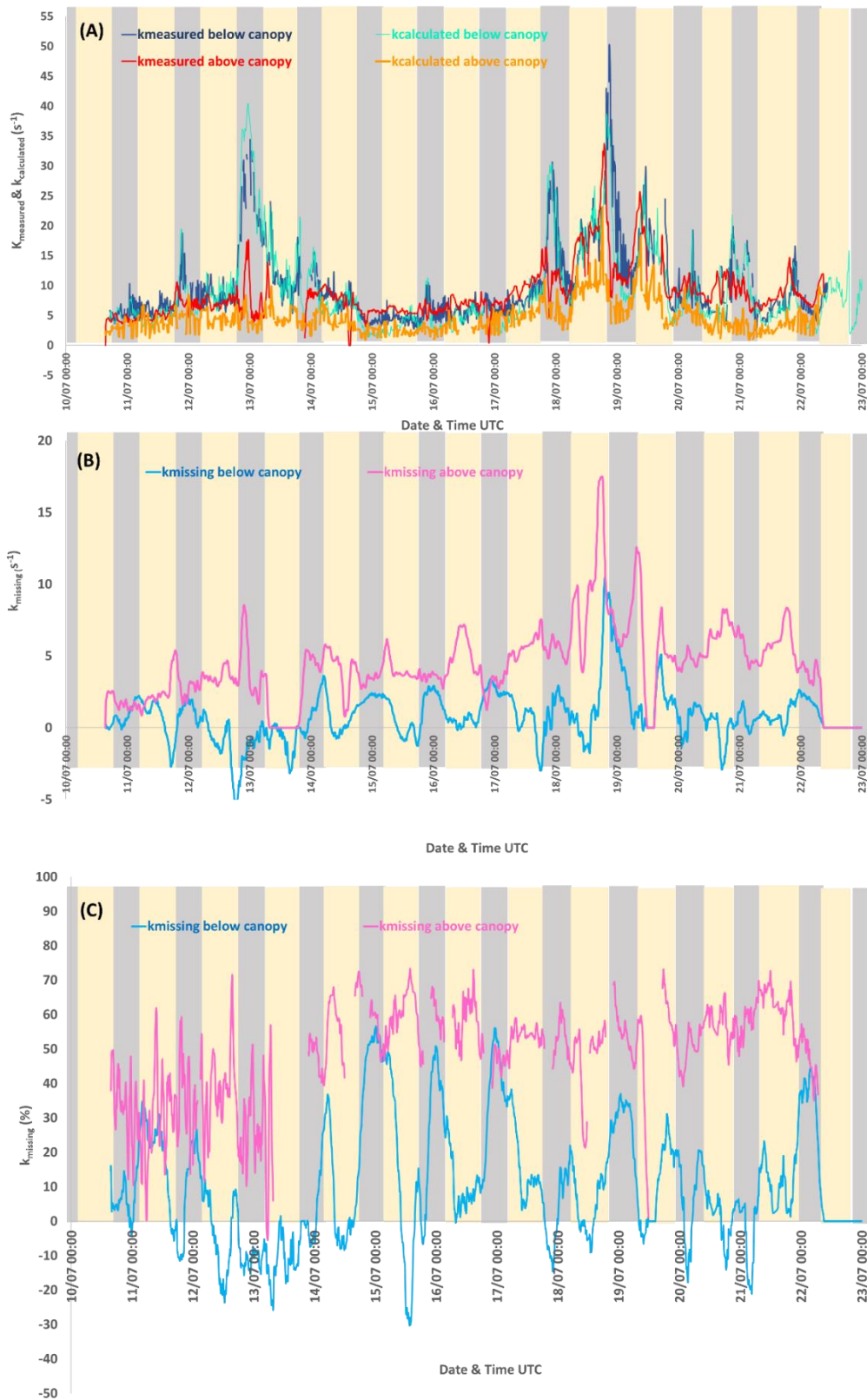


Figure 89: (A) Variability of measured and calculated OH reactivity (B) the difference between measured and calculated OH reactivity (missing OH reactivity) and (C) percentage of the missing OH reactivity at both heights

5.4.1.4. *Contribution of VOCs to calculated OH reactivity at two heights*

Figure 90 shows the breakdown of reactive components in OH reactivity below and above the canopy, considering the period for which the OH reactivity was calculated (July 10 to July 22) and including nights and days (average reactivity). As expected, isoprene being among the most reactive towards OH and the most abundant compound in this forest during the daytime (Figure 80), is the main contributor of the OH reactivity calculated. At 40 m, isoprene represented 55 % of the total OH reactivity, and 45 % at 5 m. The monoterpenes have the second contribution on the OH reactivity with around 35 % below the canopy and 13 % above the canopy. The third most reactive species was the group of MVK+MACR+ISOPOOH with 8 % below the canopy and 12 % above the canopy. Its contribution is more important above the canopy, consistent with oxidation processes. Followed by acetaldehyde with 5 % below the canopy and 12 % above the canopy, and the remaining is for other VOCs.

A deeper analysis can be done splitting the nights and days as the VOCs profiles were strongly contrasted between these periods. Figure 90 shows also the breakdown of the reactive components to the calculated OH reactivity during daytime and nighttime at the two heights. We clearly see that isoprene is the main contributor to the calculated OH reactivity during the daytime at the two heights, representing 56 % and 47 % of the calculated OH reactivity above and below the canopy, respectively. During nighttime (period considered between 21:00 to 6:00), if isoprene stays the main contributor above the canopy, monoterpenes are clearly the main contributors below the canopy, representing 52 % of the calculated OH reactivity.

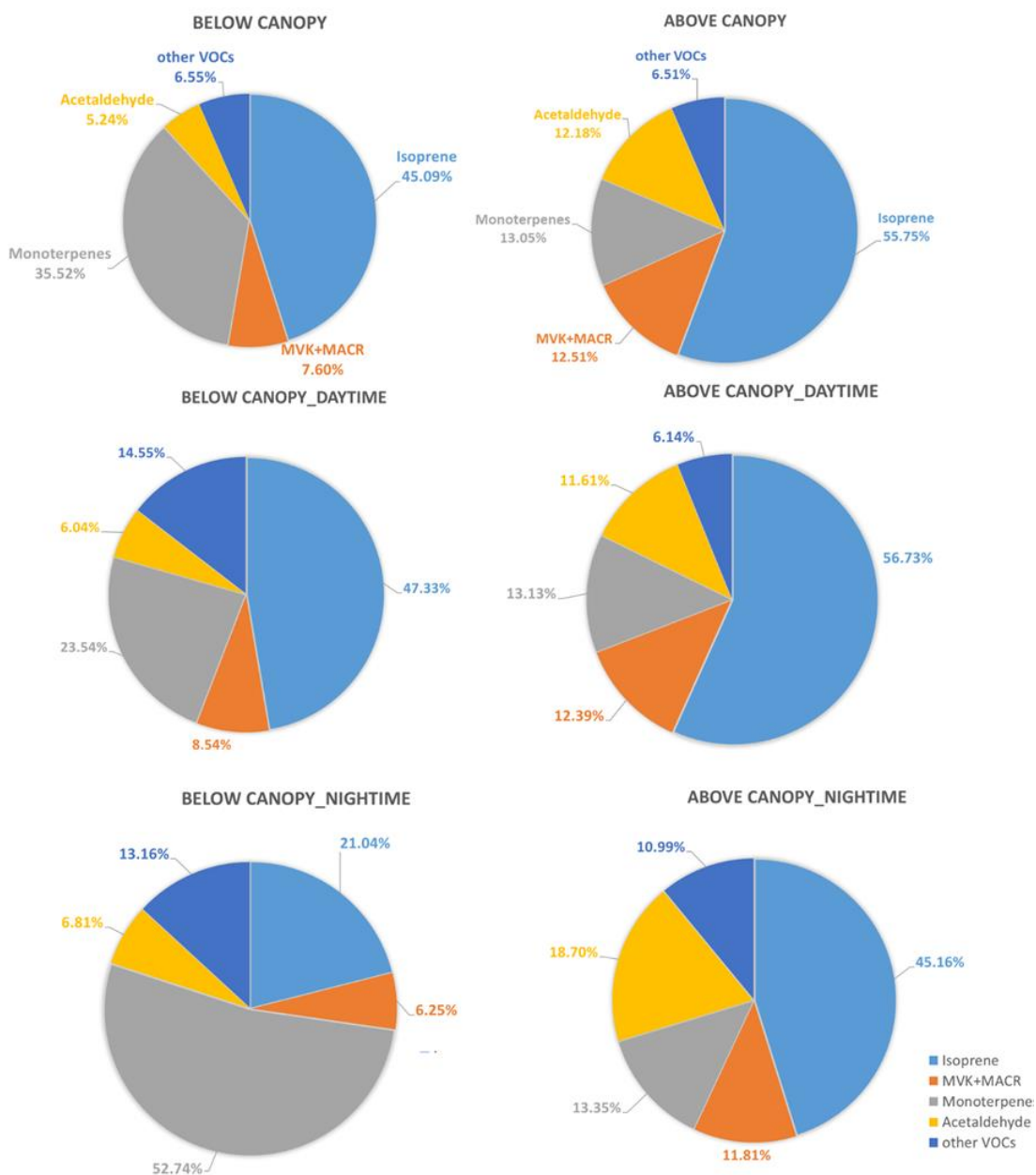


Figure 90: The components of calculated OH reactivity inside and above the canopy during the campaign period (from July 10 to July 23) from bottom to top: day and nighttime, only daytime and only nighttime

The relative contribution of monoterpenes and isoprene during ACROSS is a lot less contrasted than what has been observed during the LANDEX campaign where monoterpenes were all the time the main contributors even if isoprene contribution was relatively high during the day. It shows that depending of the type of forest, the type of emission and the related chemistry can be very different. A more detailed analysis of the relative reactivity of the different oxidants with the BVOCs such as proposed by Mermet et al. (Mermet et al., 2021) could be useful to better study the oxidation processes.

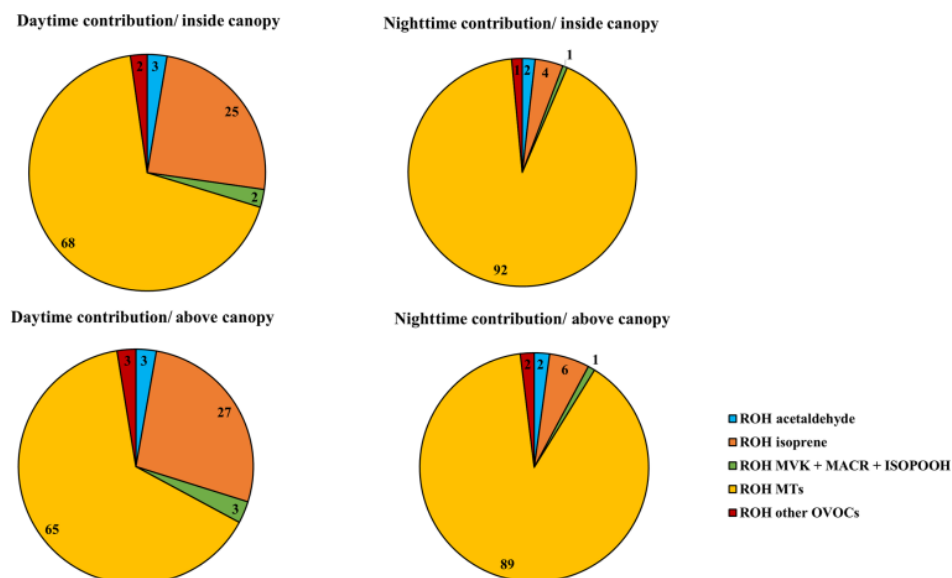


Figure 91: The components of calculated OH reactivity inside and above the canopy during the LANDEX campaign

5.4.2. Radical Quantification

The OH, HO₂ and HO₂^{*} concentrations were measured by the UL-FAGE instrument from the PC2A laboratory during the ACROSS campaign period from June 13 to July 23 with some missing days of measurements due to either technical problems or cell (OH or HO₂ cell) alignment. The OH concentration was measured in the first FAGE cell, HO₂ and HO₂^{*} concentrations were measured in the second FAGE cell placed downstream the first cell after chemical conversion to OH with NO in two modes: with low NO mode, adding small amount of NO (0.5 sccm) to quantify HO₂ without critical conversion of RO₂ from alkenes or aromatic precursors (conversion efficiency of 20 %) and alternatively with a high NO mode (NO flow = 10 sccm) to favor the conversion of RO₂ and quantify it (HO₂^{*} = HO₂ + RO₂). This flow was controlled to change the measurement mode every 10 minutes. The method used to extract the estimated concentration of HO₂ and RO₂ converted in the cell is described in detail in chapter 2.

The RO_x (HO₂ and HO₂^{*}) and HO₂^{*} concentrations were measured by the UL-RO_x-LIF setup from the PC2A laboratory for a limited period only: from July 10 to July 22, due to the optimization of the working conditions of this new setup at the beginning of the campaign. The HO₂^{*} concentration was measured during the HO_x mode where only CO is added in the conversion flow tube to convert only OH to HO₂ and RO_x (HO₂ and HO₂^{*}) concentration was measured during the RO_x mode when both CO and NO are added into the conversion flow tube to convert all ambient radicals into HO₂ that will be converted later into OH by injecting NO at

the entrance of the FAGE cell (RO_x cell). Finally, OH is detected by LIF at low pressure in the FAGE cell.

The FAGE instruments (UL-FAGE and UL-RO_x-LIF) were calibrated five times during the campaign period and the calibration factors used for the data analysis were taken from the average of five calibration points. The sensitivity of the RO_x cell was very low, giving scattered data. However, the comparison between the HO₂^{*} concentration measured in this cell with the HO₂^{*} concentration measured in the HO₂ cell is interesting to study the behaviour of our instrument in real ambient conditions.

A comparison between the OH concentration measured by our UL-FAGE and the LPC2E-CIMS is presented as well as a comparison between the RO_x measurements performed by the three different instruments: UL-FAGE, LPC2E-CIMS at L1 and IMT-PERCA at L2.

5.4.2.1. *OH quantification*

Figure 92 shows the measured OH radical from June 25 to July 20, with a missing period from July 4 to July 8 due to the disconnection and alignment of the OH FAGE cell trying to increase its sensitivity and because of other technical problems. The OH mixing ratio reached a maximum up to 0.25-0.32 ppt ($[\text{OH}] = 6-8 \times 10^6 \text{ molecule cm}^{-3}$) during the midday (around 12:00 h), while the minimum mixing ratios were measured during the night and were in the range of 0.006-0.02 ppt ($[\text{OH}] = 1-6 \times 10^5 \text{ molecule cm}^{-3}$). During the first part of the campaign, from June 25 to July 8, the temperature reached a maximum around 27 °C during the day, and it became warmer in the second part of the campaign, starting July 9, to reach a maximum of 40° C during the day on July 13, 18 and 19. This increase in temperature caused the damage of the cooling system of the pumps and thus missing some days of measurements. As can be seen in Figure 92 the O₃ concentration showed a diurnal profile in correlation with the temperature diurnal profile with a maximum reached in the afternoon and a minimum at night. During the first part of the campaign, the O₃ mixing ratio observed were similar with a maximum of 55 ppb during the day and a minimum of 2 ppb at night. On the second part of the campaign the O₃ mixing ratio stayed at approximately 70 ppb during day and 13 ppb during the night.

The photolysis of O₃ and subsequent reaction with H₂O is well known as the dominant source of OH during the daytime (Ehhalt & Rohrer, 2000). This can explain the variation in the OH concentration depending on the O₃ concentration and temperature variation (Figure 93). The HONO accumulated during the night to reach the maximum mixing ratio at 3:00-4:00 h, which starts to decrease during the day. Therefore, in the early morning hours the photolysis of HONO, which starts earlier than O₃ photolysis, is considered as the dominant source of OH. A similar behavior has been observed during the BERLIOZ field campaign (Jiang et al., 2020;

Holland et al., 2003). However, a more detailed calculation of the different contributions of the OH production should be performed as well as a comparison between measured and modelled profiles in order to better understand the OH concentration profiles.

The OH mixing ratios peaks to reach 0.25-0.32 ppt ($[OH] = 6-8 \times 10^6 \text{ molecule cm}^{-3}$) during the midday are in the same range than the measurements performed at a rural site (semi-polluted) during BELOIZ campaign (Mihelcic et al., 2003), and forested environments such as in BEARPEX-2007 (Wolfe et al., 2011). However, these ACROSS OH measurements are slightly higher than the ones measured in urban environment such as the recent ClearfLo campaign done in London in the summer of 2012 (Whalley et al., 2018) where the OH profiles varied between $2-4 \times 10^6 \text{ molecule cm}^{-3}$, while the measured concentrations in Wangdu (rural environment in China) are slightly higher ranging between $5-15 \times 10^6 \text{ molecule cm}^{-3}$ (Tan et al., 2017).

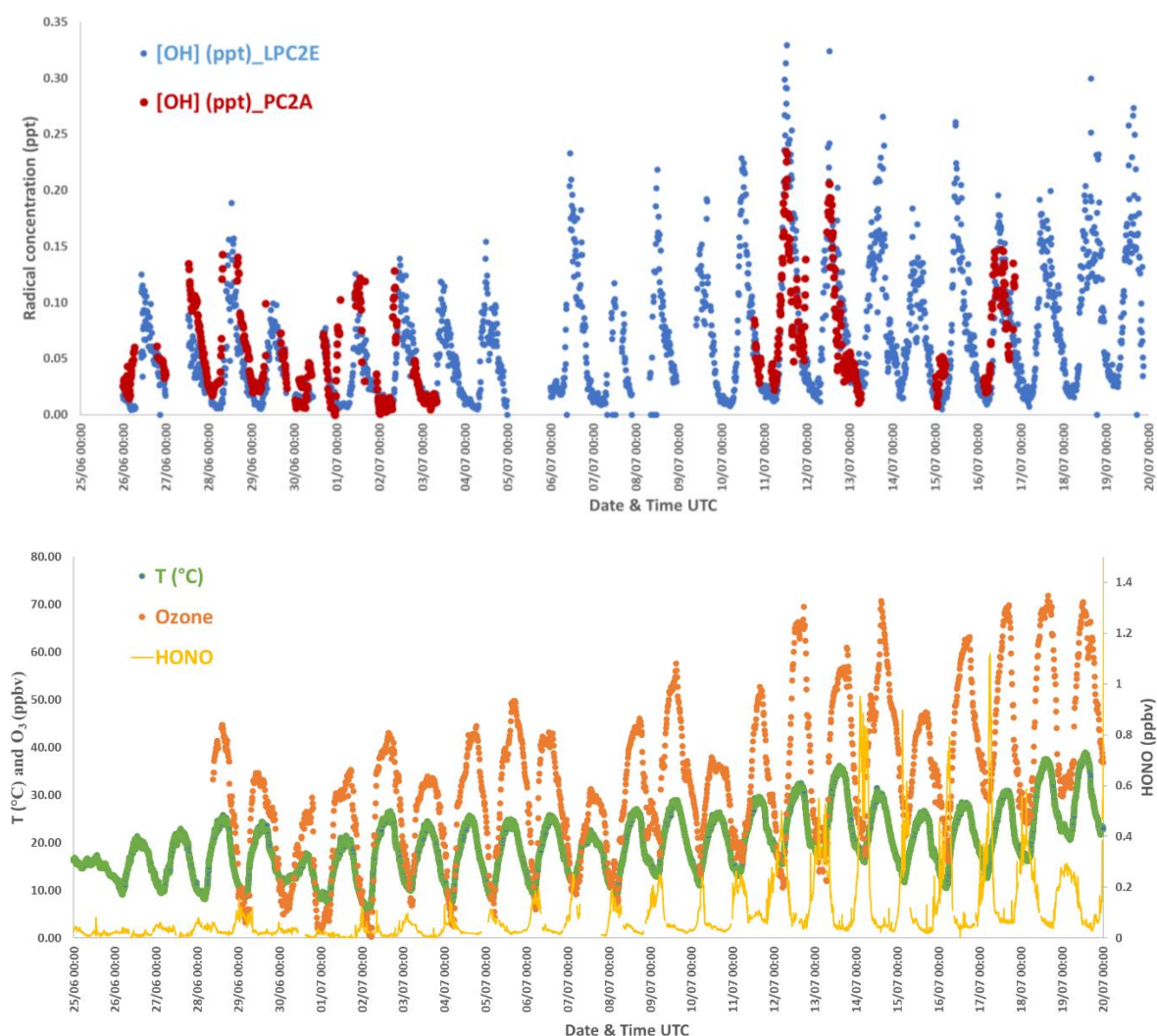


Figure 92: Time series of the OH concentration (upper graph) measured below the canopy by the UL-FAGE and LPC2E-CIMS and time series of the O₃ and HONO concentration and the temperature evolution (lower graph) during the ACROSS campaign

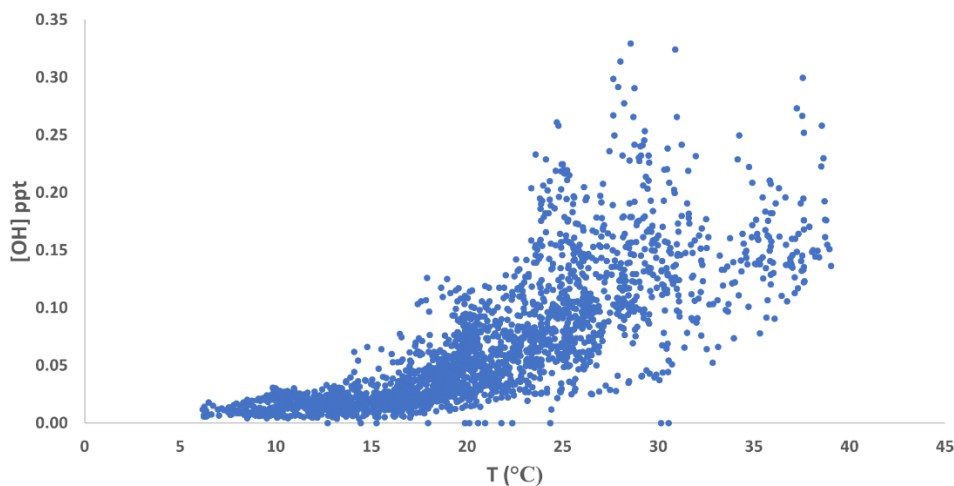


Figure 93: OH concentration as function of temperature (measured at 5 m)

The LIF-Lille data are averaged for the sampling time of the LPC2E-CIMS instrument to compare both data sets. During this campaign, both instruments measured the same OH radical concentrations within their respective uncertainties (Figure 92). The scatter plot of the two data sets shown in Figure 94 of the two data sets gives a slope of 0.62 ($r^2 = 0.61$) and an intercept of 0.025. This intercept may come from the underestimation of the OH background signal measured by the UL-FAGE.

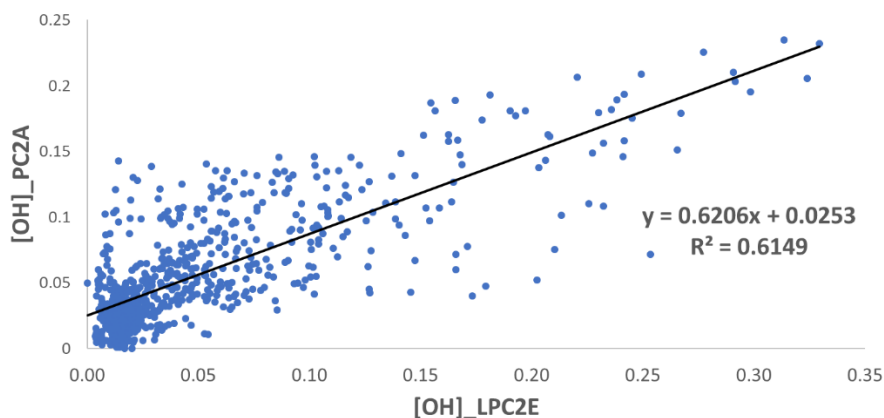


Figure 94 : Scatter plot between UL-FAGE and LPC2E-CIMS OH measurements during the ACROSS campaign

5.4.2.2. HO_2 quantification

During the campaign, HO_2 and HO_2^* were detected in the HO_2 FAGE cell. The HO_2^* corresponds to the RO_2 “double bond” converted in the FAGE at high NO concentration where its negligible at low NO concentration. The UL-FAGE measurements (Figure 95) show HO_2 mixing ratio varied between 0.33 ppt and 10 ppt ($[HO_2] = 0.8\text{-}2.5 \times 10^8$ molecule cm^{-3}) from July 26 to 30 where the ambient temperature was not high. As the temperature starts to increase during the second part of the campaign, HO_2 showed a dramatic increase reaching 30 ppt ($[HO_2] = 7.5 \times 10^8$ molecule cm^{-3}) on July 11 during the daytime. The same behavior was observed for the HO_2^* with an equal concentration than HO_2 . In addition, as shown in Figure 96, the HO_2^*

concentration measured in the HO₂ FAGE cell was in with the same range than the HO₂^{*} which was measured by the UL-RO_x-FAGE in the HO_x mode. However, the measurements done by the UL-RO_x-FAGE during this campaign were scattered because of its low sensitivity. Measurements were done using this instrument only from July 17 to July 22, as it was optimized during this campaign.

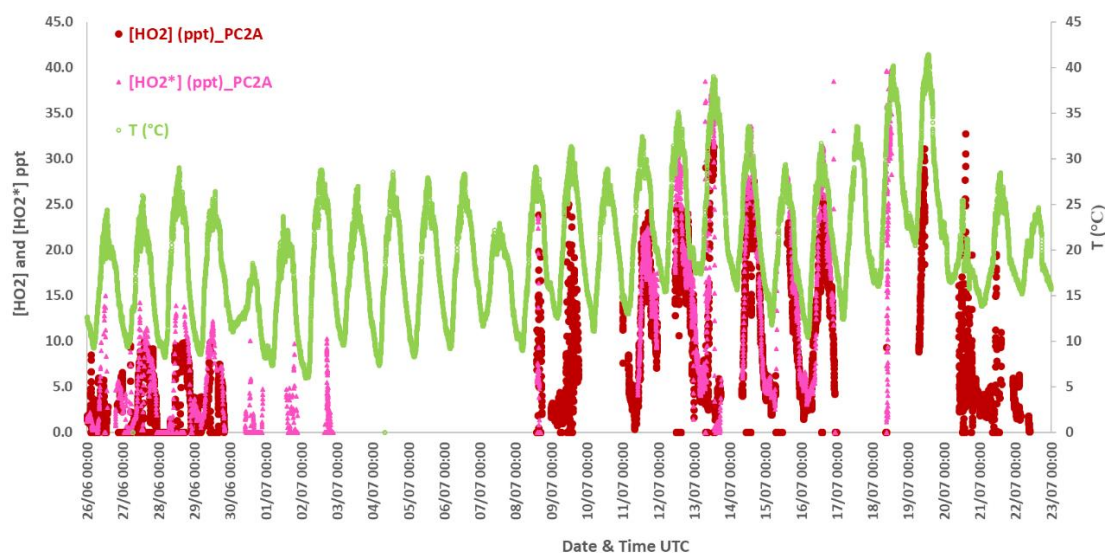


Figure 95: Time series of the HO₂ and HO₂^{*} concentration measured below the canopy by the UL-FAGE and the temperature evolution

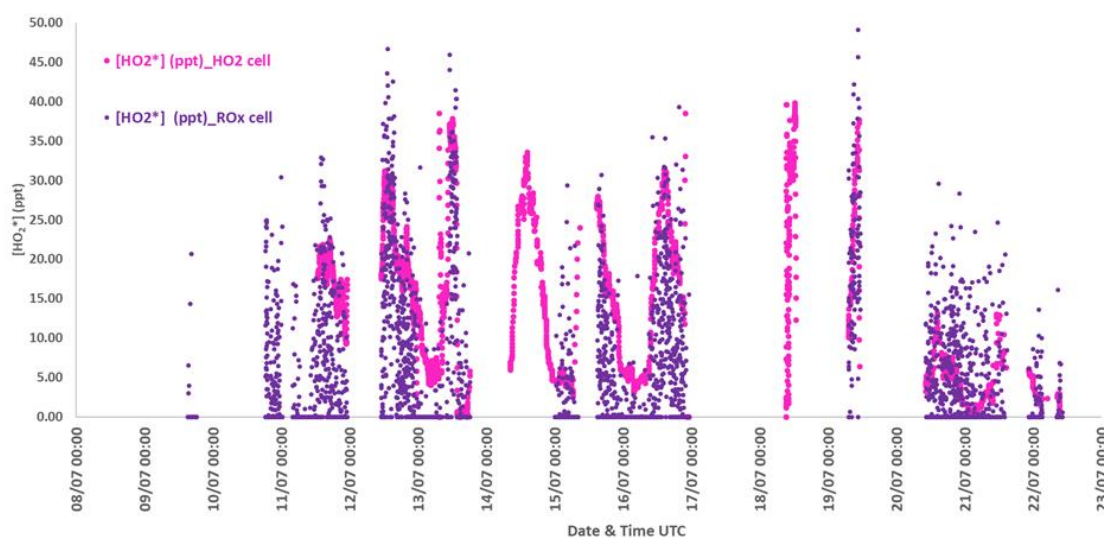


Figure 96: Time series of the HO₂^{*} concentration measured below the canopy in the HO₂ FAGE cell and RO_x FAGE cell (in the HO_x mode)

Similar to other field campaigns in biogenic environments, the measured HO₂ concentrations are in the range of $0.4\text{-}9 \times 10^8$ molecule cm⁻³ in the afternoon. However, HO₂ measured in forested environments varies between 1.2×10^8 molecule cm⁻³ such as TOPHE campaign, to 9×10^8 molecule cm⁻³ as in AEROBIC and 28×10^8 molecule cm⁻³ in BEAPREX campaigns (Stone et al., 2012). Studies in different environments also measured HO₂

concentration in the same range such as the one measured at the rural site in Wangdu ranging between 3 to 14×10^8 molecule cm^{-3} (Tan et al., 2017) and in Pabstthum ranging between 5 to 7.5×10^8 molecule cm^{-3} (Mihelcic et al., 2003). While in urban environments, the HO_2 concentration measured was lower by a factor of 3 to 10 , the concentration measured during the MILAGRO-2006 campaign was around 1.9×10^8 molecule cm^{-3} (Dusanter et al., 2009) and during was ranging between 2 to 6×10^7 molecule cm^{-3} (Whalley et al., 2018). These results agree with the fact that a lower concentration of HO_2 radicals is expected at high NO level where the conversion of HO_2 into OH is more important than in clean environments, as has been discussed previously in chapter 4 (ambient air experiment).

5.4.2.3. RO_x quantification

Preliminary results of the RO_x concentration measured by the UL-FAGE is shown in Figure 97. As mentioned above the RO_x concentration which represent the sum of HO_x and RO_2 radicals was measured by 2 groups at the ground level (PC2A and LPC2E) and at the top of the tower by the IMT group. The RO_x concentration measured during the first part of the campaign is lower than that measured during the second warmer period of the campaign. During the first part of the campaign a maximum reached 60 ppt (1.5×10^9 molecule cm^{-3}) below the canopy and 33 ppt (0.8×10^9 molecule cm^{-3}) above the canopy in the afternoon at a temperature 25 °C and minimum mixing ratios were measured during the night (T around 10 °C) of around 2 ppt. The difference of a factor 1.8 in the RO_x concentration between both measuring levels confirms the difference in the oxidation processes taking place below and above the canopy, considering that the instruments measurements are consistent. As an example, Figure 98 show that UL-FAGE and IMT-PERCA measured an equal RO_x concentration during a biogenic experiment done at the SAPHIR chamber (August 16, oxidation of β -pinene), confirming that the measurements of both instruments at the same place under controlled conditions are consistent. During the second part of the campaign, the temperature increased to reach 38 °C (heatwave period) showing maximum RO_x concentration of 160 ppt (4×10^9 molecule cm^{-3}) below the canopy and 146 ppt (3.6×10^9 molecule cm^{-3}) above the canopy in the afternoon. Comparing the RO_x concentration measured by the UL- RO_x -FAGE (preliminary data) and LPC2E-CIMS below the canopy, we can see an agreement in term of concentration range although the data measured by the UL- RO_x -FAGE is scattered due to its low sensitivity.

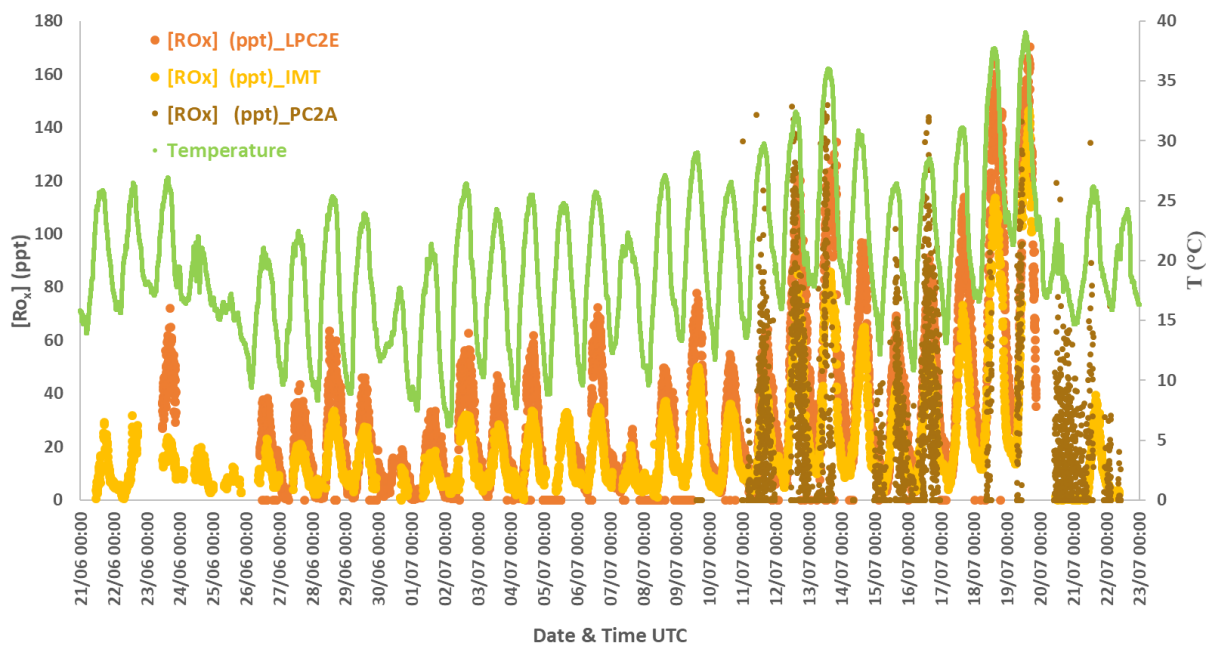


Figure 97: Time series of the RO_x concentration measured below the canopy by the UL-FAGE and LPC2E-CIMS and above canopy by the IMT-PERCA and the temperature evolution

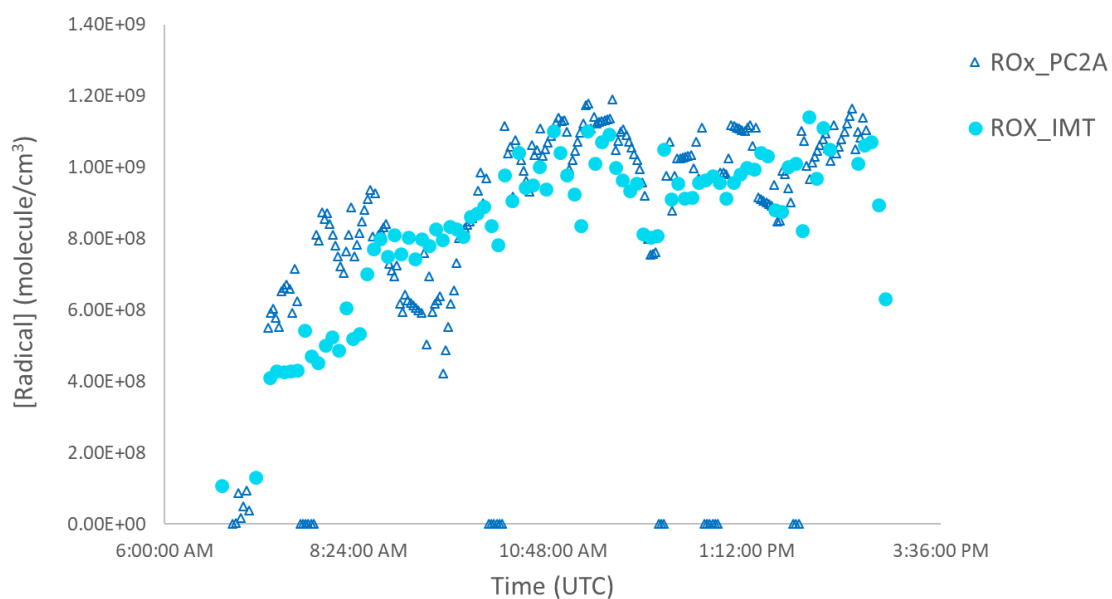


Figure 98: RO_x concentration measured by the UL-FAGE and IMT-PERCA during the β -pinene oxidation experiment at the SAPIR chamber (August 16)

5.5. Conclusion

More than 20 research groups from France and other countries performed comprehensive set of measurements during the ACROSS campaign in summer (June-July) 2022 to characterize the impacts of the BVOC oxidation when mixed with urban emissions and vice versa. The UL-FAGE instrument was deployed to measure the OH reactivity below and above the canopy level at the Rambouillet forest. In addition, quantification of OH, HO₂, HO₂^{*} and RO₂ radicals (using the newly developed RO_x-LIF instrument) were performed by the UL-FAGE at the same site.

The results of the OH reactivity measurements presented in this chapter showed that the reactivity varied with the same dynamic at both heights but significant differences were observed during some nights. Most of the time, the OH reactivity followed the isoprene profile during the daytime and monoterpene, isoprene and NO₂ concentration during the nighttime.

Interestingly, during daytime, the measured OH reactivity at both heights are close, probably due to a better mixing of air masses. The variation of BVOC concentration and OH reactivity was strongly influenced by the meteorological conditions. During daytime, the ambient temperature is an important parameter that affect the emissions of certain compounds (such as isoprene), whereas nighttime OH reactivity was influenced by the nighttime temperature and wind speed. Indeed, during warm nights and low wind speed, more stable meteorological conditions led to higher monoterpene concentration and thus higher OH reactivity below the canopy than above with clear stratification events observed during stable nights. The comparison of the measured and calculated OH reactivity at both levels showed a relatively good agreement but some missing reactivities are observed in particular above the canopy and during nights. Some VOCs data are missing and some uncertainties are still remaining to finalise the calculated OH reactivity. In addition, a model study would be interesting to perform in order to get more insights into the origin of the missing OH reactivity.

In addition to the OH reactivity measurements, the HO_x and RO_x radicals were quantified at 5 m height. The maximum concentrations of OH, HO₂ and RO_x ranged from 4 to 6 × 10⁶ molecule cm⁻³, 2.5 to 7.5 × 10⁸ molecule cm⁻³ and 1.5 to 4 × 10⁹ molecule cm⁻³, respectively. Compared to previous field campaigns, the measured radical concentrations were in the same range. The UL-FAGE OH and RO_x measurements were intercompared with the LPC2E-CIMS measuring at the same level (below the canopy). A good agreement in term of concentration range between both instruments have been shown. A comparison between measured and modeled HO_x and RO_x radical concentrations will help to better understand the oxidation process of these radicals.

General conclusion and perspectives

During this work, we focused on the understanding of HO_x chemistry in a low NO_x environment through kinetic studies and field measurements. The FAGE technique is a highly sensitive and widely used method for measuring low HO_x radical concentration in the atmosphere. Recent field campaigns have highlighted discrepancies between measurements in different environments and modelled profiles even after the improvements in the atmospheric chemical mechanism. Bias in the calibration or instrument interferences may affect the field measurements and cause lack of understanding of the atmospheric chemistry. During this thesis, improvements such as new excitation laser and optimization of UL-RO_x-FAGE setup were performed.

Laboratory studies under controlled conditions and field measurements in a biogenic environment have been carried out to better characterize these oxidation processes. Improvement and validation of the UL-FAGE measurements for radical quantification was done during the RO_xComp campaign when the instrument was coupled to the SAPHIR chamber.

The kinetic work described in chapter 3 focused on studying the influence of water vapor on the RO₂ + OH reaction. The preliminary results have shown an HO₂ yield of 0.64 ± 0.16 for the C₂H₅O₂ + OH reaction at different humidity levels but difficulties in the reproducibility of the experiments lead to be cautious about these results. More detailed experiments and extension to the reaction of larger peroxy radicals with OH as well as direct measurements of CH₃OH yield carried out at high RH would be interesting to confirm the conclusion of no impact of H₂O on this type of reactions being important under remote environments. In addition, a kinetic work on the chemistry of siloxanes was initiated. Preliminary results obtained from the kinetic studies on the reactions between L2 and OH radicals using UL-FAGE technique in its reactivity configuration showed an agreement with the literature and theoretical work done at the university of Melbourne. Future work will be done to continue studying the transformation of their primary and secondary oxidation products after the oxidation initiated by OH.

The measurements performed during the intercomparison campaign done at the SAPHIR chamber in Julich were presented in chapter 4. Lille measurements were intercompared with the Julich measurements and the results showed relatively good agreement for the OH, HO₂ and RO₂ measurement over the campaign covering a wide range of concentrations and conditions. However, different levels of agreement were observed day by day and more

analysis, like comparison with modelling profiles, could help in the understanding of these differences. The cross-calibration (exchange of the calibration sources) showed contrasted results with a good agreement when the calibration cell of Julich was on the UL-FAGE and apparently on overestimation of the calculated concentration compared to the measured one when the calibration cell from Lille was on the FZJ-FAGE by 30-50 % at high RH. Since the sensitivity of the UL-RO_x-FAGE is determined at high RH, thus, this can explain the higher RO₂ concentration measured by the UL-RO_x-FAGE compared to the FZJ-RO_x-FAGE during some experiments but it was not systematically the case. This intercomparison campaign allowed to better characterize the UL-FAGE instrument for the quantification of OH and HO₂ and the UL-RO_x-FAGE for the RO₂ measurement but further analysis have to be performed to understand the differences.

Finally, the measurements performed during the ACROSS campaign at the Rambouillet site were presented in chapter 5. The aim of this campaign was to better understand the influence of the atmospheric conditions on the oxidation processes of the emitted BVOCs at forested environments. The UL-FAGE was deployed for the quantification of OH, HO₂ and RO_x radicals below the canopy level and OH reactivity measurements below and above the canopy. It has been shown that the OH reactivity and the BVOC emissions are strongly dependent on the position in the canopy and meteorological parameters. Higher OH reactivity was observed during the night reaching a maximum of 53 s⁻¹ above the canopy and 33 s⁻¹ below the canopy. The comparison between the measurements recorded at two different levels highlighted conditions of clear stratification in the BVOCs concentration and thus OH reactivity. The preliminary results of the missing reactivity at both levels show a good understanding of the OH losses. The source of the missing OH sinks are thought to be some unmeasured oxidation products of BVOC emitted at the Rambouillet forest. Concerning the radical quantification below the canopy, a variation in the concentration depending on the temperature variation was observed where a maximum of OH, HO₂ and RO_x radicals ranged from 6 to 8 × 10⁶ molecule cm⁻³, 6 to 7.5 × 10⁸ molecule cm⁻³ 2.5 to 4 × 10⁹ molecule cm⁻³, respectively, during the second warmer period of the campaign. Higher RO_x concentration was measured below the canopy indicating difference in the oxidation processes occurring at two different heights. Compared to previous field campaigns at similar environments the measured radical concentrations were in the same range. Comparing the measured radical concentration to modeled concentrations will help to better understand the oxidation process of these radicals.

Bibliography

- Archibald, A. T. Petit, A.S., Percival, C. J., Harvey, J. N. and Shallcross, D. E. (2009). On the importance of the reaction between OH and RO₂ radicals. *Atmospheric Science Letters*, 10(2), 249–254. <https://doi.org/10.1002/asl>
- Abbatt, J. P. D. & Wang, C. (2020). The atmospheric chemistry of indoor environments. *Environmental Science: Processes and Impacts*, 22(1), 25–48. <https://doi.org/10.1039/c9em00386j>
- Abichou, G. (2023). Development of an innovative instrument dedicated to measurement of peroxy radicals and ozone production in the air. *PhD Thesis, University of Littoral Côte d'Opale*
- Ajami, M. Al. (2018). Characterization and deployment of a FAGE instrument for the study of atmospheric oxidation processes. *PhD Thesis, University of Lille*.
- Alton, M. W., & Browne, C. (2020). Atmospheric Chemistry of Volatile Methyl Siloxanes: Kinetics and Products of Oxidation by OH Radicals and Cl Atoms. *Environmental Science and Technology*, 54(10), 5992–5999. <https://doi.org/10.1021/acs.est.0c01368>
- Alvarez, E. G., Amedro, D., Afif, C., Gligorovski, S., Schoemacker, C., Fittschen, C., Doussin, J. F., & Wortham, H. (2013). Unexpectedly high indoor hydroxyl radical concentrations associated with nitrous acid. *Proceedings of the National Academy of Sciences of the United States of America*, 110(33), 13294–13299. <https://doi.org/10.1073/pnas.1308310110>
- Amedro, D. (2012). Atmospheric measurements of OH and HO₂ radicals using FAGE: Development and deployment on the field. *PhD Thesis, University of Lille*.
- Amedro, D., Miyazaki, K., Parker, A., Schoemaecker, C., & Fittschen, C. (2012). Atmospheric and kinetic studies of OH and HO₂ by the FAGE technique. *Journal of Environmental Sciences*, 24(1), 78–86. [https://doi.org/10.1016/S1001-0742\(11\)60723-7](https://doi.org/10.1016/S1001-0742(11)60723-7)
- Apel, E. C., Brauers, T., Koppmann, R., Bandowe, B., Boßmeyer, J., Holzke, C., Tillmann, R., Wahner, A., Wegener, R., Brunner, A., Jocher, M., Ruuskanen, T., Spirig, C., Steigner, D., Steinbrecher, R., Gomez Alvarez, E., Müller, K., Burrows, J. P., Schade, G., Wyche, K. P. (2008). Intercomparison of oxygenated volatile organic compound measurements at the SAPHIR atmosphere simulation chamber. *Journal of Geophysical Research Atmospheres*, 113(20), 1–24. <https://doi.org/10.1029/2008JD009865>
- Ariya, P. A., Sander, R., & Crutzen, P. J. (2000). Significance of HO_x and peroxides production due to alkene ozonolysis during fall and winter: A modeling study. *Journal of Geophysical Research Atmospheres*, 105(14), 17721–17738. <https://doi.org/10.1029/2000JD900074>
- Assaf, E., Schoemaecker, C., Vereecken, L., & Fittschen, C. (2018). Experimental and theoretical investigation of the reaction of RO₂ radicals with OH radicals: Dependence of the HO₂ yield on the size of the alkyl group. *International Journal of Chemical Kinetics*, 50(9), 670–680. <https://doi.org/10.1002/kin.21191>
- Assaf, E., Sheps, L., Whalley, L., Heard, D., Tomas, A., Schoemaecker, C., & Fittschen, C. (2017). The Reaction between CH₃O₂ and OH Radicals: Product Yields and Atmospheric Implications. *Environmental Science and Technology*, 51(4), 2170–2177. <https://doi.org/10.1021/acs.est.6b06265>
- Assaf, E., Tanaka, S., Kajii, Y., Schoemaecker, C., & Fittschen, C. (2017). Rate constants of the reaction of C₂–C₄ peroxy radicals with OH radicals. *Chemical Physics Letters*, 684, 245–249. <https://doi.org/10.1016/j.cplett.2017.06.062>
- Atkinson, R., Baulch, D. L., Cox, R. A., Crowley, J. N., Hampson, R. F., Hynes, R. G., Jenkin, M. E., Rossi, M. J., & Troe, J. (2004). Evaluated kinetic and photochemical data for atmospheric chemistry: Volume I – gas phase reactions of O_x, HO_x, NO_x and SO_x species. *Atmospheric Chemistry and Physics*, 4(6), 1461–1738. [200](https://doi.org/10.5194/acp-4-</p></div><div data-bbox=)

1461-2004

- Atkinson, R. (1997). Gas phase tropospheric chemistry of VOCs, alkanes and alkenes. *Journal of Physical and Chemical reference data*, 26(2), 215–290.
- Atkinson, R. (1991). Kinetics of the Gas-Phase Reactions of a Series of Organosilicon Compounds with OH and NO₃ Radicals and O₃ at 297 ± 2 K. *Environmental Science and Technology*, 25(5), 863–866. <https://doi.org/10.1021/es00017a005>
- Atkinson, R. (2000). Atmospheric chemistry of VOCs and NO_x. *Atmospheric Environment*, 34(1–3), 2063–2101. [https://doi.org/S1352-2310\(99\)00460-4](https://doi.org/S1352-2310(99)00460-4)
- Atkinson, R. & Arey, J. (2003). Gas-phase tropospheric chemistry of biogenic volatile organic compounds: A review. *Atmospheric Environment*, 37 (Supplement. 2), 197–219. [https://doi.org/10.1016/S1352-2310\(03\)00391-1](https://doi.org/10.1016/S1352-2310(03)00391-1)
- Atkinson, R., Aschmann, S. M., Carter, W. P. L., Winer, A. M., & Pitts, J. N. (1982). Alkyl nitrate formation from the NO_x-air photooxidations of C₂-C₈ n-alkanes. *Journal of Physical Chemistry A*, 86(23), 4563–4569. <https://doi.org/10.1021/j100220a022>
- Atkinson, R., Baulch, D. L., Cox, R. A., Crowley, J. N., Hampson, R. F., Hynes, R. G., Jenkin, M. E., Rossi, M. J. and Troe, J. (2006). Evaluated kinetic and photochemical data for atmospheric chemistry: Volume II – gas phase reactions of organic species. *Atmospheric Chemistry and Physics*, 6, 3625–4055. <https://doi.org/10.1209/epl/i2003-00571-0>
- Atkinson, R., Perry, R.A and Pitts, J. N. (1976). Kinetic of the reactions of OH radicals with CO AND N₂O. *Chemical Physical Letters*, 44(2), 0–4.
- Avzianova, E. V., & Ariya, P. A. (2002). Temperature-dependent kinetic study for ozonolysis of selected tropospheric alkenes. *International Journal of Chemical Kinetics*, 34(12), 678–684. <https://doi.org/10.1002/kin.10093>
- Baardsen, E. L., & Terhune, R. W. (1972). Detection of OH in the Atmosphere Using a Dye Laser. *Applied Physics Letter*, 21(6), 209. <https://doi.org/10.1063/1.1654347>
- Baklanov, A., Lawrence, M., Pandis, S., Mahura, A., Finardi, S., Moussiopoulos, N., Beekmann, M., Laj, P., Gomes, L., Jaffrezo, J.-L., Borbon, A., Coll, I., Gros, V., Sciare, J., Kukkonen, J., Galmarini, S., Giorgi, F., Grimmond, S., Esau, I., Rossow, W. B. (2010). MEGAPOLI: concept of multi-scale modelling of megacity impact on air quality and climate. *Advances in Science and Research*, 4(1), 115–120. <https://doi.org/10.5194/asr-4-115-2010>
- Bates, K. H., Jacob, D. J., Wang, S., Hornbrook, R. S., Apel, E. C., Kim, M. J., Millet, D. B., Wells, K. C., Chen, X., Brewer, J. F., Ray, E. A., Commane, R., Diskin, G. S., & Wofsy, S. C. (2021). The Global Budget of Atmospheric Methanol: New Constraints on Secondary, Oceanic, and Terrestrial Sources. *Journal of Geophysical Research: Atmospheres*, 126(4), 1–23. <https://doi.org/10.1029/2020JD033439>
- Beck, M., Bendura, J., McDougal, D. S., Gregory, L., Davis, D., Bradshaw, J., Rodgers, M. O., Wang, C., Davis, I., Campbell, J., Torres, L., Carroll, M. A., Ridley, B. A., Sachse, G. W., Hill, G. F., & Rasmussen, A. (1987). Operational Overview of NASA GTE / CITE 1 Airborne Instrument Intercomparisons ' Carbon Monoxide , Nitric Oxide , and Hydroxyl. *Journal of Geophysical Research*, 92(6), 1977–1985.
- Bernard, F., Papanastasiou, D. K., Papadimitriou, V. C., & Burkholder, J. B. (2018). Temperature Dependent Rate Coefficients for the Gas-Phase Reaction of the OH Radical with Linear (L₂, L₃) and Cyclic (D₃, D₄) Permethyloxanes. *Journal of Physical Chemistry A*, 122(17), 4252–4264. <https://doi.org/10.1021/acs.jpca.8b01908>
- Berresheim, H., Elste, T., Plass-Dülmer, C., Eisele, F. L., & Tanner, D. J. (2000). Chemical ionization mass spectrometer for long-term measurements of atmospheric OH and H₂SO₄. *International Journal of Mass Spectrometry*, 202(1–3), 91–109. [https://doi.org/10.1016/S1387-3806\(00\)00233-5](https://doi.org/10.1016/S1387-3806(00)00233-5)
- Bey, I. (2001). A modeling study of the nighttime radical chemistry in the lower continental

- troposphere 1. Development of a detailed chemical mechanism including nighttime chemistry. *Journal of Geophysical Research*, 106, 9959–9990.
- Blando, J. D., & Turpin, B. J. (2000). Secondary organic aerosol formation in cloud and fog droplets: a literature evaluation of plausibility. *Atmospheric Environment*, 34(10), 1623–1632. [https://doi.org/10.1016/S1352-2310\(99\)00392-1](https://doi.org/10.1016/S1352-2310(99)00392-1)
- Blocquet, M., Guo, F., Mendez, M., Ward, M., Coudert, S., Batut, S., Hecquet, C., Blond, N., Fittschen, C., & Schoemaeker, C. (2018). Impact of the spectral and spatial properties of natural light on indoor gas-phase chemistry: Experimental and modeling study. *Indoor Air*, 28(3), 426–440. <https://doi.org/10.1111/ina.12450>
- Bohn, B., Rohrer, F., Brauers, T., & Wahner, A. (2005). Actinometric measurements of NO₂ photolysis frequencies in the atmosphere simulation chamber SAPHIR. *Atmospheric Chemistry and Physics*, 5(2), 493–503. <https://doi.org/10.5194/acp-5-493-2005>
- Bonn, B., Korhonen, H., Petäjä, T., Boy, M., Kulmala, M., Bonn, B., Korhonen, H., Petäjä, T., Boy, M., & Understanding, M. K. (2007). Understanding the formation of biogenic secondary organic aerosol from α -pinene in smog chamber studies: role of organic peroxy radicals. *Atmospheric Chemistry and Physics Discussions*, 7(2), 3901–3939. <https://doi.org/10.5194/acpd-7-3901-2007>
- Bossolasco, A., Faragó, E. P., Schoemaeker, C., & Fittschen, C. (2014). Rate constant of the reaction between CH₃O₂ and OH radicals. *Chemical Physics Letters*, 593, 7–13. <https://doi.org/10.1016/j.cplett.2013.12.052>
- Bottorff, B., Lew, M. M., Woo, Y., Rickly, P., Rollings, M. D., Deming, B., Anderson, D. C., Wood, E., Alwe, H. D., Millet, D. B., Weinheimer, A., Tyndall, G., Ortega, J., Dusanter, S., Leonardis, T., Flynn, J., Erickson, M., Alvarez, S., Rivera-Rios, J. C., ... Stevens, P. S. (2023). OH, HO₂, and RO₂ radical chemistry in a rural forest environment: measurements, model comparisons, and evidence of a missing radical sink. *Atmospheric Chemistry and Physics*, 23(18), 10287–10311. <https://doi.org/10.5194/acp-23-10287-2023>
- Brandenburger, U., Brauers, T., Dorn, H. P., Hausmann, M., & Ehhalt, D. H. (1998). In-situ measurements of tropospheric hydroxyl radicals by folded long-path laser absorption during the field campaign POPCORN. *Journal of Atmospheric Chemistry*, 31(1–2), 181–204. <https://doi.org/10.1023/A:1005909328924>
- Brauers, T., Aschmutat, U., Brandenburger, U., Dorn, H., Hausmann, M., Hegling, M., Hofzumahaus, A., Holland, F., & Ehhalt, D. H. (1996). Intercomparison of tropospheric OH radical measurements by multiple folded long-path laser absorption and laser induced fluorescence. *Geophysical Researcher Letters*, 23(18), 2545–2548.
- Brauers, T., Hausmann, M., Bister, A., Kraus, A., & Dorn, H. P. (2001). OH radicals in the boundary layer of the Atlantic Ocean 1. Measurements by long-path laser absorption spectroscopy. *Journal of Geophysical Research Atmospheres*, 106(D7), 7399–7414. <https://doi.org/10.1029/2000JD900679>
- Brin, A., Bouget, C., Valladares, L., & Brustel, H. (2012). Are stumps important for the conservation of saproxylic beetles in managed forests? - Insights from a comparison of assemblages on logs and stumps in oak-dominated forests and pine plantations. *Insect Conservation and Diversity*, 6(3), 255–264. <https://doi.org/10.1111/j.1752-4598.2012.00209.x>
- Bronkhorst. (2015). *Instruction manual-CEM controlled evaporator and mixer*. 2–10.
- Bsaibes, S., Al Ajami, M., Mermet, K., Truong, F., Batut, S., Hecquet, C., Dusanter, S., Léornadis, T., Sauvage, S., Kammer, J., Flaud, P. M., Perraudin, E., Villenave, E., Locoge, N., Gros, V., & Schoemaeker, C. (2020). Variability of hydroxyl radical (OH) reactivity in the Landes maritime pine forest: Results from the LANDEX campaign 2017. *Atmospheric Chemistry and Physics*, 20(3), 1277–1300. <https://doi.org/10.5194/acp-20-1277-2020>

- Butkovskaya, N., Rayez, M. T., Rayez, J. C., Kukui, A., & Le Bras, G. (2009). Water vapor effect on the HNO₃ yield in the HO₂ + NO reaction: Experimental and theoretical evidence. *Journal of Physical Chemistry A*, *113*(42), 11327–11342. <https://doi.org/10.1021/jp811428p>
- Cambell, M. J. & Hall, B. D. (1995). Intercomparison of Local Hydroxyl Measurements by Radiocarbon and FAGE Techniques. *Journal of the Atmospheric Sciences*, *52*(19), 3421–3427.
- Cantrell, C. (2020). ACROSS: A mission to explore the atmospheric transformation of chemical compounds in mixed anthropogenic-biogenic environments.
- Cantrell, C. A., & Stedman, and D. H. (1982). A possible technique for the measurement of atmospheric peroxy radicals. *Journal of Geophysical Research*, *9*(8), 846-849.
- Cantrell, C. A., Edwards, G. D., Stephens, S., Mauldin, R. L., Zondlo, M. A., Kosciuch, E., Eisele, F. L., Shetter, R. E., Lefer, B. L., Hall, S., Flocke, F., Weinheimer, A., Fried, A., Apel, E., Kondo, Y., Blake, D. R., Blake, N. J., Simpson, I. J., Bandy, A. R., ... Clarke, A. D. (2003). Peroxy radical behavior during the Transport and Chemical Evolution over the Pacific (TRACE-P) campaign as measured aboard the NASA P-3B aircraft. *Journal of Geophysical Research: Atmospheres*, *108*(20), 8797. <https://doi.org/10.1029/2003jd003674>
- Cantrell, C. A. (1984). Measurement of Atmospheric Peroxy Radicals by Chemical Amplification. *Analytical Chemistry*, *6*(8), 1496–1502.
- Caravan, R. L., Khan, M. A. H., Zádor, J., Sheps, L., Antonov, I. O., Rotavera, B., Ramasesha, K., Au, K., Chen, M. W., Rösch, D., Osborn, D. L., Fittschen, C., Schoemaeker, C., Duncianu, M., Grira, A., Dusanter, S., Tomas, A., Percival, C. J., Shallcross, D. E., & Taatjes, C. A. (2018). The reaction of hydroxyl and methylperoxy radicals is not a major source of atmospheric methanol. *Nature Communications*, *9*(1), 1–9. <https://doi.org/10.1038/s41467-018-06716-x>
- Carlaw, N., Fletcher, L., Heard, D., Ingham, T., & Walker, H. (2017). Significant OH production under surface cleaning and air cleaning conditions: Impact on indoor air quality. *Indoor Air*, *27*(6), 1091–1100. <https://doi.org/10.1111/ina.12394>
- Carlaw, N. (2007). A new detailed chemical model for indoor air pollution. *Atmospheric Environment*, *41*(6), 1164–1179. <https://doi.org/10.1016/j.atmosenv.2006.09.038>
- Chan, C. Y., Hard, T. M., Mehrabzadeh, A. A., George, L. A., & O'Brien, R. J. (1990). Third-generation FAGE instrument for tropospheric hydroxyl radical measurement. *Journal of Geophysical Research*, *95*(11), 18569–18576. <https://doi.org/10.1029/jd095id11p18569>
- Chen, S., Ren, X., Mao, J., Chen, Z., Brune, W. H., Lefer, B., Rappenglück, B., Flynn, J., Olson, J., & Crawford, J. H. (2010). A comparison of chemical mechanisms based on TRAMP-2006 field data. *Atmospheric Environment*, *44*(33), 4116–4125. <https://doi.org/10.1016/j.atmosenv.2009.05.027>
- Chen, Y., Yang, C., Zhao, W., Fang, B., Xu, X., Gai, Y., Lin, X., Chen, W., & Zhang, W. (2016). Ultra-sensitive measurement of peroxy radicals by chemical amplification broadband cavity-enhanced spectroscopy. *Analyst*, *141*(20), 5870–5878. <https://doi.org/10.1039/c6an01038e>
- Chhantyal-Pun, R., Khan, M. A. H., Taatjes, C. A., Percival, C. J., Orr-Ewing¹, A. J., & Shallcross, D. E. (2012). Criegee intermediates: Production, Detection and Reactivity. *International Reviews in Physical Chemistry*, *14*(42), 385–424. <https://doi.org/10.1080/0144235X.2020.1792104>
- Cho, C., Fuchs, H., Hofzumahaus, A., Holland, F., Bloss, W.J., Bohn, B., Dorn, H., Glowania, M., Hohaus, T., Liu, L., Monks, P.S., Niether, D., Rohrer, F., Sommariva, R., Tan, Z., Tillmann, R., Kiendler-Scharr, A., Wahner, A., Novelli, A. (2023). Experimental chemical budgets of OH, HO₂, and RO₂ radicals in rural air in western Germany during the JULIAC

- campaign 2019. *Atmospheric Chemistry and Physics*, 23, 2003–2033, 2023. <https://doi.org/10.5194/acp-23-2003-2023>
- Choi, W., Faloon, I. C., Bouvier-Brown, N. C., McKay, M., Goldstein, A. H., Mao, J., Brune, W. H., Lafranchi, B. W., Cohen, R. C., Wolfe, G. M., Thornton, J. A., Sonnenfroh, D. M., & Millet, D. B. (2010). Observations of elevated formaldehyde over a forest canopy suggest missing sources from rapid oxidation of arboreal hydrocarbons. *Atmospheric Chemistry and Physics*, 10(18), 8761–8781. <https://doi.org/10.5194/acp-10-8761-2010>
- Clemittshaw, K. C. (2004). A Review of Instrumentation and Measurement Techniques for Ground-Based and Airborne Field Studies of Gas-Phase Tropospheric Chemistry. *Critical Reviews in Environmental Science and Technology*, 34(1), 1–108. <https://doi.org/10.1080/10643380490265117>
- Creasey, D. J., Halford-Maw, P. A., Heard, D. E., Pilling, M. J., & Whitaker, B. J. (1997). Implementation and initial deployment of a field instrument for measurement of OH and HO₂ in the troposphere by laser-induced fluorescence. *Journal of the Chemical Society - Faraday Transactions*, 93(16), 2907–2913. <https://doi.org/10.1039/a701469d>
- De Gouw, J. A., Middlebrook, A. M., Warneke, C., Goldan, P. D., Kuster, W. C., Roberts, J. M., Fehsenfeld, F. C., Worsnop, D. R., Canagaratna, M. R., Pszenny, A. A. P., Keene, W. C., Marchewka, M., Bertman, S. B., & Bates, T. S. (2005). Budget of organic carbon in a polluted atmosphere: Results from the New England Air Quality Study in 2002. *Journal of Geophysical Research*, 110(16), 1–22. <https://doi.org/10.1029/2004JD005623>
- Di Carlo, P., Brune, W. H., Martinez, M., Harder, H., Leshner, R., Ren, X., Thornberry, T., Carroll, M. A., Young, V., Shepson, P. B., Riemer, D., Apel, E., & Campbell, C. (2004). Missing OH Reactivity in a Forest: Evidence for Unknown Reactive Biogenic VOCs. *Science*, 304(5671), 722–725. <https://doi.org/10.1126/science.1094392>
- Dillon, T. J., Tucceri, M. E., Dulitz, K., Horowitz, A., Vereecken, L., & Crowley, J. N. (2012). Reaction of hydroxyl radicals with C₄H₅N (pyrrole): Temperature and pressure dependent rate coefficients. *Journal of Physical Chemistry A*, 116(24), 6051–6058. <https://doi.org/10.1021/jp211241x>
- Dlugi, R., Berger, M., Zelger, M., Hofzumahaus, A., Siese, M., Holland, F., Wisthaler, A., Grabmer, W., Hansel, A., Koppmann, R., Kramm, G., Möllmann-Coers, M., & Knaps, A. (2010). Turbulent exchange and segregation of HO_x radicals and volatile organic compounds above a deciduous forest. *Atmospheric Chemistry and Physics*, 10(13), 6215–6235. <https://doi.org/10.5194/acp-10-6215-2010>
- Dorn, H. P., Apodaca, R. L., Ball, S. M., Brauers, T., Brown, S. S., Crowley, J. N., Dubé, W. P., Fuchs, H., Häsel, R., Heitmann, U., Jones, R. L., Kiendler-Scharr, A., Labazan, I., Langridge, J. M., Meinen, J., Mentel, T. F., Platt, U., Pöhler, D., Rohrer, F., ... Wahner, A. (2013). Intercomparison of NO₃ radical detection instruments in the atmosphere simulation chamber SAPHIR. *Atmospheric Measurement Techniques*, 6(5), 1111–1140. <https://doi.org/10.5194/amt-6-1111-2013>
- Duncan, B. N., Logan, J. A., Bey, I., Megretskaia, I. A., Yantosca, R. M., Novelli, P. C., Jones, N. B., & Rinsland, C. P. (2007). Global budget of CO, 1988 - 1997: Source estimates and validation with a global model. *Journal of Geophysical Research Atmospheres*, 112(22), 1–29. <https://doi.org/10.1029/2007JD008459>
- Duncan, M., Lahib, A., Tomas, A., Stevens, P. S., & Dusanter, S. (2020). Characterization of a chemical amplifier for peroxy radical measurements in the atmosphere. *Atmospheric Environment*, 222, 1–36. <https://doi.org/10.1016/j.atmosenv.2019.117106>
- Dusanter, S., Vimal, D., Stevens, P. S., Volkamer, R., & Molina, L. T. (2009). Measurements of OH and HO₂ concentrations during the MCMA-2006 field campaign - Part 1: deployment of the indiana university laser-induced fluorescence instrument. *Atmospheric Chemistry and Physics*, 9(5), 1665–1685. <https://doi.org/10.5194/acp-9-1665-2009>

- Dusanter, S., Vimal, D., Stevens, P. S., Volkamer, R., Molina, L. T., Baker, A., Meinardi, S., Blake, D., Sheehy, P., Merten, A., Zhang, R., Zheng, J., Fortner, E. C., Junkermann, W., Dubey, M., Rann, T., Eichinger, B., Lewandowski, P., Prueger, J., & Holder, H. (2009). Measurements of OH and HO₂ concentrations during the MCMA-2006 field campaign - Part 2: Model comparison and radical budget. *Atmospheric Chemistry and Physics*, 9(18), 6655–6675. <https://doi.org/10.5194/acp-9-6655-2009>
- Edwards, P. M., Evans, M. J., Furneaux, K. L., Hopkins, J., Ingham, T., Jones, C., Lee, J. D., Lewis, A. C., Moller, S. J., Stone, D., Whalley, L. K., & Heard, D. E. (2013). OH reactivity in a South East Asian tropical rainforest during the oxidant and particle photochemical processes (OP3) project. *Atmospheric Chemistry and Physics*, 13(18), 9497–9514. <https://doi.org/10.5194/acp-13-9497-2013>
- Ehhalt, D. H., & Rohrer, F. (2000). Dependence of the OH concentration on solar UV. *Journal of Geophysical Research Atmospheres*, 105(D3), 3565–3571. <https://doi.org/10.1029/1999JD901070>
- Eisele, F. L., Tanner, D. J., Cantrell, C. A. and Calvert, J. G. (1996). Measurements and steady state calculations of OH concentrations at Mauna Loa Observatory. *Journal of Geophysical Research Atmospheres*, 101(D9), 14665–14679. <https://doi.org/10.1029/95JD03654>
- Eisele, F. L., Mauldin, L., Cantrell, C., Zondlo, M., Apel, E., Fried, A., Walega, J., Shetter, R., Lefer, B., Floke, F., Weinheimer, A., Avery, M., Vay, S., Sachse, G., Podolske, J., Diskin, G., Barrick, J. D., Singh, H. B., Brune, W., ... Dibb, J. (2003). Summary of measurement intercomparisons during TRACE-P. *Journal of Geophysical Research: Atmospheres*, 108(20), 8791. <https://doi.org/10.1029/2002jd003167>
- Eisele, F. L., Mauldin, R. L., Tanner, D. J., Cantrell, C., Kosciuch, E., Nowak, J. B., Brune, B., Faloona, I., Tan, D., Davis, D. D., Wang, L., & Chen, G. (2001). Relationship between OH measurements on two different NASA aircraft during PEM Tropics B. *Journal of Geophysical Research Atmospheres*, 106(D23), 32683–32689. <https://doi.org/10.1029/2000JD900714>
- Eisele, F.L. and Tanner, D.J. (1991). Ion-assisted Tropospheric OH measurements. *Journal of Geophysical Research*, 96(D5), 9295–9308.
- Ervens, B., George, C., Williams, J. E., Buxton, G. V., Salmon, G. A., Bydder, M., Wilkinson, F., Dentener, F., Mirabel, P., Wolke, R. and Herrmann, H. (2003). CAPRAM 2.4 (MODAC mechanism): An extended and condensed tropospheric aqueous phase mechanism and its application. *Journal of Geophysical Research: Atmospheres* 108(D14), 4426, <https://doi:10.1029/2002JD002202>, 2003
- Faloona, I. C., Tan, D., Leshner, R. L., Hazen, N. L., Frame, C. L., Simpasa, J. B., Harder, H., Martinez, M., Di Carlo, P., Ren, X., & Brune, W. H. (2004). A laser-induced fluorescence instrument for detecting tropospheric OH and HO₂: Characteristics and calibration. *Journal of Atmospheric Chemistry*, 47(2), 139–167. <https://doi.org/10.1023/B:JOCH.0000021036.53185.0e>
- Fang, P., Jiang, W., Tang, J. I. E., Lei, X., & Tan, J. (2020). Variations in friction velocity with wind speed and height for moderate-to-strong onshore winds based on measurements from a coastal tower. *Journal of Applied Meteorology and Climatology*, 59(4), 637–650. <https://doi.org/10.1175/JAMC-D-18-0327.1>
- Faragó, E. P., Schoemaeker, C., Viskolcz, B., & Fittschen, C. (2015). Experimental determination of the rate constant of the reaction between C₂H₅O₂ and OH radicals. *Chemical Physics Letters*, 619, 196–200. <https://doi.org/10.1016/j.cplett.2014.11.069>
- Feiner, P. A., Brune, W. H., Miller, D. O., Zhang, L., Cohen, R. C., Romer, P. S., Goldstein, A. H., Keutsch, F. N., Skog, K. M., Wennberg, P. O., Nguyen, T. B., Teng, A. P., DeGouw, J., Koss, A., Wild, R. J., Brown, S. S., Guenther, A., Edgerton, E., Baumann, K., & Fry, J.

- L. (2016). Testing atmospheric oxidation in an Alabama forest. *Journal of the Atmospheric Sciences*, 73(12), 4699–4710. <https://doi.org/10.1175/JAS-D-16-0044.1>
- Fittschen, C. (2019). The reaction of peroxy radicals with OH radicals. *Chemical Physics Letters*, 725(April), 102–108. <https://doi.org/10.1016/j.cplett.2019.04.002>
- Fittschen, C., Al Ajami, M., Batut, S., Ferracci, V., Archer-Nicholls, S., Archibald, A. A., & Schoemaeker, C. (2019). ROOOH: A missing piece of the puzzle for OH measurements in low-NO environments? *Atmospheric Chemistry and Physics*, 19(1), 349–362. <https://doi.org/10.5194/acp-19-349-2019>
- Fittschen, C., Whalley, L. K., & Heard, D. E. (2014). The reaction of CH₃O₂ radicals with OH radicals: A neglected sink for CH₃O₂ in the remote atmosphere. *Environmental Science and Technology*, 48(14), 7700–7701. <https://doi.org/10.1021/es502481q>
- Fu, Z., Xie, H. Bin, Elm, J., Guo, X., Fu, Z., Fu, Z., & Chen, J. (2020). Formation of Low-Volatile Products and Unexpected High Formaldehyde Yield from the Atmospheric Oxidation of Methylsiloxanes. *Environmental Science and Technology*, 54(12), 7136–7145. <https://doi.org/10.1021/acs.est.0c01090>
- Fuchs, H., Bohn, B., Hofzumahaus, A., Holland, F., Lu, K. D., Nehr, S., Rohrer, F., & Wahner, A. (2011). Detection of HO₂ by laser-induced fluorescence: Calibration and interferences from RO₂ radicals. *Atmospheric Measurement Techniques*, 4(6), 1209–1225. <https://doi.org/10.5194/amt-4-1255-2011>
- Fuchs, H., Brauers, T., Dorn, H. P., Harder, H., Häsel, R., Hofzumahaus, A., Holland, F., Kanaya, Y., Kajii, Y., Kubistin, D., Lou, S., Martinez, M., Miyamoto, K., Nishida, S., Rudolf, M., Schlosser, E., Wahner, A., Yoshino, A., & Schurath, U. (2010). Technical Note: Formal blind intercomparison of HO₂ measurements in the atmosphere simulation chamber SAPHIR during the HOxComp campaign. *Atmospheric Chemistry and Physics*, 10(24), 12233–12250. <https://doi.org/10.5194/acp-10-12233-2010>
- Fuchs, H., Brauers, T., Häsel, R., Holland, F., Mihelcic, D., Müsgen, P., Rohrer, F., Wegener, R., & Hofzumahaus, A. (2009). Intercomparison of peroxy radical measurements obtained at atmospheric conditions by laser-induced fluorescence and electron spin resonance spectroscopy. *Atmospheric Measurement Techniques*, 2(1), 55–64. <https://doi.org/10.5194/amt-2-55-2009>
- Fuchs, H., Dorn, H. P., Bachner, M., Bohn, B., Brauers, T., Gomm, S., Hofzumahaus, A., Holland, F., Nehr, S., Rohrer, F., Tillmann, R., & Wahner, A. (2012). Comparison of OH concentration measurements by DOAS and LIF during SAPHIR chamber experiments at high OH reactivity and low NO concentration. *Atmospheric Measurement Techniques*, 5(7), 2077–2110. <https://doi.org/10.5194/amt-5-1611-2012>
- Fuchs, H., Hofzumahaus, A., Rohrer, F., Bohn, B., Brauers, T., Dorn, H. P., Häsel, R., Holland, F., Kaminski, M., Li, X., Lu, K., Nehr, S., Tillmann, R., Wegener, R., & Wahner, A. (2013). Experimental evidence for efficient hydroxyl radical regeneration in isoprene oxidation. *Nature Geoscience*, 6(12), 1023–1026. <https://doi.org/10.1038/ngeo1964>
- Fuchs, H. (2006). Measurement of Peroxy Radicals using Laser-Induced Fluorescence Technique. *PhD Thesis, Forschungszentrum Jülich*.
- Fuchs, H., Holland, F., & Hofzumahaus, A. (2008). Measurement of tropospheric RO₂ and HO₂ radicals by a laser-induced fluorescence instrument. *Review of Scientific Instruments*, 79(8). <https://doi.org/10.1063/1.2968712>
- Fuchs, H., Novelli, A., Rolletter, M., Hofzumahaus, A., Pfannerstill, E. Y., Kessel, S., Edtbauer, A., Williams, J., Michoud, V., Dusanter, S., Locoge, N., Zannoni, N., Gros, V., Truong, F., Sarda-Esteve, R., Cryer, D. R., Brumby, C. A., Whalley, L. K., Stone, D., ... Wahner, A. (2017). Comparison of OH reactivity measurements in the atmospheric simulation chamber SAPHIR. *Atmospheric Measurement Techniques*, 10(10), 4023–4053. <https://doi.org/10.5194/amt-10-4023-2017>

- Fuchs, H., Tan, Z., Hofzumahaus, A., Broch, S., Dorn, H. P., Holland, F., Künstler, C., Gomm, S., Rohrer, F., Schrade, S., Tillmann, R., & Wahner, A. (2016). Investigation of potential interferences in the detection of atmospheric ROx radicals by laser-induced fluorescence under dark conditions. *Atmospheric Measurement Techniques*, 8(4), 12475–12523. <https://doi.org/10.5194/amt-9-1431-2016>
- Fuchs, H., Tan, Z., Lu, K., Bohn, B., Broch, S., Brown, S. S., Dong, H., Gomm, S., Häsel, R., He, L., Hofzumahaus, A., Holland, F., Li, X., Liu, Y., Lu, S., Min, K. E., Rohrer, F., Shao, M., Wang, B., ... Zhang, Y. (2017). OH reactivity at a rural site (Wangdu) in the North China Plain: Contributions from OH reactants and experimental OH budget. *Atmospheric Chemistry and Physics*, 17(1), 645–661. <https://doi.org/10.5194/acp-17-645-2017>
- Galbally, A., & Goldstein, A. (2007). Known and Unexplored Organic constituents in the Earth's Atmosphere. *Environmental Science and Technology*, 6(11), 1515–1521.
- Galbally, I. E., & Kirstine, W. (2002). The production of methanol by flowering plants and the global cycle of methanol. *Journal of Atmospheric Chemistry*, 43(3), 195–229. <https://doi.org/10.1023/A:1020684815474>
- Geyer, A., Bächmann, K., Hofzumahaus, A., Holland, F., Konrad, S., Klüpfel, T., Pätz, H. W., Perner, D., Mihelcic, D., Schäfer, H. J., Volz-Thomas, A., & Platt, U. (2003). Nighttime formation of peroxy and hydroxyl radicals during the BERLIOZ campaign: Observations and modeling studies. *Journal of Geophysical Research: Atmospheres*, 108(4). <https://doi.org/10.1029/2001jd000656>
- Golomb, D. S., & Fay, J. A. (1989). The Role of Methane in Tropospheric Chemistry. *Massachusetts Institute of Technology*.
- Griffith, S. M., Hansen, R. F., Dusanter, S., Stevens, P. S., Alaghmand, M., Bertman, S. B., Carroll, M. A., Erickson, M., Galloway, M., Grossberg, N., Hottle, J., Hou, J., Jobson, B. T., Kammrath, A., Keutsch, F. N., Lefer, B. L., Mielke, L. H., O'Brien, A., Shepson, P. B., ... Zhou, X. L. (2013). OH and HO₂ radical chemistry during PROPHET 2008 and CABINEX 2009 - Part 1: Measurements and model comparison. *Atmospheric Chemistry and Physics*, 13(11), 5403–5423. <https://doi.org/10.5194/acp-13-5403-2013>
- Grosjean, E., & Grosjean, D. (1997). Gas phase reaction of alkenes with ozone: Formation yields of primary carbonyls and biradicals. *Environmental Science and Technology*, 31(8), 2421–2427. <https://doi.org/10.1021/es970075b>
- Grosjean, E., & Grosjean, D. (1998). The gas-phase reaction of alkenes with ozone: Formation yields of carbonyls from biradicals in ozone-alkene-cyclohexane experiments. *Atmospheric Environment*, 32(20), 3393–3402. [https://doi.org/10.1016/S1352-2310\(98\)80005-8](https://doi.org/10.1016/S1352-2310(98)80005-8)
- Guenther, A. (1995). A global model of natural volatile organic compound emissions. *Journal of Geophysical Research*, 100(D5), 8873–8892. <https://doi.org/10.1029/94JD02950>
- Guenther, A. B., Jiang, X., Heald, C. L., Sakulyanontvittaya, T., Duhl, T., Emmons, L. K., & Wang, X. (2012). The model of emissions of gases and aerosols from nature version 2.1 (MEGAN2.1): An extended and updated framework for modeling biogenic emissions. *Geoscientific Model Development*, 5(6), 1471–1492. <https://doi.org/10.5194/gmd-5-1471-2012>
- Hansen, R. F., Blocquet, M., Schoemaeker, C., Léonardis, T., Locoge, N., Fittschen, C., Hanoune, B., Stevens, P. S., Sinha, V., & Dusanter, S. (2015). Intercomparison of the comparative reactivity method (CRM) and pump-probe technique for measuring total OH reactivity in an urban environment. *Atmospheric Measurement Techniques*, 8(10), 4243–4264. <https://doi.org/10.5194/amt-8-4243-2015>
- Hansen, R. F., Griffith, S. M., Dusanter, S., Rickly, P. S., Stevens, P. S., Bertman, S. B., Carroll, M. A., Erickson, M. H., Flynn, J. H., Grossberg, N., Jobson, B. T., Lefer, B. L., & Wallace, H. W. (2014). Measurements of total hydroxyl radical reactivity during CABINEX 2009

- ; Part 1: Field measurements. *Atmospheric Chemistry and Physics*, 14(6), 2923–2937. <https://doi.org/10.5194/acp-14-2923-2014>
- Hard, T. M., O'Brien, R. J., Cook, T. B., & Tsongas, G. A. (1979). Interference suppression in HO fluorescence detection. *Applied Optics*, 18(19), 3216–3217. <https://doi.org/10.1364/ao.18.003216>
- Hard, T. M., O'Brien, R. J., Chan, C. Y., & Mehrabzadeh, A. A. (1984). Tropospheric Free Radical Determination by FAGE. *Environmental Science and Technology*, 18(10), 768–777. <https://doi.org/10.1021/es00128a009>
- Harley, P., Greenberg, J., Niinemets, Ü., & Guenther, A. (2007). Environmental controls over methanol emission from leaves. *Biogeosciences*, 4(6), 1083–1099. <https://doi.org/10.5194/bg-4-1083-2007>
- Heard, D. E., & Pilling, M. J. (2003). Measurement of OH and HO₂ in the Troposphere. *Chemical Reviews*, 103(12), 5163–5198. <https://doi.org/10.1021/cr020522s>
- Heikes, B. G., Chang, W., Pilson, M. E. Q., Swift, E., Singh, H. B., Guenther, A., Jacob, D. J., Field, B. D., Fall, R., Reimer, D., & Brand, L. (2002). Atmospheric methanol budget and ocean implication. *Global Biogeochemical Cycles*, 16(4), 80–1–80–13. <https://doi.org/10.1029/2002gb001895>
- Herrmann, H., Schaefer, T., Tilgner, A.S., Styler, A., Weller, C., Teich, M. and Otto, T. (2015). Tropospheric Aqueous-Phase Chemistry: Kinetics, Mechanisms, and its Coupling to a Changing Gas Phase. *Chemical Reviews* 115(10): 4259–4334. <https://doi.org/10.1021/cr500447k>
- Hofzumahaus, A., Aschmutat, U., Heßling, M., Holland, F., & Ehhalt, D. H. (1996). The measurement of tropospheric OH radicals by laser-induced fluorescence spectroscopy during the POPCORN field campaign. *Geophysical Research Letters*, 23(18), 2541–2544. <https://doi.org/10.1029/96GL02205>
- Holland, F., Hessling, M., and Hofzumahaus, A. (1995). In situ measurement of tropospheric OH radicals by laser-induced fluorescence—a description of the KFA instrument. *Journal of the Atmospheric Sciences.*, 52(19), 3393–3401.
- Holland, F., Hofzumahaus, A., Schäfer, J., Kraus, A., & Pätz, H. W. (2003). Measurements of OH and HO₂ radical concentrations and photolysis frequencies during BERLIOZ. *Journal of Geophysical Research: Atmospheres*, 108(4). <https://doi.org/10.1029/2001jd001393>
- Holzinger, R., Lee, A., Paw U, K. T., & Goldstein, A. H. (2005). Observations of oxidation products above a forest imply biogenic emissions of very reactive compounds. *Atmospheric Chemistry and Physics*, 5(1), 67–75. <https://doi.org/10.5194/acp-5-67-2005>
- Horii, Y., & Kannan, K. (2008). Survey of organosilicone compounds, including cyclic and linear siloxanes, in personal-care and household products. *Archives of Environmental Contamination and Toxicology*, 55(4), 701–710. <https://doi.org/10.1007/s00244-008-9172-z>
- Hornbrook, R. S., Blake, D. R., Diskin, G. S., Fried, A., Fuelberg, H. E., Meinardi, S., Mikoviny, T., Richter, D., Sachse, G. W., Vay, S. A., Walega, J., Weibring, P., Weinheimer, A. J., Wiedinmyer, C., Wisthaler, A., Hills, A., Riemer, D. D., & Apel, E. C. (2011). Observations of nonmethane organic compounds during ARCTAS-Part 1: Biomass burning emissions and plume enhancements. *Atmospheric Chemistry and Physics*, 11(21), 11103–11130. <https://doi.org/10.5194/acp-11-11103-2011>
- Hornbrook, R. S., Crawford, J. H., Edwards, G. D., Goyea, O., Mauldin, R. L., Olson, J. S., & Cantrell, C. A. (2011). Measurements of tropospheric HO₂ and RO₂ by oxygen dilution modulation and chemical ionization mass spectrometry. *Atmospheric Measurement Techniques*, 4(4), 735–756. <https://doi.org/10.5194/amt-4-735-2011>
- Hu, J., & Stedman, D. H. (1995). Atmospheric RO_x Radicals at an Urban Site: Comparison to a Simple Theoretical Model. *Environmental Science and Technology*, 29(6), 1655–1659.

<https://doi.org/10.1021/es00006a032>

- Hu, L., Millet, D. B., Mohr, M. J., Wells, K. C., Griffis, T. J., & Helmig, D. (2011). Sources and seasonality of atmospheric methanol based on tall tower measurements in the US Upper Midwest. *Atmospheric Chemistry and Physics*, *11*(21), 11145–11156. <https://doi.org/10.5194/acp-11-11145-2011>
- Ingham, T., Goddard, A., Whalley, L. K., Furneaux, K. L., Edwards, P. M., Seal, C. P., Self, D. E., Johnson, G. P., Read, K. A., Lee, J. D., & Heard, D. E. (2009). A flow-tube based laser-induced fluorescence instrument to measure OH reactivity in the troposphere. *Atmospheric Measurement Techniques*, *2*(2), 465–477. <https://doi.org/10.5194/amt-2-465-2009>
- Jacob, D. J., Field, B. D., Li, Q., Blake, D. R., de Gouw, J., Warneke, C., Hansel, A., Wisthaler, A., Singh, H. B., & Guenther, A. (2005). Global budget of methanol: Constraints from atmospheric observations. *Journal of Geophysical Research D: Atmospheres*, *110*(8), 1–17. <https://doi.org/10.1029/2004JD005172>
- Jenkin, M. E., Valorso, R., Aumont, B., & Rickard, A. R. (2019). Estimation of rate coefficients and branching ratios for reactions of organic peroxy radicals for use in automated mechanism construction. *Atmospheric Chemistry and Physics*, *19*(11), 7691–7717. <https://doi.org/10.5194/acp-19-7691-2019>
- Jiang, Y., Xue, L., Gu, R., Jia, M., Zhang, Y., Wen, L., Zheng, P., Chen, T., Li, H., Shan, Y., Zhao, Y., Guo, Z., Bi, Y., Liu, H., Ding, A., Zhang, Q., & Wang, W. (2020). Sources of nitrous acid (HONO) in the upper boundary layer and lower free troposphere of the North China Plain: Insights from the Mount Tai Observatory. *Atmospheric Chemistry and Physics*, *20*(20), 12115–12131. <https://doi.org/10.5194/acp-20-12115-2020>
- Johnson, D., & Marston, G. (2008). The gas-phase ozonolysis of unsaturated volatile organic compounds in the troposphere. *Chemical Society Reviews*, *37*(4), 699–716. <https://doi.org/10.1039/b704260b>
- Jud, W., Fischer, L., Canaval, E., Wohlfahrt, G., Tissier, A., & Hansel, A. (2016). Plant surface reactions: An opportunistic ozone defence mechanism impacting atmospheric chemistry. *Atmospheric Chemistry and Physics*, *16*(1), 277–292. <https://doi.org/10.5194/acp-16-277-2016>
- Kanaya, Y., Sadanaga, Y., Matsumoto, J., Sharma, U. K., Hirokawa, J., Kajii, Y., & Akimoto, H. (1999). Nighttime observation of the HO₂ radical by an LIF instrument at Oki island, Japan, and its possible origins. *Geophysical Research Letters*, *26*(14), 2179–2182. <https://doi.org/10.1029/1999GL900475>
- Kari, E., Miettinen, P., Yli-Pirilä, P., Virtanen, A., & Faiola, C. L. (2018). PTR-ToF-MS product ion distributions and humidity-dependence of biogenic volatile organic compounds. *International Journal of Mass Spectrometry*, *430*, 87–97. <https://doi.org/10.1016/j.ijms.2018.05.003>
- Karl, T., Harley, P., Guenther, A., Rasmussen, R., Baker, B., Jardine, K., & Nemitz, E. (2005). The bi-directional exchange of oxygenated VOCs between a loblolly pine (*Pinus taeda*) plantation and the atmosphere. *Atmospheric Chemistry and Physics*, *5*(11), 3015–3031. <https://doi.org/10.5194/acp-5-3015-2005>
- Kartal, D., Andres-Hernandez, M. D., Reichert, L., Schlager, H., & Burrows, J. P. (2010). Technical Note: Characterisation of a DUALER instrument for the airborne measurement of peroxy radicals during AMMA 2006. *Atmospheric Chemistry and Physics*, *10*(6), 3047–3062. <https://doi.org/10.5194/acp-10-3047-2010>
- Khan, M. A. H., Cooke, M. C., Utembe, S. R., Archibald, A. T., Derwent, R. G., Jenkin, M. E., Morris, W. C., South, N., Hansen, J. C., Francisco, J. S., Percival, C. J., & Shallcross, D. E. (2015). Global analysis of peroxy radicals and peroxy radical-water complexation using the STOCHEM-CRI global chemistry and transport model. *Atmospheric Environment*, *106*(3), 278–287. <https://doi.org/10.1016/j.atmosenv.2015.02.020>

- Khan, M. A. H., Percival, C. J., Caravan, R. L., Taatjes, C. A., & Shallcross, D. E. (2018). Criegee intermediates and their impacts on the troposphere. *Environmental Science: Processes and Impacts*, 20(3), 437–453. <https://doi.org/10.1039/c7em00585g>
- Kim, J., Mackay, D., & Whelan, M. J. (2018). Predicted persistence and response times of linear and cyclic volatile methylsiloxanes in global and local environments. *Chemosphere*, 195, 325–335. <https://doi.org/10.1016/j.chemosphere.2017.12.071>
- Kim, J., & Xu, S. (2017). Quantitative structure-reactivity relationships of hydroxyl radical rate constants for linear and cyclic volatile methylsiloxanes. *Environmental Toxicology and Chemistry*, 36(12), 3240–3245. <https://doi.org/10.1002/etc.3914>
- Kirstine, W. V., & Galbally, I. E. (2012). The global atmospheric budget of ethanol revisited. *Atmospheric Chemistry and Physics*, 12(1), 545–555. <https://doi.org/10.5194/acp-12-545-2012>
- Koch, S., Winterhalter, R., Uherek, E., Kolloff, A., Neeb, P., & Moortgat, G. K. (2000). Formation of new particles in the gas-phase ozonolysis of monoterpenes. *Atmospheric Environment*, 34(23), 4031–4042. [https://doi.org/10.1016/S1352-2310\(00\)00133-3](https://doi.org/10.1016/S1352-2310(00)00133-3)
- Kroll, J. H., Donahue, N. M., Cee, V. J., Demerjian, K. L., & Anderson, J. G. (2002). Gas-phase ozonolysis of alkenes: Formation of OH from anti carbonyl oxides. *Journal of the American Chemical Society*, 124(29), 8518–8519. <https://doi.org/10.1021/ja0266060>
- Kubistin, D., Harder, H., Martinez, M., Rudolf, M., Sander, R., Bozem, H., Eerdeken, G., Fischer, H., Gurk, C., Klüpfel, T., Königstedt, R., Parchatka, U., Schiller, C. L., Stickler, A., Taraborrelli, D., Williams, J., & Lelieveld, J. (2010). Hydroxyl radicals in the tropical troposphere over the Suriname rainforest: Comparison of measurements with the box model MECCA. *Atmospheric Chemistry and Physics*, 10(19), 9705–9728. <https://doi.org/10.5194/acp-10-9705-2010>
- Kukui, A., Ancellet, G., & Le Bras, G. (2008). Chemical ionisation mass spectrometer for measurements of OH and Peroxy radical concentrations in moderately polluted atmospheres. *Journal of Atmospheric Chemistry*, 61(2), 133–154. <https://doi.org/10.1007/s10874-009-9130-9>
- Kumar, V., & Sinha, V. (2014). VOC-OHM: A new technique for rapid measurements of ambient total OH reactivity and volatile organic compounds using a single proton transfer reaction mass spectrometer. *International Journal of Mass Spectrometry*, 374, 55–63. <https://doi.org/10.1016/j.ijms.2014.10.012>
- Kundu, S., Deming, B. L., Lew, M. M., Bottorff, B. P., Rickly, P., Stevens, P. S., Dusanter, S., Sklaveniti, S., Leonardis, T., Locoge, N., & Wood, E. C. (2019). Peroxy radical measurements by ethane-nitric oxide chemical amplification and laser-induced fluorescence during the IRRONIC field campaign in a forest in Indiana. *Atmospheric Chemistry and Physics*, 19(14), 9563–9579. <https://doi.org/10.5194/acp-19-9563-2019>
- Lahib, A. (2019). Analytical Developments for measuring Atmospheric Peroxy Radicals. *PhD Thesis, Univesity of Lille*.
- Lew, M. M., Dusanter, S., & Stevens, P. S. (2018). Measurement of interferences associated with the detection of the hydroperoxy radical in the atmosphere using laser-induced fluorescence. *Atmospheric Measurement Techniques*, 11(1), 95–109. <https://doi.org/10.5194/amt-11-95-2018>
- Li, K., Jacobb, D.J., Liaoa, H., Shenb, L., Zhangd, Q. and Batesb, K.H. (2019). Anthropogenic drivers of 2013–2017 trends in summer surface ozone in China. *Proceedings of the National Academy of Sciences*, 116 (2) 422-427. <https://doi.org/10.1073/pnas.1812168116>
- Liu, Y., Morales-Cueto, R., Hargrove, J., Medina, D., & Zhang, J. (2009). Measurements of peroxy radicals using chemical amplification - Cavity Ringdown spectroscopy. *Environmental Science and Technology*, 43(20), 7791–7796. <https://doi.org/10.1021/es901146t>

- Liu, Y., & Zhang, J. (2014). Atmospheric peroxy radical measurements using dual-channel chemical amplification cavity ringdown spectroscopy. *Analytical Chemistry*, 86(11), 5391–5398. <https://doi.org/10.1021/ac5004689>
- Lu, K. D., Hofzumahaus, A., Holland, F., Bohn, B., Brauers, T., Fuchs, H., Hu, M., Häsel, R., Kita, K., Kondo, Y., Li, X., Lou, S. R., Oebel, A., Shao, M., Zeng, L. M., Wahner, A., Zhu, T., Zhang, Y. H., & Rohrer, F. (2013). Missing OH source in a suburban environment near Beijing: Observed and modelled OH and HO₂ concentrations in summer 2006. *Atmospheric Chemistry and Physics*, 13(2), 1057–1080. <https://doi.org/10.5194/acp-13-1057-2013>
- Lu, K. D., Rohrer, F., Holland, F., Fuchs, H., Bohn, B., Brauers, T., Chang, C. C., Häsel, R., Hu, M., Kita, K., Kondo, Y., Li, X., Lou, S. R., Nehr, S., Shao, M., Zeng, L. M., Wahner, A., Zhang, Y. H., & Hofzumahaus, A. (2012). Observation and modelling of OH and HO₂ concentrations in the Pearl River Delta 2006: A missing OH source in a VOC rich atmosphere. *Atmospheric Chemistry and Physics*, 12(3), 1541–1569. <https://doi.org/10.5194/acp-12-1541-2012>
- Lu, K., Guo, S., Tan, Z., Wang, H., Shang, D., Liu, Y., Li, X., Wu, Z., Hu, M., & Zhang, Y. (2019). Exploring atmospheric free-radical chemistry in China: The self-cleansing capacity and the formation of secondary air pollution. *National Science Review*, 6(3), 579–594. <https://doi.org/10.1093/nsr/nwy073>
- MacDonald, R. C., & Fall, R. (1993). Detection of substantial emissions of methanol from plants to the atmosphere. *Atmospheric Environment*, 27(11), 1709–1713. [https://doi.org/10.1016/0960-1686\(93\)90233-O](https://doi.org/10.1016/0960-1686(93)90233-O)
- Madronich, S., & Calvert, J. G. (1990). Permutation reactions of organic peroxy radicals in the troposphere. *Journal of Geophysical Research*, 95(D5), 5697–5715. <https://doi.org/10.1029/JD095iD05p05697>
- Mao, J., Ren, X., Zhang, L., Van Duin, D. M., Cohen, R. C., Park, J. H., Goldstein, A. H., Paulot, F., Beaver, M. R., Crouse, J. D., Wennberg, P. O., Digangi, J. P., Henry, S. B., Keutsch, F. N., Park, C., Schade, G. W., Wolfe, G. M., Thornton, J. A., & Brune, W. H. (2012). Insights into hydroxyl measurements and atmospheric oxidation in a California forest. *Atmospheric Chemistry and Physics*, 12(17), 8009–8020. <https://doi.org/10.5194/acp-12-8009-2012>
- Markgraf, S. J., & Wells, J. R. (1997). The hydroxyl radical reaction rate constants and atmospheric reaction products of three siloxanes. *International Journal of Chemical Kinetics*, 29(6), 445–451.
- Martin, S. T., Artaxo, P., MacHado, L. A. T., Manzi, A. O., Souza, R. A. F., Schumacher, C., Wang, J., Andreae, M. O., Barbosa, H. M. J., Fan, J., Fisch, G., Goldstein, A. H., Guenther, A., Jimenez, J. L., Pöschl, U., Silva Dias, M. A., Smith, J. N., & Wendisch, M. (2016). Introduction: Observations and Modeling of the Green Ocean Amazon (GoAmazon2014/5). *Atmospheric Chemistry and Physics*, 16(8), 4785–4797. <https://doi.org/10.5194/acp-16-4785-2016>
- Martinez, M., Harder, H., Kubistin, D., Rudolf, M., Eerdeken, G., Fischer, H., Klüpfel, T., Gurk, C., Königstedt, R., Parchatka, U., Schiller, C. L., Stickler, A., Williams, J., & Lelieveld, J. (2010). Hydroxyl radicals in the tropical troposphere over the Suriname rainforest: Airborne measurements. *Atmospheric Chemistry and Physics*, 10(8), 3759–3773. <https://doi.org/10.5194/acp-10-3759-2010>
- Matsumi, Y., Kono, M., Ichikawa, T., Takahashi, K., & Kondo, Y. (2002). Laser-induced fluorescence instrument for the detection of tropospheric OH radicals. *Bulletin of the Chemical Society of Japan*, 75(4), 711–717. <https://doi.org/10.1246/bcsj.75.711>
- Mauldin, R. L., Madronich, S., Flocke, S. J., Eisele, F. L., Frost, G. J. and Prevot, A. S. H. (1997). New insights on OH: Measurements around and in clouds. *Geophys. Res. Lett.*

24(23): 3033-3036.

- McFiggans, G., Mentel, T. F., Wildt, J., Pullinen, I., Kang, S., Kleist, E., Schmitt, S., Springer, M., Tillmann, R., Wu, C., Zhao, D., Hallquist, M., Faxon, C., Le Breton, M., Hallquist, Å. M., Simpson, D., Bergström, R., Jenkin, M. E., Ehn, M., ... Kiendler-Scharr, A. (2019). Secondary organic aerosol reduced by mixture of atmospheric vapours. *Nature*, *565*, 587–593. <https://doi.org/10.1038/s41586-018-0871-y>
- Menut, L., Vautard, R., Flamant, C., Abonnel, C., Beekmann, M., Chazette, P., Flamant, P. H., Gombert, D., Guédalia, D., Kley, D., Lefebvre, M. P., Lossec, B., Martin, D., Mégie, G., Perros, P., Sicard, M., & Toupance, G. (2000). Measurements and modelling of atmospheric pollution over the Paris area: an overview of the ESQUIF Project. *Annales Geophysicae*, *18*(11), 1467–1481. <https://doi.org/10.1007/s005850000277>
- Mermert, K., Perraudin, E., Dusanter, S., Sauvage, S., & Léonardis, T. (2021). Atmospheric Reactivity of Biogenic Volatile Organic Compounds in a Maritime Pine forest during the LANDEX episode 1 field campaign. *Science of the Total Environment*, *765*, 1–50, 144129.
- Michoud, V., Hansen, R. F., Locoge, N., Stevens, P. S., & Dusanter, S. (2015). Detailed characterizations of a Comparative Reactivity Method (CRM) instrument: experiments vs. modelling. *Atmospheric Measurement Techniques Discussions*, *8*(4), 3803–3850. <https://doi.org/10.5194/amtd-8-3803-2015>
- Mihelic, D., Klemp, D., Musgen, P., Patz, H. W. & Volz-Thomas, A. (1993). Simultaneous Measurements of Peroxy and Nitrate Radicals at Schauinsland. *Journal of Atmospheric Chemistry*, *16*, 313–335.
- Mihelcic, D., Holland, F., Hofzumahaus, A., Hoppe, L., Konrad, S., Müsgen, P., Pätz, H. W., Schäfer, H. J., Schmitz, T., Volz-Thomas, A., Bächmann, K., Schlomski, S., Platt, U., Geyer, A., Alicke, B., & Moortgat, G. K. (2003). Peroxy radicals during BERLIOZ at Pabstthum: Measurements, radical budgets and ozone production. *Journal of Geophysical Research: Atmospheres*, *108*(4), 8254. <https://doi.org/10.1029/2001jd001014>
- Millet, D. B., Guenther, A., Siegel, D., Nelson, N., Singh, H., De Gouw, J., Warneke, C., Williams, J., Eerdekens, G., Sinha, V., Karl, T., Flocke, F., Apel, E., Riemer, D. D., Palmer, P. I., & Barkley, M. (2010). Global atmospheric budget of acetaldehyde: 3-D model analysis and constraints from in-situ and satellite observations. *Atmospheric Chemistry and Physics*, *10*(7), 3405–3425. <https://doi.org/10.5194/acp-10-3405-2010>
- Millet, D. B., Jacob, D. J., Custer, T. G., De Gouw, J. A., Goldstein, A. H., Karl, T., Singh, H. B., Sive, B. C., Talbot, R. W., Warneke, C., & Williams, J. (2008). New constraints on terrestrial and oceanic sources of atmospheric methanol. *Atmospheric Chemistry and Physics*, *8*(23), 6887–6905. <https://doi.org/10.5194/acp-8-6887-2008>
- Miyazaki, K., Parker, A. E., Fittschen, C., Monks, P. S., & Kajii, Y. (2010). A new technique for the selective measurement of atmospheric peroxy radical concentrations of HO₂ and RO₂ using a denuding method. *Atmospheric Measurement Techniques*, *3*(6), 1547–1554. <https://doi.org/10.5194/amt-3-1547-2010>
- Mogensen, D., Smolander, S., Sogachev, A., Zhou, L., Sinha, V., Guenther, A., Williams, J., Nieminen, T., Kajos, M. K., Rinne, J., Kulmala, M., & Boy, M. (2011). Modelling atmospheric OH-reactivity in a boreal forest ecosystem. *Atmospheric Chemistry and Physics*, *11*(18), 9709–9719. <https://doi.org/10.5194/acp-11-9709-2011>
- Mojsiewicz-Pienkowska, K., Jamrógiewicz, M., Szymkowska, K., & Krenczkowska, D. (2016). Direct human contact with siloxanes (silicones) - safety or risk part 1. Characteristics of siloxanes (silicones). *Frontiers in Pharmacology*, *7*, 1–8. <https://doi.org/10.3389/fphar.2016.00132>
- Monks, P. S. (2005). Gas-phase radical chemistry in the troposphere. *Chemical Society Reviews*, *34*(5), 376–395. <https://doi.org/10.1039/b307982c>
- Montzka, S. A., Krol, M., Dlugokencky, E., Hall, B., Jöckel, P., & Lelieveld, J. (2011). Small

- interannual variability of global atmospheric hydroxyl. *Science*, 331, 67–69. <https://doi.org/10.1126/science.1197640>
- Moo, Z., Hao, P., DeMarsh, K.E. and Zhang, X. (2024). Efficient HO_x Radical Production from Isoprene Nighttime Chemistry. *ACS Earth Space Chem.*, 8, 2, 361–368. <https://doi.org/10.1021/acsearthspacechem.3c00323>
- Mount, G. H., Eisele, F. L., Tanner, D. J., Brault, J. W., Johnston, P. V., Harder, J. W., Williams, E. J., Fried, A., & Shetter, R. (1997). An intercomparison of spectroscopic laser long-path and ion-assisted in situ measurements of hydroxyl concentrations during the Tropospheric OH Photochemistry Experiment, fall 1993. *Journal of Geophysical Research*, 102(5), 6437–6455. <https://doi.org/10.1029/96jd02342>
- Müller, J. F., Liu, Z., Nguyen, V. S., Stavrou, T., Harvey, J. N., & Peeters, J. (2016). The reaction of methyl peroxy and hydroxyl radicals as a major source of atmospheric methanol. *Nature Communications*, 7, 1–11. <https://doi.org/10.1038/ncomms13213>
- Naik, V., Fiore, A. M., Horowitz, L. W., Singh, H. B., Wiedinmyer, C., Guenther, A., De Gouw, J. A., Millet, D. B., Goldan, P. D., Kuster, W. C., & Goldstein, A. (2010). Observational constraints on the global atmospheric budget of ethanol. *Atmospheric Chemistry and Physics*, 10(12), 5361–5370. <https://doi.org/10.5194/acp-10-5361-2010>
- Nakashima, Y., Kato, S., Greenberg, J., Harley, P., Karl, T., Turnipseed, A., Apel, E., Guenther, A., Smith, J., & Kajii, Y. (2014). Total OH reactivity measurements in ambient air in a southern Rocky mountain ponderosa pine forest during BEACHON-SRM08 summer campaign. *Atmospheric Environment*, 85, 1–8. <https://doi.org/10.1016/j.atmosenv.2013.11.042>
- Nascimento, J. P., Bela, M. M., Meller, B. B., Banducci, A. L., Rizzo, L. V., Liduvino Varavela, A., Barbosa, H. M. J., Gomes, H., Rafee, S. A. A., Franco, M. A., Carbone, S., Cirino, G. G., Souza, R. A. F., Mckeen, S. A., & Artaxo, P. (2021). Aerosols from anthropogenic and biogenic sources and their interactions-modeling aerosol formation, optical properties, and impacts over the central Amazon basin. *Atmospheric Chemistry and Physics*, 21(9), 6755–6779. <https://doi.org/10.5194/acp-21-6755-2021>
- Nehr, S., Bohn, B., Fuchs, H., Häsel, R., Hofzumahaus, A., Li, X., Rohrer, F., Tillmann, R., & Wahner, A. (2014). Atmospheric photochemistry of aromatic hydrocarbons: OH budgets during SAPHIR chamber experiments. *Atmospheric Chemistry and Physics*, 14(13), 6941–6952. <https://doi.org/10.5194/acp-14-6941-2014>
- Niki, H., Savage, C. M., Breitenbach, L. P., & Weinstock, B. (1983). Atmospheric ozone-olefin reactions. *Environmental Science and Technology*, 17(7), 312–322.
- Nölscher, A. C., Bourtsoukidis, E., Bonn, B., Kesselmeier, J., Lelieveld, J., & Williams, J. (2013). Seasonal measurements of total OH reactivity emission rates from Norway spruce in 2011. *Biogeosciences*, 10(6), 4241–4257. <https://doi.org/10.5194/bg-10-4241-2013>
- Nölscher, A. C., Sinha, V., Bockisch, S., Klüpfel, T., & Williams, J. (2012). A new method for total OH reactivity measurements using a new fast gas chromatographic photo-ionization detector (GC-PID). *Atmospheric Measurement Techniques*, 5(12), 3575–3609. <https://doi.org/10.5194/amt-5-2981-2012>
- Nölscher, A. C., Williams, J., Sinha, V., Custer, T., Song, W., Johnson, A. M., Axinte, R., Bozem, H., Fischer, H., Pouvesle, N., Phillips, G., Crowley, J. N., Rantala, P., Rinne, J., Kulmala, M., Gonzales, D., Valverde-Canossa, J., Vogel, A., Hoffmann, T., ... Lelieveld, J. (2012). Summertime total OH reactivity measurements from boreal forest during HUMPPA-COPEC 2010. *Atmospheric Chemistry and Physics*, 12(17), 8257–8270. <https://doi.org/10.5194/acp-12-8257-2012>
- Nölscher, A. C., Yañez-Serrano, A. M., Wolff, S., De Araujo, A. C., Lavrič, J. V., Kesselmeier, J., & Williams, J. (2016). Unexpected seasonality in quantity and composition of Amazon rainforest air reactivity. *Nature Communications*, 7.

<https://doi.org/10.1038/ncomms10383>

- Novelli, A., Vereecken, L., Bohn, B., Dorn, H. P., Gkatzelis, G. I., Hofzumahaus, A., Holland, F., Reimer, D., Rohrer, F., Rosanka, S., Taraborrelli, D., Tillmann, R., Wegener, R., Yu, Z., Kiendler-Scharr, A., Wahner, A., & Fuchs, H. (2020). Importance of isomerization reactions for OH radical regeneration from the photo-oxidation of isoprene investigated in the atmospheric simulation chamber SAPHIR. *Atmospheric Chemistry and Physics*, 20(6), 3333–3355. <https://doi.org/10.5194/acp-20-3333-2020>
- Orlando, J. J., & Tyndall, G. S. (2012). Laboratory studies of organic peroxy radical chemistry: An overview with emphasis on recent issues of atmospheric significance. *Chemical Society Reviews*, 41(19), 6294–6317. <https://doi.org/10.1039/c2cs35166h>
- Parker, A. E., Monks, P. S., Wyche, K. P., Balzani-Lööv, J. M., Staehelin, J., Reimann, S., Legreid, G., Vollmer, M. K., & Steinbacher, M. (2009). Peroxy radicals in the summer free troposphere: Seasonality and potential for heterogeneous loss. *Atmospheric Chemistry and Physics*, 9(6), 1989–2006. <https://doi.org/10.5194/acp-9-1989-2009>
- Parker, A. E., Amédro, D., Schoemaeker, C., & Fittschen, C. (2011). OH radical reactivity measurements by FAGE. *Environmental Engineering and Management Journal*, 10(1), 107–114. <https://doi.org/10.30638/eemj.2011.015>
- Perring, A. E., Wisthaler, A., Graus, M., Wooldridge, P. J., Lockwood, A. L., Mielke, L. H., Shepson, P. B., Hansel, A. and Cohen R. C. (2009). A product study of the isoprene+NO₃ reaction. *Atmospheric Chemistry and Physics*, 9, 4945–4956.
- Peeters, J., Nguyen, T. L., & Vereecken, L. (2009). HO_x radical regeneration in the oxidation of isoprene. *Physical Chemistry Chemical Physics*, 11(28), 5935–5939. <https://doi.org/10.1039/b908511d>
- Peeters, J., & Müller, J. F. (2010). HO_x radical regeneration in isoprene oxidation via peroxy radical isomerisations. II: Experimental evidence and global impact. *Physical Chemistry Chemical Physics*, 12(42), 14227–14235. <https://doi.org/10.1039/c0cp00811g>
- Pekey, H., & Arslanbaş, D. (2008). The relationship between indoor, outdoor and personal VOC concentrations in homes, offices and schools in the metropolitan region of Kocaeli, Turkey. *Water, Air, and Soil Pollution*, 191(1–4), 113–129. <https://doi.org/10.1007/s11270-007-9610-y>
- Pieri, F., Katsoyiannis, A., Martellini, T., Hughes, D., Jones, K. C., & Cincinelli, A. (2013). Occurrence of linear and cyclic volatile methyl siloxanes in indoor air samples (UK and Italy) and their isotopic characterization. *Environment International*, 59, 363–371. <https://doi.org/10.1016/j.envint.2013.06.006>
- Platt, U., Alicke, B., Dubois, R., Geyer, A., Hofzumahaus, A., Holland, F., Martinez, M., Mihelcic, D., Klüpfel, T., Lohrmann, B., Pätz, W., Perner, D., Rohrer, F., Schäfer, J., & Stutz, J. (2002). Free radicals and fast photochemistry during BERLIOZ. *Journal of Atmospheric Chemistry*, 42(1), 359–394. <https://doi.org/10.1023/A:1015707531660>
- Platt, U., and Hausmann, M. (1994). Spectroscopic measurement of the free radicals NO₃, BRO, IO, and OH in the troposphere. *Research on Chemical Intermediates*, 20(3–5), 557–578. <https://doi.org/10.1163/156856794X00450>
- Platt, U. and Perner, D. (1980). Direct Measurements of Atmospheric CH₂O, HNO₂, O₃, NO₂, and SO₂ by Differential Optical Absorption in the Near UV. *Journal of Geophysical Research*, 85, 7453–7458.
- Ravishankara, A-R. and Thompson, R-L. (1983). Kinetic study of the reaction of OH with CO from 250 to 1040 K. *Chemical Physics letters*, 99(5), 377-381.
- Ren, X., Brune, W. H., Cantrell, C. A., Edwards, G. D., Shirley, T., Metcalf, A. R., & Leshner, R. L. (2005). Hydroxyl and peroxy radical chemistry in a rural area of central Pennsylvania: Observations and model comparisons. *Journal of Atmospheric Chemistry*, 52(3), 231–257. <https://doi.org/10.1007/s10874-005-3651-7>

- Ren, X., Brune, W. H., Mao, J., Mitchell, M. J., Leshner, R. L., Simpasa, J. B., Metcalf, A. R., Schwab, J. J., Cai, C., Li, Y., Demerjian, K. L., Felton, H. D., Boynton, G., Adams, A., Perry, J., He, Y., Zhou, X., & Hou, J. (2006). Behavior of OH and HO₂ in the winter atmosphere in New York City. *Atmospheric Environment*, *40*(2), 252–263. <https://doi.org/10.1016/j.atmosenv.2005.11.073>
- Ren, X., Brune, W. H., Oligier, A., Metcalf, A. R., Simpasa, J. B., Shirley, T., Schwab, J. J., Bai, C., Roychowdhury, U., Li, Y., Cai, C., Demerjian, K. L., He, Y., Zhou, X., Gao, H., & Hou, J. (2006). OH, HO₂, and OH reactivity during the PMTACS-NY Whiteface Mountain 2002 campaign: Observations and model comparison. *Journal of Geophysical Research Atmospheres*, *111*(10), 1–12. <https://doi.org/10.1029/2005JD006126>
- Ren, X., Edwards, G. D., Cantrell, C. A., Leshner, R. L., Metcalf, A. R., Shirley, T., & Brune, W. H. (2003). Intercomparison of peroxy radical measurements at a rural site using laser-induced fluorescence and Peroxy Radical Chemical Ionization Mass Spectrometer (PerCIMS) techniques. *Journal of Geophysical Research: Atmospheres*, *108*(19), 4605. <https://doi.org/10.1029/2003jd003644>
- Ren, X., Harder, H., Martinez, M., Faloon, I. C., Tan, D., Leshner, R. L., Di Carlo, P., Simpasa, J. B., & Brune, W. H. (2004). Interference testing for atmospheric HO_x measurements by laser-induced fluorescence. *Journal of Atmospheric Chemistry*, *47*(2), 169–190. <https://doi.org/10.1023/B:JOCH.0000021037.46866.81>
- Ren, Z., & Da Silva, G. (2020). Auto-Oxidation of a Volatile Silicon Compound: A Theoretical Study of the Atmospheric Chemistry of Tetramethylsilane. *Journal of Physical Chemistry A*, *124*(32), 6544–6551. <https://doi.org/10.1021/acs.jpca.0c02922>
- Rigby, M., Prinn, R. G., Fraser, P. J., Simmonds, P. G., Langenfelds, R. L., Huang, J., Cunnold, D. M., Steele, L. P., Krummel, P. B., Weiss, R. F., O'Doherty, S., Salameh, P. K., Wang, H. J., Harth, C. M., Mühle, J., & Porter, L. W. (2008). Renewed growth of atmospheric methane. *Geophysical Research Letters*, *35*(22), 22805. <https://doi.org/10.1029/2008GL036037>
- Rohrer, F., Bohn, B., Brauers, T., Brüning, D., Johnen, F. J., Wahner, A., & Kleffmann, J. (2005). Characterisation of the photolytic HONO-source in the atmosphere simulation chamber SAPHIR. *Atmospheric Chemistry and Physics*, *5*(8), 2189–2201. <https://doi.org/10.5194/acp-5-2189-2005>
- Rohrer, F., Lu, K., Hofzumahaus, A., Bohn, B., Brauers, T., Chang, C. C., Fuchs, H., Häsel, R., Holland, F., Hu, M., Kita, K., Kondo, Y., Li, X., Lou, S., Oebel, A., Shao, M., Zeng, L., Zhu, T., Zhang, Y., & Wahner, A. (2014). Maximum efficiency in the hydroxyl-radical-based self-cleansing of the troposphere. *Nature Geoscience*, *7*(8), 559–563. <https://doi.org/10.1038/ngeo2199>
- Sadanaga, Y., Yoshino, A., Watanabe, K., Yoshioka, A., Wakazono, Y., Kanaya, Y., & Kajii, Y. (2004). Development of a measurement system of OH reactivity in the atmosphere by using a laser-induced pump and probe technique. *Review of Scientific Instruments*, *75*(8), 2648–2655. <https://doi.org/10.1063/1.1775311>
- Safron, A., Strandell, M., Kierkegaard, A., & Macleod, M. (2015). Rate constants and activation energies for gas-phase reactions of three cyclic volatile methyl siloxanes with the hydroxyl radical. *International Journal of Chemical Kinetics*, *47*(7), 420–428. <https://doi.org/10.1002/kin.20919>
- Sander, S. P., Friedl, R. R., Golden, D. M., Kurylo, M. J., Moortgat, G. K., Wine, P. H., Ravishankara, A. R., Kolb, C. E., Molina, M. J., Finlayson-Pitts, B. J., Huie, R. E., & Orkin, V. L. (2006). Chemical Kinetics and Photochemical Data for Use in Atmospheric Studies. *Evaluation Number 15*, 1–153. <http://jpldataeval.jpl.nasa.gov/>
- Saraiva, L., & Krusche, N. (2013). Estimation of the Boundary Layer Height in the Southern Region of Brazil. *American Journal of Environmental Engineering*, *3*(1), 63–70.

- <https://doi.org/10.5923/j.ajee.20130301.09>
- Sarwar, G., Corsi, R., Kimura, Y., Allen, D., & Weschler, C. J. (2002). Hydroxyl radicals in indoor environments. *Atmospheric Environment*, *36*(24), 3973–3988. [https://doi.org/10.1016/S1352-2310\(02\)00278-9](https://doi.org/10.1016/S1352-2310(02)00278-9)
- Schlosser, E., Brauers, T., Dorn, H. P., Fuchs, H., Häsel, R., Hofzumahaus, A., Holland, F., Wahner, A., Kanaya, Y., Kajii, Y., Miyamoto, K., Nishida, S., Watanabe, K., Yoshino, A., Kubistin, D., Martinez, M., Rudolf, M., Harder, H., Berresheim, H., ... Schurath, U. (2009). Technical note: Formal blind intercomparison of OH measurements: Results from the international campaign HOxComp. *Atmospheric Chemistry and Physics*, *9*(20), 7923–7948. <https://doi.org/10.5194/acp-9-7923-2009>
- Schlosser, E., Bohn, B., Brauers, T., Dorn, H. P., Fuchs, H., Häsel, R., Hofzumahaus, A., Holland, F., Rohrer, F., Rupp, L. O., Siese, M., Tillmann, R., & Wahner, A. (2007). Intercomparison of two hydroxyl radical measurement techniques at the atmosphere simulation chamber SAPHIR. *Journal of Atmospheric Chemistry*, *56*(2), 187–205. <https://doi.org/10.1007/s10874-006-9049-3>
- Schultz, M., Heitlinger, M., Mihelcic, D., & Volz-Thomas, A. (1995). Calibration source for peroxy radicals with built-in actinometry using H₂O and O₂ photolysis at 185 nm. *Journal of Geophysical Research*, *100*(D9), 18811–18816. <https://doi.org/10.1029/95jd01642>
- Setyan, A., Song, C., Merkel, M., Knighton, W. B., Onasch, T. B., Canagaratna, M. R., Worsnop, D. R., Wiedensohler, A., Shilling, J. E., & Zhang, Q. (2014). Chemistry of new particle growth in mixed urban and biogenic emissions - Insights from CARES. *Atmospheric Chemistry and Physics*, *14*(13), 6477–6494. <https://doi.org/10.5194/acp-14-6477-2014>
- Sharma, B., Felix, J. D., Myles, L. T., Butler, T., Summerlin, S., & Shimizu, M. S. (2021). Wet deposition ethanol concentration at US atmospheric integrated research monitoring network (AIRMoN) sites. *Journal of Atmospheric Chemistry*, *78*(2), 125–138. <https://doi.org/10.1007/s10874-020-09414-5>
- Sheehy, P. M., Volkamer, R., Molina, L. T., & Molina, M. J. (2010). Oxidative capacity of the Mexico City atmosphere-Part 2: A RO_x radical cycling perspective. *Atmospheric Chemistry and Physics*, *10*(14), 6993–7008. <https://doi.org/10.5194/acp-10-6993-2010>
- Showman, A. P., & Dowling, T. E. (2014). Earth as a Planet: Atmosphere and Oceans. In *Encyclopedia of the Solar System (Third Edition)*, 423–444. <https://doi.org/10.1016/b978-0-12-415845-0.00020-7>
- Simon, V., Clement, B., Nationale, E., & Chimie, D. (1994). The Landes experiment: Monoterpenes emitted from the maritime pine. *Journal of Geophysical Research*, *99* (D8), 16501–16510.
- Sindelarova, K., Granier, C., Bouarar, I., Guenther, A., Tilmes, S., Stavrakou, T., Müller, J. F., Kuhn, U., Stefani, P., & Knorr, W. (2014). Global data set of biogenic VOC emissions calculated by the MEGAN model over the last 30 years. *Atmospheric Chemistry and Physics*, *14*(17), 9317–9341. <https://doi.org/10.5194/acp-14-9317-2014>
- Singh, H. B., Salas, L. J., Chatfield, R. B., Czech, E., Fried, A., Walega, J., Evans, M. J., Field, B. D., Jacob, D. J., Blake, D., Heikes, B., Talbot, R., Sachse, G., Crawford, J. H., Avery, M. A., Sandholm, S., & Fuelberg, H. (2004). Analysis of the atmospheric distribution, sources, and sinks of oxygenated volatile organic chemicals based on measurements over the Pacific during TRACE-P. *Journal of Geophysical Research D: Atmospheres*, *109*(15). <https://doi.org/10.1029/2003JD003883>
- Singh, H., Chen, Y., Tabazadeh, A., Fukui, Y., Bey, I., Yantosca, R., Jacob, D., Arnold, F., Wohlfrom, K., Atlas, E., Flocke, F., Blake, D., Blake, N., Heikes, B., Snow, J., Talbot, R., Gregory, G., Sachse, G., Vay, S., & Kondo, Y. (2000). Distribution and fate of selected oxygenated organic species in the troposphere and lower stratosphere over the Atlantic.

- Journal of Geophysical Research Atmospheres*, 105(D3), 3795–3805. <https://doi.org/10.1029/1999JD900779>
- Sinha, V., Williams, J., Crowley, J. N., & Lelieveld, J. (2008). The comparative reactivity method - A new tool to measure total OH Reactivity in ambient air. *Atmospheric Chemistry and Physics*, 8(8), 2213–2227. <https://doi.org/10.5194/acp-8-2213-2008>
- Sinha, V., Williams, J., Lelieveld, J., Ruuskanen, T. M., Kajos, M. K., Patokoski, J., Hellen, H., Hakola, H., Mogensen, D., Boy, M., Rinne, J., & Kulmala, M. (2010). OH reactivity measurements within a boreal forest: Evidence for unknown reactive emissions. *Environmental Science and Technology*, 44(17), 6614–6620. <https://doi.org/10.1021/es101780b>
- Song, H., Chen, X., Lu, K., Zou, Q., Tan, Z., Fuchs, H., Wiedensohler, A., Moon, D.R., Heard, D.E., Baeza-Romero, María-T., Zheng, M., Wahner, A., Kiendler-Scharr, A. and Zhang, Y. (2020). Influence of aerosol copper on HO₂ uptake: a novel parameterized equation. *Atmospheric Chemistry and Physics*, 20, 15835–15850. <https://doi.org/10.5194/acp-20-15835-2020>
- Stavrakou, T., Guenther, A., Razavi, A., Clarisse, L., Clerbaux, C., Coheur, P. F., Hurtmans, D., Karagulian, F., De Mazière, M., Vigouroux, C., Amelynck, C., Schoon, N., Laffineur, Q., Heinesch, B., Aubinet, M., Rinsland, C., & Müller, J. F. (2011). First space-based derivation of the global atmospheric methanol emission fluxes. *Atmospheric Chemistry and Physics*, 11(10), 4873–4898. <https://doi.org/10.5194/acp-11-4873-2011>
- Stavrakou, T., Peeters, J., & Müller, J. F. (2010). Improved global modelling of HO_x recycling in isoprene oxidation: Evaluation against the GABRIEL and INTEX-A aircraft campaign measurements. *Atmospheric Chemistry and Physics*, 10(20), 9863–9878. <https://doi.org/10.5194/acp-10-9863-2010>
- Stevens, P. S., Mather, J. H., & Brune, W. H. (1994). Measurement of tropospheric OH and HO₂ by laser-induced fluorescence at low pressure. *Journal of Geophysical Research*, 79(D2), 3543–3557. <https://doi.org/10.1029/93JD03342>
- Stone, D., Evans, M. J., Walker, H., Ingham, T., Vaughan, S., Ouyang, B., Kennedy, O. J., McLeod, M. W., Jones, R. L., Hopkins, J., Punjabi, S., Lidster, R., Hamilton, J. F., Lee, J. D., Lewis, A. C., Carpenter, L. J., Forster, G., Oram, D. E., Reeves, C. E., ... Heard, D. E. (2014). Radical chemistry at night: Comparisons between observed and modelled HO_x, NO₃ and N₂O₅ during the RONOCO project. *Atmospheric Chemistry and Physics*, 14(3), 1299–1321. <https://doi.org/10.5194/acp-14-1299-2014>
- Stone, D., Whalley, L. K., & Heard, D. E. (2012). Tropospheric OH and HO₂ radicals: Field measurements and model comparisons. *Chemical Society Reviews*, 41(19), 6348–6404. <https://doi.org/10.1039/c2cs35140d>
- Stone, D., Whalley, L. K., Ingham, T., Edwards, P. M., Cryer, D. R., Brumby, C. A., Seakins, P. W., & Heard, D. E. (2016). Measurement of OH reactivity by laser flash photolysis coupled with laser-induced fluorescence spectroscopy. *Atmospheric Measurement Techniques*, 9(7), 2827–2844. <https://doi.org/10.5194/amt-9-2827-2016>
- Talbot, R., Mao, H., & Sive, B. (2005). Diurnal characteristics of surface level O₃ and other important trace gases in New England. *Journal of Geophysical Research*, 110(9), 1–16. <https://doi.org/10.1029/2004JD005449>
- Tan, Z., Fuchs, H., Lu, K., Hofzumahaus, A., Bohn, B., Broch, S., Dong, H., Gomm, S., Häsel, R., He, L., Holland, F., Li, X., Liu, Y., Lu, S., Rohrer, F., Shao, M., Wang, B., Wang, M., Wu, Y., ... Zhang, Y. (2017). Radical chemistry at a rural site (Wangdu) in the North China Plain: Observation and model calculations of OH, HO₂ and RO₂ radicals. *Atmospheric Chemistry and Physics*, 17(1), 663–690. <https://doi.org/10.5194/acp-17-663-2017>
- Tan, Z., Lu, K., Hofzumahaus, A., Fuchs, H., Bohn, B., Holland, F., Liu, Y., Rohrer, F., Shao,

- M., Sun, K., Wu, Y., Zeng, L., Zhang, Y., Zou, Q., Kiendler-Scharr, A., Wahner, A., & Zhang, Y. (2019). Experimental budgets of OH, HO₂, and RO₂ radicals and implications for ozone formation in the Pearl River Delta in China 2014. *Atmospheric Chemistry and Physics*, *19*(10), 7129–7150. <https://doi.org/10.5194/acp-19-7129-2019>
- Tan, Z., Rohrer, F., Lu, K., Ma, X., Bohn, B., Broch, S., Dong, H., Fuchs, H., Gkatzelis, G. I., Hofzumahaus, A., Holland, F., Li, X., Liu, Y., Liu, Y., Novelli, A., Shao, M., Wang, H., Wu, Y., Zeng, L., ... Zhang, Y. (2018). Wintertime photochemistry in Beijing: Observations of RO_x radical concentrations in the North China Plain during the BEST-ONE campaign. *Atmospheric Chemistry and Physics*, *18*(16), 12391–12411. <https://doi.org/10.5194/acp-18-12391-2018>
- Tani, A. (2013). Fragmentation and reaction rate constants of terpenoids determined by proton transfer reaction-mass spectrometry. *Environmental Control in Biology*, *51*(1), 23–29. <https://doi.org/10.2525/ecb.51.23>
- Tanner, D. J. and Eisele, F. L. (1995). Present OH measurement limits and associated uncertainties. *Journal of Geophysical Research*, *100*(D2), 2883–2892.
- Tie, X., Guenther, A., & Holland, E. (2003). Biogenic methanol and its impacts on tropospheric oxidants. *Geophysical Research Letters*, *30*(17), 3–6. <https://doi.org/10.1029/2003GL017167>
- Tyndall, G.S., Cox, R.A., Granier, C., Lesclaux, R., Moortagt, G.K., Pillling, M.J., Ravishankara, A.R., Wallington, T. J. (2001). Atmospheric chemistry of small organic peroxy radicals. *Journal of Geophysical Research*, *106*(D11), 12157–12182.
- Vaida, V. (2011). Perspective: Water cluster mediated atmospheric chemistry. *Journal of Chemical Physics*, *135*(2). <https://doi.org/10.1063/1.3608919>
- Velasco, E., Pressley, S., Grivicke, R., Allwine, E., Coons, T., Foster, W., Jobson, B. T., Westberg, H., Ramos, R., Hernández, F., Molina, L. T., & Lamb, B. (2009). Eddy covariance flux measurements of pollutant gases in urban Mexico City. *Atmospheric Chemistry and Physics*, *9*(19), 7325–7342. <https://doi.org/10.5194/acp-9-7325-2009>
- Verrièle, M., Schoemaeker, C., Hanoune, B., Leclerc, N., Germain, S., Gaudion, V., & Locoge, N. (2016). The MERMAID study: indoor and outdoor average pollutant concentrations in 10 low-energy school buildings in France. *Indoor Air*, *26*(5), 702–713. <https://doi.org/10.1111/ina.12258>
- Vrekoussis, M., Kanakidou, M., Mihalopoulos, N., Crutzen, P. J., Lelieveld, J., Perner, D., Berresheim, H., & Baboukas, E. (2004). Role of the NO₃ radicals in oxidation processes in the eastern Mediterranean troposphere during the MINOS campaign. *Atmospheric Chemistry and Physics*, *4*(1), 169–182. <https://doi.org/10.5194/acp-4-169-2004>
- Wang, H., Chen, X., Lu, K., Hu, R., Li, Z., Wang, H., Ma, X., Yang, X., Chen, S., Dong, H., Liu, Y., Fang, X., Zeng, L., Hu, M., & Zhang, Y. (2020). NO₃ and N₂O₅ chemistry at a suburban site during the EXPLORE-YRD campaign in 2018. *Atmospheric Environment*, *224*(3), 117180. <https://doi.org/10.1016/j.atmosenv.2019.117180>
- Wang, H. L., Nie, L., Li, J., Wang, Y. F., Wang, G., Wang, J. H., & Hao, Z. P. (2013). Characterization and assessment of volatile organic compounds (VOCs) emissions from typical industries. *Chinese Science Bulletin*, *58*(7), 724–730. <https://doi.org/10.1007/s11434-012-5345-2>
- Wang, X. M., Lee, S. C., Sheng, G. Y., Chan, L. Y., Fu, J. M., Li, X. D., Min, Y. S., & Chan, C. Y. (2001). Cyclic organosilicon compounds in ambient air in Guangzhou, Macau and Nanhai, Pearl River Delta. *Applied Geochemistry*, *16*(11–12), 1447–1454. [https://doi.org/10.1016/S0883-2927\(01\)00044-0](https://doi.org/10.1016/S0883-2927(01)00044-0)
- Warneke, C., de Gouw, J. A., Goldan, P. D., Kuster, W. C., Williams, E. J., Lerner, B. M., Jakoubek, R., Brown, S. S., Stark, H., Aldener, M., Ravishankara, A. R., Roberts, J. M., Marchewka, M., Bertman, S., Sueper, D. T., McKeen, S. A., Meagher, J. F., & Fehsenfeld,

- F. C. (2004). Comparison of daytime and nighttime oxidation of biogenic and anthropogenic VOCs along the New England coast in summer during New England Air Quality Study 2002. *Journal of Geophysical Research*, 109(10), 1–14. <https://doi.org/10.1029/2003JD004424>
- Wei, N., Fang, B., Zhao, W., Wang, C., Yang, N., Zhang, W., Chen, W., & Fittschen, C. (2020). Time-Resolved Laser-Flash Photolysis Faraday Rotation Spectrometer: A New Tool for Total OH Reactivity Measurement and Free Radical Kinetics Research. *Analytical Chemistry*, 92(6), 4334–4339. <https://doi.org/10.1021/acs.analchem.9b05117>
- Wells, K. C., Millet, D. B., Cady-Pereira, K. E., Shephard, M. W., Henze, D. K., Bousserez, N., Apel, E. C., De Gouw, J., Warneke, C., & Singh, H. B. (2014). Quantifying global terrestrial methanol emissions using observations from the TES satellite sensor. *Atmospheric Chemistry and Physics*, 14(5), 2555–2570. <https://doi.org/10.5194/acp-14-2555-2014>
- Wennberg, P.O., Bates, K.H., Crouse, J.D., Dodson, L.G., McVay, R.C., Mertens, L.A., Nguyen, T.B., Praske, E., Schwantes, R.H., Smarte, M.D., St Clair, J.M., Teng, XuanZhang, A.P. and Seinfeld. J.H. (2018). Gas-Phase Reactions of Isoprene and Its Major Oxidation Products. *Chemical Reviews*. 118,3337–3390.
- Wentworth, G. R., Aklilu, Y. abeba, Landis, M. S., & Hsu, Y. M. (2018). Impacts of a large boreal wildfire on ground level atmospheric concentrations of PAHs, VOCs and ozone. *Atmospheric Environment*, 178, 19–30. <https://doi.org/10.1016/j.atmosenv.2018.01.013>
- Weschler, C. J., & Carslaw, N. (2018). Indoor Chemistry. *Environmental Science and Technology*, 52(5), 2419–2428. <https://doi.org/10.1021/acs.est.7b06387>
- Whalley, L.K., Blitz, M.A., Desservettaz, M., Seakins, P.W., Heard, D. E. (2013). Reporting the sensitivity detection to an interference from that enables HO₂ and certain RO₂ types to be selectively measured. *Atmospheric Measurement Techniques*, 6, 6249–6292. <https://doi.org/10.5194/amtd-6-6249-2013>
- Whalley, L. K., Edwards, P. M., Furneaux, K. L., Goddard, A., Ingham, T., Evans, M. J., Stone, D., Hopkins, J. R., Jones, C. E., Karunaharan, A., Lee, J. D., Lewis, A. C., Monks, P. S., Moller, S. J., & Heard, D. E. (2011). Quantifying the magnitude of a missing hydroxyl radical source in a tropical rainforest. *Atmospheric Chemistry and Physics*, 11(14), 7223–7233. <https://doi.org/10.5194/acp-11-7223-2011>
- Whalley, L. K., Stone, D., George, I. J., Mertes, S., Pinxteren, D. van., Tilgner, A., Herrmann, H., Evans, M. J. and Heard, D. E. (2015). The influence of clouds on radical concentrations: observations and modelling studies of HO_x during the Hill Cap Cloud Thuringia (HCCT) campaign in 2010. *Atmospheric Chemistry and Physics* 15(6): 3289–3301.
- Whalley, L.K., Stone, D., Bandy, B., Dunmore, R., Hamilton, J. F., Hopkins, J., Lee, J. D., Lewis, A. C., & Heard, D. E. (2016). Atmospheric OH reactivity in central London: Observations, model predictions and estimates of in situ ozone production. *Atmospheric Chemistry and Physics*, 16(4), 2109–2122. <https://doi.org/10.5194/acp-16-2109-2016>
- Whalley, Lisa K., Stone, D., Dunmore, R., Hamilton, J., Hopkins, J. R., Lee, J. D., Lewis, A. C., Williams, P., Kleffmann, J., Laufs, S., Woodward-Massey, R., & Heard, D. E. (2018). Understanding in situ ozone production in the summertime through radical observations and modelling studies during the Clean air for London project (ClearfLo). *Atmospheric Chemistry and Physics*, 18(4), 2547–2571. <https://doi.org/10.5194/acp-18-2547-2018>
- Williams, J., Holzinger, R., Gros, V., Xu, X., Atlas, E., & Wallace, D. W. R. (2004). Measurements of organic species in air and seawater from the tropical Atlantic. *Geophysical Research Letters*, 31(23), 1–5. <https://doi.org/10.1029/2004GL020012>
- Wisthaler, A., Apel, E. C., Bossmeyer, J., Hansel, A., Junkermann, W., Koppmann, R., Meier, R., Muller, K., Solomon, S. J., Steinbrecher, R., Tillmann, R., & Brauers, T. (2008).

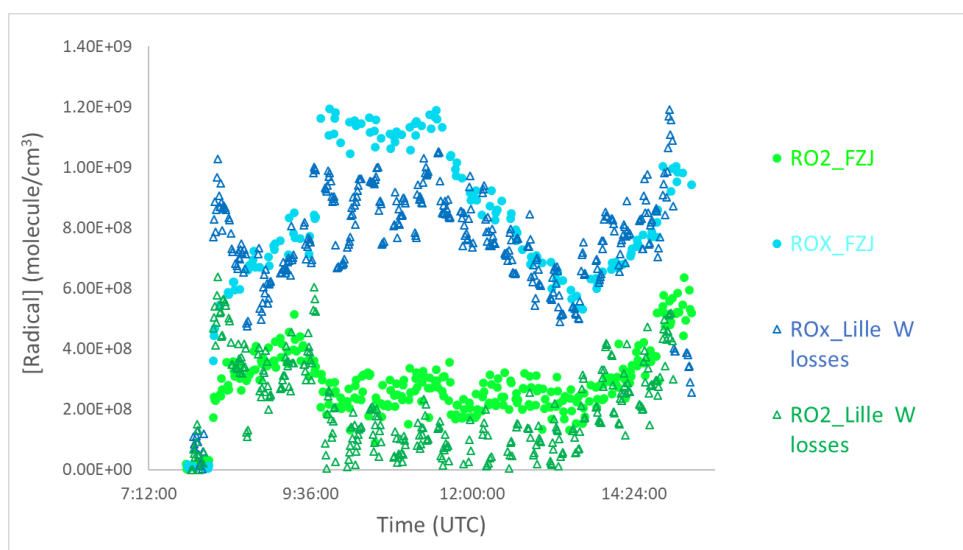
- Technical Note: Intercomparison of formaldehyde measurements at the atmosphere simulation chamber SAPHIR. *Atmospheric Chemistry and Physics*, 8(8), 2189–2200. <https://doi.org/10.5194/acp-8-2189-2008>
- Wolfe, G. M., Thornton, J. A., Bouvier-Brown, N. C., Goldstein, A. H., Park, J. H., McKay, M., Matross, D. M., Mao, J., Brune, W. H., LaFranchi, B. W., Browne, E. C., Min, K. E., Wooldridge, P. J., Cohen, R. C., Crouse, J. D., Faloon, I. C., Gilman, J. B., Kuster, W. C., De Gouw, J. A., ... Keutsch, F. N. (2011). The chemistry of atmosphere-forest exchange (CAFE) model-part 2: Application to BEARPEX-2007 observations. *Atmospheric Chemistry and Physics*, 11(3), 1269–1294. <https://doi.org/10.5194/acp-11-1269-2011>
- Won, Y., Waring, M., & Rim, D. (2019). Understanding the Spatial Heterogeneity of Indoor OH and HO₂ due to Photolysis of HONO Using Computational Fluid Dynamics Simulation. *Environmental Science and Technology*, 53(24), 14470–14478. <https://doi.org/10.1021/acs.est.9b06315>
- Wood, E. C., & Charest, J. R. (2014). Chemical amplification - Cavity attenuated phase shift spectroscopy measurements of atmospheric peroxy radicals. *Analytical Chemistry*, 86(20), 10266–10273. <https://doi.org/10.1021/ac502451m>
- Woodward-massey, R. (2018). Observations of radicals in the atmosphere: measurement validation and model comparisons. *PhD Thesis, University of Leeds*.
- Xia, G., Zhou, L., Freedman, J. M., Roy, S. B., Harris, R. A., & Cervarich, M. C. (2016). A case study of effects of atmospheric boundary layer turbulence, wind speed, and stability on wind farm induced temperature changes using observations from a field campaign. *Climate Dynamics*, 46(7–8), 2179–2196. <https://doi.org/10.1007/s00382-015-2696-9>
- Xiao, R., Zammit, I., Wei, Z., Hu, W. P., MacLeod, M., & Spinney, R. (2015). Kinetics and Mechanism of the Oxidation of Cyclic Methylsiloxanes by Hydroxyl Radical in the Gas Phase: An Experimental and Theoretical Study. *Environmental Science and Technology*, 49(22), 13322–13330. <https://doi.org/10.1021/acs.est.5b03744>
- Yan, C., Kocevska, S., & Krasnoperov, L. N. (2016). Kinetics of the Reaction of CH₃O₂ Radicals with OH Studied over the 292–526 K Temperature Range. *Journal of Physical Chemistry A*, 120(31), 6111–6121. <https://doi.org/10.1021/acs.jpca.6b04213>
- Yang, C., Zhao, W., Fang, B., Yu, H., Xu, X., Zhang, Y., Gai, Y., Zhang, W., Chen, W., & Fittschen, C. (2019). Improved Chemical Amplification Instrument by Using a Nafion Dryer as an Amplification Reactor for Quantifying Atmospheric Peroxy Radicals under Ambient Conditions. *Analytical Chemistry*, 91(1), 776–779. <https://doi.org/10.1021/acs.analchem.8b04907>
- Yang, X., Lu, K., Ma, X., Liu, Y., Wang, H., Hu, R., Li, X., Lou, S., Chen, S., Dong, H., Wang, F., Wang, Y., Zhang, G., Li, S., Yang, S., Yang, Y., Kuang, C., Tan, Z., Chen, X., ... Zhang, Y. (2021). Observations and modeling of OH and HO₂ radicals in Chengdu, China in summer 2019. *Science of the Total Environment*, 772, 144829. <https://doi.org/10.1016/j.scitotenv.2020.144829>
- Yang, Y., Shao, M., Keßel, S., Li, Y., Lu, K., Lu, S., Williams, J., Zhang, Y., Zeng, L., Nölscher, A. C., Wu, Y., Wang, X., & Zheng, J. (2017). How the OH reactivity affects the ozone production efficiency: Case studies in Beijing and Heshan, China. *Atmospheric Chemistry and Physics*, 17(11), 7127–7142. <https://doi.org/10.5194/acp-17-7127-2017>
- Yao, P., Holzinger, R., Materić, D., Oyama, B. S., de Fátima Andrade, M., Paul, D., Ni, H., Noto, H., Huang, R.-J., & Dusek, U. (2023). Methylsiloxanes from Vehicle Emissions Detected in Aerosol Particles. *Environmental Science & Technology*, 57, 14269–14279. <https://doi.org/10.1021/acs.est.3c03797>
- Yoshino, A., Nakashima, Y., Miyazaki, K., Kato, S., Suthawaree, J., Shimo, N., Matsunaga, S., Chatani, S., Apel, E., Greenberg, J., Guenther, A., Ueno, H., Sasaki, H., Hoshi, J. ya,

- Yokota, H., Ishii, K., & Kajii, Y. (2012). Air quality diagnosis from comprehensive observations of total OH reactivity and reactive trace species in urban central Tokyo. *Atmospheric Environment*, *49*, 51–59. <https://doi.org/10.1016/j.atmosenv.2011.12.029>
- Yoshino, A., Sadanaga, Y., Watanabe, K., Kato, S., Miyakawa, Y., Matsumoto, J., & Kajii, Y. (2006). Measurement of total OH reactivity by laser-induced pump and probe technique-comprehensive observations in the urban atmosphere of Tokyo. *Atmospheric Environment*, *40*, 7869–7881. <https://doi.org/10.1016/j.atmosenv.2006.07.023>
- Zannoni, N., Gros, V., Lanza, M., Sarda, R., Bonsang, B., Kalogridis, C., Preunkert, S., Legrand, M., Jambert, C., Boissard, C., & Lathiere, J. (2016). OH reactivity and concentrations of biogenic volatile organic compounds in a Mediterranean forest of downy oak trees. *Atmospheric Chemistry and Physics*, *16*(3), 1619–1636. <https://doi.org/10.5194/acp-16-1619-2016>
- Zeng, M., & Wilson, K. R. (2020). Efficient Coupling of Reaction Pathways of Criegee Intermediates and Free Radicals in the Heterogeneous Ozonolysis of Alkenes. *Journal of Physical Chemistry Letters*, *11*(16), 6580–6585. <https://doi.org/10.1021/acs.jpcclett.0c01823>
- Zhang, G., Hu, R., Xie, P., Lou, S., Wang, F., Wang, Y., Qin, M., Li, X., Liu, X., Wang, Y., & Liu, W. (2022). Observation and simulation of HOx radicals in an urban area in Shanghai, China. *Science of the Total Environment*, *810*, 152275. <https://doi.org/10.1016/j.scitotenv.2021.152275>
- Zhang, J., Dransfield, T., & Donahue, N. M. (2004). On the mechanism for nitrate formation via the peroxy radical + NO reaction. *Journal of Physical Chemistry A*, *108*(42), 9082–9095. <https://doi.org/10.1021/jp048096x>

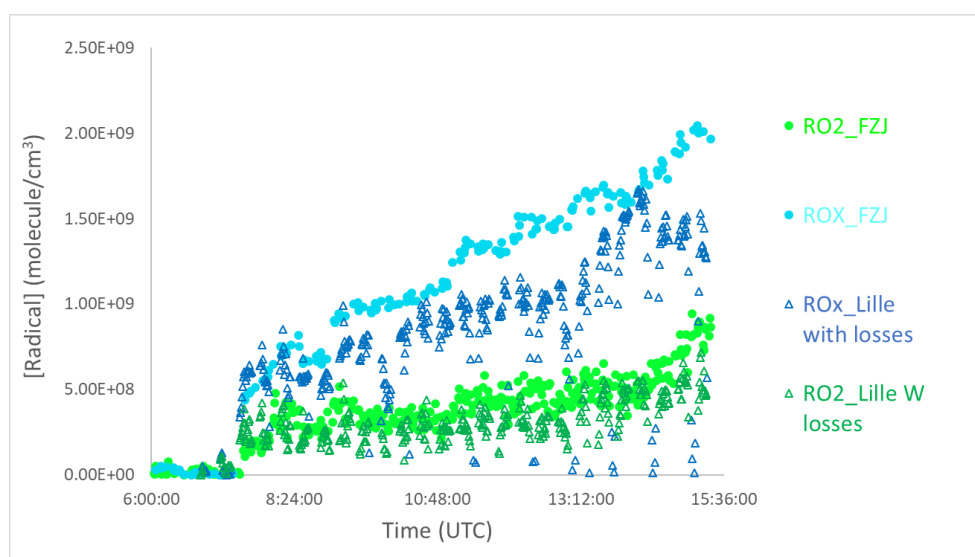
Annex

RO_xComp experiment results not shown in the manuscript:

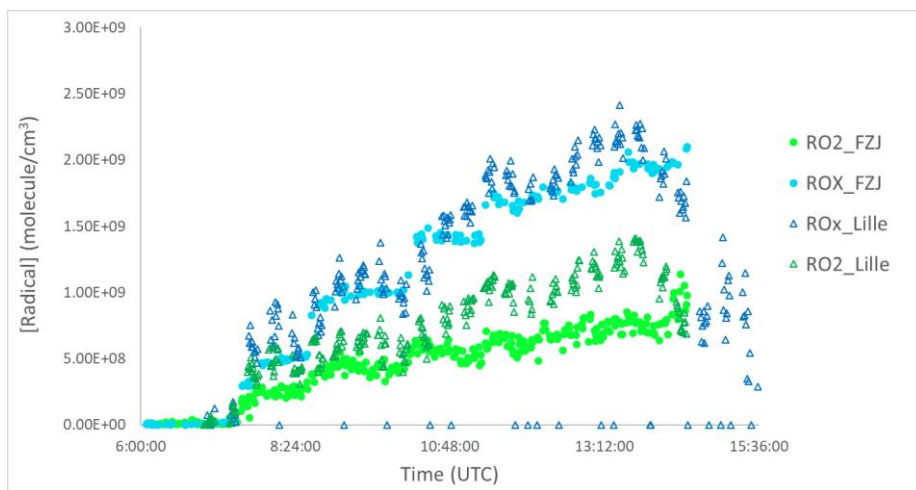
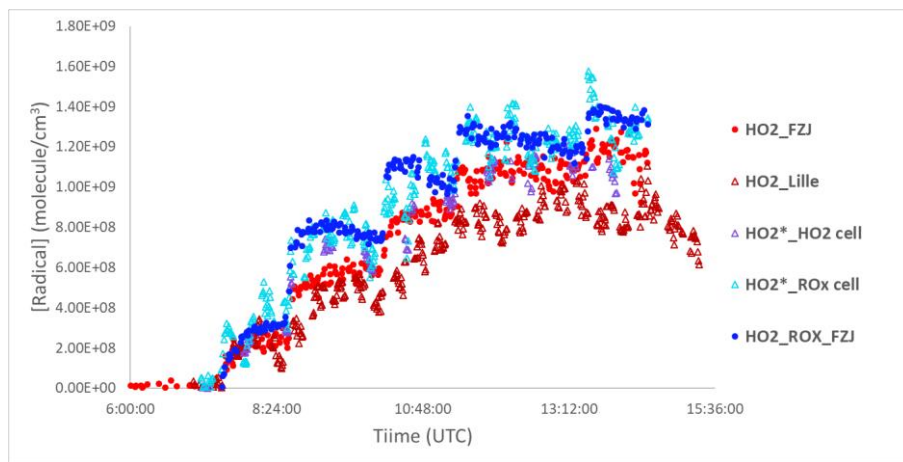
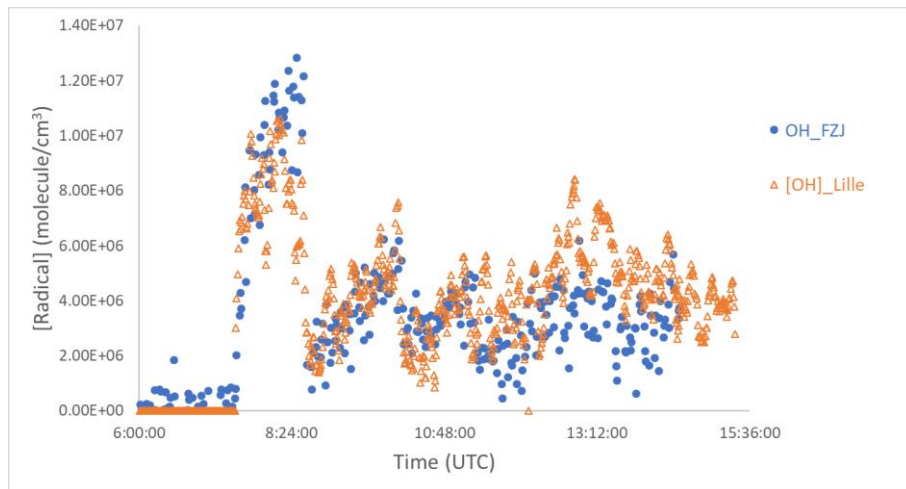
- CO/CH₄ oxidation by OH experiment done on August 8:

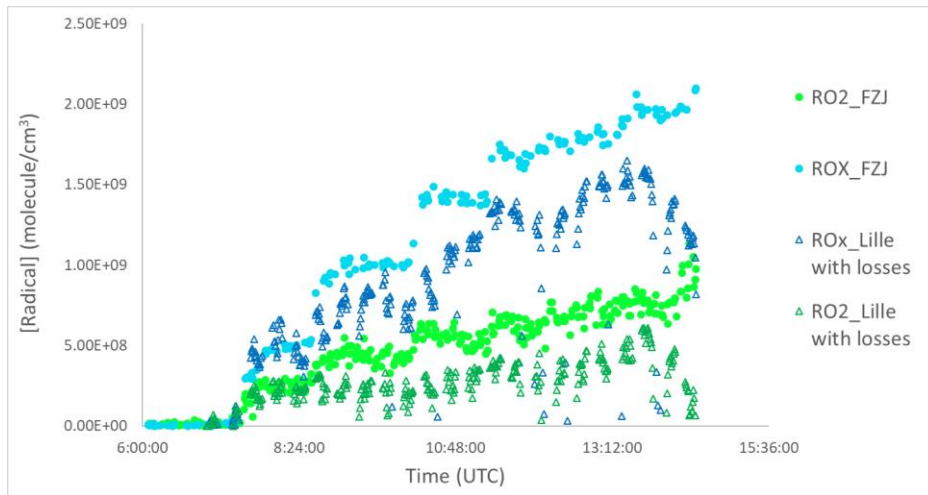


- Isoprene OH oxidation experiment done on August 9:

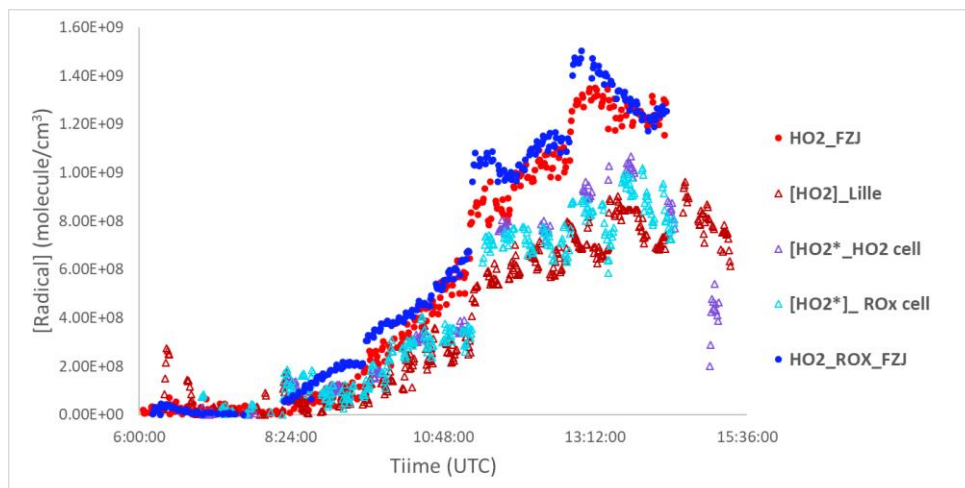
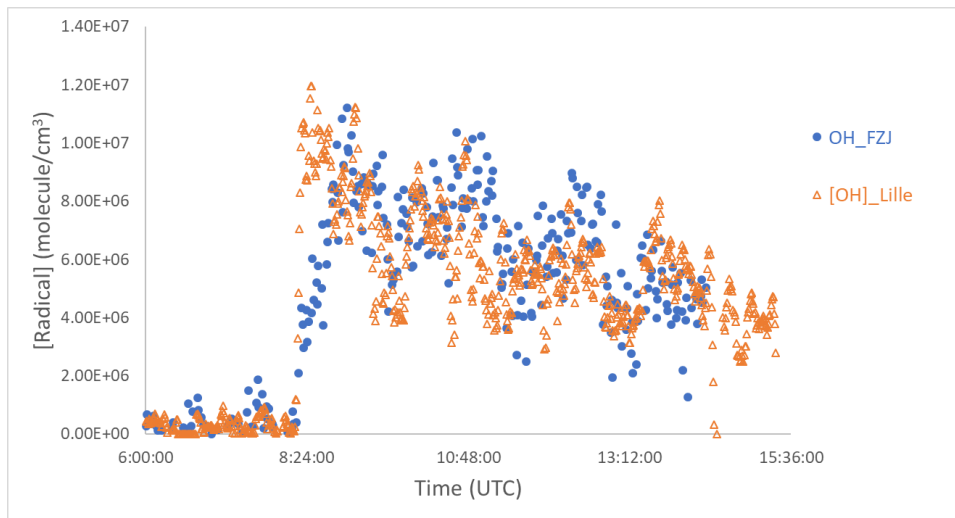


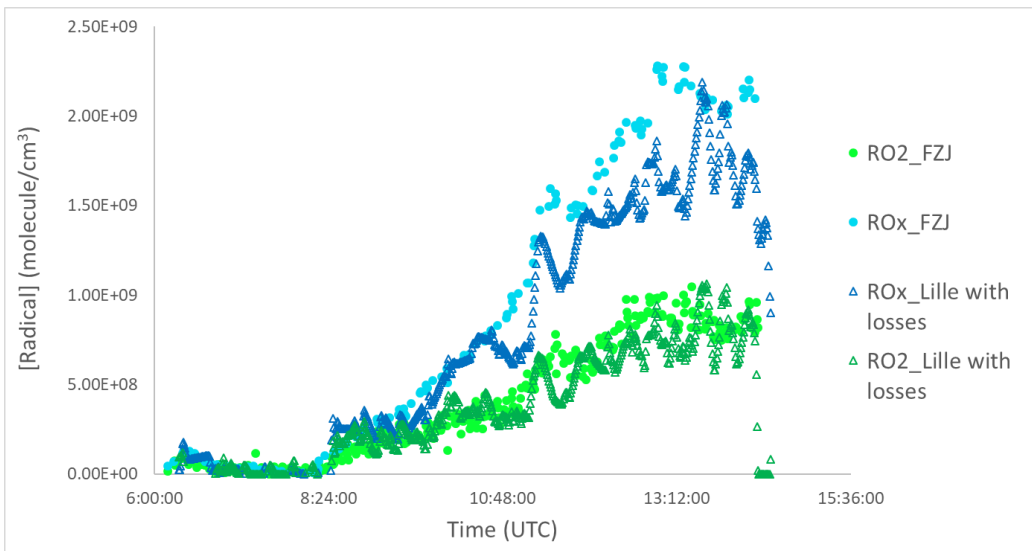
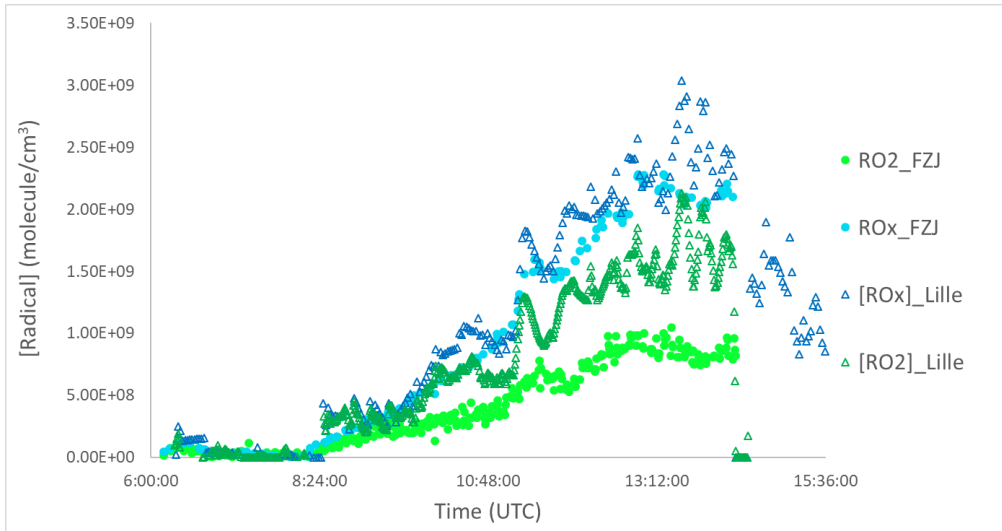
- Isoprene OH oxidation, O₃ change experiment done on August 10:



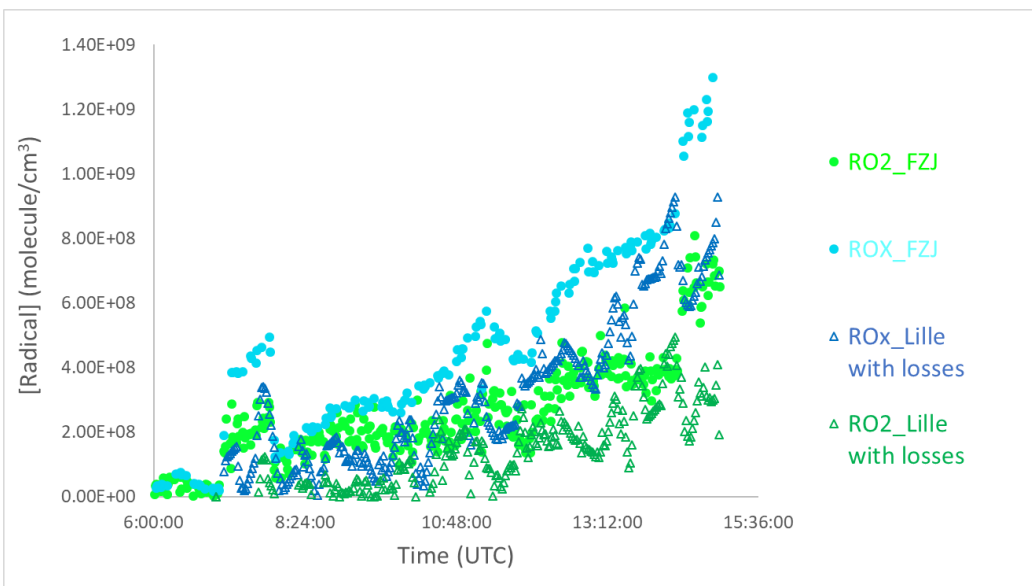


- Isoprene OH oxidation, NO_x change experiment done on August 11:

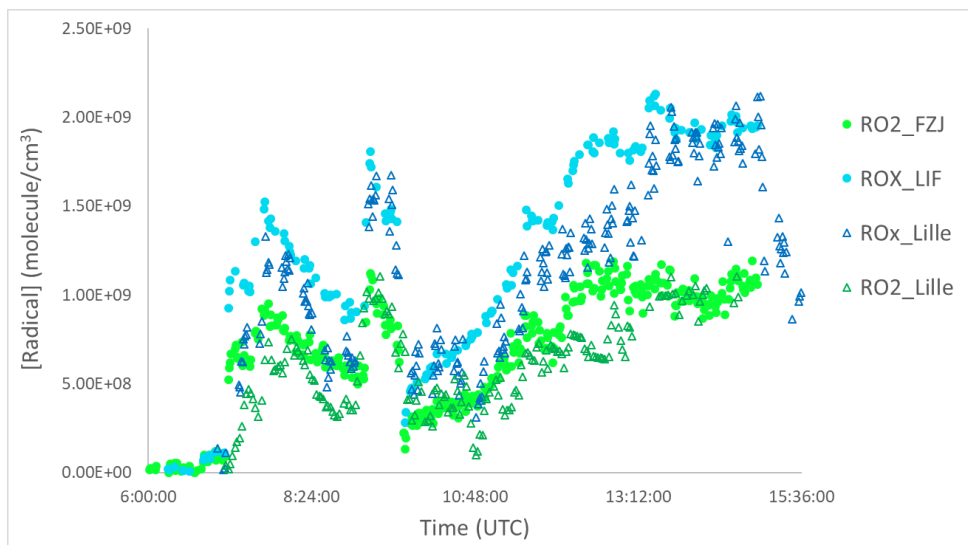
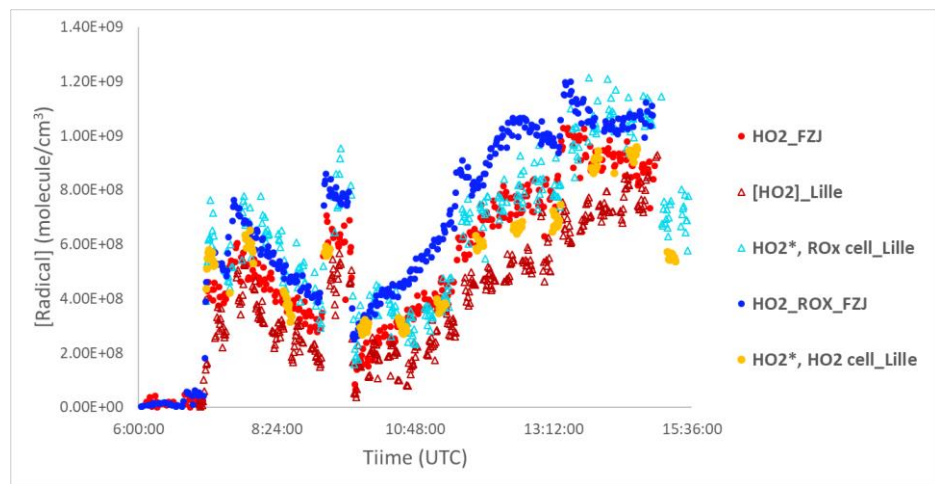
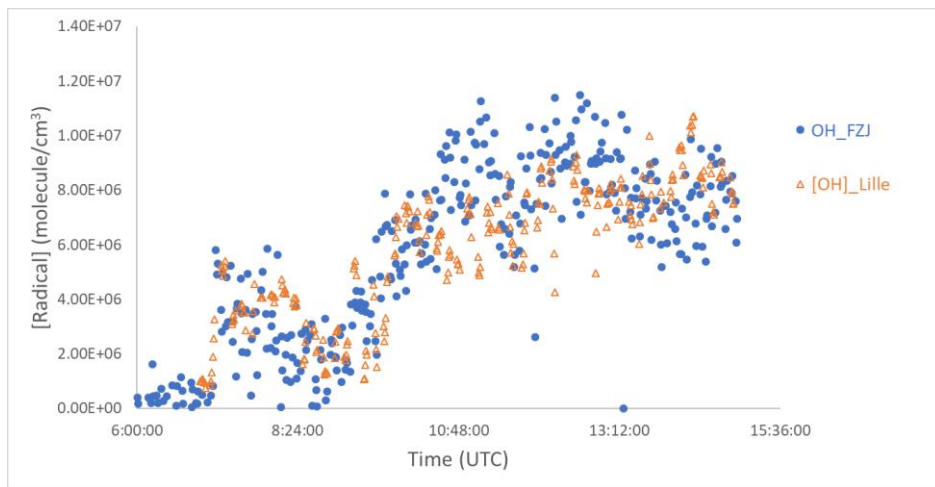


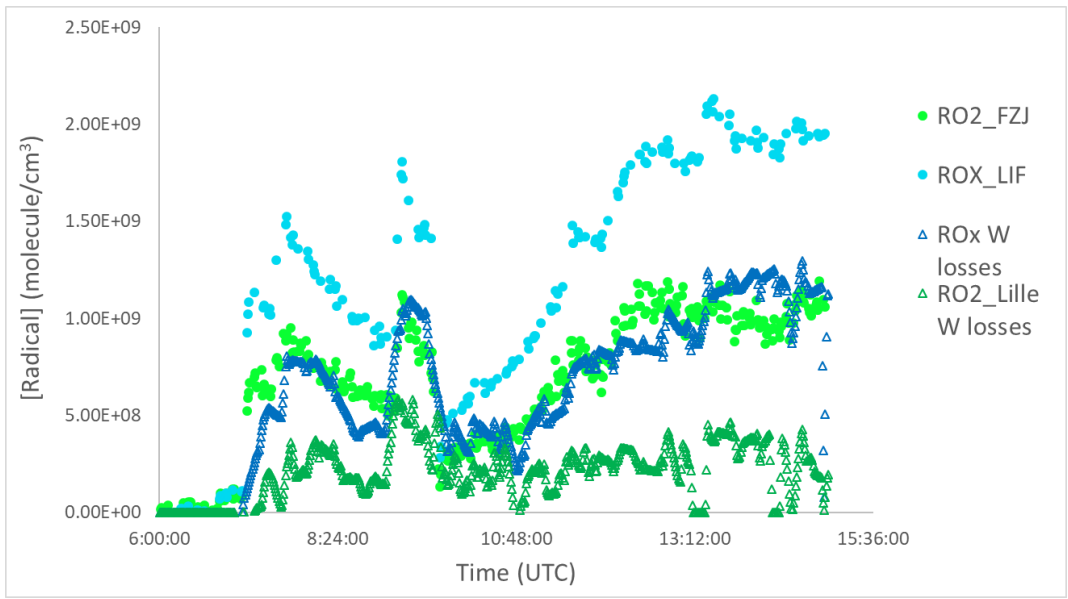


- 1-pentane and n-hexane photo-oxidation experiment done on August 12:

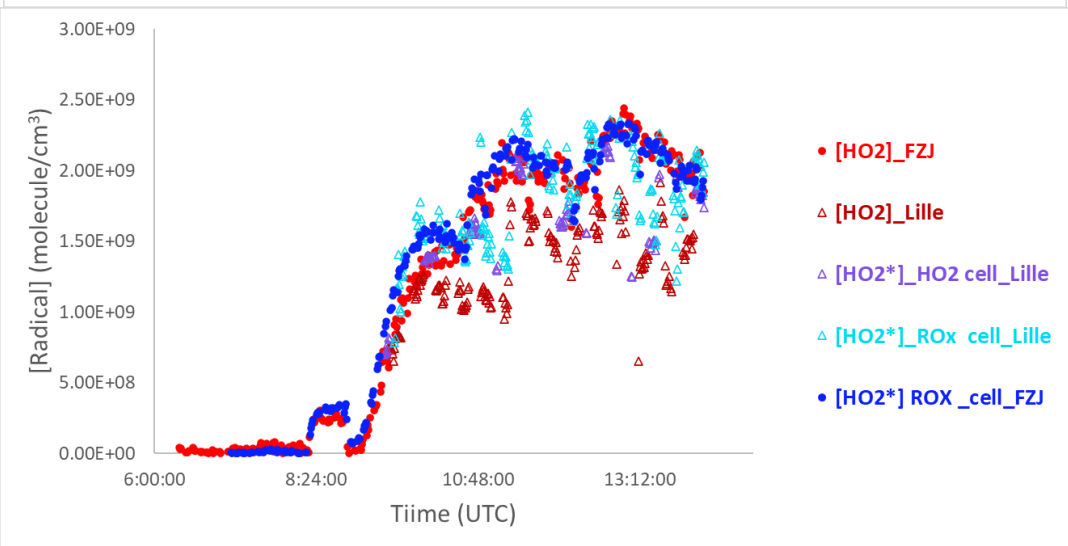
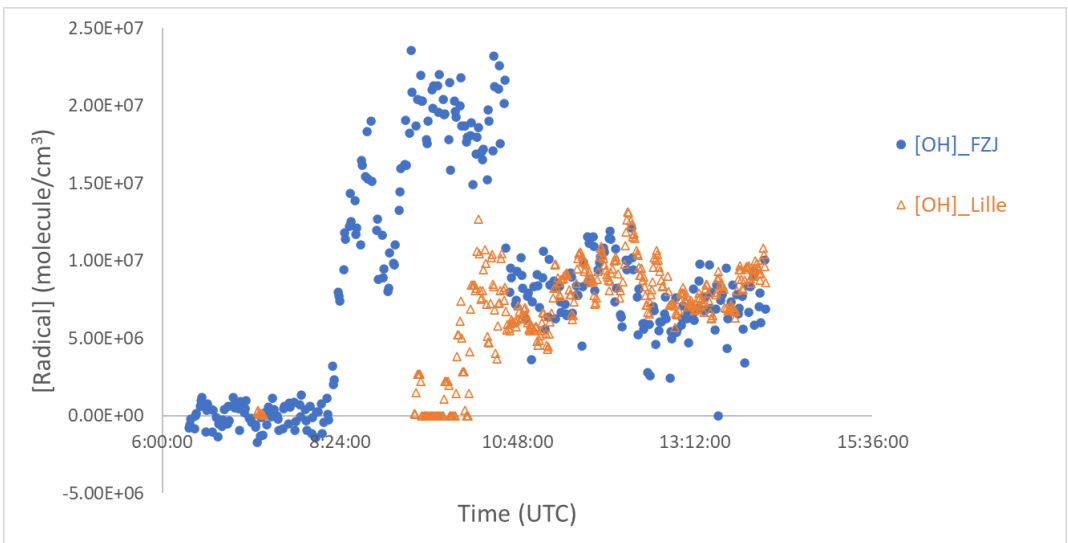


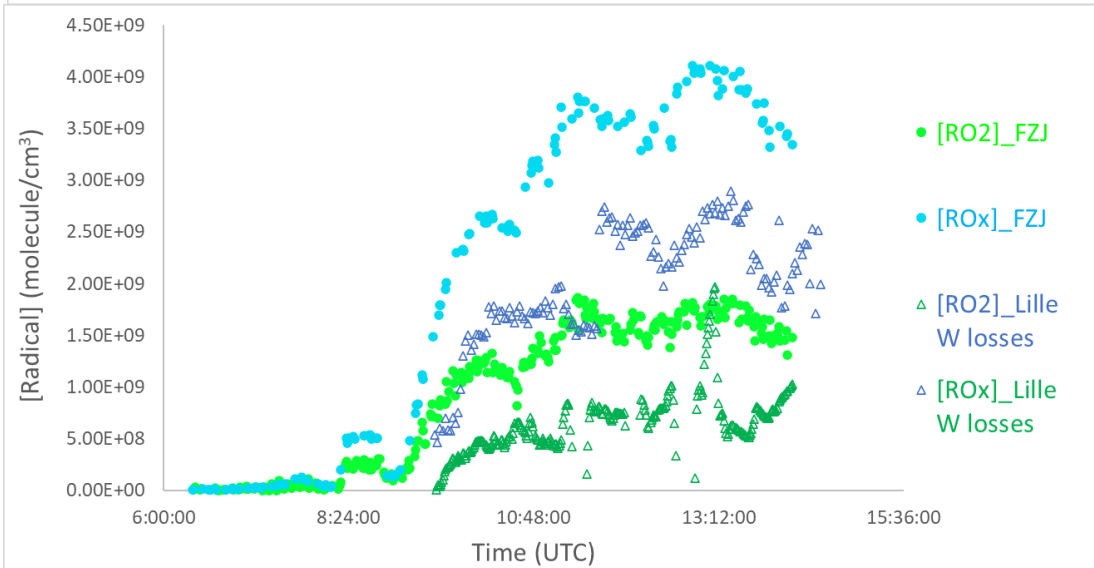
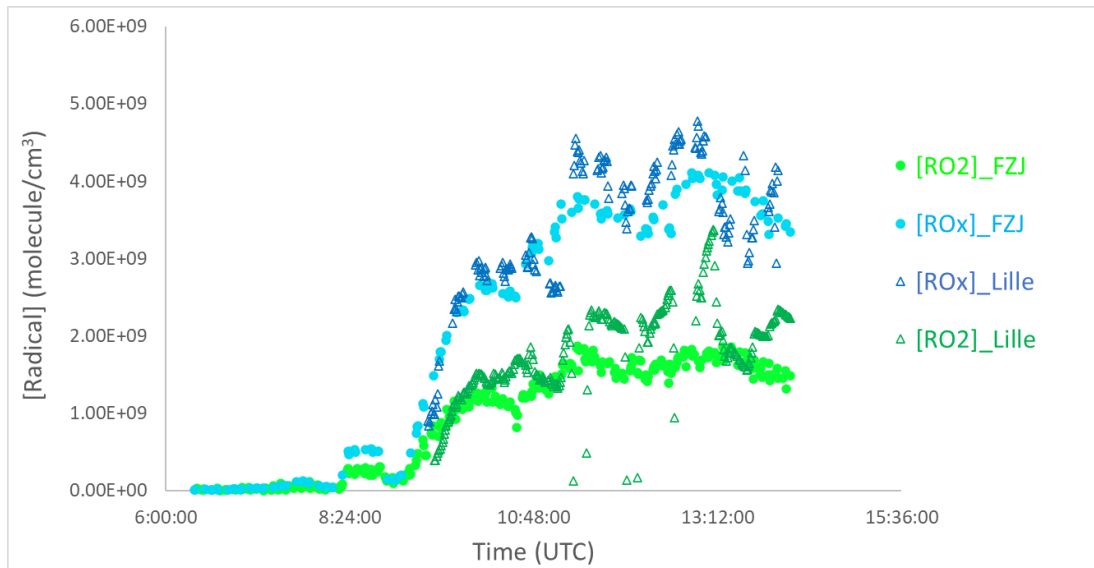
- α -pinene ozonolysis dark/ photooxidation experiment done on August 13:



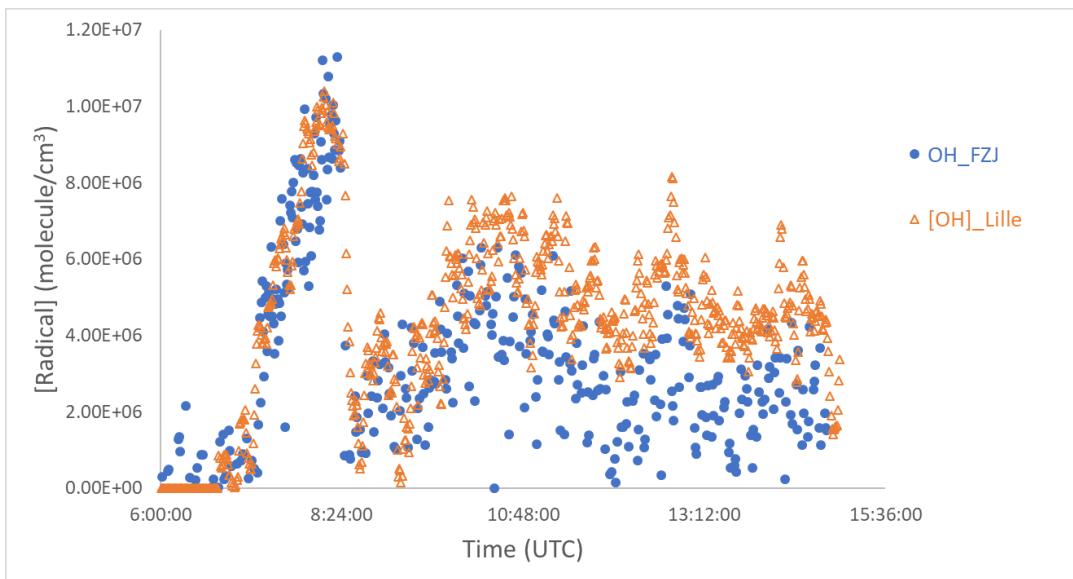


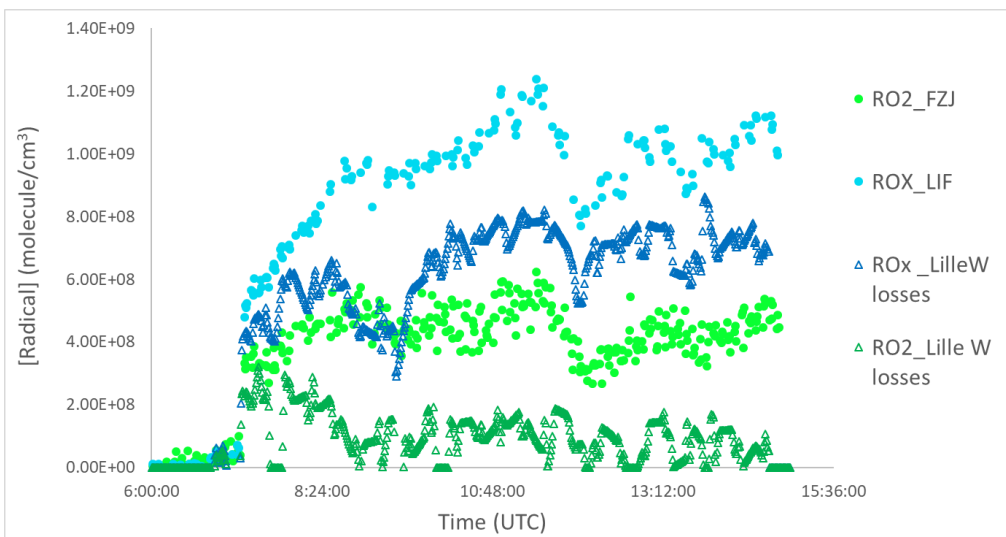
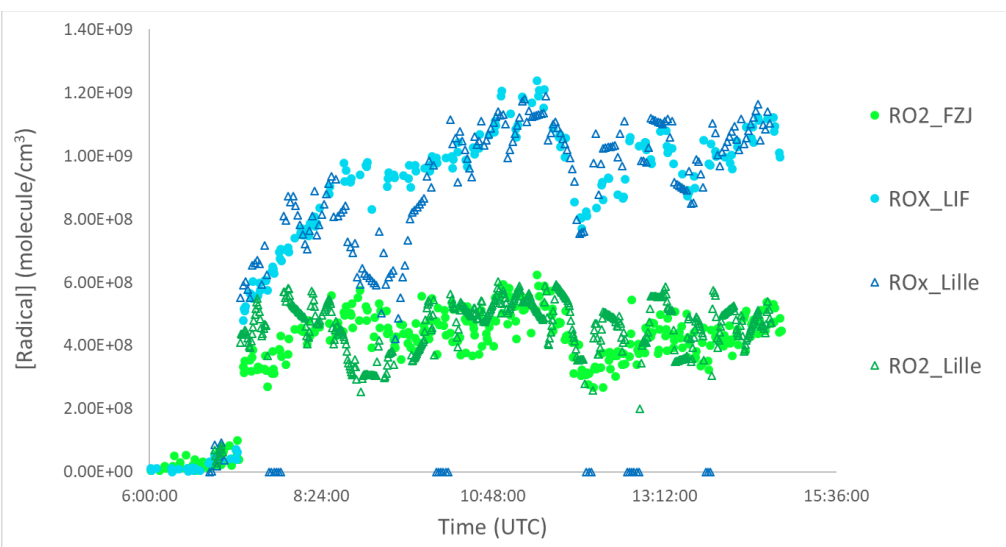
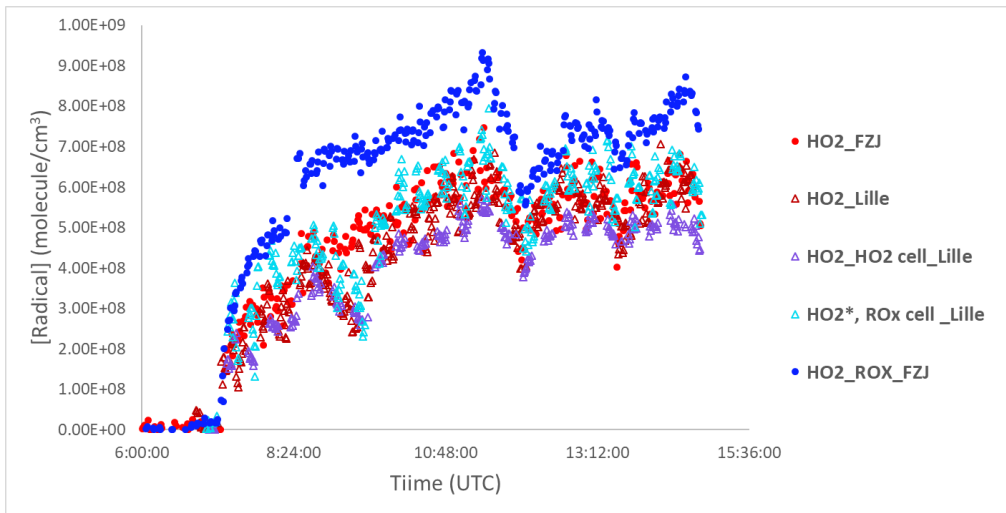
- β -pinene photooxidation experiment done on August 14:



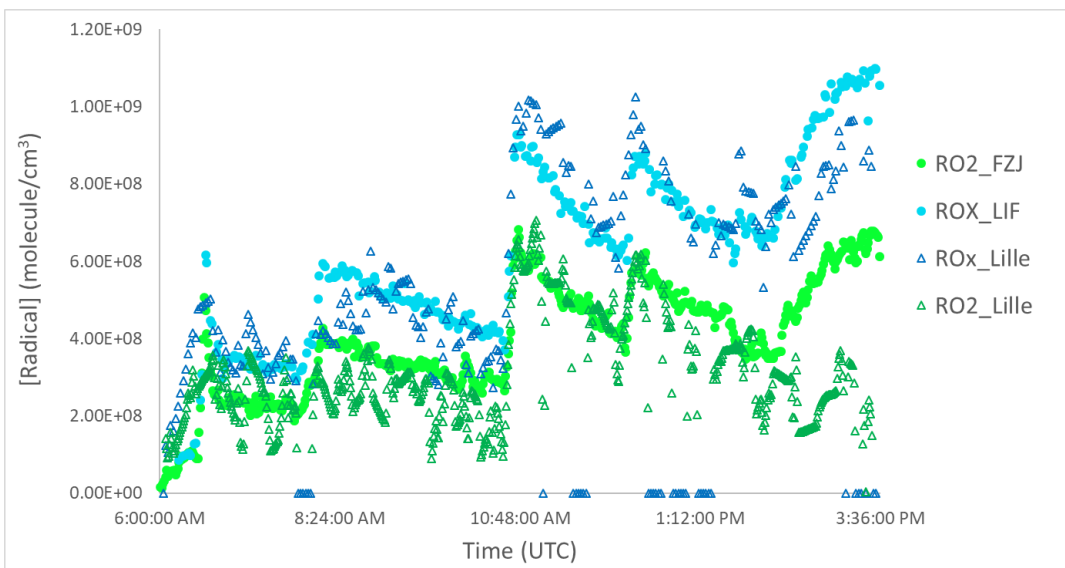
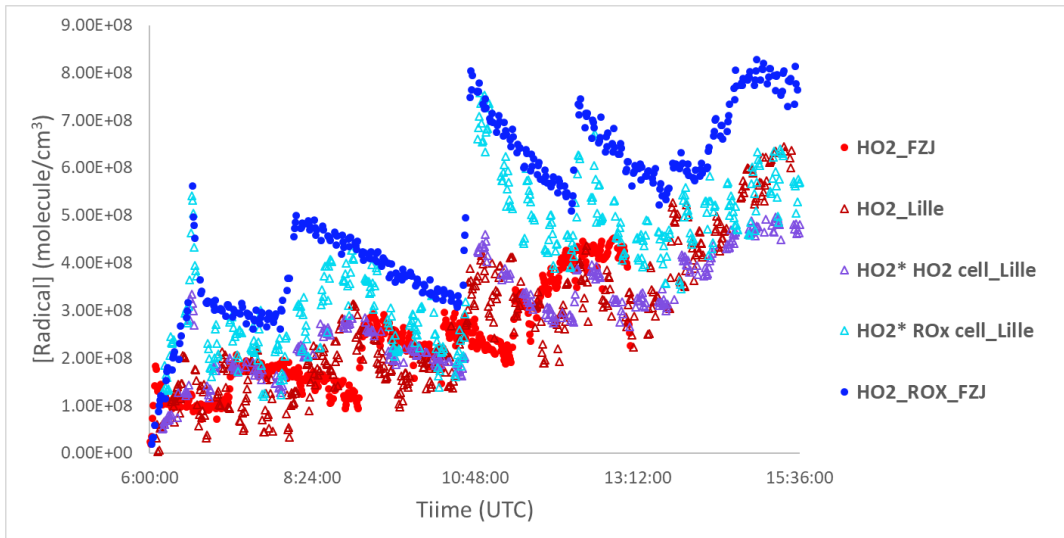
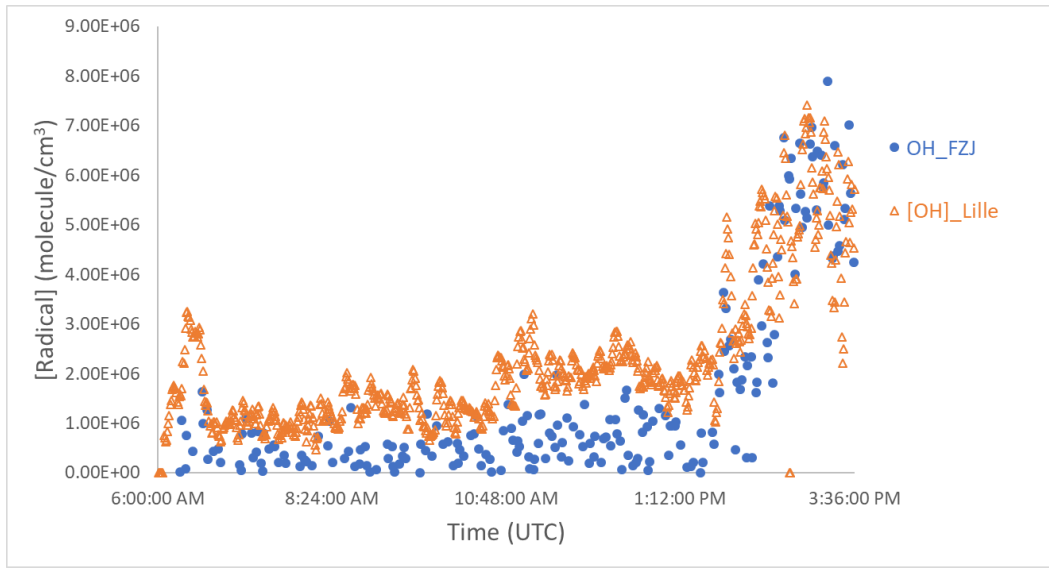


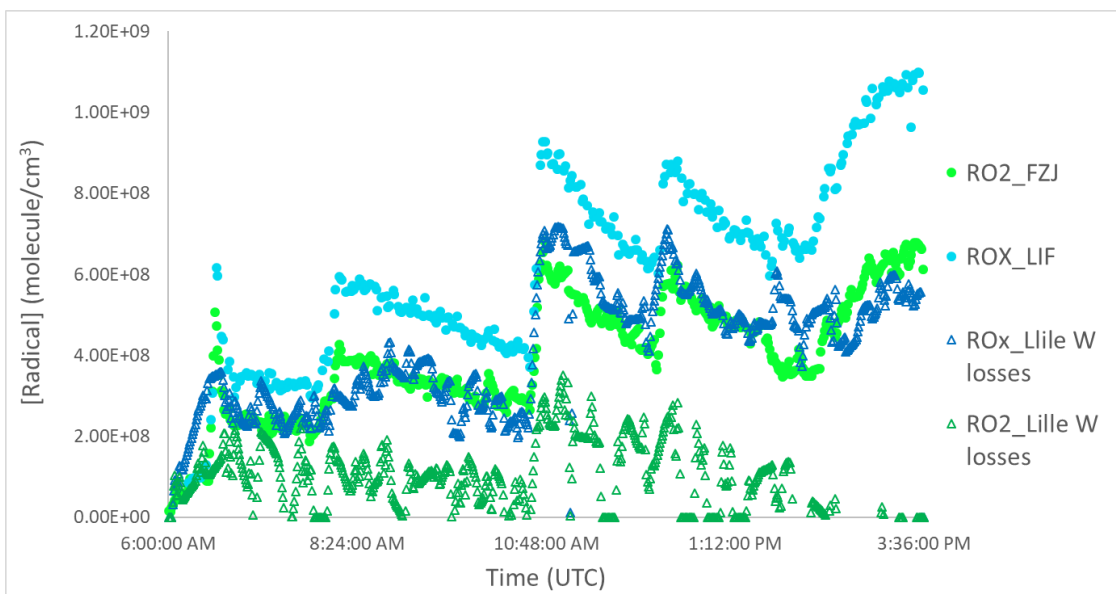
- β -pinene photooxidation experiment done on August 16:



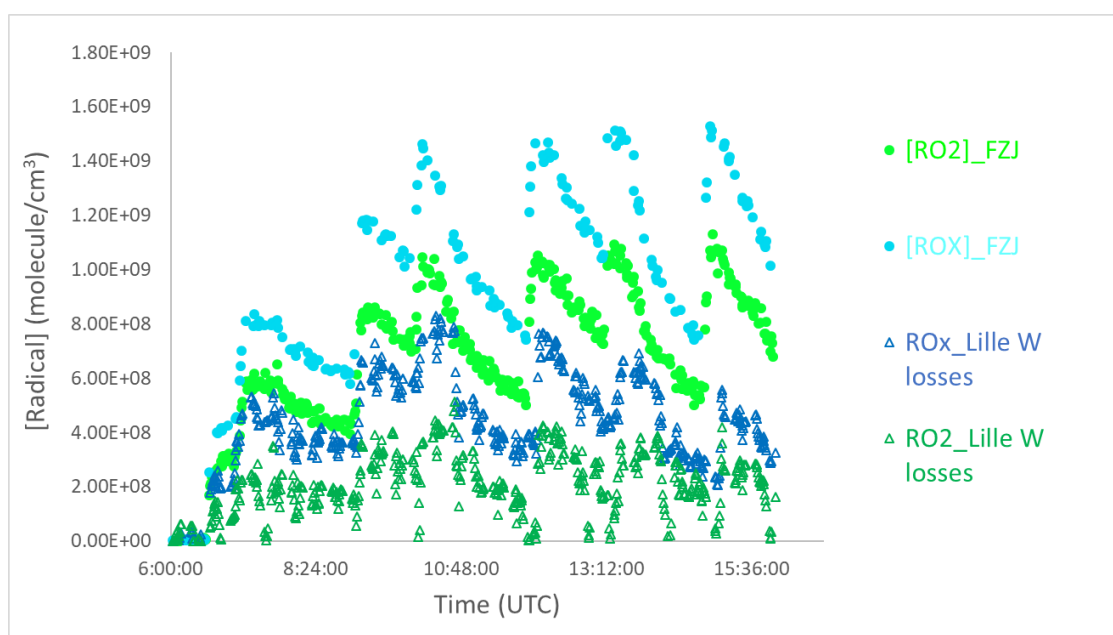


- Isoprene NO₃ oxidation experiment done on August 17:

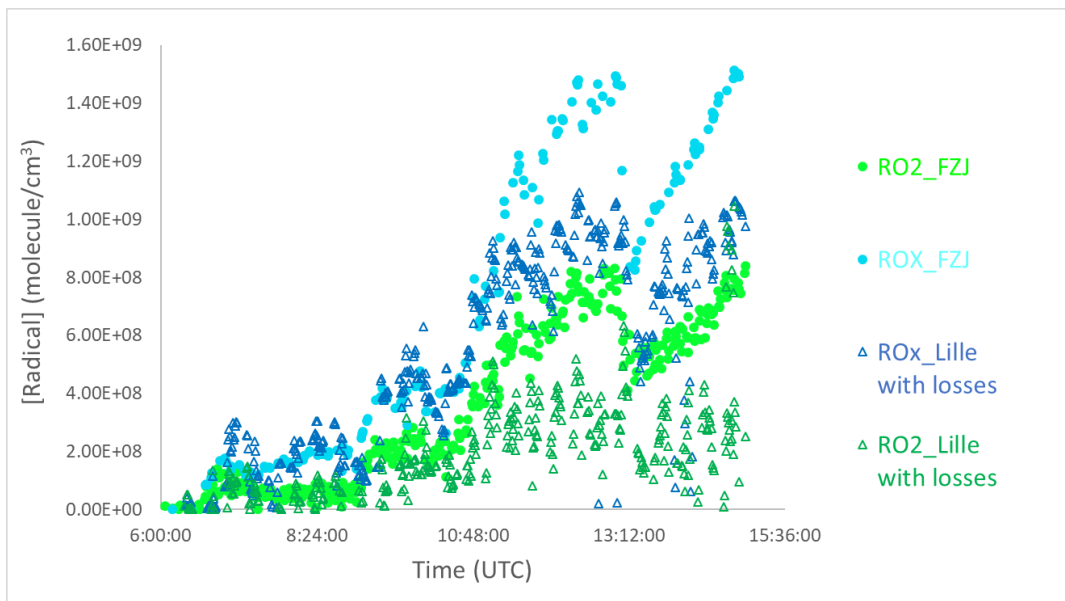
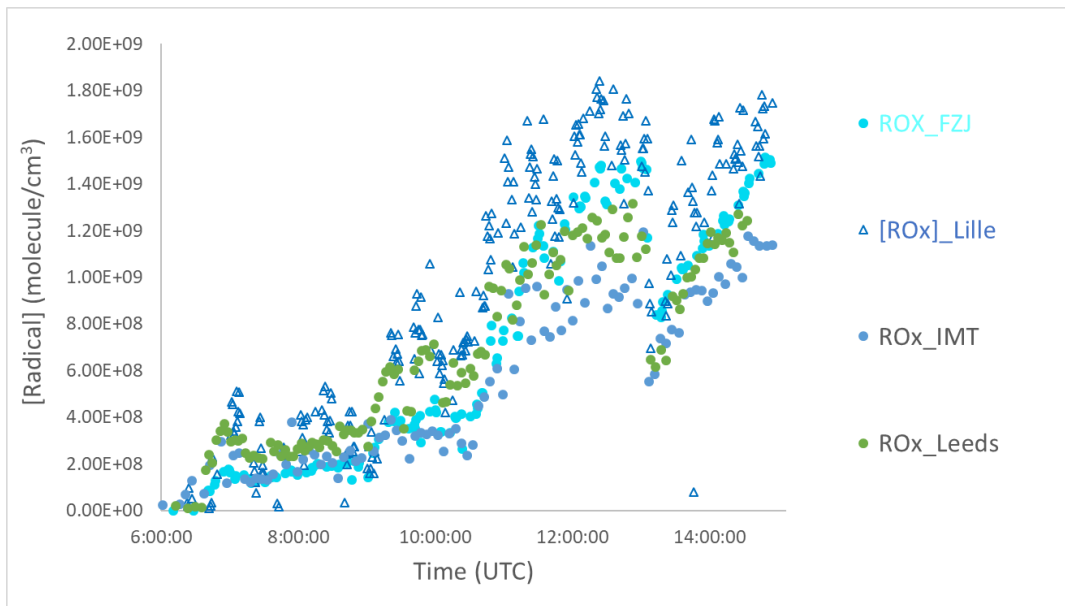




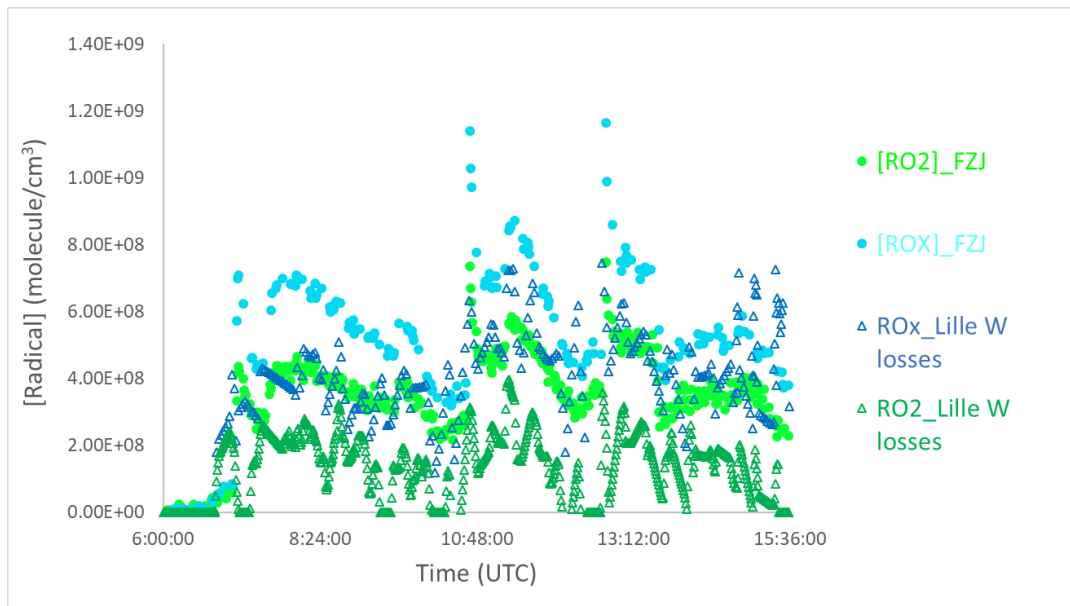
- Hexene ozonolysis: humidity change experiment done on August 19:



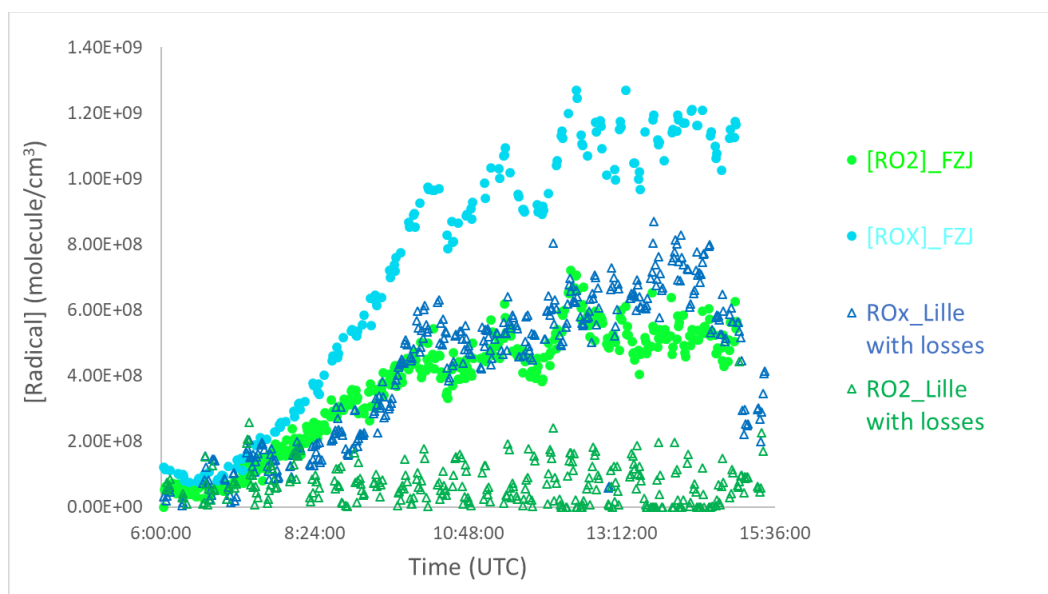
- CO/CH₄ oxidation by OH experiment done on August 20:



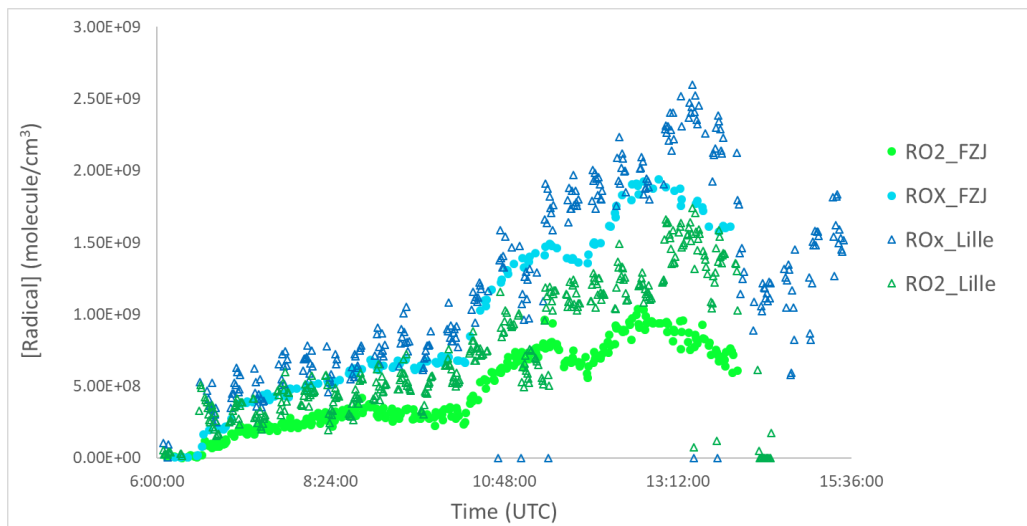
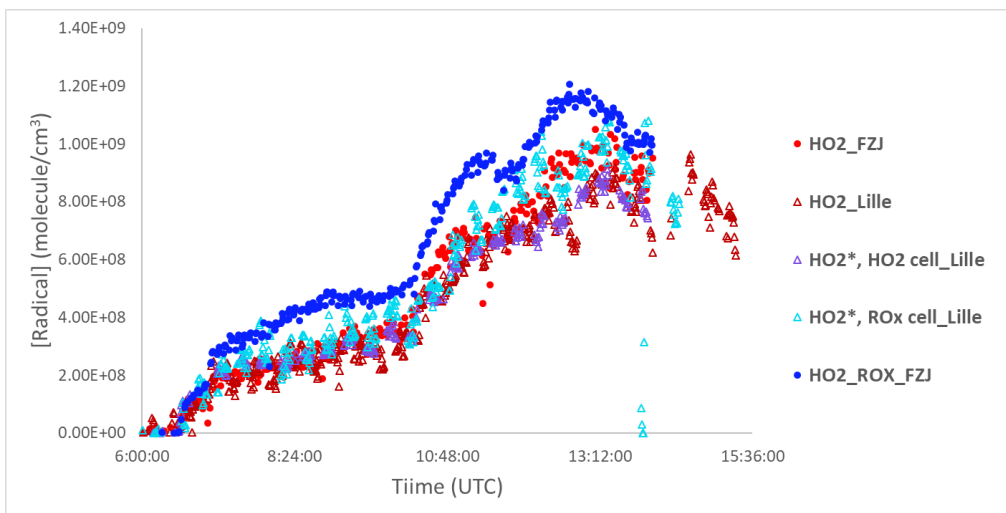
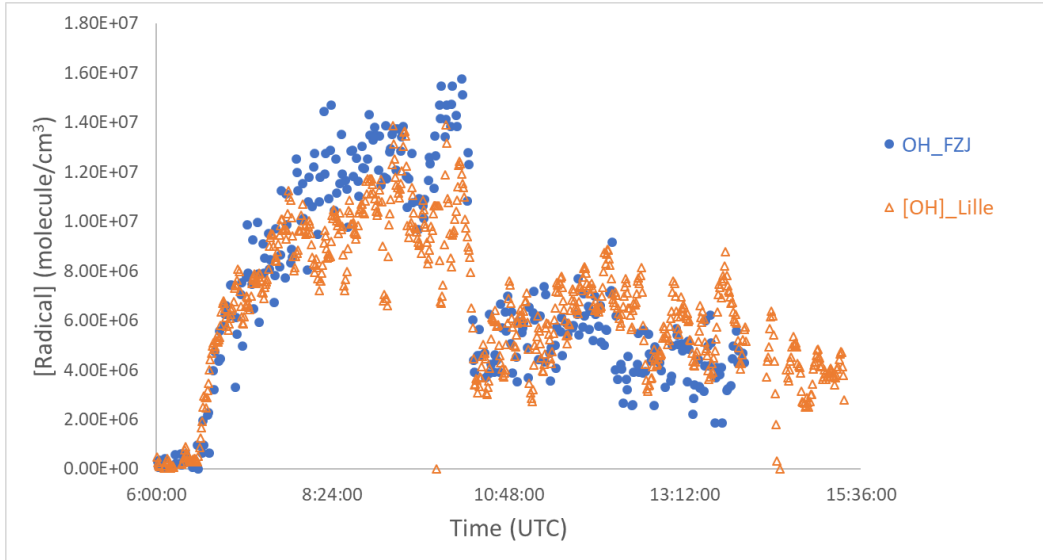
- β -pinene NO_3 oxidation experiment done on August 22:

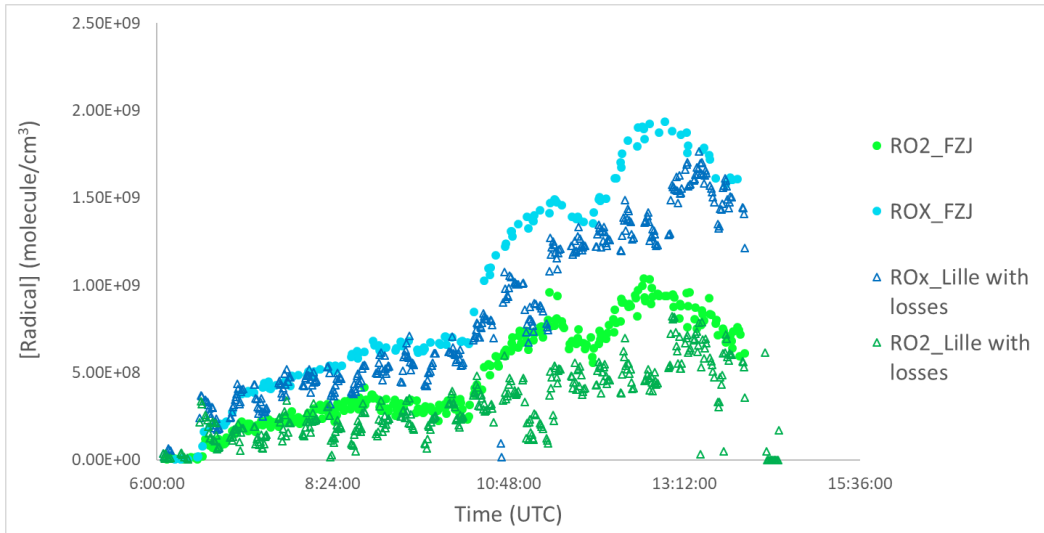


- Ambient air experiment done on August 23:

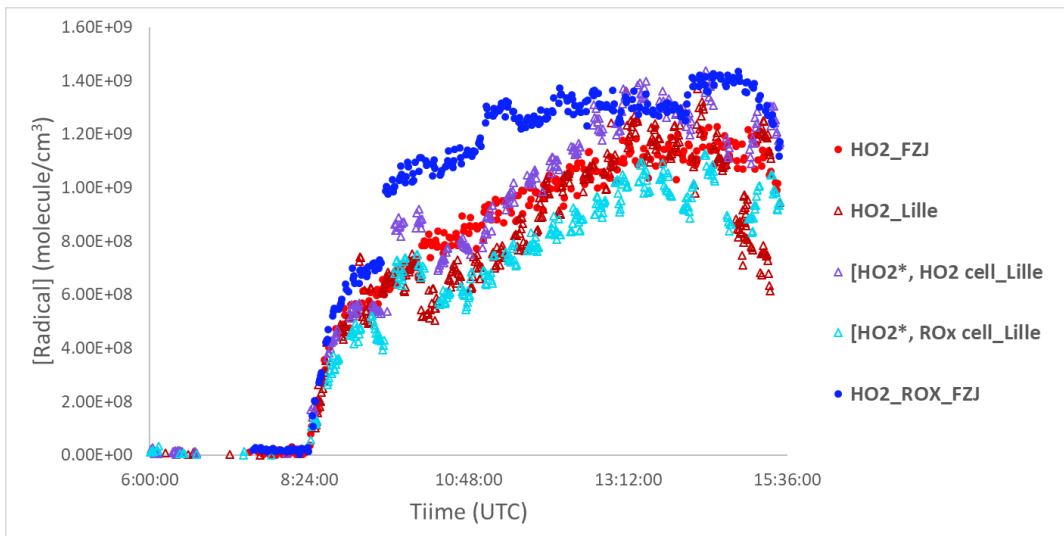
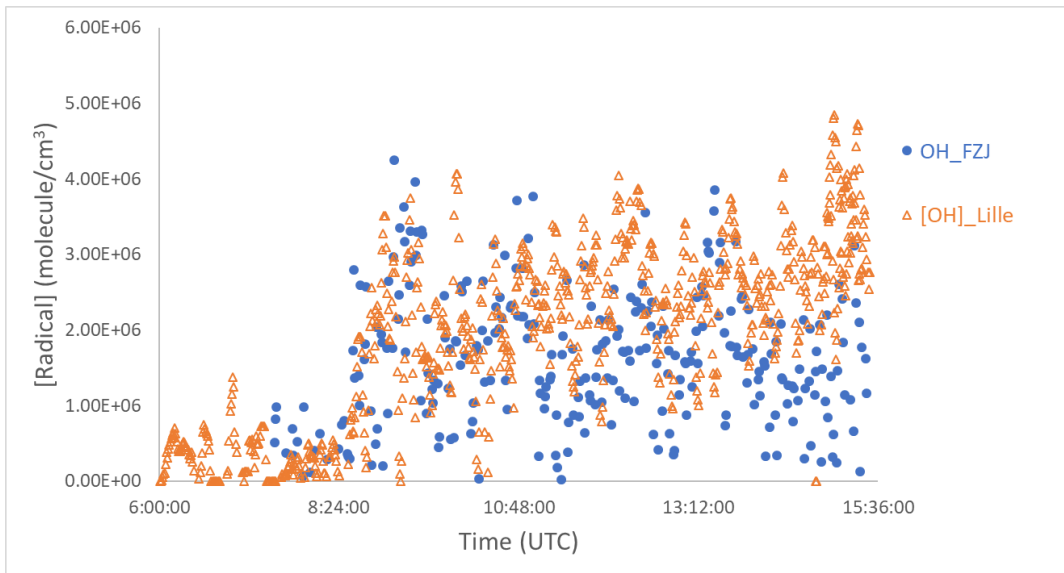


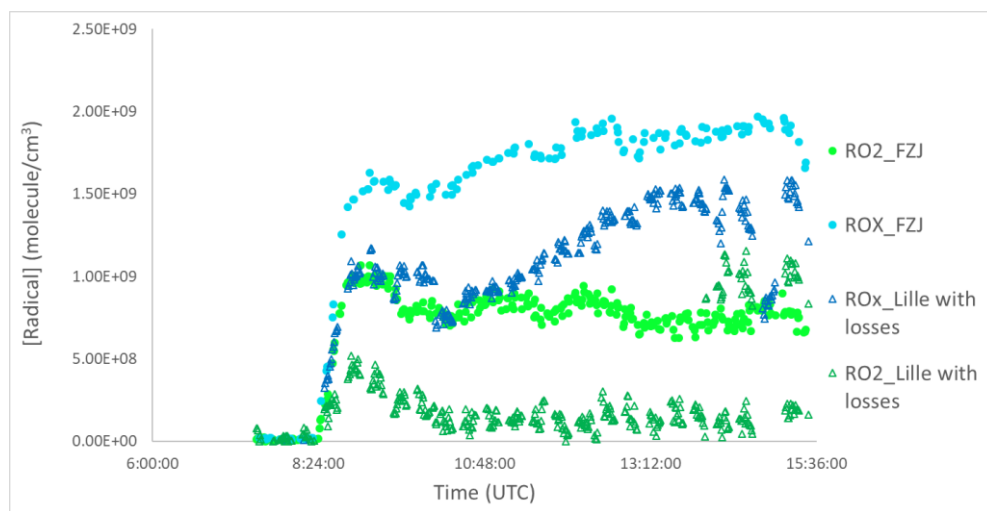
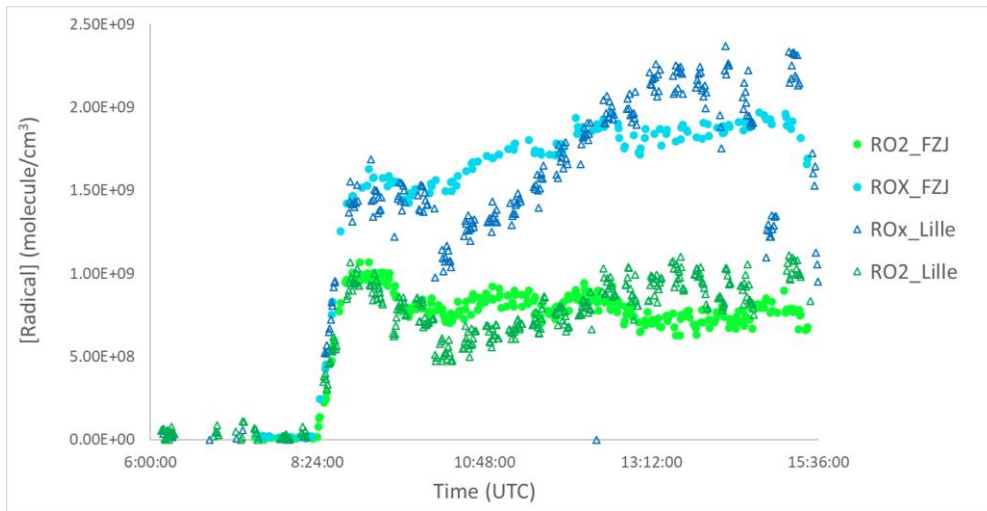
- MVK oxidation experiment done on August 24:



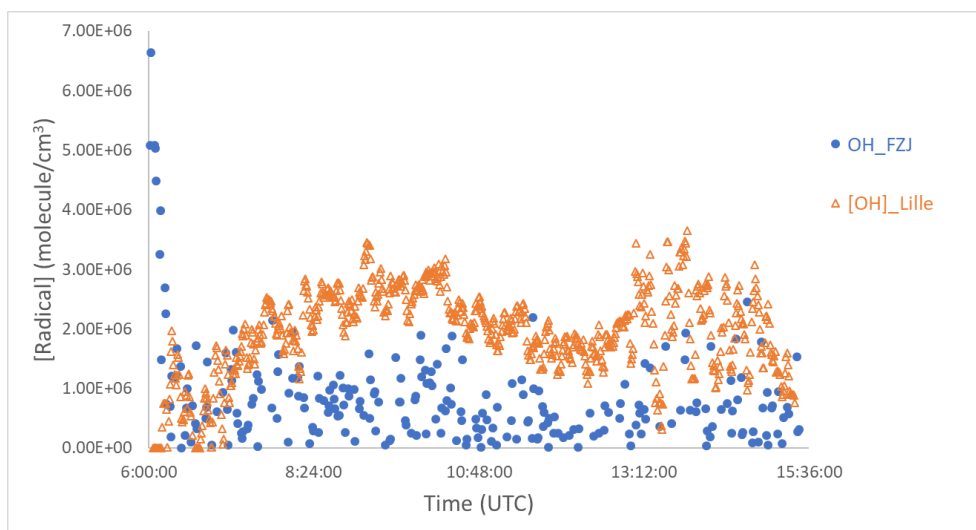


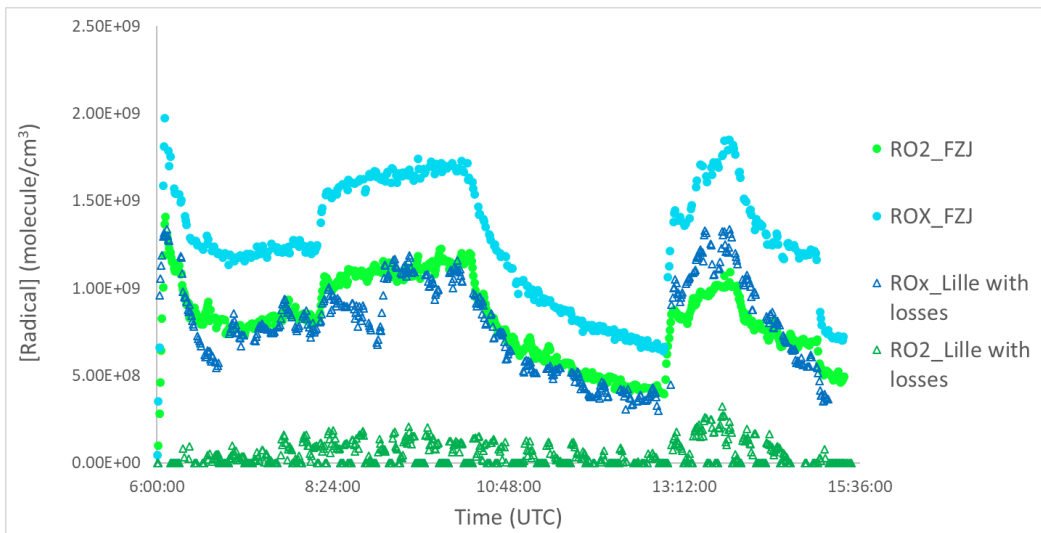
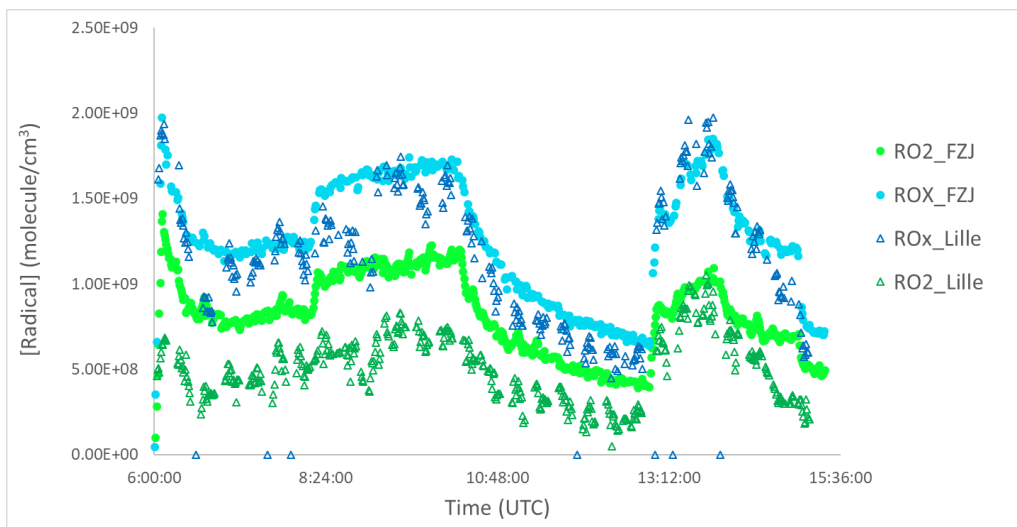
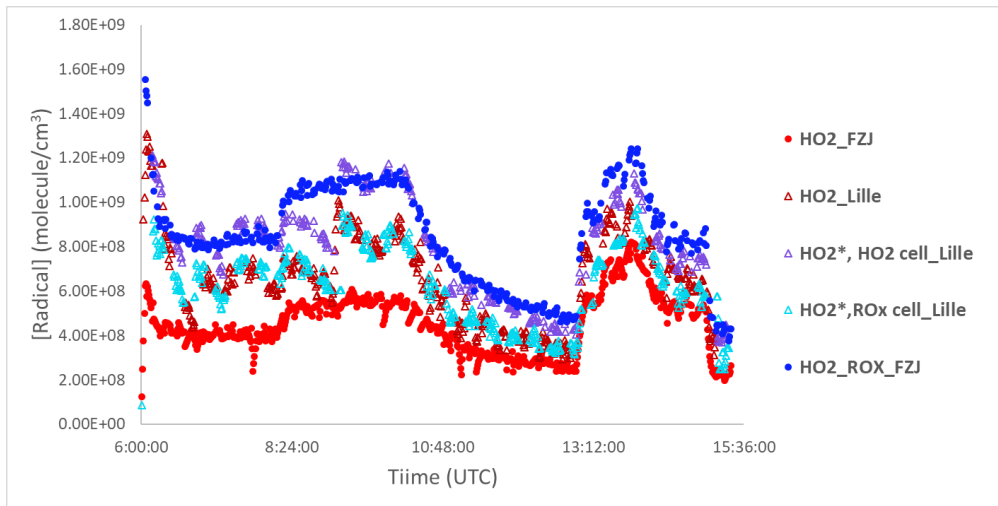
- Cl chemistry with isoprene experiment done on August 25:





- Isoprene, TME ozonolysis + photooxidation experiment done on August 26:





Résumé

Les radicaux HO_x ($\text{OH}+\text{HO}_2$) et RO_2 sont impliqués dans les processus d'oxydation en phase gazeuse, générant des produits secondaires ayant un impact sur la qualité de l'air et la santé humaine. La compréhension de ces processus d'oxydation par la quantification de ces radicaux reste un défi en raison de leurs faibles concentrations ($< \text{ppt}$) et de leur réactivité élevée. Il n'existe que quelques instruments dans le monde permettant d'effectuer de telles mesures, dont l'instrument de l'Université de Lille (UL-FAGE : Fluorescence Assay by Gas Expansion). Il est basé sur la détection par LIF (Laser Induced Fluorescence) de OH à basse pression. Il permet la mesure directe de OH et la mesure indirecte de HO_2 par conversion chimique en OH après l'ajout d'une faible concentration de NO à l'entrée de la cellule FAGE. Au cours de cette thèse, l'instrument a été amélioré pour la quantification des radicaux RO_2 . Deux mesures complémentaires permettent d'accéder à la concentration de RO_2 , soit en utilisant la cellule HO_2 et en injectant une concentration élevée de NO à l'entrée de la cellule de détection, soit en couplant un réacteur de conversion RO_x à une cellule FAGE. Cette technique est basée sur la conversion chimique en deux étapes des radicaux RO_2 en HO_2 dans le réacteur de conversion couplé à une cellule FAGE. Nous pouvons également mesurer un autre paramètre en utilisant une cellule FAGE couplée à une cellule de photolyse : la réactivité d'OH (somme des pertes OH).

L'instrument UL-FAGE a été amélioré et utilisé au cours de cette thèse pour des mesures en laboratoire (configuration de réactivité) afin d'étudier les mécanismes d'oxydation importants pour la chimie intérieure et extérieure impliquant les radicaux HO_x . Au cours de l'été 2022, l'UL-FAGE a participé à une campagne d'intercomparaison RO_2 qui s'est déroulée dans la chambre SAPHIR (Jülich, Allemagne). Neuf groupes utilisant différents instruments ont participé à cette campagne. Les performances des instruments UL-FAGE pour la mesure de OH, HO_2 et RO_2 dans une large gamme de conditions chimiques atmosphériques (tels que la vapeur d'eau, le niveau en oxydes d'azote, la présence de divers composés organiques, chimie de jour et de nuit) ont été étudiées au cours de cette campagne. Enfin, l'UL-FAGE en configuration de quantification et de réactivité a été déployé pour une campagne de terrain (ACROSS) dans la forêt de Rambouillet, avec des mesures de réactivité à deux hauteurs différentes (au sol et au-dessus de la canopée) et des mesures de concentrations en radicaux au sol.

Mots-clés: Chimie atmosphérique, radicaux HO_x et RO_2 , instrument FAGE, campagnes de terrain, chambre de simulation, études cinétique